



## Nagoya City University Academic Repository

学位の種類	博士（芸術工学）
報告番号	甲第1833号
学位記番号	第20号
氏名	Phuntsho Wangmo
授与年月日	令和3年3月24日
学位論文の題名	Seismic Vulnerability Assessment and Possible Strengthening Strategies for Traditional Bhutanese Rammed Earth Residential Houses（ブータンの伝統的版築住宅の地震脆弱性評価と可能な補強計画）
論文審査担当者	主査： 青木 孝義 副査： 木村 俊明， 溝口正人， 中川 隆， Kshitij Charana SHRESTHA

**Seismic Vulnerability Assessment and Possible Strengthening  
Strategies for Traditional Bhutanese Rammed Earth  
Residential Houses**

**ブータンの伝統的版築住宅の地震脆弱性評価と可能な補強計画**

**Phuntsho Wangmo**

A thesis submitted in partial fulfilment  
of the requirements for the degree of  
Doctor of Philosophy

Graduate School of Design and Architecture

Nagoya City University

March 2021

## **Acknowledgement**

This thesis would not have been possible without the support of many people. I take this opportunity to extend my sincere gratitude and appreciation to all those who contributed to this thesis.

First of all, I would like to express my gratitude to Professor Takayoshi Aoki for seeing the potential in me amongst other candidates and accepting me to pursue PhD under his guidance. I am grateful for his support and guidance that he provided all along these years.

I am also grateful to Associate Professor Kshitij Charana Shrestha for his advice and who was always willing to share his experience and expertise through these three years. He taught me how to be a researcher and will always be grateful.

A special thanks to Associate Professor Mitsuhiro Miyamoto of Kagawa University, Associate Professor Jingyao Zhang of Kyoto University, Associate Professor Noriyuki Takahashi of Tohoku University for their time to read my manuscript and for their valuable reviews and comments. Further, thanks to my Exam Committee members Professor Masato Mizoguchi, Lecturer Toshiaki Kimura and Associate Professor Ryu Nakagawa for their role in making this thesis more valuable.

The part of this research work was conducted in the Research Equipment Sharing Center at Nagoya City University. I, therefore, thank its staff, in particular, Mr. Kenji Kawakami, who shared with me the “weight” of all the specimen preparation and experimental activities.

A part of this research was conducted in Bhutan. Therefore, I would like to thank my office colleagues from Department of Culture, Ministry of Home and Cultural Affairs, Royal Government of Bhutan, particularly Engineer Pema, Engineer Kunzang Tenzin, Engineer Ugyen Dorji and Technician Lhendup for monitoring the all construction works and assisting in experimental works.

I acknowledge the financial support from the JST/JICA, SATREPS (Science and Technology Research Partnership for Sustainable Development) project (Grant No. JPMJSA1611) and JSPS KAKENHI (Grant No. 16H06363).

Lastly, I would like to thank my family for all their love and encouragement. A special thanks to my husband, Khagesh, for his support, patience and understanding throughout this journey.

## **Abstract**

Bhutan has a rich repository of rammed earth structures, which includes an excellent variety of architectures ranging from simple houses to magnificent fortresses. These structures are preserved and promoted as cultural heritage buildings. However, their performance during the recent earthquakes was found very poor, where the seismic intervention was deemed necessary. Studies on rammed earth structures are limited, and the ones available do not necessarily represent the actual behaviour of typical Bhutanese rammed earth buildings.

In this context, this thesis focuses on the investigation of Bhutanese rammed earth walls achieved through an experimental program under various loading conditions and theoretical analysis. The experimental campaign involves from conducting the material test to understand the essential characteristics of soil used for rammed earth buildings, element test on reduced scale wall, out-of-plane test on full-scale walls, and finally full-scale test on real sized prototype building. Appropriate and feasible strengthening measures are proposed for both new construction and existing buildings. Mesh-wrap retrofitting technique is proposed for existing buildings, and RC bands and RC posts are proposed for new constructions. Conventional fragility curves are developed based on the Capacity Spectrum Method. Further, the thesis also presents the finite element modelling to reproduce the experimental observation.

***Keywords: Rammed earth, compression behaviour, in-plane behaviour, out-of-plane behaviour, full-scale test, retrofitting, strengthening, finite element modelling, Bhutan.***

## List of Tables

Table 1.1 Advantages and disadvantages of rammed earth walls. ....	2
Table 1.2 Damage to structures by recent earthquakes.....	5
Table 2.1 British soil classification based on grain size. ....	13
Table 2.2 EMS 98 Vulnerability Table.....	17
Table 2.3 Failure mechanism observed in rammed earth buildings under seismic action. ....	20
Table 2.4 Material properties of unstabilised rammed earth. ....	22
Table 2.5 Soil used in the study. ....	26
Table 2.6 Influence of specimen size on the compaction energy. ....	30
Table 2.7 Proposed strengthening measures for new construction.....	32
Table 2.8 Proposed strengthening measures for the existing building. ....	34
Table 3.1 Material properties of unstabilised rammed earth. ....	45
Table 3.2 Summary of test results from the literature available on RE wall under in-plane loading. .....	46
Table 3.3 Sample preparation details for Proctor test.....	49
Table 3.4 Material properties of retrofitting materials.....	54
Table 3.5 Test matrix for element test under compression.....	55
Table 3.6 Summary of compression test results. ....	64
Table 3.7 Test matrix for element test under shear.....	68
Table 3.8 Shear test summary.....	76
Table 3.9 Mohr-Coulomb parameters of RE wallettes. ....	80
Table 3.10 Recommended values for numerical analysis of rammed earth. ....	85
Table 3.11 Material properties for FE model.....	88
Table 3.12 Experimental and FE results. ....	90
Table 3.13 Parameters considered for sensitivity analysis and their corresponding FE-IDs.....	94
Table 3.14 Interface layer parameters for sensitivity analysis and their corresponding FE-IDs..	94
Table 3.15 Sensitivity analysis for retrofitted RE wall and their corresponding FE-IDs. ....	96
Table 4.1 Material characterization of rammed earth samples. ....	120
Table 4.2 Reported mechanical characteristics of rammed earth samples. ....	121
Table 4.3 Result of a material test of PCC.....	123
Table 4.4 Material properties of stabilized mud mortar. ....	124
Table 4.5 Material properties of timber specimens. ....	126
Table 4.6 Peak load and corresponding displacement in each sensor of U-RE.....	129
Table 4.7 Peak load and corresponding displacement in each sensor of Mesh-RE.....	131
Table 4.8 Peak load and corresponding displacement in each sensor of Timber-RE.....	132
Table 4.9 Peak load and corresponding displacement in each sensor of New-RE-A.....	135
Table 4.10 Peak load and corresponding displacement in each sensor of New-RE_B. ....	137
Table 4.11 Material properties for FE model.....	142
Table 4.12 Experimental and FE results for the pull-down tests. ....	142
Table 4.13 Details for parametric study of micro-model. ....	144
Table 4.14 Material parameters for sensitivity study and corresponding FE model IDs. ....	146
Table 4.15 Properties of rammed earth from material characterization tests. ....	151
Table 4.16 Material properties of rammed earth from material characterization tests. ....	159
Table 5.1 Maximum wall length in each floor level.....	171
Table 5.2 Floor height in each floor level.....	171

Table 5.3 Aspect ratio in each floor level. ....	171
Table 5.4 Shear span ratio in each floor level.....	172
Table 5.5 Standard and minimum wall length (mm/m <sup>2</sup> ).....	172
Table 5.6 Judgment for wall length (mm/m <sup>2</sup> ).....	173
Table 5.7 Dead load and live load. ....	174
Table 5.8 Vibration Characteristics Factor. ....	175
Table 5.9 Classification of soil. ....	176
Table 5.10 Value of $\beta$ for different soil foundation systems. ....	176
Table 5.11 Parameters for the structural calculations.....	177
Table 5.12 Summary of structural calculation for seismic shear force.....	177
Table 5.13 Lateral Force distribution in each floor. ....	178
Table 5.14 Allowable unit stress.....	179
Table 5.15 Confirmation results of shear stress for medium-level EQ.....	179
Table 5.16 Allowable shear stress for a large-level earthquake. ....	179
Table 5.17 Storey drift angle verification. ....	180
Table 5.18 Stiffness ratio verification.....	180
Table 5.19 Eccentricity ratio verification. ....	181
Table 5.20 Confirmation results for third phase of seismic design. ....	182
Table 5.21 Material characterization of rammed earth samples.....	197
Table 5.22 Result of a material test of PCC.....	199
Table 5.23 Result of a material test of cement mortar.....	200
Table 5.24 Limit states for rammed earth building.....	219

## List of Figures

Figure 1.1 Regions having rammed earth structures. ....	2
Figure 1.2 Details of traditional formwork and ramming tools. ....	3
Figure 1.3 Rammed earth structures (DCHS).....	3
Figure 1.4 Historical earthquakes larger than magnitude M5 in South Asia since 1960.....	4
Figure 1.5 Summary of earthquakes: (a) Narang Earthquake, (b) Sikkim Earthquake . ....	5
Figure 1.6 Rammed earth buildings damaged by the 2011 earthquake. ....	6
Figure 1.7 Scope of work.....	9
Figure 2.1 Soil profile with different layers.....	12
Figure 2.2 Lower and upper range limits of the particle size distribution of rammed earth construction.....	13
Figure 2.3 Recommended envelopes for RE construction by Houben and Guillaud. ....	14
Figure 2.4 Traditional wooden formwork.....	15
Figure 2.5 Traditional wooden ramming tools. ....	16
Figure 2.6 Damages observed in rammed earth houses: (a) structural collapse; (b) gable wall fall-over; (c) longitudinal wall fall-over, (d) vertical corner crack; (e) Crack at loading point. ....	19
Figure 2.7 Specimens and apparatus for: (a) Direct tension test; (b) Splitting test. ....	23
Figure 2.8 Tensile strength vs compressive strength: (a) Bui et al.; (b) DCHS. ....	24
Figure 2.9 Tensile strength as a function of water content.....	24
Figure 2.10 Diagonal compression test: (a) Test setup; (b) Shear stress vs shear strain. ....	25
Figure 2.11 Variation of compressive strength with moisture content. ....	26
Figure 2.12 Variation of compressive strength with dry density.....	27
Figure 2.13 Variation of dry density with water content. ....	28
Figure 2.14 Variation of dry density with number of blow and hammer weight. ....	29
Figure 2.15 Variation of dry density with drop distance of rammer. ....	29
Figure 2.16 Effect of layer thickness in compressive strength: (a) In dry state; (b) In wet state. ....	31
Figure 2.17 Test set up and placement of post-tensioned bar: (a) Out-of-plane; (b) In-plane. ....	33
Figure 2.18 Proposed seismic measures for new construction. ....	34
Figure 2.19 Retrofitting with tarpaulin: (a) In horizontal direction; (b) In diagonal direction.....	35
Figure 2.20 Model details tested under shaking table.....	35
Figure 2.21 Overview of shaking table set up and steel plate placement. ....	36
Figure 2.22 Reinforcement layout details. ....	36
Figure 2.23 Strengthening procedures with polyester fabric strips in vertical. ....	37
Figure 3.1 Lift and layer in rammed earth wall. ....	47
Figure 3.2 Particle size distribution of soil used for preparing specimens. ....	48
Figure 3.3 Range limits for particle size distribution for natural rammed earth: (a) Lower; (b) Upper .....	48
Figure 3.4 Proctor test results: (a) Relationship between density and water content; (b) Relationship between compressive strength and drying period; (c) Relationship between moisture content and drying period. ....	49
Figure 3.5 Specimen preparation process. ....	50
Figure 3.6 Temperature and relative humidity recorded during drying time. ....	51
Figure 3.7 Compaction difference within the layer in microscopic view and specimen. ....	52
Figure 3.8 Comparing mechanical characteristics with the previous study: (a) Compressive strength vs density; (b) Compressive strength vs Young's modulus.....	52



Figure 3.9 Retrofitting details: (a) Fixation of mesh and screws; (b) Final view after plastering.	53
Figure 3.10 Material test: (a) test setup; (b) results; (c) failure pattern.	54
Figure 3.11 Tensile coupon test: (a) Setup; (b) Stress-strain graph; (c) Typical failure pattern.	55
Figure 3.12 Compression test setup: (a) Schematic diagram; (b) Instrumentation; (c) Close up view of specimen.	56
Figure 3.13 Stress-strain relationship of one month dried specimen.	57
Figure 3.14 Failure pattern of U-100-C1-1.	57
Figure 3.15 Compressive stress vs strain of 100 mm wallettes dried for three months.	58
Figure 3.16 Failure pattern of U-100-C3-1.	59
Figure 3.17 Failure pattern of U-100-C3-2.	59
Figure 3.18 Compressive stress vs strain of 100 mm wallettes dried for twelve months.	60
Figure 3.19 Failure pattern of U-100-C12-1.	60
Figure 3.20 Failure pattern of U-100-C12-2.	60
Figure 3.21 Compressive stress vs strain of 50 mm wallettes dried for three months.	61
Figure 3.22 Failure pattern of U-50-C3-1.	61
Figure 3.23 Failure pattern of U-50-C3-2.	62
Figure 3.24 Compressive stress vs strain of 50 mm wallettes dried for twelve months.	62
Figure 3.25 Failure pattern of U-50-C12-1.	63
Figure 3.26 ASTM standard of calculating young's modulus for thermal insulation material.	63
Figure 3.27 Typical failure patterns of RE wallettes observed under compression loading.	64
Figure 3.28 Effects of drying period in compressive strength.	65
Figure 3.29 Relationship between stress and strain.	66
Figure 3.30 Relationship between stress and strain.	67
Figure 3.31 Failure observed in retrofitted RE wallettes.	68
Figure 3.32 Shear test setup and instrumentation.	69
Figure 3.33 Shear load vs displacement of 100 mm wallettes dried for three months.	70
Figure 3.34 Failure pattern of U-100-S3-0.1.	71
Figure 3.35 Failure pattern of U-100-S3-0.15.	71
Figure 3.36 Failure pattern of U-100-S3-0.2.	71
Figure 3.37 Shear load vs displacement of 100 mm wallettes dried for twelve months.	72
Figure 3.38 Failure pattern of U-100-S12-0.1.	72
Figure 3.39 Failure pattern of U-100-S12-0.15.	73
Figure 3.40 Failure pattern of U-100-S12-0.2.	73
Figure 3.41 Shear load vs displacement of 50 mm wallette dried for three months.	74
Figure 3.42 Failure pattern of U-50-S3-0.15.	74
Figure 3.43 Failure mode of U-50-S3-0.2.	74
Figure 3.44 Shear load vs displacement of 50 mm wallettes dried for twelve months.	75
Figure 3.45 Failure pattern of U-50-S12-0.15.	75
Figure 3.46 Failure pattern of U-50-S12-0.2.	75
Figure 3.47 Illustration showing the calculation of: (a) Energy absorption; (b) Ductility from the load-displacement curve.	76
Figure 3.48 Typical failure mode of RE wallettes observed under shear loading.	77
Figure 3.49 Shear strength of RE wallettes with varying drying periods.	77
Figure 3.50 Shear load vs displacement of 100 mm and 50 mm layered RE wallettes.	78
Figure 3.51 Mohr-Coulomb failure envelopes of rammed earth wall.	79
Figure 3.52. Shear load vs displacement of unreinforced and retrofitted RE wallettes.	81

Figure 3.53 Final failure mode of RE wallettes under in-plane shear loading. ....	81
Figure 3.54 Comparison of the numerical and experimental results. ....	82
Figure 3.55 Comparison of the numerical and experimental results under: (a) Compression loading; (b) Diagonal shear without interface; (c) Diagonal shear with interface.....	83
Figure 3.56 Behaviour of macro and micro models: (a) Using initial parameters; (b) After calibration. ....	85
Figure 3.57 Shear force vs shear displacement for experimental and FE simulation.....	86
Figure 3.58 Modeling strategies for masonry structures. ....	87
Figure 3.59 Material model adopted for FE.....	89
Figure 3.60 FE model: (a) Mesh for macro model; (b) Mesh for micro model of 100 mm layer.	90
Figure 3.61 Experimental and FE results of unreinforced RE wallettes of 100 mm layer. ....	91
Figure 3.62 Experimental and FE results of unreinforced RE wallettes of 50 mm layer. ....	91
Figure 3.63 Failure mode observed in FE model of unreinforced RE wall of 100 mm layer. ....	92
Figure 3.64 Failure mode observed in FE model of unreinforced RE wall of 50 mm layer. ....	92
Figure 3.65 Experimental and FE results of strengthened wallettes of 50 mm layer. ....	93
Figure 3.66 Failure mode observed in FE model of strengthened RE wall of 50 mm layer. ....	93
Figure 3.67 Results of sensitivity analysis showing shear load-displacement diagram under varying parameters considered.....	95
Figure 3.68 Results of sensitivity analysis for normalized peak horizontal load, under varying parameters considered.....	95
Figure 3.69 Results of sensitivity analysis showing shear load-displacement diagram under varying stress-strain curve of mesh composite: (a) User-defined tensile stress-strain curve of mesh composite; (b) 50 mm layer RE wall with vertical stress 0.15 MPa, (c) 50 mm layer RE wall with vertical stress 0.2 MPa. ....	96
Figure 4.1 Details of U-RE. ....	104
Figure 4.2 Construction process details of U-RE. ....	105
Figure 4.3 Grain size distribution of the soil used for specimens.....	106
Figure 4.4 Material test: (a) test setup; (b) test results.....	107
Figure 4.5 Details of mesh-wrap retrofitted rammed earth specimen (Mesh-RE). ....	108
Figure 4.6 Construction details of retrofitted rammed earth specimen (Mesh-RE). ....	109
Figure 4.7 Details of timber frame retrofitting method. ....	110
Figure 4.8 Construction details of Timber-RE. ....	111
Figure 4.9 Details of reinforced rammed earth specimen of New-RE-A. ....	112
Figure 4.10 Reinforcing method practised in vernacular buildings in Bhutan. ....	113
Figure 4.11 Construction details of New-RE-A. ....	113
Figure 4.12 Details of reinforced rammed earth specimen (New-RE-B). ....	114
Figure 4.13 RC post and reinforcement details. ....	115
Figure 4.14 RC wedge and reinforcement details.....	115
Figure 4.15 RC band and reinforcement details. ....	116
Figure 4.16 The sequence of placing strengthening components in New-RE-B.....	117
Figure 4.17 Construction process details of New-RE-B.....	117
Figure 4.18 Sample collection for the material test. ....	118
Figure 4.19 Material test setup and instrumentation.....	119
Figure 4.20 Material test results of rammed earth. ....	121
Figure 4.21 Failure patterns observed: (a) Tensile test; (b) Compression test. ....	122
Figure 4.22 Test set up for material characterization of PCC.....	122

Figure 4.23 Test set up for material characterization of stabilized mud mortar. ....	123
Figure 4.24 Test results: (a) Stress-strain curve; (b) Failure patterns. ....	124
Figure 4.25 Test set up of 3-point bending test. ....	125
Figure 4.26 Test results from bending test. ....	126
Figure 4.27 Overview of out-of-plane pull-down test. ....	127
Figure 4.28 Location of transducers: 3D representation and on the field. ....	128
Figure 4.29 Load-displacement curve of U-RE. ....	129
Figure 4.30 Failure mode of U-RE. ....	129
Figure 4.31 Relationship between pull-down load and horizontal displacement for Mesh-RE. ....	130
Figure 4.32 Failure mode of Mesh-RE. ....	131
Figure 4.33 Relationship between pull-down load and horizontal displacement for Timber-RE. ....	133
Figure 4.34 Failure mode observed for Timber-RE. ....	134
Figure 4.35 Load displacement relationship of New-RE-A. ....	135
Figure 4.36 Failure modes of New-RE-A. ....	136
Figure 4.37 Relationship between pull-down load and horizontal displacement for New-RE-B. ....	137
Figure 4.38 Failure mode for New-RE-B: (a) During loading; (b) Final failure. ....	138
Figure 4.39 FE mesh generated for micro-model. ....	140
Figure 4.40 Material models adopted in FE. ....	141
Figure 4.41 Experiment and FE results for pull-down test. ....	143
Figure 4.42 Failure modes observed for FE-macro. ....	143
Figure 4.43 Failure modes observed for FE-micro. ....	144
Figure 4.44 Pull-down force vs displacement for parametric study on micro models with variation in interface properties. ....	145
Figure 4.45 Failure patterns for FE models. ....	145
Figure 4.46 Pull-down force vs displacement for parametric study on micro models with variation in interface properties. ....	147
Figure 4.47 Comparison of parametric study for normalized response quantity. ....	148
Figure 4.48 Details of reinforced rammed earth specimen (RRE). ....	149
Figure 4.49 Details of: (a) Wedge; (b) Dowel; (c) Photo showing dowels and wedges at the site. ....	150
Figure 4.50 Details of: (a) Beam end anchorage; (b) Photo details of beam end anchorage at site. ....	150
Figure 4.51 Process of floor beam placement within the RE wall. ....	151
Figure 4.52 Pull-down test set up and location of displacement sensors. ....	152
Figure 4.53 Pull-down force versus deformation characteristics for Pull-down-1 test. ....	153
Figure 4.54 Damage of U-RE and R-RE specimens during “Pull-down-1” test. ....	154
Figure 4.55 Pull-down force versus deformation characteristics for “Pull-down-2” test. ....	155
Figure 4.56 Damage of U-RE and R-RE specimens during “Pull-down-2” test. ....	155
Figure 4.57 Test specimen details and measuring points: (a) R-120-S; (b) R-60-S. ....	157
Figure 4.58 Specimen construction: (a) Insertion of RC dowel; (b) RC dowel details. ....	157
Figure 4.59 Material characterization test. ....	158
Figure 4.60 Compressive test results on cylindrical core samples at 6 months drying period. ..	159
Figure 4.61 Test set up and instrumentation for R-120-S. ....	160
Figure 4.62 Shear force vs shear displacement: Experimental and Theoretical. ....	160

Figure 4.63 Failure pattern observed for U-120-S, R-120-S and R-60-S.....	162
Figure 5.1 Classification of traditional houses based on the plans [4]. .....	167
Figure 5.2 Rammed earth house with type D plan (Photo credit: NRICPT and DOC). .....	168
Figure 5.3 Plans of U-RE-SHORT. ....	169
Figure 5.4 Sections of U-RE-SHORT. ....	169
Figure 5.5 Elevations of U-RE-SHORT. ....	170
Figure 5.6 Lumped mass on the floor level. ....	173
Figure 5.7 Shape factor by stiffness ratio and Shape factor by eccentricity ratio. ....	182
Figure 5.8 Isometric view of U-RE-SHORT. ....	185
Figure 5.9 Shrinkage cracks observed in U-RE-SHORT during the drying period. ....	185
Figure 5.10 Isometric view of U-RE-LONG. ....	186
Figure 5.11 Shrinkage cracks observed in U-RE-LONG during the drying period. ....	186
Figure 5.12 Material test set up: (a) and (b); (c) test results. ....	187
Figure 5.13 Fastener and anchorage: (a) U-hook; (b) Anchor rod. ....	188
Figure 5. 14 Details of mesh–layout in U-RE-SHORT. ....	189
Figure 5.15 Retrofitting details of R-RE-SHORT. ....	190
Figure 5.16 Details of mesh–layout in U-RE-LONG. ....	191
Figure 5.17 Retrofitting details of R–RE-LONG. ....	191
Figure 5.18 Details of reinforced rammed earth specimen (New-RE-SHORT).....	192
Figure 5.19 RC post and reinforcement details. ....	193
Figure 5.20 RC band and reinforcement details. ....	194
Figure 5.21 Construction process of New-RE-SHORT.....	195
Figure 5.22 Sample extractions from wall: (a) Core sampling; (b) Extracted samples. ....	196
Figure 5.23 Test setup: (a) Compression test; (b) Tensile test. ....	197
Figure 5.24 Failure patterns observed: (a) Compression test; (b) Tensile test. ....	198
Figure 5.25 Test setup for plain cement concrete. ....	198
Figure 5.26 Failure patterns observed under compression test.....	199
Figure 5.27 Test setup: (a) Compression test; (b) Tensile test. ....	199
Figure 5.28 Failure patterns observed: (a) Compression test; (b) Tensile test. ....	200
Figure 5.29 Sample preparation for tensile coupon test. ....	201
Figure 5.30 Tensile coupon test set up with clevis type grip.....	201
Figure 5.31 Tensile coupon test results: (a) Stress-strain curve; (b) Failure pattern. ....	202
Figure 5.32 Overview of the fullscale test. ....	202
Figure 5.33 The test setup and instrumentations. ....	203
Figure 5.34 Test set up and instrumentation on the field (R-RE-LONG). ....	204
Figure 5.35 Sensor locations: (a) Loaded in short-span; (b) Loaded in long-span.....	204
Figure 5.36 Capacity curve of U-RE-SHORT.....	205
Figure 5.37 Failure mode of U-RE-SHORT.....	206
Figure 5.38 Capacity curve of U-RE-LONG.....	208
Figure 5.39 Failure mode of U-RE-LONG.....	209
Figure 5.40 Capacity curve of R-RE-SHORT.....	210
Figure 5.41 Failure mode of R-RE-SHORT.....	212
Figure 5.42 Capacity curve of R-RE-LONG.....	213
Figure 5.43 Failure modes of R-RE-LONG.....	215
Figure 5.44 Capacity curve of New-RE-SHORT.....	216
Figure 5.45 Cracks near RC posts of New-RE-SHORT.....	216

Figure 5.46 Failure modes of New-RE-SHORT.....	218
Figure 5.47 Limit states for: (a) U-RE-SHORT; (b) R-RE-SHORT; and (c) New-RE-SHORT. .....	219
Figure 5.48 Capacity curve of U-RE-SHORT in ADRS.....	221
Figure 5.49 (a) Response spectrum for medium soil; (b) Demand spectrum for Design Level earthquake.....	222
Figure 5.50 Performance point of U-RE-SHORT at various PGA level for medium soil. ....	224
Figure 5.51 Performance point of R-RE-SHORT at various PGA level for medium soil.....	224
Figure 5.52 Performance point of New-RE-SHORT at various PGA level for medium soil.....	225
Figure 5.53 Linear aggression analysis for: (a) U-RE-SHORT; (b) R-RE-SHORT; (c) New-RE- SHORT. ....	226
Figure 5.54 Fragility curve for (a) U-RE-SHORT; (b) R-RE-SHORT; (c) New-RE-SHORT. .	227
Figure 5.55 Comparisons of fragility curves at: (a) IO; (b) LS; (c) CP.....	227
Figure 6.1 Schematic illustration of compaction technique with steel plate .....	235

# Table of Contents

Acknowledgement .....	i
Abstract .....	iii
List of Tables .....	iv
List of Figures .....	vi
INTRODUCTION .....	1
1.1 Background .....	1
1.2 Motivation .....	2
1.2.1 Traditional Construction Practice in Bhutan: Rammed Earth .....	2
1.2.2 History of Earthquakes in Bhutan .....	4
1.2.3 Science and Technology Research Partnership for Sustainable Development (SATREPS) Projects .....	6
1.3 Aims and Objectives .....	7
1.4 Thesis Outline .....	9
References .....	10
AN OVERVIEW OF RAMMED EARTH .....	12
2.1 Rammed Earth Construction .....	12
2.1.1 Soil Classification .....	12
2.1.2 Particle Size Distribution .....	12
2.1.3 Formwork .....	14
2.1.4 Ramming Tools for Compaction .....	15
2.2 Vulnerability of Rammed Earth Buildings .....	16
2.2.1 Introduction .....	16
2.2.2 Vulnerability against Seismic Force .....	18
2.3 Mechanical Behaviour of Rammed Earth .....	22
2.3.1 Compressive strength .....	22
2.3.2 Tensile strength .....	22
2.3.3 Shear strength .....	25
2.4 Factors Influencing Mechanical Behaviour of Rammed Earth: Compressive Strength .....	25
2.4.1 Effect of Moisture content .....	25
2.4.2 Effect of Dry density .....	26
2.4.3 Effect of Rammed Earth Layer Thickness .....	30
2.5 Improving Mechanical Properties of Rammed Earth through Stabilization .....	31
2.5.1 Cement .....	31
2.5.2 Lime .....	31
2.5.3 Using Fibers .....	32
2.5.4 Using Dung .....	32
2.6 Strengthening Measures Proposed for Rammed Earth Structures .....	32
2.6.1 For New Construction .....	32
2.6.2 For Existing Buildings (retrofitting measures) .....	34
2.7 Conclusion .....	37

References .....	38
ELEMENT TEST ON RAMMED EARTH WALLS .....	43
3.1 Introduction.....	43
3.1.1 Rammed Earth under Compression Loading.....	44
3.1.2 Rammed Earth under In-Plane Loading .....	45
3.1.3 Effect of Rammed Earth Layer Thickness .....	46
3.2 Test Parameters.....	46
3.2.1 Rammed Earth Layer Thickness .....	46
3.2.2 Drying Period.....	47
3.3 Specimens and Materials .....	47
3.3.1 Soil .....	47
3.3.2 Proctor Compaction Test .....	48
3.3.3 Walette .....	49
3.3.4 Compaction Energy .....	51
3.3.5 Comparison of mechanical characteristics with the previous study .....	52
3.3.5 Retrofitting details .....	53
3.6 Compression Test.....	55
3.6.1 Test Matrix and Setup.....	55
3.6.2 Results and Discussion .....	56
3.6.4 Effect of Drying Period.....	65
3.6.5 Effect of Layer Thickness of Rammed Earth .....	66
3.6.6 Effect of Mesh-Wrap Retrofitting Technique.....	67
3.7 Shear Test.....	68
3.7.1 Test Matrix and Setup.....	68
3.7.2 Results and Discussion .....	70
3.7.3 Effect of Drying Period.....	77
3.7.4 Effect of Layer Thickness .....	78
3.7.5 Mohr-Coulomb Failure Envelopes .....	79
3.7.6 Effect of Mesh-Wrap Retrofitting Technique.....	80
3.8 Finite Element Modelling of In-Plane Loaded Rammed Earth Wall .....	82
3.8.1 Modelling of Rammed Earth from Literature .....	82
3.8.2 Modelling Strategy.....	86
3.8.3 Geometry, Boundary and Loading Conditions .....	87
3.8.4 Constitutive Laws .....	89
3.8.2 Results and Discussion .....	90
3.8.3 Sensitivity Analysis .....	93
3.7 Summary.....	96
References.....	98
PULL-DOWN TEST OF RAMMED EARTH WALLS .....	102
4.1 Introduction .....	102
4.2 Out-of-plane behaviour of rammed earth wall and their possible strengthening strategies .....	103
4.2.1 Specimens and Materials .....	103

4.2.3 Material Characterization.....	118
4.2.4 Test Setup.....	126
4.2.5 Results and Discussion .....	128
4.3 Finite Element Modelling.....	139
4.3.1 Geometry, Boundary and Loading Conditions .....	139
4.3.2 Constitutive Laws .....	140
4.3.3 Results and Discussion .....	142
4.3.4 Sensitivity Analysis .....	144
4.4 Assessment of effectiveness of strengthened rammed earth wall with rigid floor .....	148
4.4.1 Specimens and Materials .....	148
4.4.2 Material Characterization.....	151
4.4.3 Test Setup.....	151
4.4.4 Results and Discussion .....	152
4.5 In-Plane Shear Resistance between the Rammed Earth Blocks offered by RC Dowels ..	156
4.5.1 Specimen and Materials.....	156
4.5.2 Material Characterization.....	157
4.5.3 Test Setup and Instrumentation.....	159
4.5.4 Result and Discussion .....	160
4.6 Conclusions.....	162
References.....	163
FULL-SCALE QUASI-STATIC TEST: ASSESSMENT OF SEISMIC PERFORMANCE OF RAMMED EARTH STRUCTURES.....	166
5.1 Introduction.....	166
5.2 Seismic Evaluation of Rammed Earth Building.....	168
5.2.1. First phase of seismic design: specification code .....	170
5.2.2 Second phase of seismic design: Allowable unit stress calculation .....	173
5.2.3 Third phase of seismic design: Horizontal load-carrying capacity.....	181
5.3 Specimens and Materials .....	183
5.3.1 Unreinforced RE Loaded in the Short Span (U-RE-SHORT).....	184
5.3.2 Unreinforced RE Loaded in Long Span (U-RE-LONG).....	185
5.3.3 Retrofitted RE Loaded in Short Span (R-RE-SHORT).....	186
5.3.4 Retrofitted RE Loaded in Long Span (R-RE-LONG) .....	190
5.3.5 Reinforced RE Loaded in Short Span (New-RE-SHORT).....	192
5.4 Material Characterization.....	195
5.4.1 Rammed Earth Wall.....	195
5.4.2 Plain Cement Concrete .....	198
5.4.3 Cement Mortar .....	199
5.4.4 Tensile Coupon Test for Mesh Composite .....	200
5.5 Test Setup.....	202
5.6 Results and Discussion .....	205
5.6.1 Unreinforced RE Loaded in Short Span (U-RE-SHORT).....	205
5.6.2 Unreinforced RE Loaded in Long Span (U-RE-LONG).....	207



5.6.3 Retrofitted RE Loaded in Short Span (R-RE-SHORT) .....	209
5.6.3 Retrofitted RE Loaded in Long Span (R-RE-LONG) .....	212
5.6.4 Reinforced RE Loaded in Short Span (New-RE-SHORT).....	215
5.6.5 Defining Limit States for Rammed Earth Buildings.....	219
5.7 Nonlinear Pushover Analysis in Seismic Evaluation.....	219
5.7.1 Introduction.....	219
5.7.2 The Capacity Spectrum Method (CSM) .....	220
5.7.3 Performance Point.....	222
5.7.4 Fragility Curves .....	225
5.8 Conclusions.....	228
References.....	229
SUMMARY AND FUTURE SCOPE .....	232
6.1 Summary.....	232
6.2 Future Work .....	236
References.....	237
List of Publications .....	238

**INTRODUCTION****1.1 Background**

The earth is one of the most abundant resources available on the planet used as a natural building material for over 9000 years [1]. Even today, 40% of the world population lives in earth dwellings according to the UNCHS statistics. Furthermore, UNESCO's statistics show that 15% of the world's cultural heritage is built with earth [2]. The three most common forms of earth used in construction are adobe block, cob, and rammed earth. Together with other forms of unbaked earthen construction, such as mud-brick, rammed earth has been used as a traditional building technique throughout many parts of the world by humanity. The major centres for earthen structures include Asia (China, India, Nepal, Bhutan), North Africa, Australia, regions of North and South America, and Europe (France, Germany, and Spain). Rammed earth refers to a construction procedure involving compaction of moistened earth mixtures inside the formwork to form a solid wall. The mixture usually consists of clay, silt, sand, and gravel. For the unstabilised rammed earth, clay is the only binding material which provides cohesion and strength. Clay is also responsible for complex mechanical behaviour, such as swelling and shrinkage, when subjected to hydric changes [3]. The clay content proportion should thus be sufficient to ensure a good material stiffness and strength. However, excessive clay might result in cracking of the wall.

The traditional rammed earth technique has gained its popularity due to various advantages associated with it. Rammed earth being natural resources and local material, it can be taken and used immediately on the construction site without the industrial processing [4]. It is not renewable but is a reusable material; it requires no treatment to be reused and therefore, has a shallow impact in terms of energy use [1]. Nevertheless, it has its drawbacks resulting in poor performance during the seismic actions. The major advantages and disadvantages of the rammed earth walls have been summarized in Table 1.1.

Table 1.1 Advantages and disadvantages of rammed earth walls.

Advantages	Disadvantages
Cost-effective	Brittle (Weak in shear and tension)
Environmentally sustainable	Low water resistance
Potential for recycling	Heavy weight due to wall thickness
Natural moisture regulator	

## 1.2 Motivation

### 1.2.1 Traditional Construction Practice in Bhutan: Rammed Earth

Most buildings in Bhutan are predominantly constructed using traditional materials and techniques, such as rammed earth and random stone masonry in mud mortar. According to recent statistics, 66% of households in the country live in such traditional buildings. Even today, almost every new construction and renovation of heritage structures like Dzongs, temples, and stupas are carried out using traditional materials and techniques. The rammed earth, in particular, has been practised in the western region of the country. Figure 1.1 highlights the regions where rammed earth structures are primarily widespread.

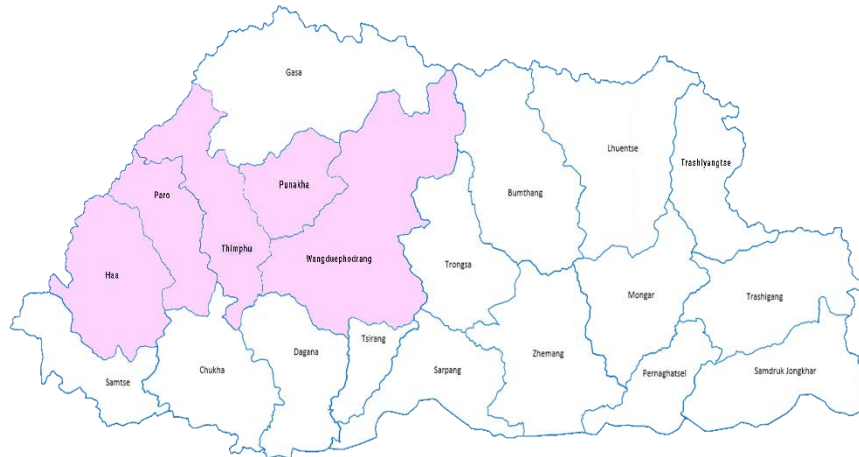


Figure 1.1 Regions having rammed earth structures.

The local community traditionally builds rammed earth constructions, not requiring highly specialized labour, and it is the only construction practice where women play a crucial role in the whole construction process. This traditional construction technique is considered as powerful expressions of our human ability to create a built environment that is still alive in the region, particularly the rural areas. This indigenous construction technique has been passed down from generation to generation through oral transmission and hands-on practices. However, such

practices were rarely documented in written format, if found are in religious literature [5]. The rammed earth structures are constructed above random rubble masonry foundation characterized by a massive wall (thickness ranging from 580 mm -900 mm) integrated with timber components. The basic technique involves a selection of suitable soil from the nearby site by Pazops, which is then laid in layers inside a formwork made of wooden boards and hardened by ramming tools, as presented in Figure 1.2.

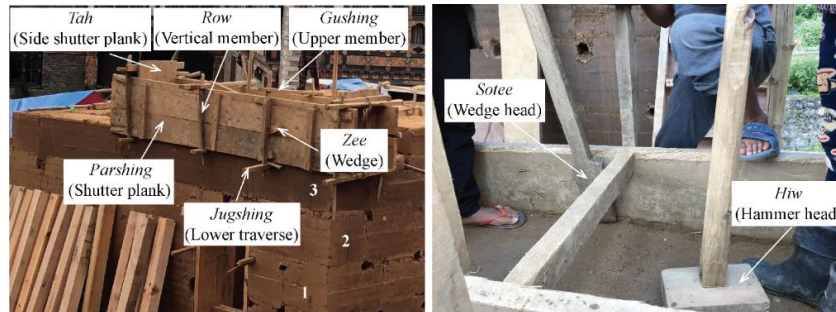


Figure 1.2 Details of traditional formwork and ramming tools.

The rammed earth structure includes an excellent variety of architectures ranging from simple houses to temples (*Lhakhangs*) and fortresses (*Dzongs*), and they are preserved and promoted as an indigenous construction technique. Although the exact time of its practice in the region is unknown, some religious structures still existing today date back to the 8th century. It is believed that rammed earth construction techniques originated in Tibet and the southern parts of the Himalayan kingdoms of Ladakh, Mustang [6]. Few examples of rammed earth structures found in the country are presented in Figure 1.3, showing clusters of rammed earth houses in Eusana, Paro (Figure 1.3(a)), Private house (Figure 1.3(b)) and Nebab monastery in Shelgana, Punakha.

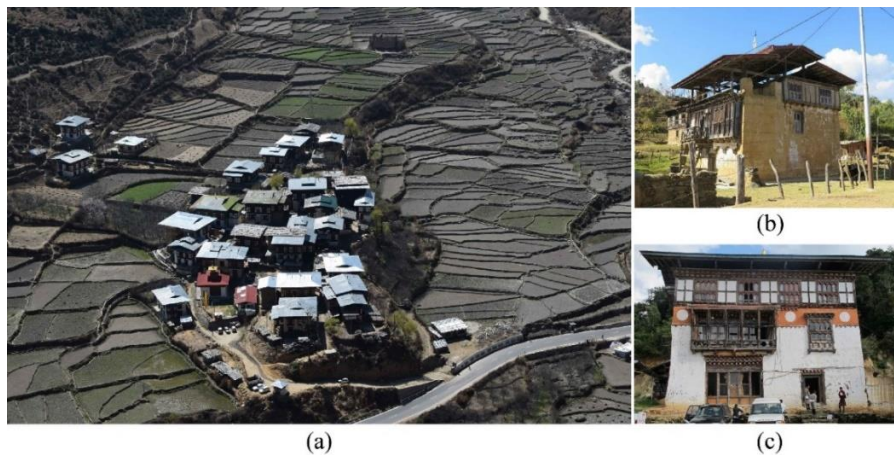


Figure 1.3 Rammed earth structures (DCHS)

### 1.2.2 History of Earthquakes in Bhutan

Bhutan, along with India, Nepal and Pakistan lie in the Himalayan range formed by the collision of Eurasian and Indian plates (Figure 1.4). The Himalayan range is one of the world's most active earthquake occurrence, and several significant earthquakes have occurred. Several major earthquakes within the Himalayan ranges includes in western Nepal (1505 AD, M8.7), in Bihar-Nepal (1934, M8.1) claiming more than 8000 lives and destroying 19% of the buildings [6], in Assam (1950, M8.4), and Shillong earthquake (1897, M8.1), that occurred in Assam region of India close to the southern part of Bhutan. The most recent earthquake to occur in this India-Eurasia collision zone is Gorkha earthquake in central Nepal, with magnitude M7.8 on April 25, 2015, resulting in 8,800 casualties with damages spread across the country [7]. Further, there was Kashmir earthquake of magnitude M7.6 in western Pakistan in the year 2005, with 90,000 deaths in the region. Bhutan, on the other hand, is thought to be the only segment of the Himalayas not having experienced any major earthquake over the past half-millennium. However, the findings of 1714 A.D earthquake reclassifies the apparent seismic gap to a former information gap and imply that the entire Himalayan arc has a high level of earthquake potential [8].

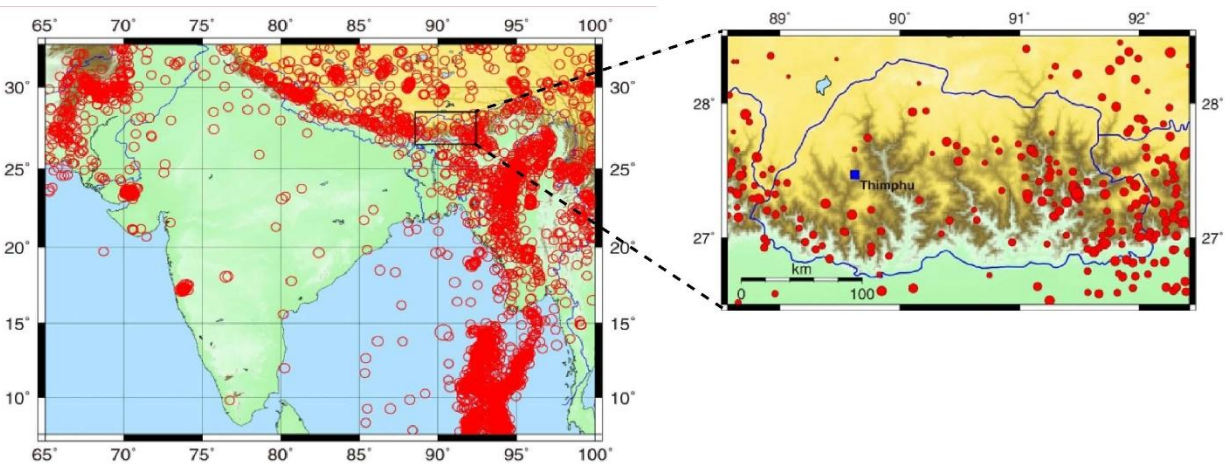


Figure 1.4 Historical earthquakes larger than magnitude M5 in South Asia since 1960 (ISC catalogue).

The Narang earthquake (Figure 1.5(a)) of magnitude M6.3 on the Richter Scale, that struck Eastern Bhutan, with its epicentre in Narang, Mongar, on September 21, 2009, at 2:53 p.m. has been the most damaging disaster that Bhutan has experienced in recent times claiming human lives and homes (mostly constructed with random rubble masonry). Furthermore, in September 2011, the India-Sikkim earthquake (Figure 1.5(b)) of magnitude M6.9 resulted in significant damage to the existing infrastructures, mostly constructed with rammed earth, in the western part of Bhutan.

Table 1.2 reports several affected structures and the severity of damages caused by the two earthquakes. It is noted that rural houses are the most affected ones. According to the statistics based on the National Recovery and Reconstruction Plan (NRRP) documents [9,10], the 2009 Narang earthquake affected 4950 rural homes, of which 11.08% were beyond repair, and 19.75% required a major repair. The 2011 Sikkim earthquake affected 6,977 rural homes in the country where 7.32% collapsed, and 15.06% were severely damaged, requiring a significant repair.

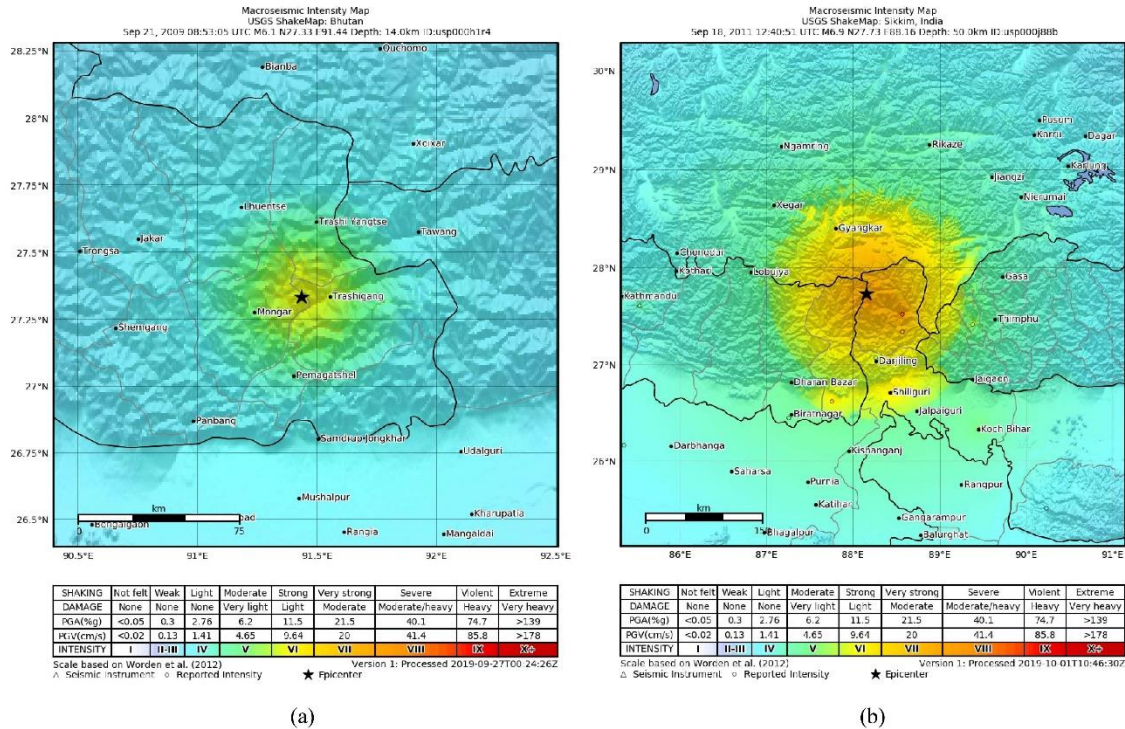


Figure 1.5 Summary of earthquakes: (a) Narang Earthquake, (b) Sikkim Earthquake (<https://earthquake.usgs.gov/>).

Table 1.2 Damage to structures by recent earthquakes [9,10].

Type of structures	Narang Earthquake (2009)			Sikkim earthquake (2011)		
	Beyond repair	Major repair	Total Damages	Beyond repair	Major repair	Total Damages
Stupas	142	163	539	40	5	55
Temples	36	91	281	90	88	280
Fortress	-	3	8	5	1	6
Rural homes	462	884	4950	401	1008	6977
Total	640	1141	5778	536	1102	7318

The survey undertaken by the Division for Conservation of Heritage Sites (DCHS) showed that the majority of the affected houses have vertical corner cracks (89%), separation at wall

intersection (58%), and cracks originating from the openings (73%) [10]. Some failure patterns observed in rammed earth houses are presented in Figure 1.6 [10,11].

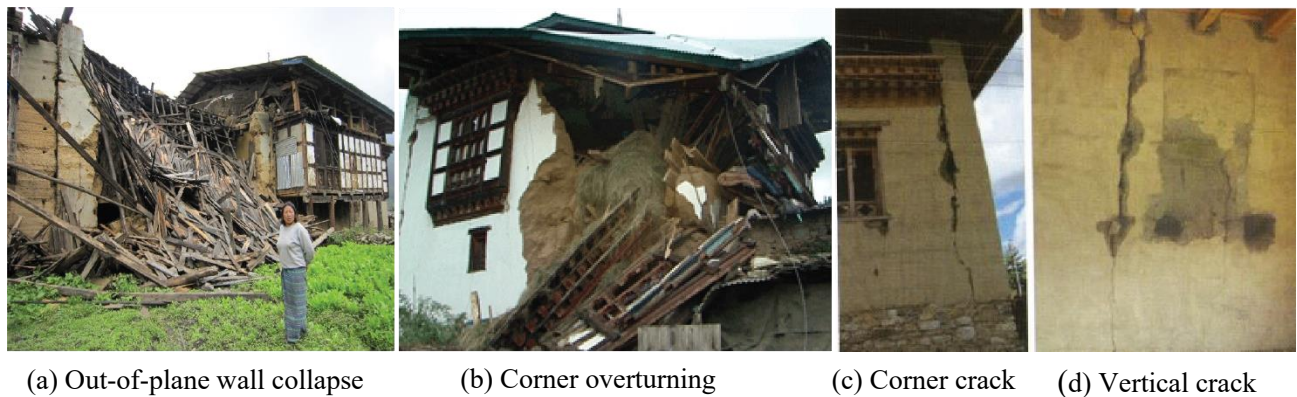


Figure 1.6 Rammed earth buildings damaged by the 2011 earthquake.

### **1.2.3 Science and Technology Research Partnership for Sustainable Development (SATREPS) Projects**

After suffering colossal damage to traditional rammed earth and stone masonry houses caused by two recent earthquakes, their stability was questioned, creating perplexity in public to continue the construction. It became a critical task for the Royal Government of Bhutan, in particular, the Department of Culture (DoC), the key central office for the protection of heritage sites and the sustainability of the cultural landscape of Bhutan, to guide the citizens to improve seismic resilient construction. Therefore, in collaboration with various Japanese institutes, the Royal Government of Bhutan formulated and initiated the five-year-long project entitled “Project for Evaluation and Mitigation of Seismic Risk for Composite Masonry Buildings in Bhutan” under the scheme of SATREPS (Science and Technology Research Partnership for Sustainable Development).

The work presented in this thesis is part of the SATREPS project funded by Japan Science and Technology Agency (JST), Japan International Cooperation Agency (JICA). The project’s overall goal is to disseminate the seismic technology for disaster mitigation of the composite masonry buildings, wherein the seismic risk of composite masonry buildings is evaluated, seismic technology for constructing and strengthening composite masonry buildings are developed, and the dissemination mechanism for the seismic technology is enhanced.

### **1.3 Aims and Objectives**

The past earthquakes have proven that the vulnerabilities of rammed earth structures under seismic loading. Its poor performance during the earthquake can be associated due to its rigid and fragile structural behaviour as monolithic masonry or exposure to water infiltrations and rising damp. These problems related to its rigid and fragile characteristics can be solved if appropriate strengthening techniques are provided. Therefore, the main aim of this thesis is to propose appropriate strengthening measures for both new construction and existing structures and check their effectiveness, which is met through the following objectives:

1. Gather information on mechanical properties of un-stabilized rammed earth walls through comprehensive literature reviews for rammed earth practised in Bhutan and other parts of the world;
2. Carry experimental study to highlight rammed earth performance under compression and shear loadings for both unreinforced and retrofitted walls;
3. Conduct pull-down test on rammed earth wall to understand their out-of-plane behaviour for unreinforced, reinforced, and retrofitted walls;
4. Full-scale test on prototype two-storied Bhutanese rammed earth building to understand their behaviour under static loadings;
5. Develop efficient FE models to predict and support the experimental test results mentioned in serial no. 2 and 3.

The scope of the work is divided into two categories depending on the location of the experimentation conducted: i) small-scale element test and the structural analysis were conducted in Nagoya City University (NCU), and ii) full-scale experimental work was carried out in Bhutan. The overall scope of the work is summarized in Figure 1.7.



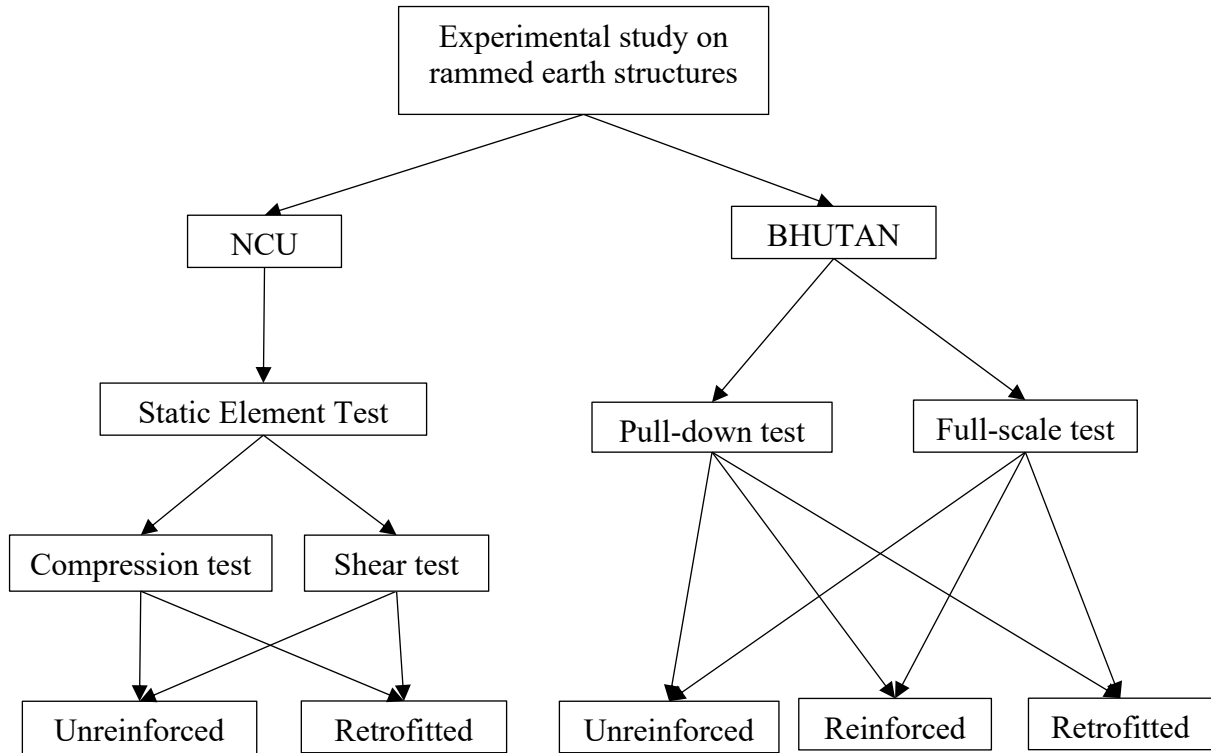


Figure 1.7 Scope of work.

#### 1.4 Thesis Outline

The thesis contains six chapters, briefly summarized as follows:

Chapter 1 provides a general background of the rammed earth construction. The motivation of the study presented, which is derived from the current situation of rammed earth structures (including homes and religious structures) in Bhutan, affected by the 2009 and 2011 earthquake, which requires retrofitting and preparing for the next major earthquake with appropriate strengthening measures for the new construction. The aims, objectives, and scope of the thesis are also highlighted.

Chapter 2 is solely dedicated to literature reviews related to the current study. It first presents the overview of rammed earth with the construction details practised in Bhutan. The vulnerability and failure patterns of rammed earth observed during the earthquake are presented. It also discusses the mechanical behaviour of rammed earth (compressive strength, tensile strength and shear strength) and factors affecting them in particular the compressive strength. The work conducted

for improving the mechanical properties of rammed earth is outlined. Following the strengthening measures proposed for both new construction and existing structures are highlighted.

Chapter 3 reports on the element tests conducted on small-scaled rammed earth walls under compression and shear loading while evaluating the efficacy of the mesh-wrap retrofitting technique. It also discusses the effects of rammed earth layer thickness and drying period in the strength characteristic of the rammed earth wall. The critical parameters like cohesion and frictional angle in shear strength of rammed earth are deduced. The experimental results are supported by numerical analysis.

Chapter 4 presents the out-of-plane behaviour of rammed earth walls with the pull-down test of U-shaped specimens having a wall thickness of 600 mm. It also presents the experimental campaign to study the effectiveness of proposed retrofitting and strengthening measures to enhance the performance of rammed earth walls in out-of-plane direction. A simple method to improve the floor rigidity is also discussed. Further, the pull-down test on the small-scale wall is carried out to assess RE's in-plane behaviour.

In Chapter 5, the effectiveness and feasibility of proposed retrofitting and strengthening measures adopted in Chapter 4 is further verified through conducting the full-scale test on prototype traditional Bhutanese rammed earth house having two-stories. The limit states of rammed earth house are derived based on the degree of damage observed during the experimentation. Fragility curves are developed based on the experimental results.

Chapter 6 summarizes the general conclusion of each chapter and discusses the future scope of the work.

## **References**

- [1] M. Gernot, *Building with Earth: Design and Technology of a Sustainable Architecture*, Birkhauser. Basel, Berlin, Boston: Birkhäuser – Publishers for Architecture, 2006.
- [2] L. Gandreau, David; Delboy, *World Heritage Inventory of Earthen Architecture*. CRAterre-ENSAG, 2012.
- [3] B. Harries, Kent, A; Sharma, *Nonconventional and Vernacular Construction Material: Characterisation, Properties and Applications*. Woodhead Publishing, 2020.

- [4] Pema, K. Tenzin, K. C. Shrestha, and T. Aoki, “Construction management of test facility in Bhutan,” 2019.
- [5] DCHS, *General Guideline for improved seismic resilient construction techniques for rammed earth structures in Bhutan*. Division for Conservation of Heritage Sites, Department of Culture, Ministry of Home and Cultural Affairs, Royal Government of Bhutan, 2017.
- [6] A. M. Dixit, R. Yatabe, R. K. Dahal, and N. P. Bhandary, “Initiatives for earthquake disaster risk management in the Kathmandu Valley,” *Nat. Hazards*, vol. 69, no. 1, pp. 631–654, 2013, doi: 10.1007/s11069-013-0732-9.
- [7] N. Takai *et al.*, “Strong ground motion in the Kathmandu Valley during the 2015 Gorkha, Nepal, earthquake,” *Earth, Planets Sp.*, vol. 68, no. 1, p. 10, 2016, doi: 10.1186/s40623-016-0383-7.
- [8] G. Hetényi *et al.*, “Joint approach combining damage and paleoseismology observations constrains the 1714 A.D. Bhutan earthquake at magnitude  $8 \pm 0.5$ ,” *Geophys. Res. Lett.*, 2016, doi: 10.1002/2016GL071033.
- [9] DDM, “National Recovery and Reconstruction Plan ‘Building back better’ (September 21, 2009 Earthquake),” Thimphu, 2009. [Online]. Available: <https://www.ddm.gov.bt/downloads-and-publications/>.
- [10] DDM, “National Recovery and Reconstruction Plan ‘Building back better’ (September 18, 2011 Earthquake),” Department of Disaster Management, Ministry of Home and Cultural Affairs, Royal Government of Bhutan, Thimphu, 2011. [Online]. Available: <https://www.ddm.gov.bt/downloads-and-publications/>.
- [11] DCHS, *Damage Assessment of Rammed Earth Buildings-After the September 18, 2011 Earthquake*. Division for Conservation of Heritage Sites, Department of Culture, Ministry of Home and Cultural Affairs, Royal Government of Bhutan, 2011.

### 2.1 Rammed Earth Construction

#### 2.1.1 Soil Classification

Soil is the product from the alteration of the parent rock due to physical and chemical weathering. The resulting material undergoes further transformations as it is continuously transported, deposited, compressed, and chemically modified. Soil is usually seen in different layers, as seen in Figure 2.1. The suitable material for rammed earth construction is an inorganic subsoil found beneath the organic topsoil.

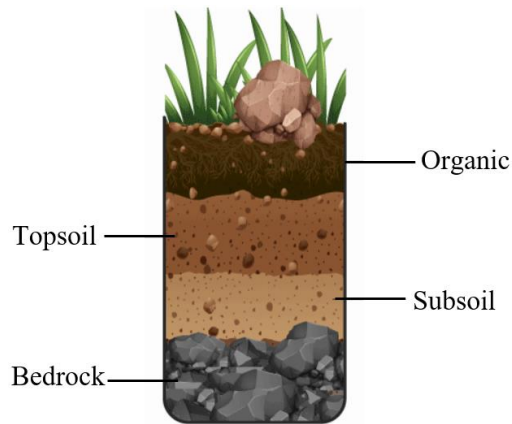


Figure 2.1 Soil profile with different layers [1].

#### 2.1.2 Particle Size Distribution

The mechanical properties of unstabilised soils depend upon the grain size of their composition rather than their chemical composition of alteration [2]. Therefore, engineering soils are classified based on the relative size proportion of their main elements, namely gravel, sand, silt and clay. The particle size limits vary depending on the country and the standard being followed, but fractions remain the same. In this thesis, the grading limits follow the British Standard as in Table 2.1.

Table 2.1 British soil classification based on grain size [3].

Very coarse soil	Boulders		> 200 mm
	Cobbles		60 - 200 mm
Coarse soils	Gravel	coarse	20 - 60 mm
		medium	6 - 20 mm
		fine	2 - 6 mm
	Sand	coarse	0.6 - 2.0 mm
		medium	0.2 - 0.6 mm
		fine	0.06 - 0.2 mm
Fine soils	Silt	coarse	0.02 - 0.06 mm
		medium	0.006 - 0.02 mm
		fine	0.002 - 0.006 mm
	Clay	< 0.002 mm	

Each particle type plays a vital role in the structural integrity of rammed earth. Gravel is the skeleton that provides underlying structural stability. Together with the sand, it enhances weathering resistance of exposed surfaces and shrinkage resistance. The clay and silt are the binding agents that make possible the existence of strong capillary forces, ensuring the material's overall cohesion. However, not all soil compositions are suitable for rammed earth construction. Ideally, the soil should have a high sand and gravel content with some silt and just enough clay to act as a binder and assist soil compaction [4]. A wide variety of selection criteria for natural rammed earth has been proposed by many researchers around the world with upper and lower range limits for clay, silt, sand and gravel, compiled by Walker et al. [5] which is reproduced in Figure 2.2. The minimum clay content ranges between 0-30% while the maximum ranges between 15-35%. For silt, the minimum percentage ranges between 0-50% and the maximum ranges between 0-80%. The minimum percentage of combined sand and gravel is between 10-70%, and

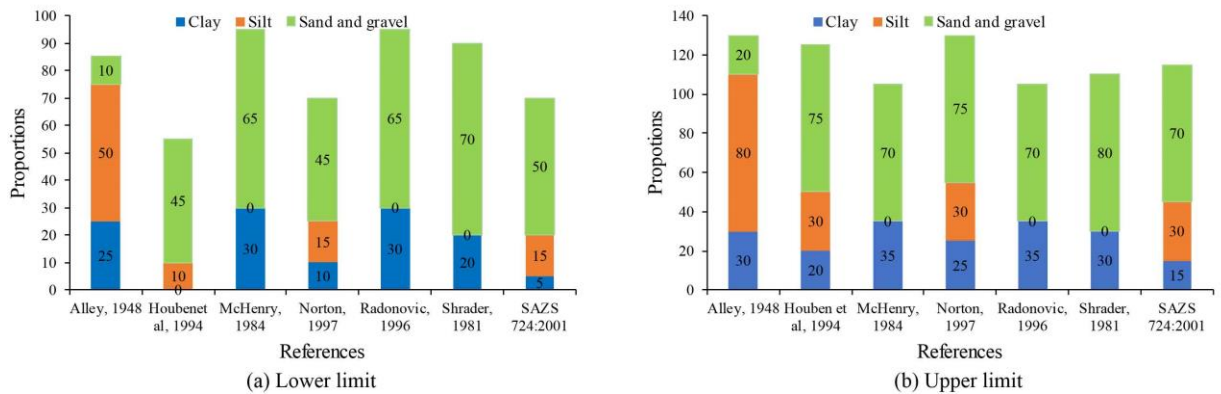


Figure 2.2 Lower and upper range limits of the particle size distribution of rammed earth construction.

the maximum is between 20-80%. Figure 2.3 shows the recommended envelope for a suitable rammed earth particle-size distribution by Houben and Guillaud [6]. The rammed earth is considered to have required performance if the soil fits within the limit values.

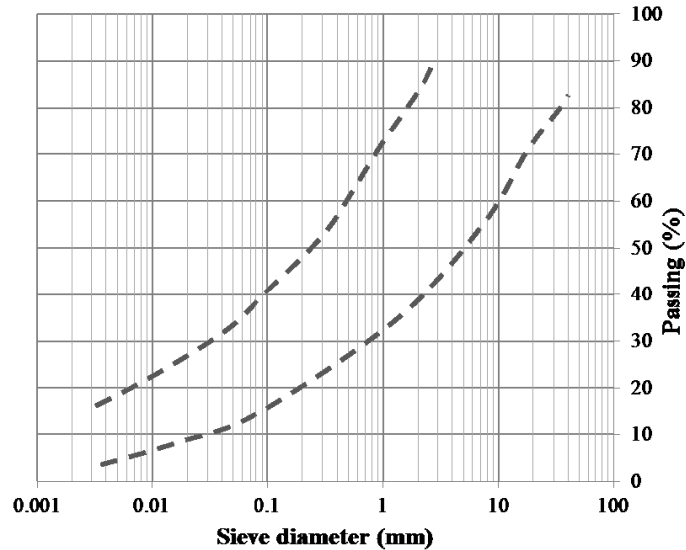


Figure 2.3 Recommended envelopes for RE construction by Houben and Guillaud [6].

Interestingly in Bhutan, no grain size distribution analysis or field tests are performed. Soil suitability is usually assessed visually by local craftsmen and carpenters' experience, mainly through a colour analysis. Most used soils in the country have shown quite a wide colour range, including red, different shades of brown and less frequently yellow. Red and brown soils are preferred in Tana and Phatari, in Phunaka region, brown soils in Paro while light yellow soils in Wangdue valley [7]. The reddish showed higher contents of clay while the yellow showed higher contents of sand. Further, red soil specimen showed higher compressive strength and Young's modulus; while most craftsmen report using red and brown soils mixtures, only few seem to use yellow soil [7].

### 2.1.3 Formwork

Formwork is used as a temporary support during the soil compaction. A typical traditional Bhutanese formwork is presented in Figure 2.4. They are usually made of hardwoods having sufficient strength, stiffness, and stability to resist the pressure during compaction. Inadequate strength of formwork will result in deformation of the wall due to the high compressive force induced by the rammer during the compaction process. The formwork consists of two shutter

planks (*Parshing*) connected by horizontal members at top and bottom, namely *Gushing* and *Jugshing*. The vertical member “*Row*” connects the horizontal members. Wedges are driven between vertical members and side planks to stabilise them. Unlike formwork for concrete, the formwork for rammed earth can be removed almost immediately after compaction, and subsequently be reused.

Although Bhutan continues to use the traditional formwork, the other parts of the world are seen using modern formwork made up of steel. They are proven to be stiffer and enable the creation of higher wall elements at one time.

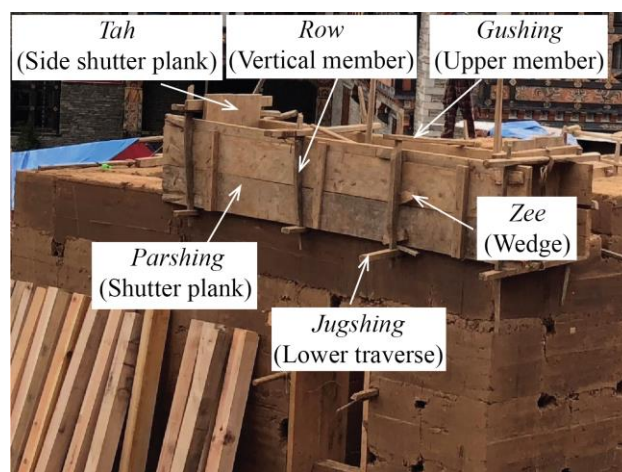


Figure 2.4 Traditional wooden formwork [8].

#### 2.1.4 Ramming Tools for Compaction

Compaction is the process where the volume of soil is reduced by removal of air from the pore spaces, leading to an increase in the density of the soil. The compaction of rammed earth layers is traditionally performed manually using a wooden rammer with different base shape. Figure 2.5 shows the ramming tools used in the traditional Bhutanese rammed earth construction. The rammer with hammerhead (*Hiw*) is used for standard compaction while a rammer with wedge head (*Sotee*) is at the edges. The traditional rammers are less expensive but require an extra effort. Therefore, they are being replaced by pneumatic rammer, operated with compressed air, which increases the manufacturing process and density of the material with minimal effort.

The degree of compaction of a soil is measured by the dry density, and it depends on the initial water content of the soil, and the amount of energy supplied, known as compactive effort. The

relationship between dry density, moisture content and compaction energy is later described in detail. In geotechnical engineering, three main tests are used to determine the optimum water content, namely, Standard Proctor test, Heavy Proctor test and Vibrating hammer test [9]. However, the moisture content is checked through a traditional field test as following in Bhutan [10]:

- a) Squeezing a handful of the earth: if a lump is formed, the moisture content is considered mostly adequate
- b) Throwing a ball against the wall: if the ball falls and does not stick on the wall, the water content is considered correct.
- c) Forming a ball of earth and tossing it up in the air: if it breaks into two or three major pieces, the mixture is considered suitable; if it remains compact, it contains too much water.

The drop test method described in the third is also outlined in Keable et al. [4] and Houben and Guillaud [5].



Figure 2.5 Traditional wooden ramming tools [8].

## 2.2 Vulnerability of Rammed Earth Buildings

### 2.2.1 Introduction

The term “vulnerability” can be used in several contexts, depending on the purpose of the study. Here, the vulnerability focuses primarily on physical aspects, so from this point of view, the vulnerability can be defined as: “The degree of loss to a given element at risk or a set of elements at risk resulting from the occurrence of a natural phenomenon of a given magnitude and expressed on a scale from 0 (no damage) to 1 (total damage)” [11]. Another definition of vulnerability can



be found in the European Macroseismic Scale (EMS 98) wherein: “The term vulnerability is used to express differences in the way that buildings respond to earthquake shaking. If two groups of buildings are subjected to exactly the same earthquake shaking, and one group performs better than the other, then it can be said that the buildings that were less damaged had lower earthquake vulnerability than the ones that were more damaged, or it can be stated that the buildings that were less damaged are more earthquake-resistant, and vice versa” [12].

Table 2.2 EMS 98 Vulnerability Table [12].

Type of Structure		Vulnerability Class					
		A	B	C	D	E	F
MASONRY	Rubble stone, fieldstone	○					
	Rammed earth	○—					
	Adobe (earth brick)	○—					
	Simple stone	—○					
	Massive stone		—○—				
	Unreinforced, with manufactured stone units	—○—					
	Unreinforced, with RC floors		—○—				
	Reinforced or confined			—○—			
REINFORCED CONCRETE (RC)	Frame without earthquake-resistant design (ERD)	—○—					
	Frame with moderate level of ERD		—○—				
	Frame with high level of ERD			—○—			
	Walls without ERD		—○—				
	Walls with moderate level of ERD			—○—			
	Walls with high level of ERD				—○—		
STEEL	Steel structure			—○—			
WOOD	Timber structures			—○—			

○ Most likely vulnerability class; — probable range; ..... range of less probable, exceptional cases

any seismic resilient features. Such building structures, if not properly reinforced, can present an inadequate response to earthquake loadings due to their difficulty to keep the box-like behaviour during an earthquake. The Vulnerability Table (Table 2.1) by EMS 98 [12], classifies buildings into six vulnerability classes, ranging from A to F, with A indicating highest vulnerability and F

indicating highest resistance. The buildings types are classified by their four main groups, i.e. masonry, reinforced concrete (RC), steel and wood. According to the Vulnerability Table, rubble stone, fieldstone, rammed earth and adobe (earth bricks), categorized as masonry with the highest vulnerability with vulnerability class A.

### **2.2.2 Vulnerability against Seismic Force**

The high seismic vulnerability of rammed earth structures is a consequence of several factors such as high mass, limited tensile strength, fragile behaviour, and softening and loss of strength upon saturation. When under seismic actions, these structures can suffer severe and cumulative structural damage and collapse, causing innumerable human and material losses. The rammed earth as a building material inherent other key factors contributing to its high seismic vulnerability is their exposure to water infiltrations and rising damp, causing vertical cracks as material erosion and consequent wall section reduction. Moreover, unreinforced masonry structures related critical issues, such as irregular and inadequate plan distribution, wall to wall inadequate or weak connection; lack of diaphragms, excessive floors structures flexibility, vertical loads irregular distribution on the masonry and lack of anchorage between horizontal structures and walls, also assume a crucial role in rammed earth structures seismic vulnerability degree.

The recent earthquakes around the world have repeatedly proven the vulnerabilities of rammed earth buildings against the seismic forces. The Yiliang Earthquake of magnitude M5.7 that occurred on September 7, 2012, in Yunnan Province, China destroyed over 30,600 houses with 80 casualties [13]. The Ludan earthquake with magnitude M6.5 hit the same province in 2014, where more than 66,400 houses experienced severe damage, and 90% of affected houses were rammed earth structures [14]. A remarkable number (around 26% as total collapse) of rammed earth buildings in Bhutan was reported to be affected by the Sikkim Earthquake with the magnitude of M6.9, which occurred near Nepal-India border on September 18, 2011 [15]. The other devastating earthquakes which affected the earthen structures include the 2001 El Salvador earthquake (magnitude M7.6), destroying nearly 108,000 houses, Bam, Iran earthquake, in 2003, the Pisco, Peru earthquake, in 2007 and the Maule, Chile earthquake, in 2010 [16].

#### **2.2.2.1 Failure Inventory from Past Earthquakes**

The survey undertaken by Division for Conservation of Heritage Sites (DCHS) [17] showed that majority of the affected rammed earth houses have vertical corner cracks (89%), separation at wall

intersection (58%), and cracks originating from the openings (73%). The survey was taken in the area where a maximum number of RE buildings were damaged. From the surveyed buildings, 26% of the rammed earth walls were reported as total collapse (out-of-plane). Some failure patterns observed are already presented in Figure 1.6 under Chapter 1. The collapse of the wall was either at the facade or at the corner. Similar damage patterns are reported for the rammed earth houses in rural Yunnan Province, China by Wang et al. [13], it is presented in Figure 2.6. Typical damages included out-of-plane fall over, vertical cracking at corners or at loading points.

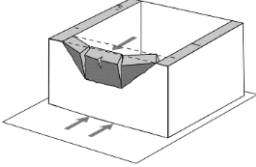

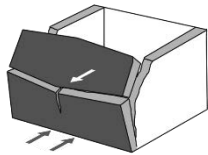

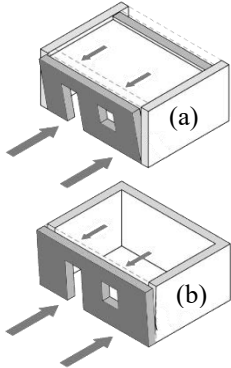



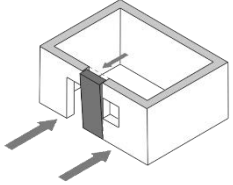

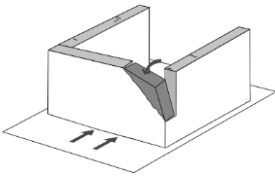

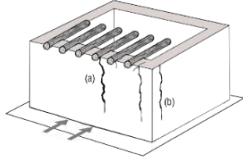

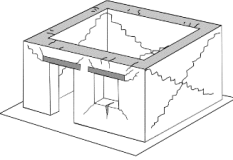

Figure 2.6 Damages observed in rammed earth houses: (a) structural collapse; (b) gable wall fall-over; (c) longitudinal wall fall-over, (d) vertical corner crack; (e) Crack at loading point [13].

### 2.2.2.2 Types of Failure Mechanism

The occurrence of different failure mechanisms depends on several parameters: a) the geometry of the pier; b) the boundary conditions; c) the acting axial load; d) the mechanical characteristics of the masonry constituents; and e) the masonry geometrical characteristics [18]. The observations of failure mechanisms under earthquake loadings have been already studied and classified by several authors for unreinforced masonry and earthen buildings [18-20]. The summary has been modified after Roberto et al. [10] in Table 2.3.

Table 2.3 Failure mechanism observed in rammed earth buildings under seismic action [10].

MAIN FAILURES OCCURRED	MAIN POSSIBLE CAUSES	FAILURE MECHANISM scheme	PHOTO INVENTORY
<p>Mechanism A  <b>Out of plane Wall collapse:</b> Toppling (horizontal arch)                      Wall plane perpendicular bending with horizontal and further vertical cracking, causing upper wall portion overturning outwards.</p>	<ul style="list-style-type: none"> <li>- Excessive bending efforts due to diaphragms flexibility</li> <li>- Lack of floor/roof to wall connections</li> <li>- Long, thin and slender unbraced wall length</li> </ul>		
<p>Mechanism B  <b>Out of plane Wall collapse:</b> Buckling (vertical arch)                      The wall buckles overturning inwards as cracking horizontally in the middle.</p>	<p>Stress due to higher floor/roof structures horizontal slip during an earthquake, and ring beams, ties or rigid floors restraining action.</p> <ul style="list-style-type: none"> <li>- Lack of floor to wall connections at top floor or wall to wall connection at orthogonal corner or intermediate junctions</li> <li>- Rammed earth brittle behaviour: low walls bending strength and elasticity.</li> </ul>		 <p>Photo: Wang et al. [13]</p>
<p>Mechanism C  <b>Out of plane Wall Collapse:</b>                      Whole wall vertical overturning outwards.                      Rammed earth wall collapse in straight sections, for perpendicular bending, detaching vertically in T-walls or corners junctions, or due to vertical slits on the wall plane.</p>	<p>Bending stress and Vertical structural slits occurred along perpendicular junctions, due to:</p> <ul style="list-style-type: none"> <li>- Lack of adequate blocks overlapping on the horizontal plane in T-shape walls or corners</li> <li>- Lack of adequate horizontal plane junction between old and newly built walls</li> <li>- Lack of floor/roof to wall connection</li> <li>- Large roof mass generates larger inertial forces, which in turn causes a larger response</li> </ul>		 <p>Photo: DCHS [17]</p>

<p>Mechanism D <b>Out-of-plane Wall Collapse:</b> Wall section vertical overturning outwards. Out-of-plane vertical overturning of wall strips, detaching from the rest of the wall.</p>	<p>Bending stress perpendicular to the wall and Vertical cracks due to:</p> <ul style="list-style-type: none"> <li>- Vertical openings alignment on the wall plane</li> <li>- Lack of floor/roof to wall connection</li> </ul>		 <p>Photo: DCHS [17]</p>
<p>Mechanism E <b>Out-of-plane corner overturning:</b> Dislocation of corner Out-of-plane failure of the corner, detaching from orthogonal wall junction and outward overturning</p>	<ul style="list-style-type: none"> <li>- High stress concentrations due to poor roof anchoring and lack of uniform distribution of roof loads</li> <li>- Vertical corner cracks, due to: <ul style="list-style-type: none"> <li>- Different in-plane/out-of-plane walls movements, splitting walls' joints.</li> <li>- Inadequate orthogonal walls connections on the horizontal plane</li> <li>- Poor wall fabric quality and uneven connections</li> </ul> </li> </ul>		 <p>Photo: DCHS [17]</p>
<p>Mechanism F <b>Local failures:</b> Vertical cracks In the middle of long walls (a) or in the corner (b), affecting the wall monolithic behaviour and the whole building box-behaviour.</p>	<ul style="list-style-type: none"> <li>- Floor or roof beams unthreading and hammering, due to displacement caused by horizontal seismic actions, (a), (b). [17]</li> <li>- Vertical blocks junctions and openings alignment on the wall plane (a), (b) [20]</li> </ul>		 <p>Photo: DCHS [17]</p>
<p>Mechanism G <b>Local failures:</b> Lintel Cracks Cracks vertically or diagonally developing from lintels above walls' openings.</p>	<ul style="list-style-type: none"> <li>- Rammed earth-wooden lintels different shrinkage [20]</li> <li>- Asymmetric openings and inefficiency of lintel insertion in the wall masonry.</li> <li>- Excessive openings dimensions.</li> <li>- Shear efforts due to in-plane movements. [17]</li> </ul>		 <p>Photo: DCHS [17]</p>

## 2.3 Mechanical Behaviour of Rammed Earth

This section reports on the previous study carried out to understand the mechanical behaviour of rammed earth. In particular, three important mechanical characteristics i.e., compressive strength, tensile strength and shear strength is described.

### 2.3.1 Compressive strength

The compressive strength of rammed earth is evaluated through compression test on either cylinder or prism specimens, and also on wallettes. The summary of compressive strength and the material properties of unstabilised rammed earth is reproduced in Table 2.4 after Bui et al. [21]. The material properties values reported varied from each study. From Table 3.1, the highest strength reported is 2.46 MPa and the lowest is 0.5 MPa. The density ranges from 1700 – 2160 kg/m<sup>3</sup>. The highest Young's modulus reported is 540 MPa while the lowest reported in 50 MPa.

Table 2.4 Material properties of unstabilised rammed earth.

Specimens	Compressive strength (MPa)	Density (kg/m <sup>3</sup> )	Slenderness	E <sub>tangent</sub> (MPa)	Reference
100 × 100 × 30	0.6-0.7	-	3.3	60	[9]
d=16 cm, h=26.5 cm	2.2		1.6		[21]
40 × 40 × 65 cm <sup>3</sup>	1	1820-1980	1.6	100	[21]
10 × 10 × 10 cm <sup>3</sup>	0.5-1.3	2020-2160	1	-	[22]
15 × 15 × 15 cm <sup>3</sup>	1.8-2	2020-2160	1	-	[23]
d=10 cm, h=20 cm	2.46	1850	2	70	[24]
30 × 30 × 60 cm <sup>3</sup>	0.62-0.97	1760-1970	2	160-205	[24]
d=16 cm, h=30 cm	1.7-2.1	1920	1.88	460-540	[25]
d=20 cm, h=40 cm	2	1848-1899	2	708-817	[26]
25 × 25 × 50 cm	1.15	1785-1798	2	310-440	[26]
d=10 cm, h=20cm	0.5-0.9	1700-1800	2	50-232	[27]
d=10 cm, h=20cm	1.4-1.7	1900-2000	2	100-320	[27]

### 2.3.2 Tensile strength

The tensile strength of rammed earth is neglected due to its low value. However, in an extreme loading condition such as earthquakes, neglecting tensile strength could be disadvantageous for the design purpose. The tensile strength of rammed earth in previous studies are evaluated through unconfined tensile test or estimated indirectly through a Brazilian test (splitting test). The test set up for both the test is presented in Figure 2.7 [28]. For unconfined tensile test, the specimen is

directly tensioned until it reaches failure. In splitting tensile test, a cylinder specimen is loaded uniformly in compression along the length. This condition creates tensile forces perpendicular to the loading direction and one can evaluate the tensile strength indirectly.

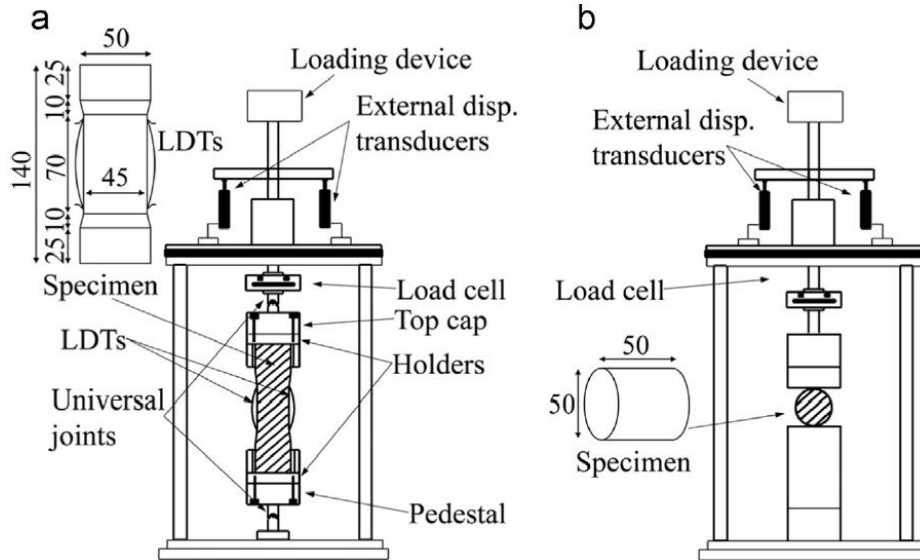
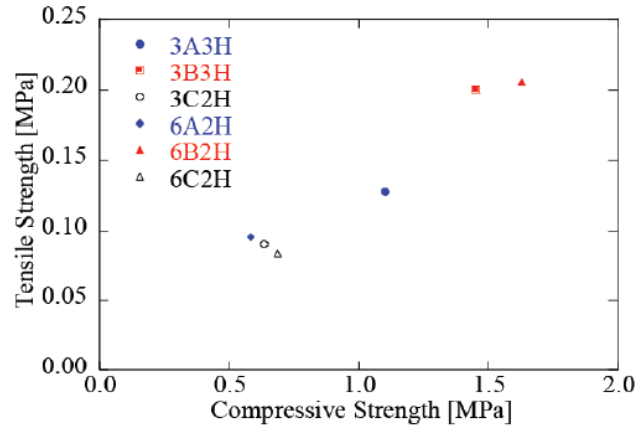
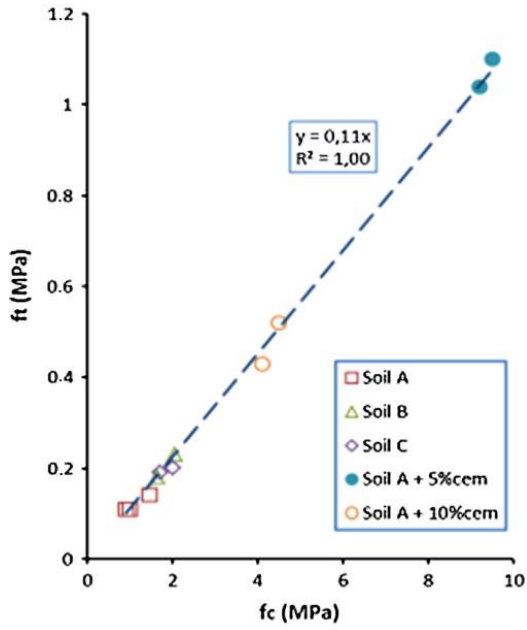


Figure 2.7 Specimens and apparatus for: (a) Direct tension test; (b) Splitting test [28].

Bui et al. [25] conducted splitting tensile strength on three different soils, and the result is presented in Figure 2.8(a). The results showed that the tensile strength of rammed earth was 11% of the corresponding compressive strength. Figure 2.8(b) reports on the results of tensile splitting test conducted for a Bhutanese rammed earth of various samples by DCHS [27]. According to the study, the tensile strength was 7-14% of the compressive strength.

Araki et al. [28] examined the tensile strength of unstabilized rammed earth through both unconfined and splitting test, and the result is presented in Figure 2.9. The figure shows the relationship between the tensile strength of rammed earth as a function of water content. Clearly, the tensile strength is influenced by the water content. Here, the tensile strength of rammed earth is found 7.5-12.5% of the compressive strength, and the percentage value is almost close to the one reported by DCHS [27].



(a)

(b)

Figure 2.8 Tensile strength vs compressive strength: (a) Bui et al. [25]; (b) DCHS [27].

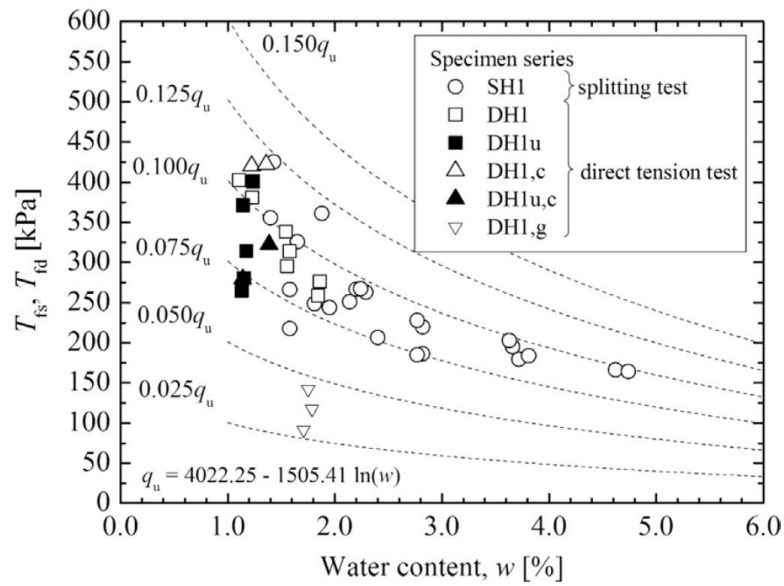


Figure 2.9 Tensile strength as a function of water content [28].



### 2.3.3 Shear strength

The diagonal compression test is a typical test to study the shear strength of rammed earth walls. The wallette is inclined to  $45^\circ$  and loaded vertically along the diagonal of the wallette. Miccoli et al. [29] used a diagonal compression test (Figure 2.10(a)) to examine the shear strength of unstabilised rammed earth. The test results are presented in Figure 2.10(b) in terms of shear stress vs shear strain. The shear strength varied between 0.54 and 0.83 MPa, and shear modulus varied between 1260 and 2146 MPa. The shear modulus was computed between 5 and 30% of shear strength by the linear fitting.

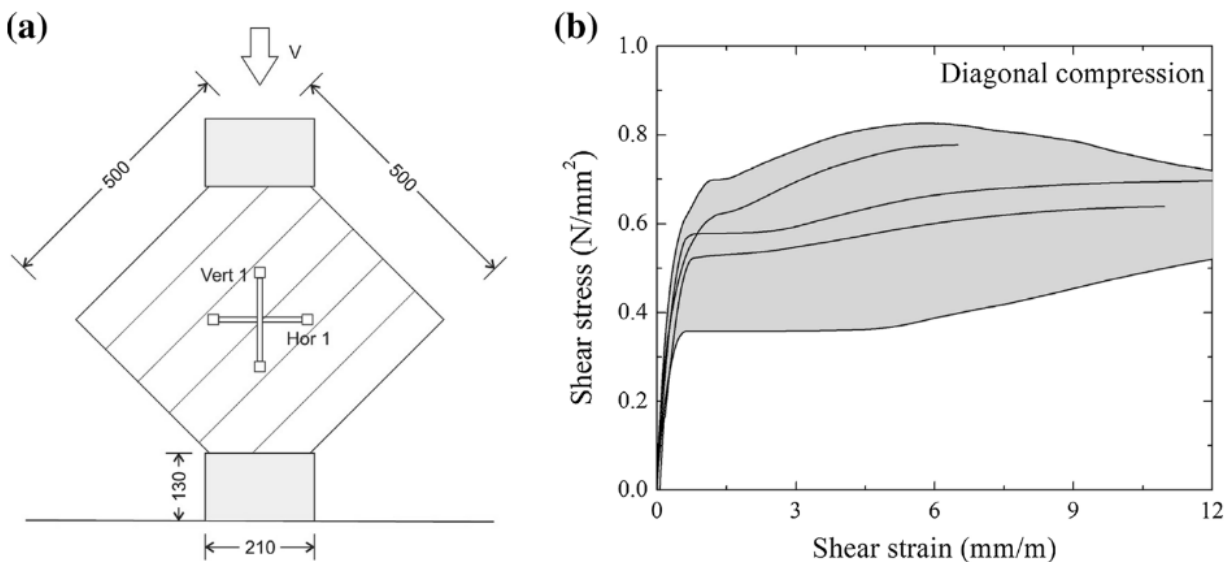


Figure 2.10 Diagonal compression test: (a) Test setup; (b) Shear stress vs shear strain [29].

## 2.4 Factors Influencing Mechanical Behaviour of Rammed Earth: Compressive Strength

The compressive strength of rammed earth is affected by many parameters like manufacturing moisture content, compaction energy, dry density and sample geometry. The influences of these parameters are studied by various researchers in the past which is described in detail below.

### 2.4.1 Effect of Moisture content

One disadvantage of rammed earth is its sensitivity to the water, and the moisture content in it affects the compressive strength. Bui et al. [30] studied the effects of moisture content on rammed earth's compressive strength with different soils (listed in Table 2.5) under unconfined compression at several moisture contents, and the results are depicted in Figure 2.11. It was observed that when the moisture content was below 4% by weight, the strength was almost

constant. However, at moisture content greater than 4%, the compressive strength decreased as the moisture content increased for all the tested samples.

Table 2.5 Soil used in the study [30].

Soil	Clay (%)	Silt (%)	Sand (%)	Gravel (%)
A	5	30	49	16
B	4	35	59	2
C	9	38	50	3
D	10	30	12	48
E	10	22	43	25

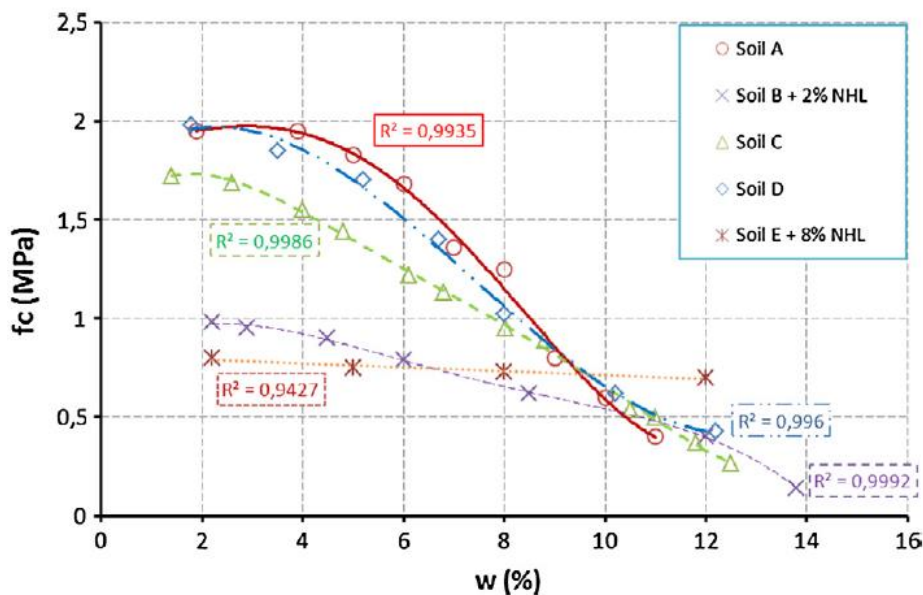


Figure 2.11 Variation of compressive strength with moisture content [30].

#### 2.4.2 Effect of Dry density

The compressive strength of rammed earth is affected by the dry density which is dependent on water content and compaction energy. Several authors have investigated the relationship between density and compressive strength. For example, Morel et al. [31] examined the strength of rammed earth blocks for both unstabilized and stabilized earth. The variation of compressive strength with the dry density is presented in Figure 2.12. It is seen that the compressive strength increases as the dry density increases for both unstabilized and stabilized rammed earth blocks.

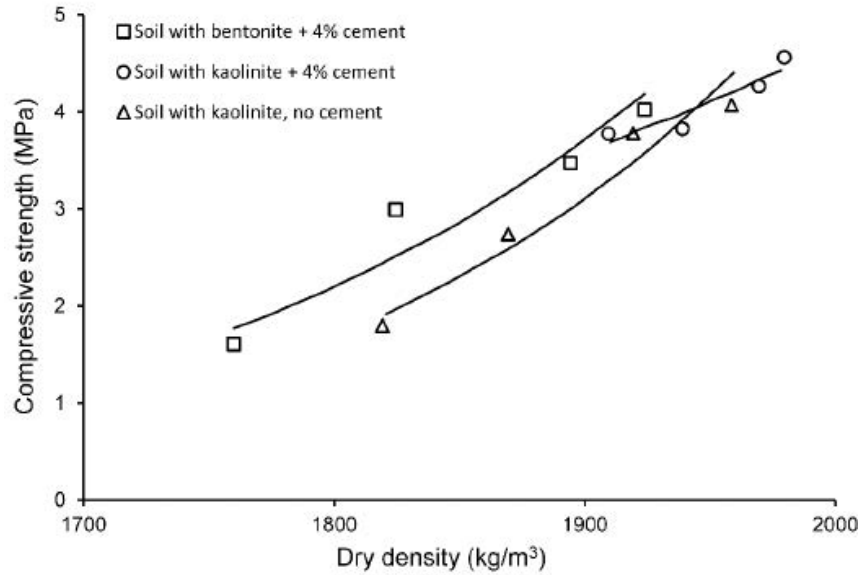


Figure 2.12 Variation of compressive strength with dry density [31].

### 2.5.2.1 Influence of compaction energy on dry density

Dry density is dependent on moisture content and compaction energy. The relationship between dry density, moisture content and compaction energy is studied by Jaquin [9]. The results from this study are shown in Figure 2.13 shows the zero air voids line for a given soil. Clearly, the optimum water content decreases with higher compaction effort. And the dry density is higher for higher compaction energy. From the figure, it is also seen that for higher mass of rammer, the compaction energy achieved is greater. In addition to rammer's mass, the compaction energy is influenced by drop distance of rammer and number of blows per layer.

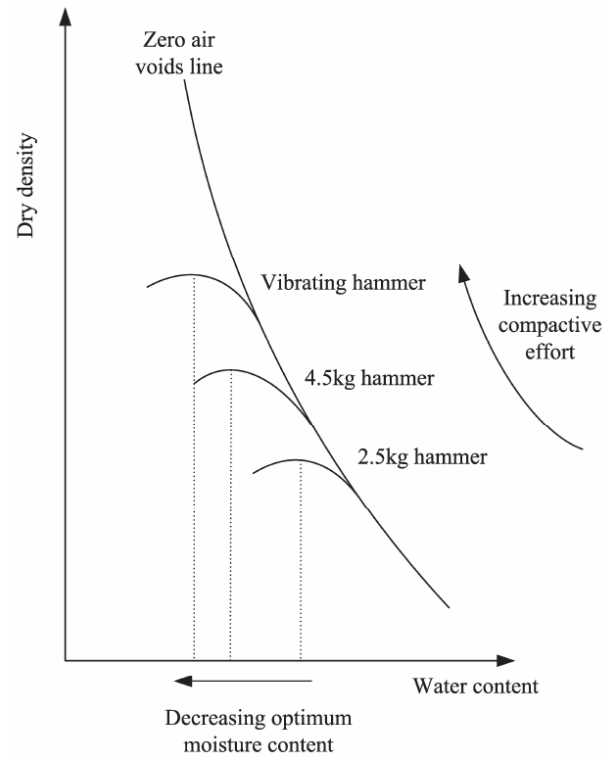


Figure 2.13 Variation of dry density with water content [9].

### 2.5.2.2 Influence of rammer weight, drop distance and number of blows on dry density

Kong et al. [32] conducted a triaxial compression test to see the influence of three parameters on dry density. The parameters considered are: i) Rammer weight ( 2.5 kg, 5 kg, 10 kg and 20 kg), ii) hammer blow number per layer (25, 50, 100 and 200), and iii) drop distance of hammer (305 mm, 610 mm and 1220 mm). The influence of hammer weight and the number of blows per layer on dry density is shown in Figure 2.14. The results show that the dry density is proportional to the hammer weight and the number of blows per layer. The effect of drop distance of hammer on dry density is also studied in the same program. The result is presented in Figure 2.15 for various hammer weight, and it is clear from the figure that the dry density increases with increasing drop distance of hammer.

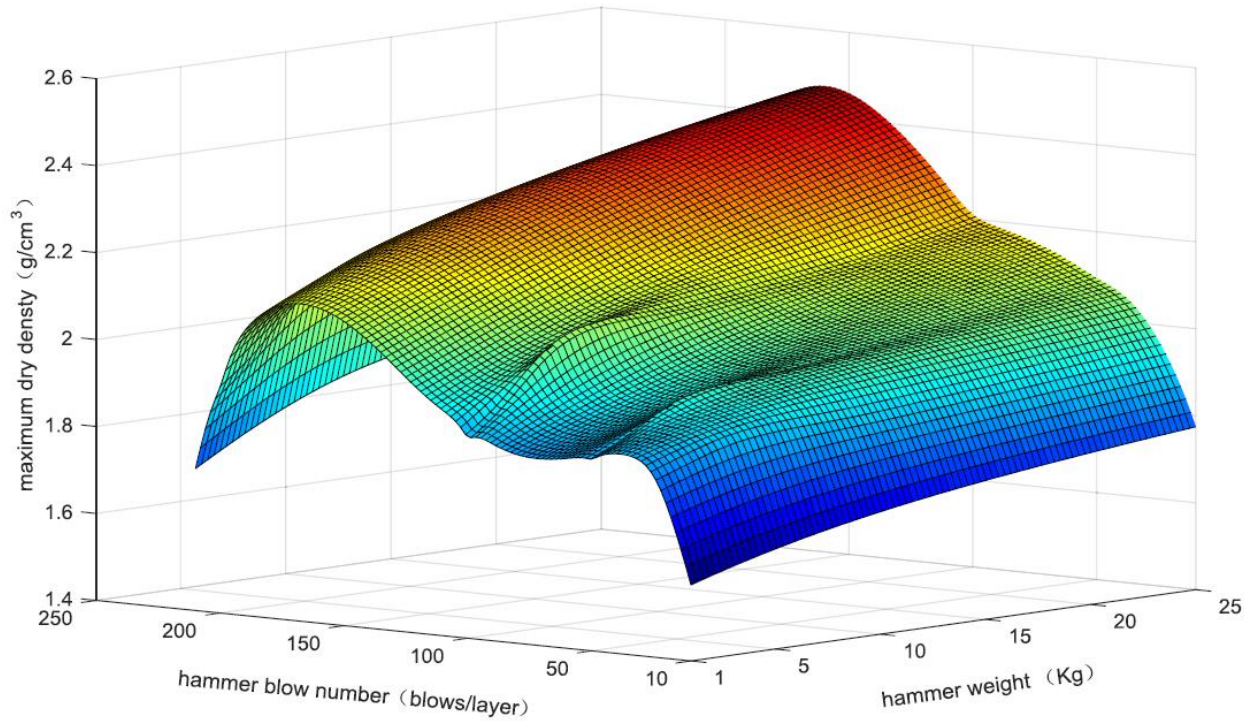


Figure 2.14 Variation of dry density with number of blow and hammer weight [32].

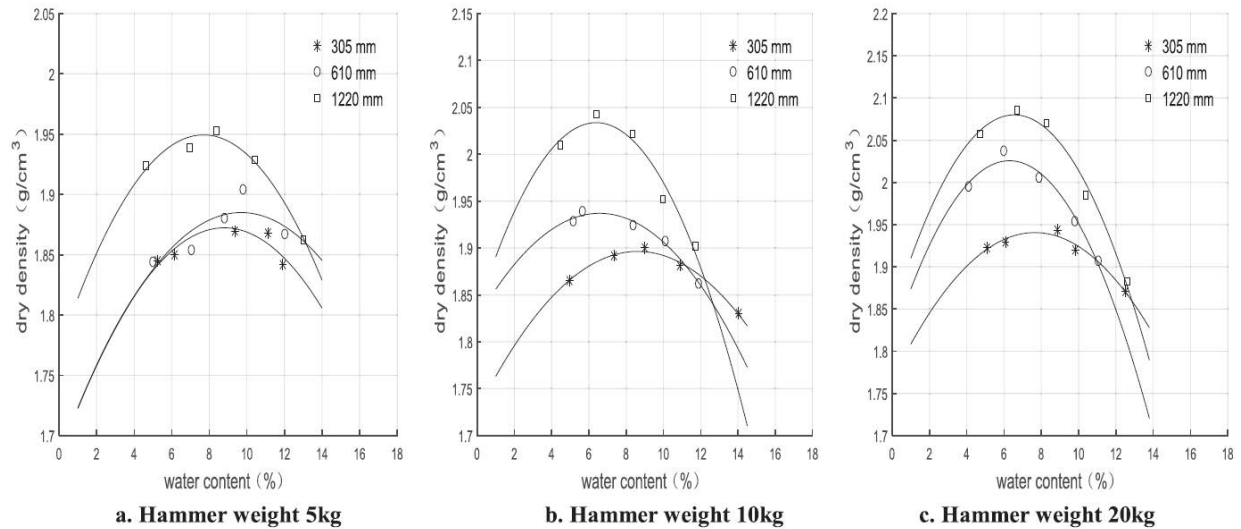


Figure 2.15 Variation of dry density with drop distance of rammer [32].

### 2.5.2.3 Influence of specimen size

The specimen size influences the compaction energy required in making stabilized rammed earth [33]. The compaction energy required for making rammed earth from different sources is compiled and presented in Table 2.6 reproduced after Raju et al. [33]. The table details specimen size, layer

thickness, cement content, dry density, and compaction energy of cement stabilized rammed earth. The results show that compaction energy increases with decrease in specimen size. Comparing the cylindrical specimen in the table, the energy input for 102 mm diameter and 116 mm diameter is 0.6 MJ/m<sup>3</sup> whereas, for a specimen with 150 mm diameter and 300 mm tall, it is 0.44 MJ/m<sup>3</sup>. For a bigger specimen like the walette (155 × 600 × 700 mm), the compaction energy is 0.2, which is lower than the energy required for smaller cylindrical specimens. The table also reports on the compaction energy required for rammed earth wall construction in building having wall thickness 200 and 400 mm thick. From there, the wall with lower thickness is observed to have higher compaction energy compared to the wall with 400 mm thick.

Table 2.6 Influence of specimen size on the compaction energy [33].

Specimen size (mm)	Layer thickness (mm)	Cement content (%)	Dry density (kg/m <sup>3</sup> )	<i>E</i> (MJ/m <sup>3</sup> )	References
d=102, h=116	38	7	1917	0.6	[33]
d=150, h=300	100	7	1900	0.44	[33]
155 × 600 × 700	100	8	1900	0.2	[34]
Wall, t= 200	35	8	1800	0.17	[34]
Wall, t=400	70	8	1800	0.08	[34]

d – diameter; h – height; t – wall thickness; *E* – compaction energy;

#### 2.4.3 Effect of Rammed Earth Layer Thickness

Raju et al. [16] examined the influence of layer thickness on characteristics of cement-stabilised rammed earth (CSRE) in the both dry and wet state. Cylindrical specimens of 150 mm diameter and 300 mm height were prepared with soil mixed with 7% of cement (by mass) and dry density 1800 kg/m<sup>3</sup>. Four compacted layers were chosen, i.e., 75 mm, 100 mm, 150 mm and 300 mm. Five samples were tested for each series. The results from the study are presented in Figure 2.16(a) for CSRE in a dry state, and Figure 2.16(b) for the wet state. The test results showed that 100 mm layer thickness had the highest stiffness and strength, while 300 mm layer thickness has both the lowest values. The optimum compacted layer thickness giving maximum compressive strength for CSRE is 90 - 100 mm.

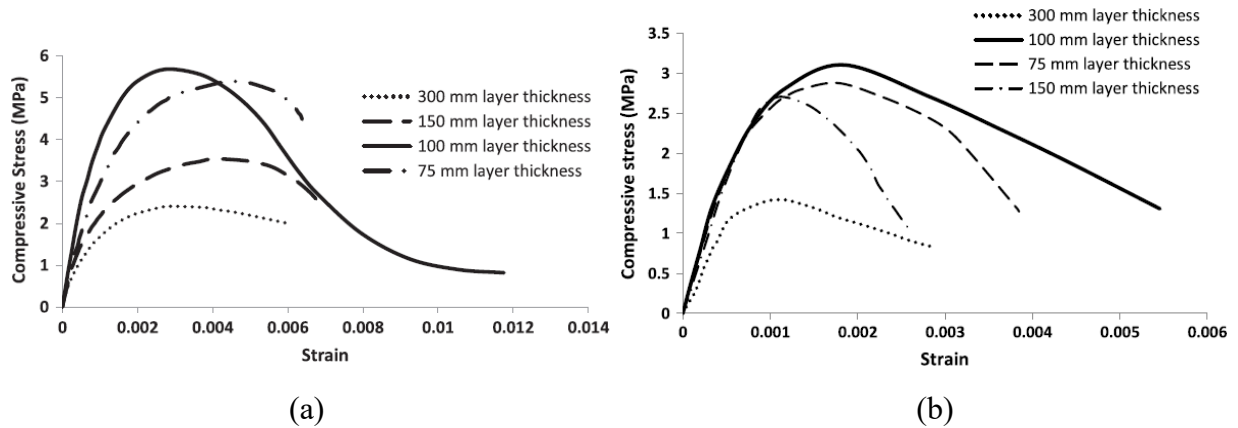


Figure 2.16 Effect of layer thickness in compressive strength: (a) In dry state; (b) In wet state [33].

## 2.5 Improving Mechanical Properties of Rammed Earth through Stabilization

The low mechanical properties of rammed earth have been repeatedly highlighted. It has become common in modern rammed earth construction to stabilize soil with a small portion of cement and lime or the addition of a small number of natural fibres. This section will discuss the type of materials used for stabilizing the soil and their proportion recommended by various authors.

### 2.5.1 Cement

The use of cement has emerged out of a need to improve wet compressive strength and erosion resistance (durability) in every exposed wall [6,31]. The presence of cement increases the compressive strength of rammed earth. Cement is typically used in proportions between 4% and 15% [5]; however, the range commonly specified lies between 5% [35] and 10% the most [36-37]. Stabilization with cement can be expensive; therefore, Victor et al. [38] investigated the feasibility of using Rice Husk Ash (RHA) as a partial replacement of cement. It was recommended to stabilize soil blocks with at least 5% cement and 7.5% RHA to achieve minimum strength of 2.5 MPa.

### 2.5.2 Lime

Lime is usually used in earthen buildings of heritage importance, where the use of cement is prohibited by some regulations. The dosage of lime depends on the clay content, and the recommended ratio is between 6-12% by its dry weight [5].

### 2.5.3 Using Fibers

Fibres are usually used to improve the thermal performance, bending and tensile strength of the soil. Some of the fibre used includes straw, sisal fibres and timber. The ideal soil for fibre stabilization should have a plasticity index between 15% and 35% with the liquid limit from 30% to 50% [39]. However, the use of fibre like straw results into decrease in compressive strength of soil [40].

### 2.5.4 Using Dung

Mixing dung with soil improves cohesion and plasticity of soils, according to Khadka et al. [37]. The compressive strength of soil with 5% of dung was observed higher than the soil with 10% dung. More intensive study is required to have a perfect proportion to be used.

## 2.6 Strengthening Measures Proposed for Rammed Earth Structures

This section presents a review on strengthening techniques proposed by various authors for both new and old construction.

### 2.6.1 For New Construction

Some of the works which were carried out to reinforce the new construction for rammed earth are summarized in Table 2.7.

Table 2.7 Proposed strengthening measures for new construction.

Ref.	Material and method	Specimen size (m)	Test type	Remarks
[38]	Fibre grids (Glass, carbon, steel, Poliparafenil-benzobisoxazole and basalt)	Prism (0.35×0.1×0.1)	Flexural	-Not available -Cannot be afforded by ordinary people
[39]	Post-tensioned bar embedded with RE wall	Wall (2.4×2.1×0.6)	Out-of-plane	-Post tensioning system not available -Can be expensive -Test results confirm ineffective in out-of-plane
[40]	reinforced concrete (RC) beams and columns inside RE wall	Reduced scale model (2.6×2.4×2.1×0.4)	Shake table test	-Use of larger sections increases the cost -Might compromise the compaction -Time-consuming as ties and stirrups are used



Fibre grids are used [40] to improve the seismic performance of the rammed earth. However, it would cost extra due to the non-availability of the material in the local market, and importing will result in an unnecessary escalation of the building cost, which is undesirable.

Hamilton et al. [41] conducted laboratory testing on eight full-scale rammed earth walls, containing vertical post-tensioned reinforcement within the rammed earth wall. The details of the test set up and reinforcement placement are shown in Figure 2.17. The test results showed that the wall tested in in-plane performed well; however, the walls tested in out-of-plane did not perform as well as expected. Moreover, the effectiveness of the embedded post-tensioned bar reduced as the height of the wall increased. Use of post-tensioned bar can be expensive, particularly in a region where such systems are not available, which is the case in Bhutan. However, regular rebar can be used in adopting a similar technique.

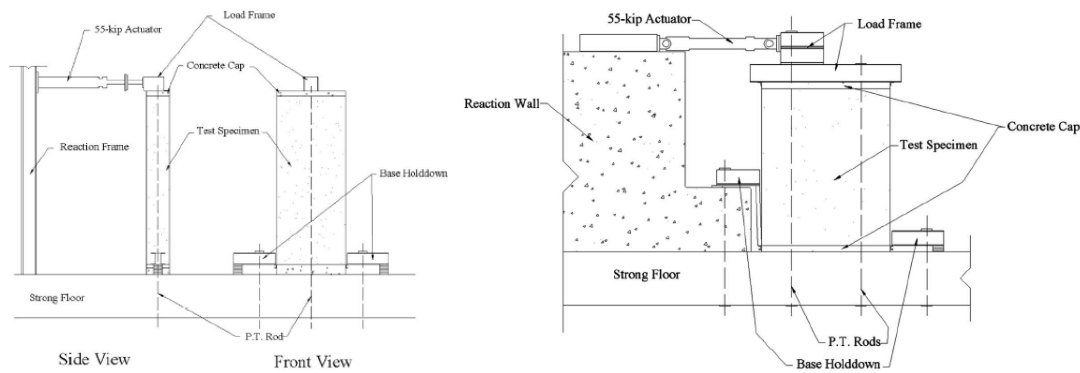


Figure 2.17 Test set up and placement of post-tensioned bar: (a) Out-of-plane; (b) In-plane [41].

Another seismic measure proposed, which includes employment of reinforced concrete (RC) beams and columns inside the RE wall, transforming the load-bearing mode of RE buildings to the RC structures [42], the details are presented in Figure 2.18. These inner RC structures enabled the RE buildings to undertake extra earthquake actions even after the building attained elastic-plastic stage or complete destruction condition. The proposed technique is more realistic for Bhutanese rammed earth considering the materials are available in the local market. However, reducing the size of RC sections can reduce the cost. Also, avoiding the stirrups in the vertical post can save both time and cost. Despite its advantages, the placement of the aforementioned reinforcements in rammed earth wall can be cumbersome, and proper compaction may not be achieved around those components. Thus, extra attention should be paid during the construction to avoid such compromise while ramming.

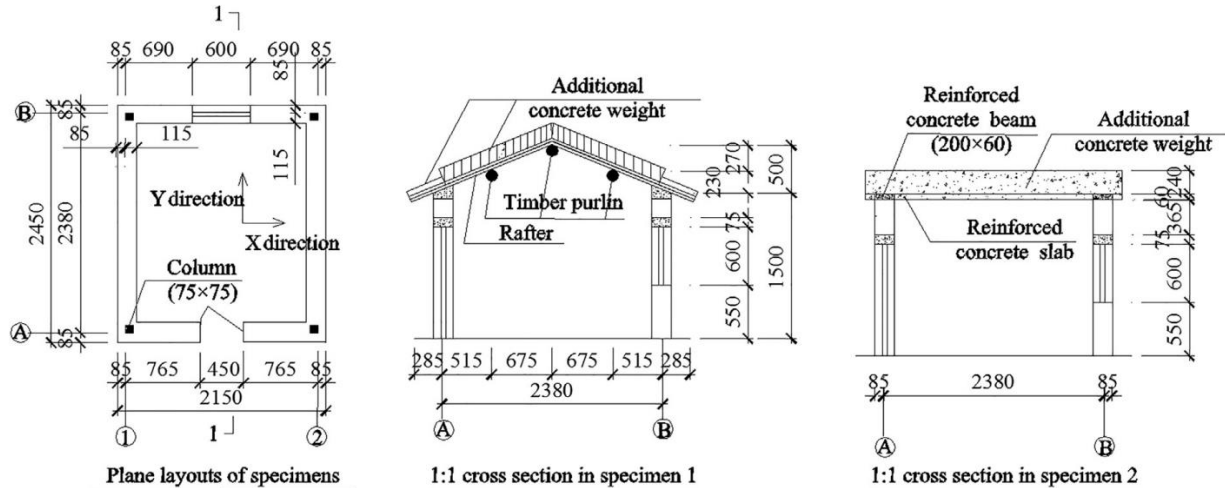


Figure 2.18 Proposed seismic measures for new construction [42].

### 2.6.2 For Existing Buildings (retrofitting measures)

A wide range of retrofitting measures was explored involving different materials and techniques, some of which are listed below Table 2.8.

Table 2.8 Proposed strengthening measures for the existing building.

Ref.	Material and method	Binding material	Specimen size (m)	Test type
[14]	Externally bonded with tarpaulin, canvas and bamboo	NF compound, epoxy adhesive and Sodium silicate	Wall (2.4×2.1× 0.6)	In-plane
[13]	Externally bonded with tarpaulin	NF compound	Reduced scale model (2.6×2.4×2.1× 0.4)	Shake table test
[44]	Steel plates configured in grid systems	Plates connected by transverse steel	L-shaped wall (2×3.45×0.6)	Out-of-plane
[45]	Rebar configured in grid system	Connected by tie bar and plastered with cement mortar	Walette (2×1.5×0.25)	
[46]	Polyester fabric strips in vertical direction	Base coat mortar and Polymer primer	Walette (1.3×1.05×0.25)	In-plane

Liu et al. [14] proposed tarpaulin (double layered) with NF compound (Figure 2.19) as the most practical considering the cost and reinforcement effect. The retrofitting technique improved the lateral load capacity of the rammed earth wall by up to 38% and the maximum horizontal displacement by up to 75%. This technique provides simple and effective measures to strengthen the rammed earth wall against seismic action with minimal increase in the mass of the structure. This retrofitting scheme was applied in a horizontal direction to two full-scale single storey model with dimensions 2600 × 2400 × 2100 mm and a wall thickness of 400 mm (Figure 2.20), and

testing under shaking table [13]. The seismic resistance of rammed earth structures was improved using the proposed retrofitting method.

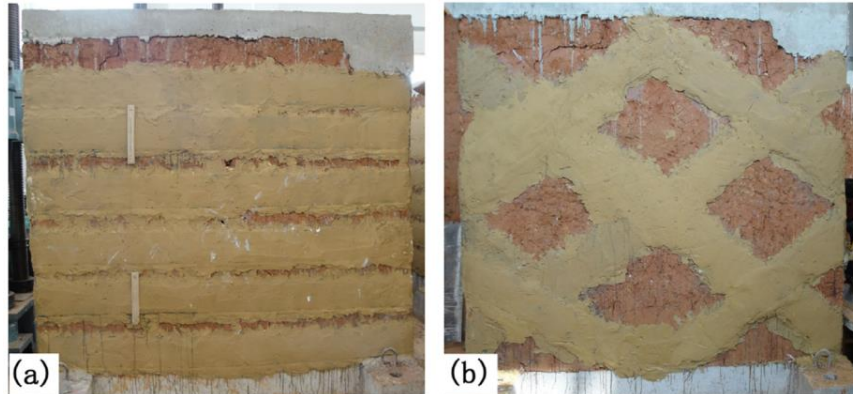


Figure 2.19 Retrofitting with tarpaulin: (a) In horizontal direction; (b) In diagonal direction [14].

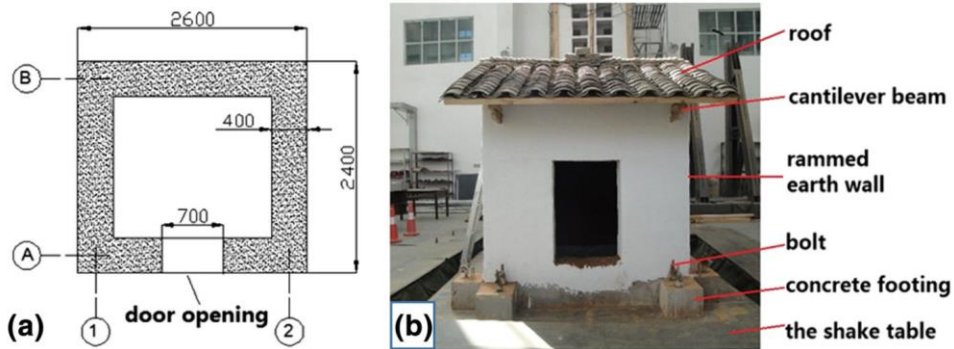


Figure 2.20 Model details tested under shaking table [13].

Reyes et al. [44] placed steel plates on both faces of the wall, configured in a grid system, as shown in Figure 2.21. The proposed measure improved to sustain the out-of-plane demands and delayed the appearance of larger cracks. It is essential to provide plates on both faces of the wall and have them connected by rods to avoid mechanical incompatibility. Furthermore, using thinner plates will reduce the cost and also minimize the weights on the structures.

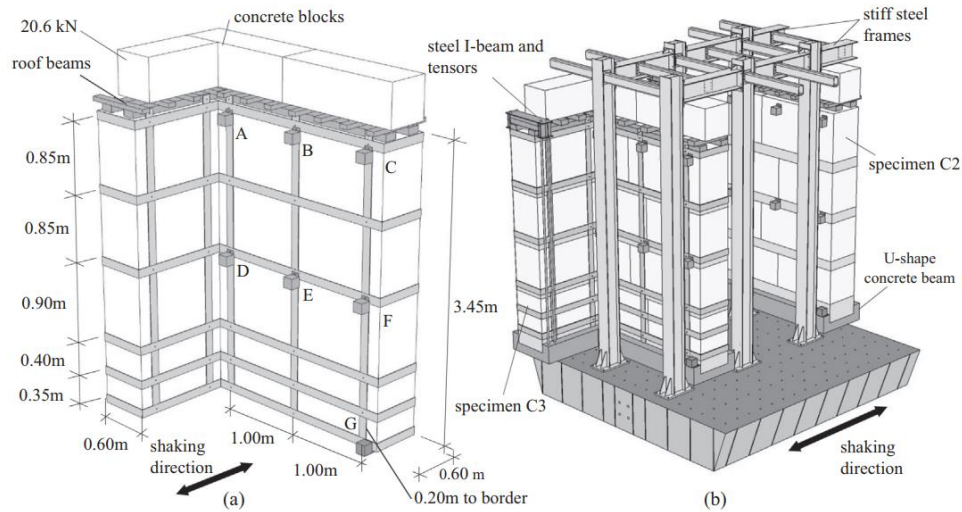


Figure 2.21 Overview of shaking table set up and steel plate placement [44].

A similar retrofitting method, providing reinforcement in grid system was also explored by Pang et al. [45], however using bars in place of steel plates. The reinforcement was provided in both faces of the wall connected by tie bars. The reinforcement was covered by providing cement mortar M10 with a thickness of 30mm. The detail of the reinforcement layout is shown in Figure 2.22. Such a reinforcing technique was observed to improve the ultimate bearing capacity of rammed earth walls. However, separation of mortar layer from the wall was observed due to rammed earth cohesive failure.

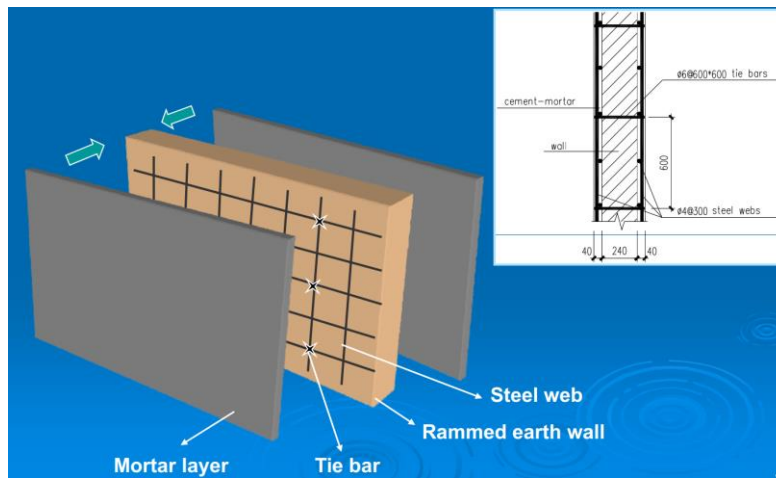


Figure 2.22 Reinforcement layout details [45].

Other strengthening measures in the literature include providing polyester fabric strips in the vertical direction of rammed earth wall of size  $1300 \times 1050 \times 250$  mm [46]. The overview of the

strengthening technique and material is shown in Figure 2.26. The walls were tested under cyclic loading. The strengthening technique prevented the extension of diagonal cracks, and horizontal load-carrying capacity and displacement capacity was improved. However, improvement in ductile behaviour was negligible.

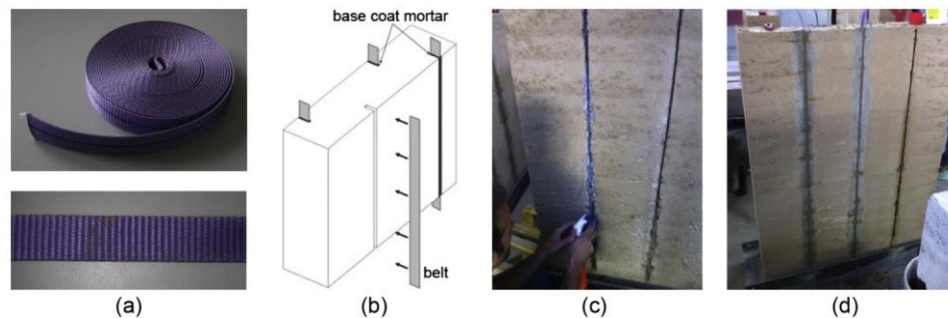


Figure 2.23 Strengthening procedures with polyester fabric strips in vertical [46].

Although the above proposed retrofitting measures are reported to be effective in improving the strength, it can be discouraging as it disrupts the visual aspects of the rammed earth wall.

## 2.7 Conclusion

The chapter presented the overview of rammed earth, including its construction details. The study carried out for understanding the critical mechanical parameters of rammed earth, in particular compressive strength, tensile strength and shear strength from the previous works is presented. The compressive strength reported varied from 0.5 MPa to 2.46 MPa, density from 1700 kg/m<sup>3</sup> to 2160 kg/m<sup>3</sup> and Young's modulus from 50 MPa to 540 MPa. The tensile strength of rammed earth was observed 7-14% of the corresponding compressive strength. The shear strength ranged from 0.54 MPa to 0.83 MPa with shear modulus ranging from 1260 MPa to 2146 MPa. The influences of various factors like construction process, moisture content, dry density and compaction energy on the mechanical behaviour of rammed earth (compressive strength) are also highlighted.

Further, the chapter discussed the vulnerability of rammed earth and their common failures observed for rammed earth buildings during the earthquakes, referring to the previous earthquake events. It is observed that the rammed earth wall mostly fails in out-of-plane. The previous studies focused on exploring the strengthening measures to improve the seismic performance of rammed earth for both existing and new construction have been highlighted. However, some of the proposed measures are not feasible for Bhutanese rammed earth buildings mainly because the

material proposed are expensive and are not readily available in the local market, while some strengthening measures are a tedious process. Further, few works are carried out on small-scale walls which do not necessarily reproduce the actual behaviour of the real sized building. In order to ensure widespread utilization of the proposed technique and to be accepted by the locality, the proposed strengthening techniques should be kept simple, cost-effective and the materials used should be readily available in the local market. Therefore, in this thesis, these guiding principles are followed while selecting the strengthening measures and technique for both existing and new construction. Their feasibility and effectiveness are verified by conducting the experimental test on small scale walls to real-sized buildings.

## References

- [1] BYJU's The Learning App, "Soil profile definition," *BYJU's The Learning App*. [online]. Available: <https://byjus.com/biology/soil-profile/>. [Accessed: Jan. 25, 2021].
- [2] G. Torraca, "Lectures on Materials Science for Architectural Conservation," *Getty Conserv. Inst.*, 2009, doi: 10.1007/s13398-014-0173-7.2.
- [3] BS 5930, "Code of practice for site investigations," *Br. Stand. Inst.*, pp. 1–192, 2009.
- [4] J. Keable and R. Keable, *Rammed Earth Structures: A Code of Practice*, Second Edition. 2011.
- [5] V. Maniatidis and P. Walker, "A review of rammed earth construction," in *Developing rammed earth for UK housing*, 2003.
- [6] H. Houben, H. and Guillaud, *Earth construction: a comprehensive guide*. 1994.
- [7] DCHS, *Typology study on Bhutanese rammed earth buildings*. Thimphu: Division for Conservation of Heritage Sites, Department of Culture, Ministry of Home and Cultural Affairs, Royal government of Bhutan, 2017.
- [8] P. Wangmo, K.C. Shrestha, T.Aoki, M.Miyamoto, N.Takahashi, J.Zhang, N.Yuasa, S.Shin, Pema, F.DE Filippi, and R. Pennacchio, "Mesh-wrap retrofitting for rammed earth buildings – Test results of full-scale static tests" 17<sup>th</sup> World Conference on Earthquake Engineering, 2020.
- [9] P. A. Jaquin, "Analysis of Historic Rammed Earth construction," Durham University, 2008.

- [10] P. Roberto, F. De Filippi, M. Bosetti, T. Aoki, and P. Wangmo, “Influence of Traditional Building Practices in Seismic Vulnerability of Bhutanese Vernacular Rammed Earth Architecture,” *Int. J. Archit. Herit.*, pp. 1–20, 2020, doi: 10.1080/15583058.2020.1785044.
- [11] UNDRO, “Natural disasters and vulnerability analysis: report of Experts Group Meeting of 9–12 July 1979,” 1980. doi: 10.1103/PhysRevA.47.4474.
- [12] G. Grünthal, *European Macroseismic Scale 1998*. 1998.
- [13] Y. Wang, M. Wang, K. Liu, W. Pan, and X. Yang, “Shaking table tests on seismic retrofitting of rammed-earth structures,” *Bull. Earthq. Eng.*, vol. 15, no. 3, pp. 1037–1055, 2017, doi: 10.1007/s10518-016-9996-2.
- [14] K. Liu, M. Wang, and Y. Wang, “Seismic retrofitting of rural rammed earth buildings using externally bonded fibers,” *Constr. Build. Mater.*, vol. 100, pp. 91–101, 2015, doi: 10.1016/j.conbuildmat.2015.09.048.
- [15] K. C. Shrestha, T. Aoki, M. Miyamoto, P. Wangmo, and Pema, “In-plane shear resistance between the rammed earth blocks with simple interventions: Experimentation and finite element study,” *Buildings*, vol. 10, no. 3, pp. 1–13, 2020, doi: 10.3390/buildings10030057.
- [16] C. F. Oliveira, H. Varum, and J. Vargas, “Earthen Construction: Structural Vulnerabilities and Retrofit Solutions for Seismic Actions,” 2012.
- [17] DCHS, *Damage Assessment of Rammed Earth Buildings-After the September 18, 2011 Earthquake*. Division for Conservation of Heritage Sites, Department of Culture, Ministry of Home and Cultural Affairs, Royal Government of Bhutan, 2011.
- [18] EARRD, *Retrofitting manual for load bearing structures*. Thimphu: Engineering Adaptation & Risk Reduction Division, Department of Engineering Services, Ministry of Works and Human Settlement, 2017.
- [19] D. M. Dowling, “Adobe housing in El Salvador: Earthquake performance and seismic improvement,” in *Special Paper 375: Natural Hazards in El Salvador*, 2007.
- [20] D. D’Ayala and E. Speranza, “An integrated procedure for the assessment of seismic vulnerability of historic buildings,” *12th Eur. Conf. Earthq. Eng.*, 2002.

- [21] Q. B. Bui, J. C. Morel, S. Hans, and N. Meunier, “Compression behaviour of non-industrial materials in civil engineering by three scale experiments: The case of rammed earth,” *Mater. Struct. Constr.*, vol. 42, pp. 1101–1116, 2009, doi: 10.1617/s11527-008-9446-y.
- [22] M. Hall and Y. Djerbib, “Rammed earth sample production: Context, recommendations and consistency,” *Constr. Build. Mater.*, 2004, doi: 10.1016/j.conbuildmat.2003.11.001.
- [23] D. M. Lilley and J. Robinson, “Ultimate strength of rammed earth walls with openings,” *Proc. Inst. Civ. Eng. Struct. Build.*, 1995, doi: 10.1680/istbu.1995.27872.
- [24] V. Maniatidis and P. Walker, “Structural capacity of rammed earth in compression,” *J. Mater. Civ. Eng.*, 2008, doi: 10.1061/(ASCE)0899-1561(2008)20:3(230).
- [25] T. T. Bui, Q. B. Bui, A. Limam, and S. Maximilien, “Failure of rammed earth walls: From observations to quantifications,” *Constr. Build. Mater.*, vol. 51, pp. 295–302, 2014, doi: 10.1016/j.conbuildmat.2013.10.053.
- [26] R. El-Nabouch, “Mechanical behavior of rammed earth walls under Pushover tests,” 2017.
- [27] DCHS, *General Guideline for improved seismic resilient construction techniques for rammed earth structures in Bhutan*. Division for Conservation of Heritage Sites, Department of Culture, Ministry of Home and Cultural Affairs, Royal Government of Bhutan, 2017.
- [28] H. Araki, J. Koseki, and T. Sato, “Tensile strength of compacted rammed earth materials,” *Soils Found.*, 2016, doi: 10.1016/j.sandf.2016.02.003.
- [29] L. Miccoli, D. V. Oliveira, R. A. Silva, U. Müller, and L. Schueremans, “Static behaviour of rammed earth: experimental testing and finite element modelling,” *Mater. Struct. Constr.*, vol. 48, pp. 3443–3456, 2015, doi: 10.1617/s11527-014-0411-7.
- [30] Q. B. Bui, J. C. Morel, S. Hans, and P. Walker, “Effect of moisture content on the mechanical characteristics of rammed earth,” *Constr. Build. Mater.*, vol. 54, pp. 163–169, 2014, doi: 10.1016/j.conbuildmat.2013.12.067.



- [31] J. C. Morel, A. Pkka, and P. Walker, “Compressive strength testing of compressed earth blocks,” *Constr. Build. Mater.*, vol. 21, no. 2, pp. 303–309, 2007, doi: 10.1016/j.conbuildmat.2005.08.021.
- [32] D. Kong, R. Wan, J. Chen, Y. Jing, W. Huang, and Y. Wang, “The study on engineering characteristics and compression mechanisms of typical historical earthen site soil,” *Constr. Build. Mater.*, vol. 213, pp. 386–403, 2019, doi: 10.1016/j.conbuildmat.2019.04.028.
- [33] L. Raju and B. V. V. Reddy, “Influence of layer thickness and plasticizers on the characteristics of cement-stabilized rammed earth,” *J. Mater. Civ. Eng.*, vol. 30, no. 12, pp. 1–10, 2018, doi: 10.1061/(ASCE)MT.1943-5533.0002539.
- [34] B. V. Venkatarama Reddy and P. Prasanna Kumar, “Embodied energy in cement stabilised rammed earth walls,” *Energy Build.*, vol. 42, no. 3, pp. 380–385, 2010, doi: 10.1016/j.enbuild.2009.10.005.
- [35] B. Khadka and M. Shakya, “Comparative compressive strength of stabilized and unstabilized rammed earth,” *Mater. Struct. Constr.*, 2016, doi: 10.1617/s11527-015-0765-5.
- [36] X. Dong, M. Griffith, and V. Soebarto, “Feasibility of rammed earth constructions for seismic loads in Australia,” *Aust. J. Struct. Eng.*, 2015, doi: 10.1080/13287982.2015.1092685.
- [37] M. E. Arslan, M. Emiroğlu, and A. Yalama, “Structural behavior of rammed earth walls under lateral cyclic loading: A comparative experimental study,” *Constr. Build. Mater.*, 2017, doi: 10.1016/j.conbuildmat.2016.12.093.
- [38] V. Ronoh, J. W. Kaluli, and J. K. Too, “Characteristics of Earth Blocks Stabilized With Rice Husk Ash and Cement,” *J. Sustain. Res. Eng.*, vol. 2, no. 4, pp. 121–126, 2015.
- [39] Standards Australia, *The Australian earth building handbook*. 2002.
- [40] M. Gernot, *Building with Earth: Design and Technology of a Sustainable Architecture*, Birkhauser. Basel, Berlin, Boston: Birkhäuser – Publishers for Architecture, 2006.
- [41] H. R. Hamilton, J. McBride, and J. Grill, “Cyclic testing of rammed-earth walls containing post-tensioned reinforcement,” *Earthq. Spectra*, 2006, doi: 10.1193/1.2358382.

- [42] T. Zhou and B. Liu, “Experimental study on the shaking table tests of a modern inner-reinforced rammed earth structure,” *Constr. Build. Mater.*, 2019, doi: 10.1016/j.conbuildmat.2019.01.070.
- [43] T. L. Bui, T. T. Bui, Q. B. Bui, X. H. Nguyen, and A. Limam, “Out-of-plane behavior of rammed earth walls under seismic loading: Finite element simulation,” *Structures*, vol. 24, pp. 191–208, 2020, doi: 10.1016/j.istruc.2020.01.009.
- [44] J. C. Reyes *et al.*, “Seismic retrofitting of existing earthen structures using steel plates,” *Constr. Build. Mater.*, vol. 230, pp. 0950–0618, 2020, doi: 10.1016/j.conbuildmat.2019.117039.
- [45] M. Pang, S. Yang, and Y. Zhang, “Experimental study of cement mortar-steel fiber reinforced rammed earth wall,” *Sustainability*, vol. 4, pp. 2630–2638, 2012, doi: 10.3390/su4102630.
- [46] L. Miccoli, U. Müller, and S. Pospíšil, “Rammed earth walls strengthened with polyester fabric strips: Experimental analysis under in-plane cyclic loading,” *Constr. Build. Mater.*, vol. 149, 2017, doi: 10.1016/j.conbuildmat.2017.05.115.

*This chapter is written with reference to the authors' journal paper titled "Exploratory study of rammed earth walls under static element test", 2020 [1].*

### **3.1 Introduction**

This chapter reports on the series of element test conducted on unstabilised rammed earth walls to understand their structural behaviour under compression and shear loading. The strength characteristic of rammed earth wall is dependent on many parameters such as compaction, binding forces of mineral clays, the relative proportion between clays and aggregates, the water content of the mixture, dry density and specimen geometry [2]. In the present chapter, the author explores two parameters, namely rammed earth layer thickness (50 mm and 100 mm) and drying period of the walls (three months and twelve months), which is rarely discussed. The rammed earth walls in this study are manufactured from a reconstituted soil which closely represents the soil used in Bhutanese rammed earth construction.

Despite several studies being conducted to understand the compressive strength of the rammed earth in previous years [3-9], it was necessary to conduct the compression test again in the present study mainly to understand the actual behaviour of Bhutanese rammed earth under compression loading. Furthermore, compressive strength is the essential mechanical parameters, and the value from this test is used in the numerical analysis, reported in the final section of the chapter. Therefore, the first part of the Chapter reports on the rammed earth wall's structural behaviour and strength under compression loading. The influence of rammed earth layer thickness and drying periods on the wall's compressive strength is evaluated. Furthermore, a simple retrofitting method is explored using the wire mesh wrapped around the wall.

The second part of the Chapter reports on in-plane behaviour of the rammed earth walls under shear loading. Literature dealing with rammed earth under vertical loading is rich; however, only a few studies have been carried out to investigate the rammed earth wall under horizontal loading [10-13]. Therefore, the work presented here is expected to add value to the limited literature

involving rammed earth wall under in-plane loading. Even here, the effects of rammed earth layer and drying period are studied. Further, the effect of the mesh wrap retrofitting technique is also assessed under the horizontal static loading. Their effects on rammed earth walls' strength are studied in terms of load-displacement relationship and failure patterns. Another main objective of this test is to derive the essential parameter under shear strength of rammed earth, i.e., cohesion and friction angle. For this purpose, the walls before applying the horizontal load are subjected to normal pre-compression, which is referred to as “vertical stress” in this thesis. Three different vertical stresses are applied, and the values are 0.1 MPa, 0.15MPa and 0.2 MPa, which corresponds to the stresses at the roof, second and first floor level of typical Bhutanese rammed earth buildings.

In the final section, numerical modelling of RE wall tested under shear loading is carried out for both unreinforced and retrofitted samples, presenting details on the modelling of rammed earth wall as well as mesh composite, used as retrofitting technique. The numerical analysis aims to compare and support the experimental results. A sensitivity analysis is also carried out with different mechanical properties to analyze the effect of their variabilities on the shear strength of RE wall.

The main objectives of this chapter are highlighted below:

1. Study the structural behaviour of rammed earth under compression and shear loading.
2. Assess the critical mechanical parameters such as compressive strength, Young modulus, shear strength, cohesion and friction angle.
3. Study the possible influence of rammed earth layer thickness and drying periods on the rammed earth wall's compressive and shear strength.
4. Check the effectiveness of mesh-wrap strengthening method.

### **3.1.1 Rammed Earth under Compression Loading**

Rammed earth walls are mostly constructed as a load-bearing for any structure of varying functional like heritage buildings, residential house and boundary walls. For any load-bearing wall, the compressive strength is one of the most critical strength parameters. As already stated, the compressive strength of rammed earth is affected by many parameters, which have been explored by various researchers in recent times. The compressive strength of rammed earth is evaluated through compression test on either cylinder or prism specimens, and also on wallettes. The

summary of compressive strength and the material properties of unstabilised rammed earth is reproduced in Table 3.1 after Bui et al. [3]. However, it should be noted that Table 3.1 does not report on the material properties from wall specimens but only from the cylindrical and prismatic specimens.

Table 3.1 Material properties of unstabilised rammed earth.

Specimens	Compressive strength (MPa)	Density (kg/m <sup>3</sup> )	Slenderness	E <sub>tangent</sub> (MPa)	Reference
10 × 10 × 10 cm <sup>3</sup>	0.5-1.3	2020-2160	1	-	[4]
15 × 15 × 15 cm <sup>3</sup>	1.8-2	2020-2160	1	-	[5]
d=10 cm, h=20 cm	2.46	1850	2	70	[6]
30 × 30 × 60 cm <sup>3</sup>	0.62-0.97	1760-1970	2	160-205	[6]
100 × 100 × 30	0.6-0.7	-	3.3	60	[7]
d=16 cm, h=26.5 cm	2.2		1.6		[3]
40 × 40 × 65 cm <sup>3</sup>	1	1820-1980	1.6	100	[3]
d=16 cm, h=30 cm	1.7-2.1	1920	1.88	460-540	[8]
d=20 cm, h=40 cm	2	1848-1899	2	708-817	[9]
25 × 25 × 50 cm	1.15	1785-1798	2	310-440	[9]

The minimum compressive strength reported is 0.5 MPa, and the maximum is 2.46 MPa. The variation in values reported can be related to many factors like testing procedures, the workmanship and material constituent of the soil used. The other exciting thing noted from the above data is, the compressive strength of cylindrical specimens is observed to be higher than the prismatic specimens of the same material constituent, same slenderness ratio. For example, the compressive value of cylindrical specimen reported by the Miniatis and Walker [6] is 2.46 MPa while this value for prismatic specimen ranges between 0.62 to 0.97 MPa. Similarly, in a study conducted by Bui et al. [3] and Nobouch [9] the compressive strength of cylindrical specimens are almost double the compressive strength of the prismatic specimens. The substantial difference in the results of the compressive strength of the prismatic and cylindrical specimens is a consequence of the ramming process. The friction between rammed earth and formwork in prismatic specimens was more significant than in cylindrical specimens, resulting in improper compaction, which as a consequence has lower strength.

### 3.1.2 Rammed Earth under In-Plane Loading

The one deficit of rammed earth walls is their poor resistance in shear. However, the studies conducted to investigate the shear behaviour of rammed earth walls are few. Various test have been conducted in previous work like diagonal compression test [14,15], pushover test under

monotonic loading [9,12,13] and pushover test under cyclic loading [10,11] to shear behaviour of rammed earth wall. However, Table 3.2 reports the maximum lateral load obtained from those studies in which the walls are tested under in-plane loading. In most of these studies that investigated walls subjected to an in-plane loading, the diagonal shear was observed. Besides that, some of these tested specimens also suffered from localized horizontal cracks that were located at the interface of earth layers.

Table 3.2 Summary of test results from the literature available on RE wall under in-plane loading.

Wall	Slenderness	Ultimate lateral load (kN)	Failure mode	Reference
1300 × 1050 × 250	5.2	60-70	Shear failure	[10]
2400 × 2100 × 600	4	72.94	Shear failure	[11]
1000 × 1500 × 250	4	44.46	Shear failure	[12]
1500 × 1500 × 250	6	41.4	Shear failure	[12]
1200 × 1200 × 600	2	13.55	Shear failure	[13]

### 3.1.3 Effect of Rammed Earth Layer Thickness

The effects of layer thickness are rarely discussed in previous works [16]. Raju et al. [16] examined the influence of layer thickness on characteristics of cement-stabilised rammed earth (CSRE). The study discussed the effects of layer thickness only under the compression loading. In the present study, its effects will be discussed for the rammed earth wallette under compression as well as the shear loading. Furthermore, the rammed earth wallette will represent the actual wall on the site.

## 3.2 Test Parameters

Two main parameters are considered for the element test besides the loading type (compression and shear) as outlined in 3.2.1 and 3.2.2.

### 3.2.1 Rammed Earth Layer Thickness

Rammed earth wall consists of lifts which again consists of layers. Figure 3.1 illustrates having two lifts, highlighted by two different colours to distinguish them, and each lift comprises of five layers. Based on the typology study undertaken by Division for Conservation of Heritage Sites [17], the Bhutanese rammed earth houses have four to five lifts in each storey, and the average dimensions of the lifts are 3000 mm length, 600 mm height and 600 mm thickness. The layers in each lift range from five to fifteen with their thickness varying from 50 mm to 150 mm. For the current study, two different layer thickness is chosen for rammed earth wall specimens; i) 50 mm and ii) 100 mm.

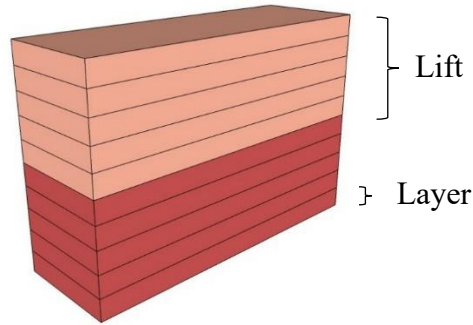


Figure 3.1 Lift and layer in rammed earth wall.

### 3.2.2 Drying Period

The “drying period” is referred to the period during which wet loam reaches its equilibrium moisture content [18]. However, in this thesis, the drying period is referred to the number of months allowed for rammed earth walleets to dry before the testing. The effect of drying period on rammed earth strength is never discussed before as far as the author is concerned. The effects on strength are discussed in terms of moisture content [19,20] but not directly with the number of days that the wall is being dried. Two drying periods are chosen for the rammed earth wall specimens; i) three months and ii) twelve months.

## 3.3 Specimens and Materials

### 3.3.1 Soil

To have a representative Bhutanese rammed earth wall, the soil used for the present study is reconstituted with a soil-sand ratio of 1:0.5 by mass (1121 kg/m<sup>3</sup> clay and 660 kg/m<sup>3</sup> fine sand) [21], which are close to the rammed earth material used in Bhutan. The grain size distribution of the soil sample used has a particle size ranging from 0 to 10 mm, as shown in Figure 3.2. For reference, a plot for the grain size distribution of rammed earth from one of the heritage project sites in Bhutan (Drukgyel Dzong) is available in the same figure. Both the soil sample are found clayey in nature. The soil selected for the current specimens is considered suitable for rammed earth construction as it fits within the lower and upper limit proposed by, many researchers (Figure 3.3). The figures are reproduced after Miniatis and Walker [22].

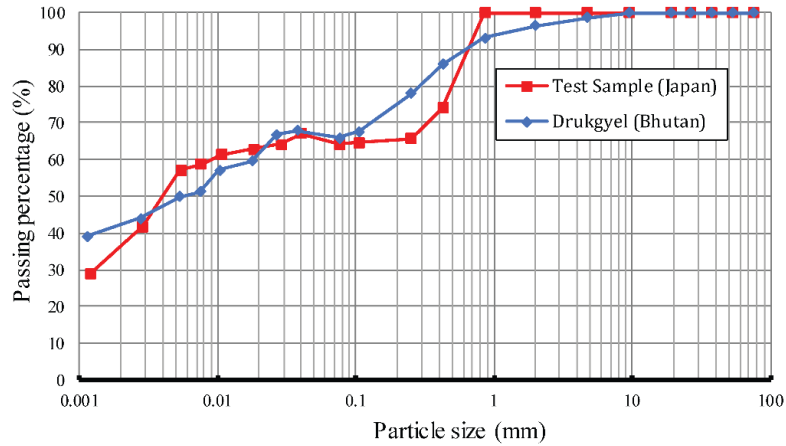


Figure 3.2 Particle size distribution of soil used for preparing specimens.

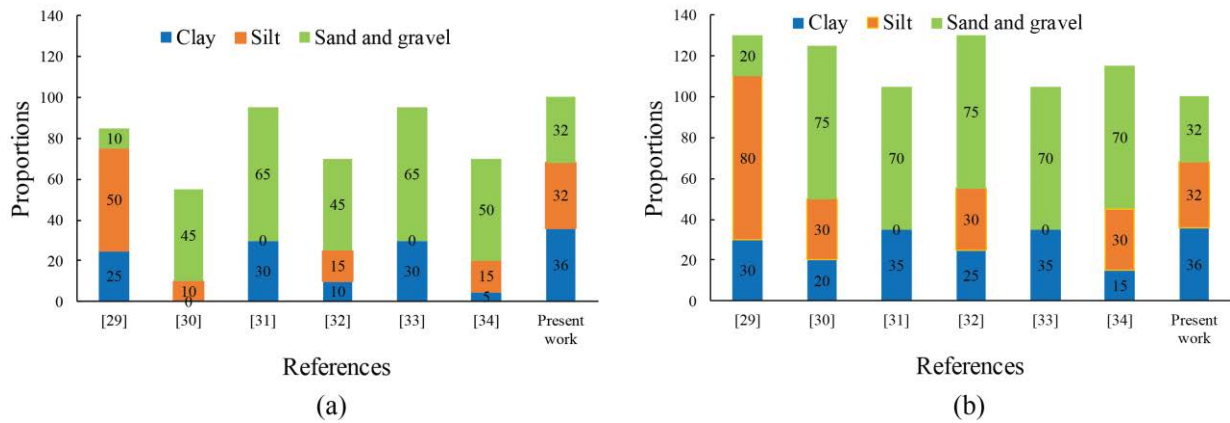


Figure 3.3 Range limits for particle size distribution for natural rammed earth: (a) Lower; (b) Upper [1].

### 3.3.2 Proctor Compaction Test

The optimum water content was derived from the proctor compaction test. The details of sample preparation are listed in Table 3.3, and the results of the test are presented in Figure 3.5. From the Figure 3.4(a), it is observed that the maximum dry density is achieved at about 15% of water content. Figure 3.4(b) presents the compressive strength measured at various drying periods for four different moisture content. The specimens with 15% water content were recorded with highest strength at all ages. Figure 3.4(c) shows the moisture content measured over a period of time. There is rapid decrement of moisture content until 14<sup>th</sup> day. After that, the rate of change of moisture content is relatively low. The moisture content after 90 days is almost constant.



Table 3.3 Sample preparation details for Proctor test [21].

Soil formulation	Clay:sand (mass ratio in the air-dried state)	1 : 0.5
	Water content	7%, 11%, 15% 19%
Compaction details	Specimen Dimensions	Φ100 × 200 mm
	Rammer mass	2.5 kg
	Rammer fall height	30 cm
	No. of layers	6
	No. of blows	25 blows/layer
Curing details	Curing temperature	20°C

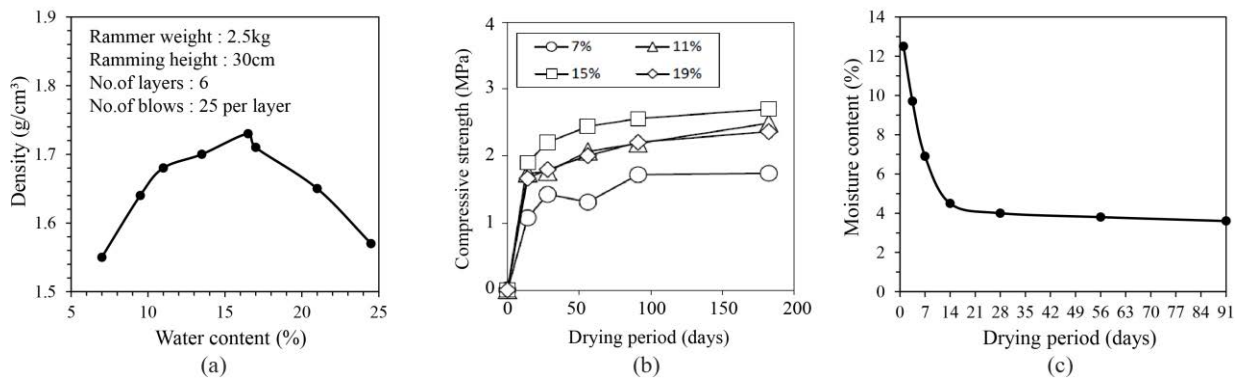


Figure 3.4 Proctor test results: (a) Relationship between density and water content; (b) Relationship between compressive strength and drying period; (c) Relationship between moisture content and drying period [1].

### 3.3.3 Wallette

The rammed earth wallettes having dimensions 500x500x110 mm<sup>3</sup> are prepared. The dimension of the rammed earth wallettes is chosen keeping the same aspect ratio (height/thickness) of Bhutanese rammed earth houses, and they are reduced to 1/6<sup>th</sup> scale. From each test specimen type, at least two specimens are prepared for the compression test, and three specimens are prepared for the shear test. The details of specimen preparation are shown in Figure 3.5. After quantifying the material required (Figure 3.5(a)), they were mixed thoroughly in its dry state with a shovel to obtain a uniform mixture (Figure 3.5(b)). Following, 15% of water by mass was sprinkled, and the mixing was continued. The mixture was shovelled until a homogeneous mix was obtained (Figure 3.5(c)). The mix was then boarded inside the formwork (Figure 3.5(d)), and the quantity was measured, as shown in Figure 3.5(e). It was followed by manual compaction (Figure 3.5(f)) until the desired layer thickness was achieved. A rammer weighing 2.5 kg was used (Figure 3.5(g)), releasing from a constant height of 300 mm to compact the soil. A rough surface is made over the

completed layer, as shown in Figure 3.5(h), to have proper bonding with the next layer. The process is repeated until one complete specimen is manufactured. The formwork is then removed, allowing the specimen to dry, as shown in Figure 3.5(i). The specimens were kept inside a room having a minimum temperature of 11.2 °C and a maximum of 30.6 °C. The minimum relative humidity recorded was 29%, and the maximum was 85%. The temperature and humidity data for one year is presented in Figure 3.6.

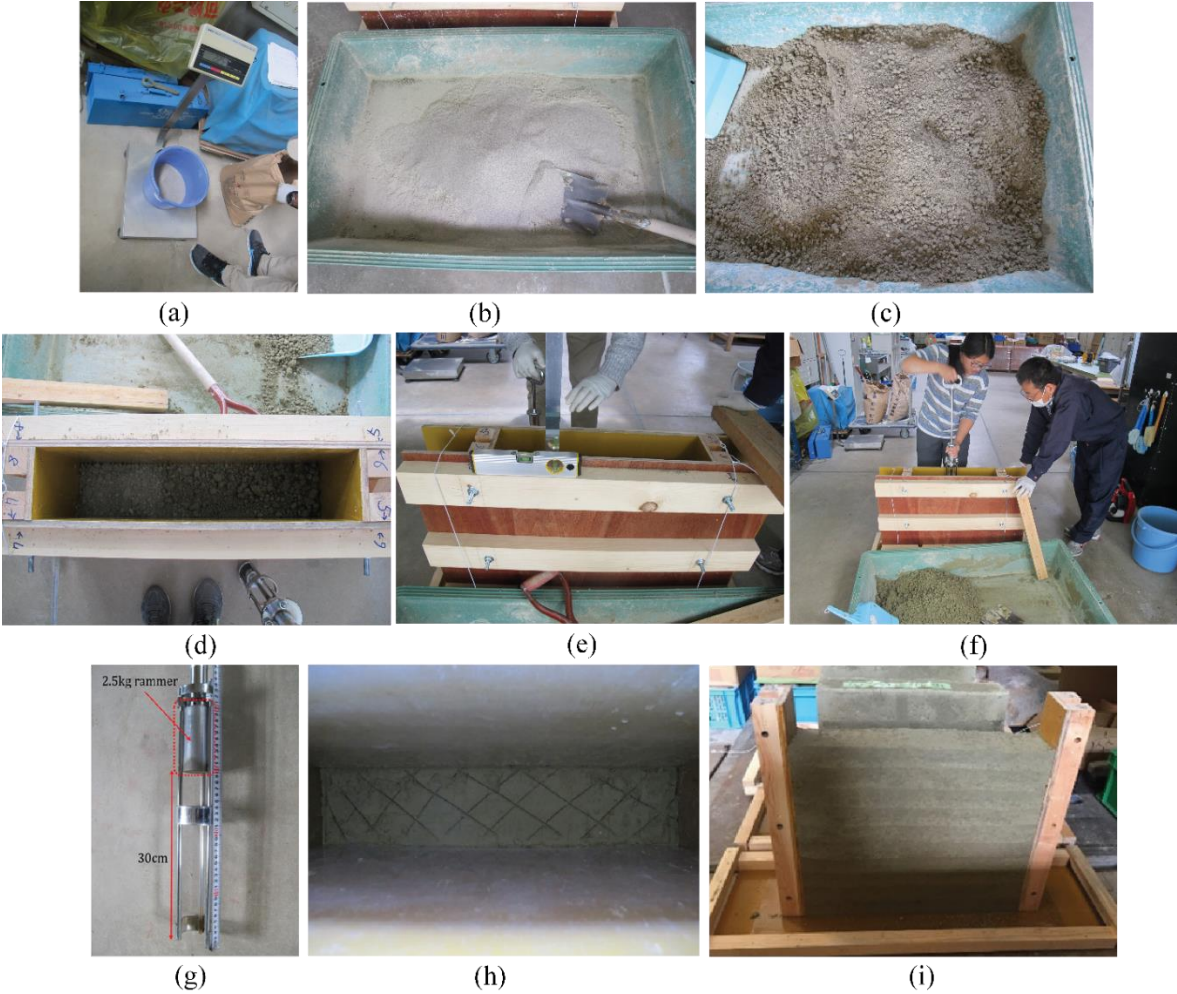


Figure 3.5 Specimen preparation process.

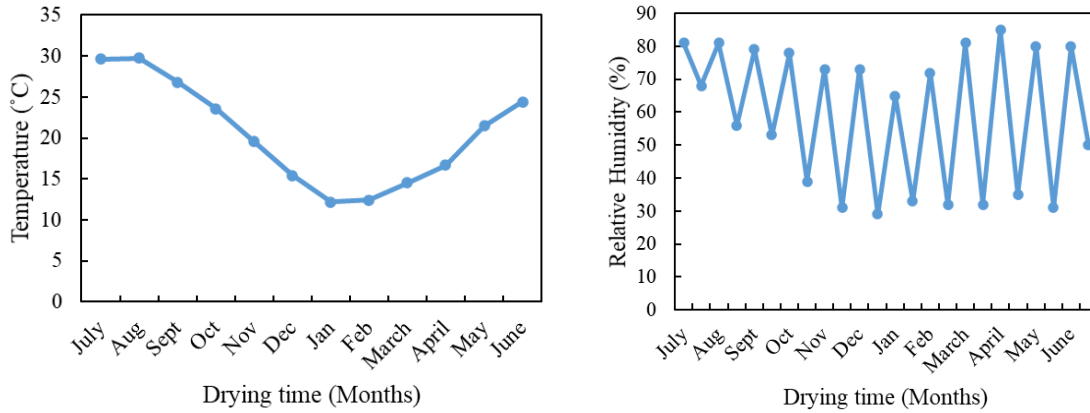


Figure 3.6 Temperature and relative humidity recorded during drying time.

### 3.3.4 Compaction Energy

The rammed earth wallette constituted five compacted layers (100 mm each) for 100 mm layered wallette, and ten compacted layers (50 mm each) for 50 mm layered wallette. Rammed earth with 50 mm layer thickness was achieved with around 84 to 100 blows while 100 mm layer thickness was achieved with around 200 to 240 blows. The compaction energy required to produce each specimen is estimated as follows [17]:

$$E = \frac{\sum E_i}{V} \quad (3.1)$$

Where

$E$  = compaction energy per unit

$E_i$  = compaction energy of  $i$ th layer

$V$  = total volume of compacted wallette

$$E_i = M_r N_b H_f \quad (3.2)$$

Where

$M_r$  = mass of rammer (2.5 kg)

$N_b$  = Number of blows per layer

$H_f$  = Height of fall (30 cm)

The compaction energy required for 50 mm layered wallette was 0.225-0.268 MJ/m<sup>3</sup> while the compaction energy required for 100 mm layered wallette was 0.268-0.321 MJ/m<sup>3</sup>. Clearly, less compaction energy was required for thinner layer wallette than the thicker layer wallette to achieve

almost the same final density. Further, the finishing was also achieved better in thinner layered wallette. The upper part of the layer achieved better compaction than the lower one (Figure 3.7(a)), which was also reported in a previous study. This difference was observed more prominent with visual observation in case of 100 mm layered than in a 50 mm layered, as shown in Figure 3.7(b).

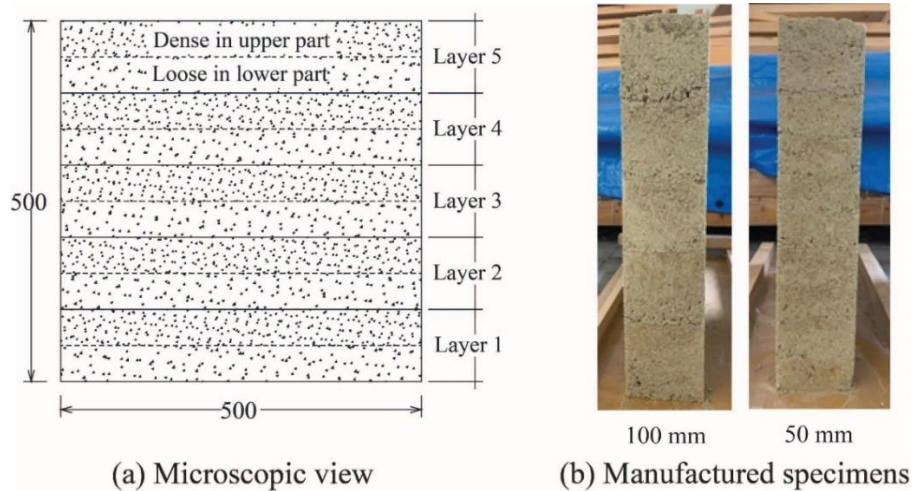


Figure 3.7 Compaction difference within the layer in microscopic view and specimen.

### 3.3.5 Comparison of mechanical characteristics with the previous study

The essential mechanical properties like compressive strength and Young’s modulus obtained from the present study is compared with the previous data collected from various rammed earth structures located in different sites in Bhutan, as shown in Figure 3.8. The density varied from 1463 kg/m<sup>3</sup> to 2061 kg/m<sup>3</sup>, Young’s modulus varied from 18.66 MPa to 320.65 MPa, and compressive strength varied from 0.15 MPa 1.66 MPa. These value from the present study are on

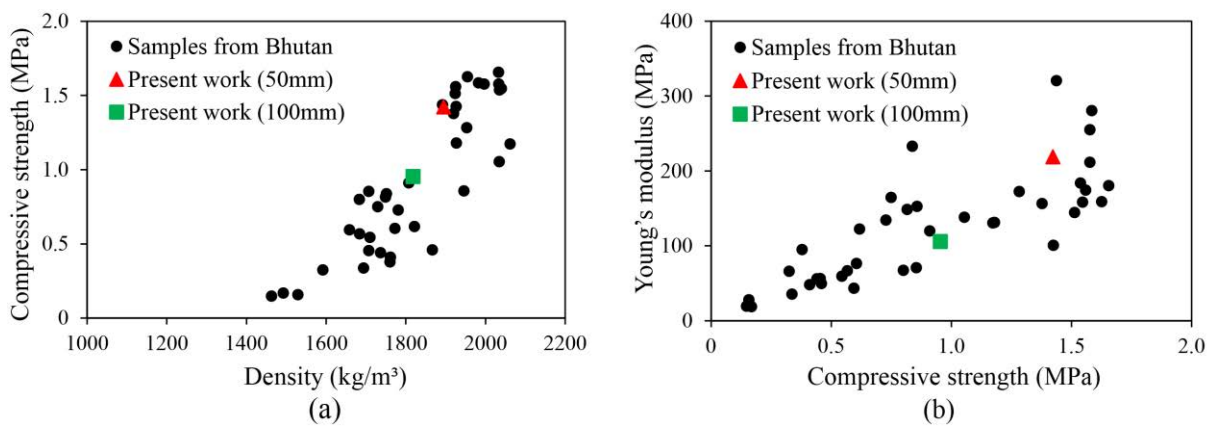


Figure 3.8 Comparing mechanical characteristics with the previous study: (a) Compressive strength vs density; (b) Compressive strength vs Young’s modulus [1].

an average 1818 kg/m<sup>3</sup>, 106 MPa and 0.95 MPa, respectively for 100 mm layered wallette, and 1895 kg/m<sup>3</sup>, 220 MPa and 1.42 MPa, respectively for 50 mm layered wallette. Clearly, the mechanical characteristics of the present specimens are found within the range limit of previous data collected. Therefore, the present specimens can represent the Bhutanese rammed earth.

### 3.3.5 Retrofitting details

The previous study by Pang et al. [23] has shown the effectiveness of using composite material, where rods were placed in grid system on both face of the rammed earth wall, and later plastered with cement mortar. Inspired by this, the author in present study explores the similar method of retrofitting rammed earth wall with composite material using a mesh which is much lighter than rods and more comfortable and faster to fix on the wall (reducing time taken for weaving rods in grid system). A hexagonal turtle-shaped wire mesh having 0.4 mm diameter with pitch 16 mm was used as a possible retrofitting material, whose mechanical properties are detailed later. Delamination of mortar from the wall surface was reported in an earlier study [23], thus at least twelve screws were provided in each face of the RE wallettes to avoid such mechanical incompatibility, shown in Figure 3.9(a). Additional screws were also provided at the locations where the transducers and PI-gauges were fixed. The screws were embedded to the depth of 55 mm inside the wall. The remaining 20 mm length was kept for cement plaster and fixing transducers and PI-gauges. Prior to applying plaster, the RE wall surface was moistened to avoid excessive absorption of water from the cement mortar. The final stage of retrofitting work included the application of a 10 mm thick cement plaster throughout the wall surface with a cement-sand ratio of 1:3 (Figure 3.9(b)).

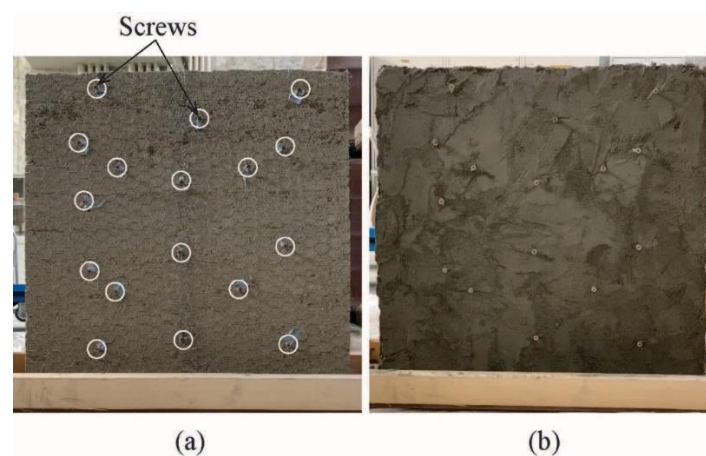


Figure 3.9 Retrofitting details: (a) Fixation of mesh and screws; (b) Final view after plastering.

The mechanical properties of the mesh were derived on three samples, according to ASTM E8 2016 [24], test setup shown in Figure 3.10(a). The mean yield and ultimate stresses were 235.67 MPa and 277.32 MPa, respectively, the stress-strain relationship obtained is presented in Figure 3.10(b). The typical failure included breakage of weakest wire, as shown in Figure 3.10(c). A tensile coupon test was conducted on mesh composite samples to acquire their tensile strength. The test setup for the tensile coupon test is illustrated in Figure 3.11(a). Three samples were prepared with dimensions 200 mm long, 50 mm wide, and 10 mm thick. The mesh was sandwiched between the cement plaster with cement-sand ratio 1:3. The samples were tested after 28 days of curing period. The results from the coupon test are presented in Table 3.4 and graph in Figure 3.11(b). The typical failure of samples is presented in Figure 3.11(c), where the first sample failed forming crack in the centre and two samples failed with the formation of crack near the joint.

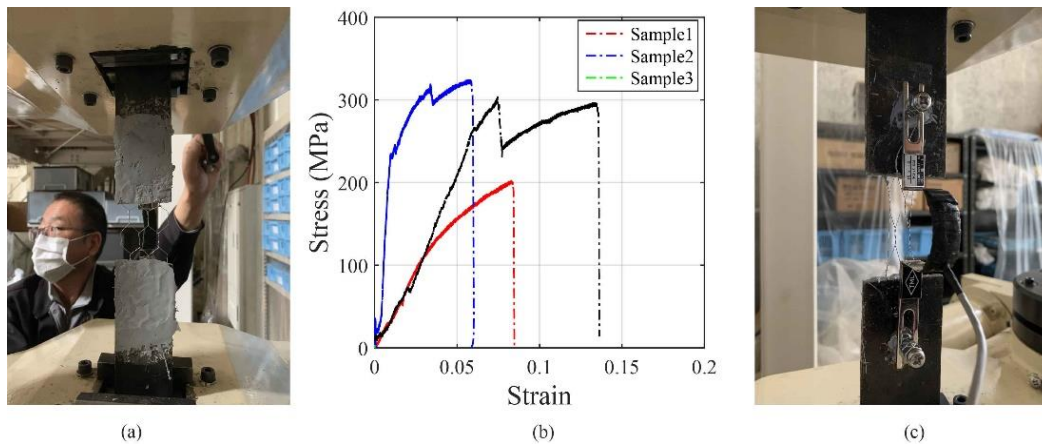


Figure 3.10 Material test: (a) test setup; (b) results; (c) failure pattern.

Table 3.4 Material properties of retrofitting materials.

Specimen	Mesh composite		
	$\rho_b$ (kg/m <sup>3</sup> )	$f_t$ (MPa)	$E$ (MPa)
Average	2295.67	2.86	4206.53
Std. dev.	7.93	0.05	706.38

$\rho_b$  – density,  $f_t$  – tensile strength,  $E$  – Elastic modulus

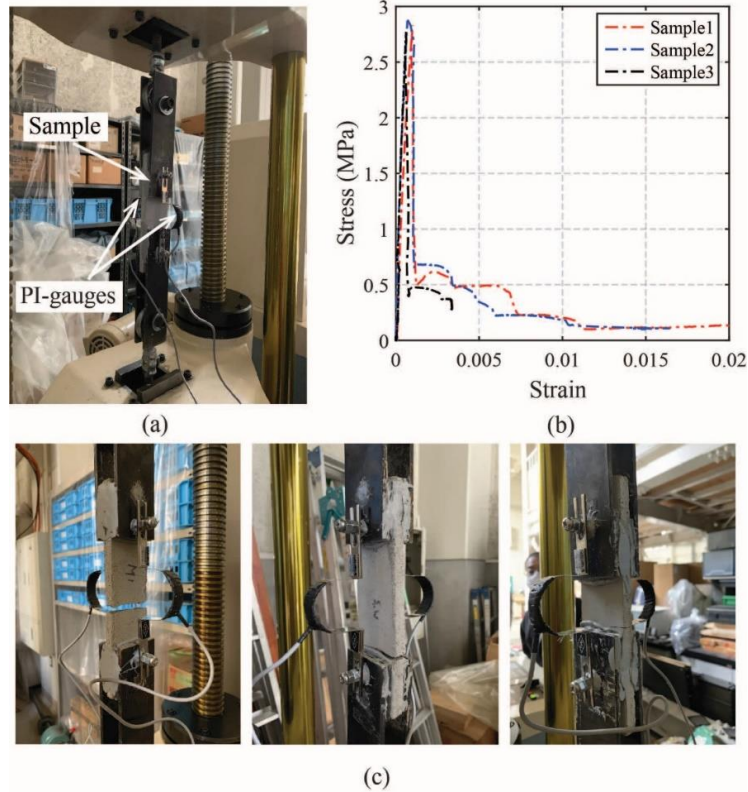


Figure 3.11 Tensile coupon test: (a) Setup; (b) Stress-strain graph: (c) Typical failure pattern.

### 3.6 Compression Test

#### 3.6.1 Test Matrix and Setup

The details of the element test conducted on rammed earth wallettes under compression are listed in Table 3.5. Based on the identified test parameters, each specimen is named in “A-B-CD” format. Here, “A” denotes the unreinforced (U) or reinforced (R). “B” denotes the rammed earth layer thickness, either 50 mm or 100 mm. “C” denotes the test type, in this case, is the compression (C) and D denotes the drying period in months either three months (3) or twelve months (12).

Table 3.5 Test matrix for element test under compression.

Specimen ID	Number of Specimen	Layer Thickness (mm)	Drying duration	Reinforced Type
U-100-C1	1	100	1 month	Un-reinforced
U-100-C3	2	100	3 months	
U-50-C3	2	50	3 months	
U-100-C12	3	100	12 months	
U-50-C12	1	50	12 months	
R-50-C3	2	50	3 months	Reinforced
R-50-C12	1	50	12 months	
Total Specimens			13	

The experimental setup for a compression test is shown in Figure 3.12. The specimens were capped with white cement to have smooth finishes at the top surface, and then a steel plate was placed over it to distribute the uniform load to the specimen. The Universal Testing Machine applied the vertical load (UTM) positioned in the middle of the specimen, and the load was recorded using a digital data logger. To determine the average deformation of the specimens, two displacement transducers and two PI-gauges (with gauge length 250 mm) were fixed at both faces of the wall.

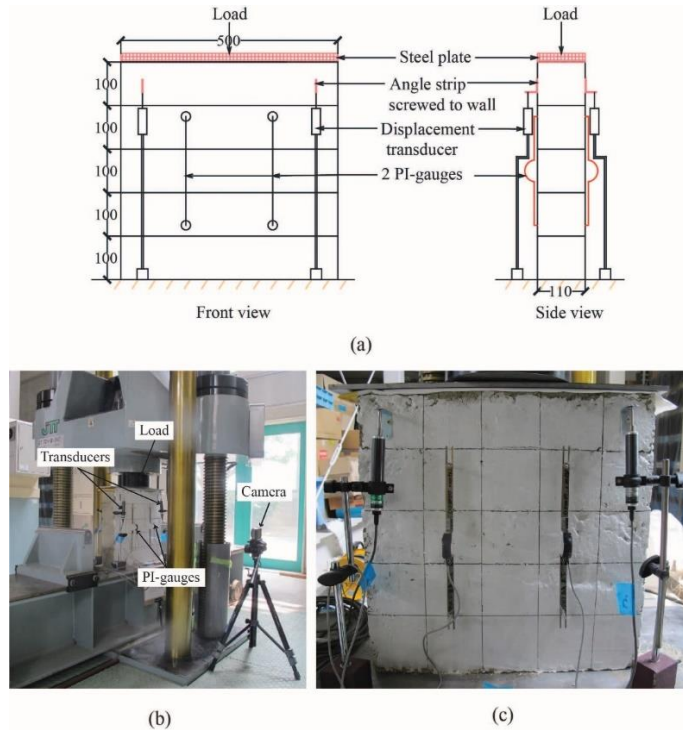


Figure 3.12 Compression test setup: (a) Schematic diagram; (b) Instrumentation; (c) Close up view of specimen.

### 3.6.2 Results and Discussion

#### 3.6.2.1 100 mm layer thickness

##### *One month dried specimen*

The first compression test was conducted on a specimen type U-100-C1, un-reinforced rammed earth specimen, rammed with 100 mm layer thickness and dried for a month. The stress-strain relationship obtained from the displacement transducer placed at the top layer is shown in Figure 3.13. The maximum stress recorded was 0.55 MPa, with a corresponding displacement of 4.69 mm.



Figure 3.14 presents the failure patterns of the specimen during testing. The first crack was observed at the bottom corner of the specimen with crushing at its toe, indicated by a bold line. At this, the load was 30 kN (0.54 MPa) and is characterized by a drop in the slope of the stress-strain graph in Figure 3.13. The crack extended in the horizontal direction shown by a regular line marked as (2) followed by diagonal crack represented by a dotted line. After attaining its peak load at 30.42 kN (0.55 MPa), the specimen failed where the bottom layer was crushed completely. The crushing at the bottom resulted due to insufficient drying of the wall. Therefore, the rest of the specimens were tested only after three and twelve months drying period.

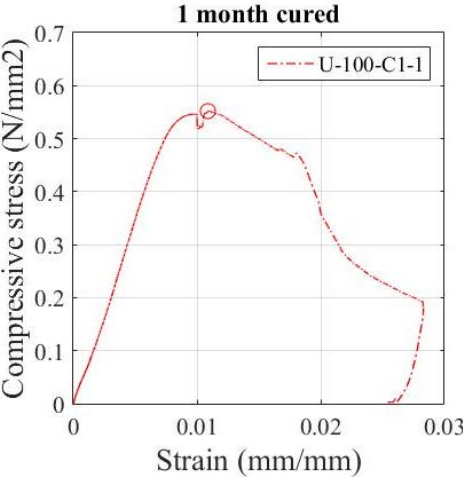


Figure 3.13 Stress-strain relationship of one month dried specimen.

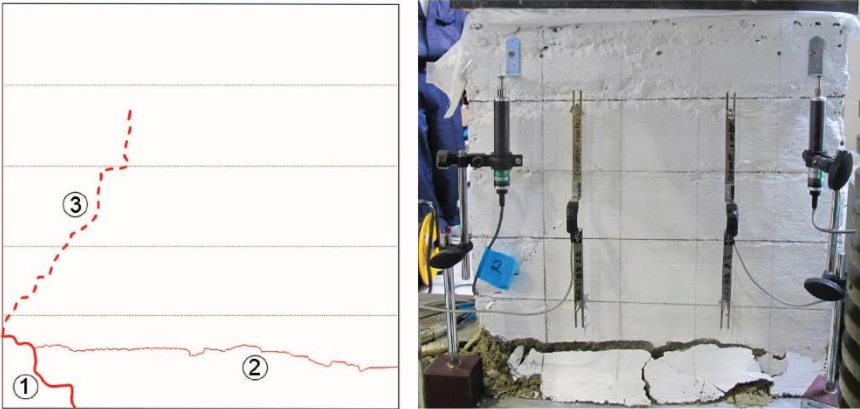


Figure 3.14 Failure pattern of U-100-C1-1.

**Three months dried specimen**

Two specimens were prepared, and they were dried for three months. The test results from the experiments are plotted in Figure 3.15 in terms of stress-strain. Both curves showed similar

behaviour where the initial has linear in nature, and there is a slight decrease in the slope after the appearance of the cracks. The peak load recorded in each specimen were 43.96 kN and 47.3 kN for U-100-C3-1 and U-100-C3-2, respectively. A sudden drop is observed in the curve after attaining the peak load for both the specimens, indicating the brittle nature of the material.

The failure mode, which usually occurred in the rammed earth wallettes are the appearance of vertical cracks in the central part of the specimen and inclined cracks at the corners [11]. The crack patterns are also characterized by the formation of a cone shape at the top, bottom or at both the regions [12]. For the present study, the appearance of cracks was monitored through visual observation and by recording in the camera. For the specimen U-100-C3-1, the first vertical crack appeared right below the applied load in 2<sup>nd</sup> and 3<sup>rd</sup> layer of the specimen, and the applied load was around 24 kN. The crack extended both ways in up and down directions. It was followed by crushing between the 2<sup>nd</sup> and 3<sup>rd</sup> layer and also between 4<sup>th</sup> and 5<sup>th</sup> layer. A vertical crack also appeared on the right side of the specimen when the load was around 37 kN. At the final stage, the portion of the wall from 5<sup>th</sup> layer and 2<sup>nd</sup> layer fell off. The final failure mode of the specimen is shown in Figure 3.16. The peak compressive strength recorded at the final failure was 0.897 MPa.

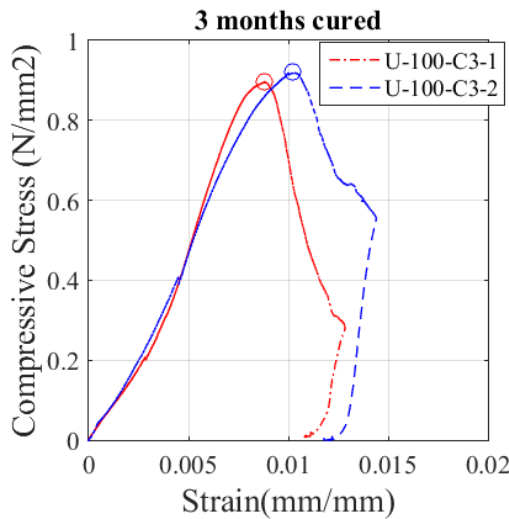


Figure 3.15 Compressive stress vs strain of 100 mm wallettes dried for three months.

For the second specimen (U-100-C3-2), there was crushing between the 4<sup>th</sup> and 5<sup>th</sup> layer followed by the appearance of thin vertical crack right below the applied load. This deformation in the specimen was observed when the applied load applied was around 20.1 kN. A splitting crack was also observed within the thickness of the wall. The final failure mode of U-100-C3-2 is shown in

Figure 3.17. The peak strength recorded at the failure was 0.92 MPa which is close to the strength of 1<sup>st</sup> wall.

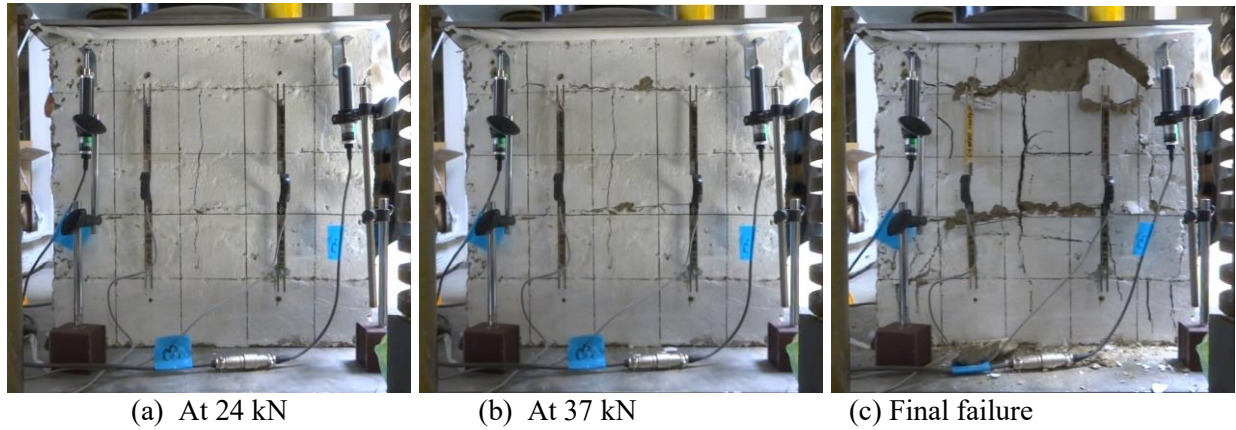


Figure 3.16 Failure pattern of U-100-C3-1.

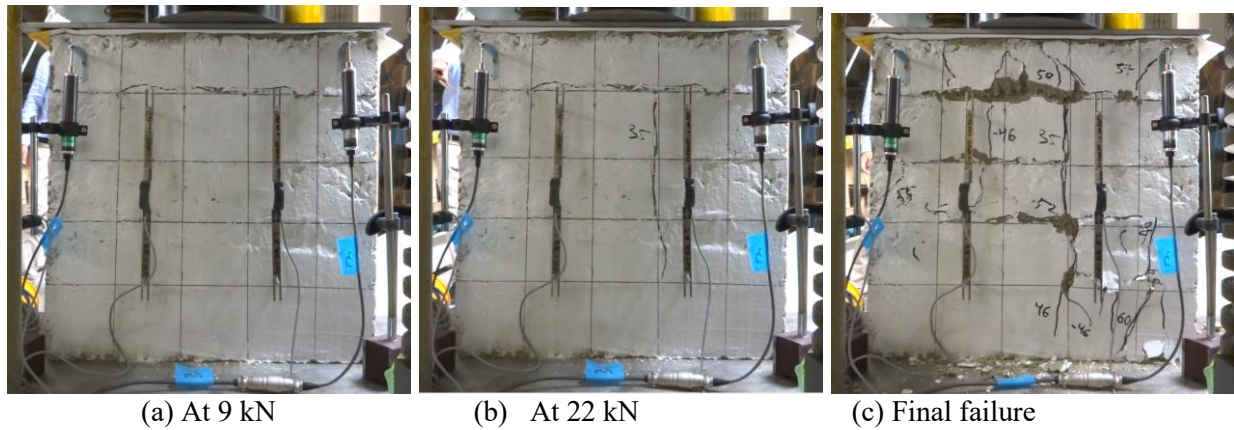


Figure 3.17 Failure pattern of U-100-C3-2.

***Twelve months dried specimen***

The relationship between compressive stress and strain is plotted in Figure 3.18 for both the specimens. The peak strength recorded for the wallettes is 0.99 MPa and 0.79 MPa respectively for U-100-C12-1 and U-100-C12-2. The strength of the specimen kept in open space is found slightly lower than the specimen kept in a closed room. The curves are found similar in nature like those of 100 mm layered specimens dried for three months. For both the specimens, there is an increase in the stress until the occurrence of the cracks. Figure 3.19 and Figure 3.20 illustrate the failure patterns observed in U-100-C12-1 and U-100-C12-2, respectively. In both the wallettes, the cracks initiated from the loaded region and extended downward to the two extreme corners forming diagonal shear. There was spalling of a portion of the wall at the final failure.

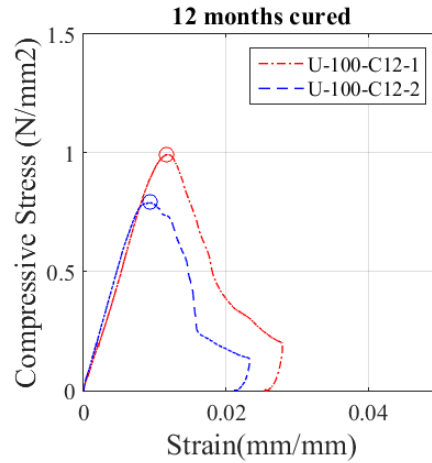


Figure 3.18 Compressive stress vs strain of 100 mm wallettes dried for twelve months.

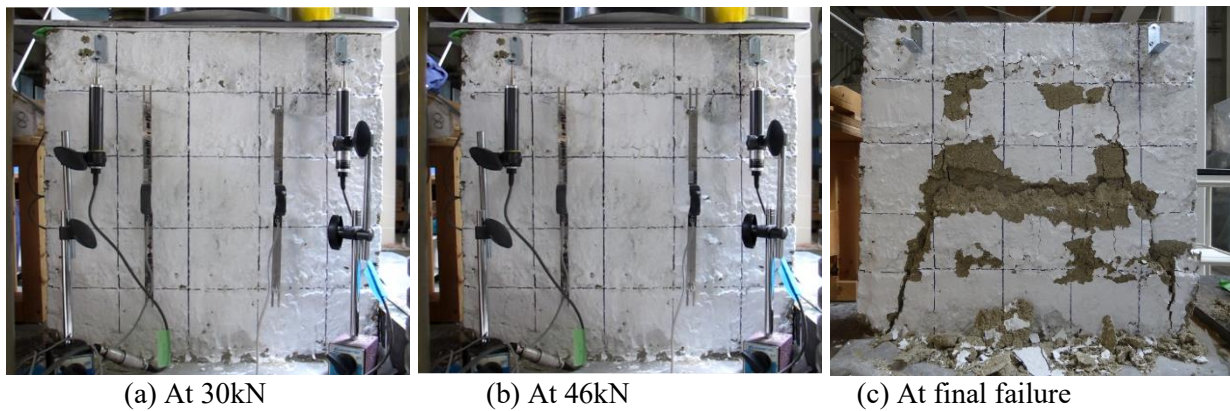


Figure 3.19 Failure pattern of U-100-C12-1.

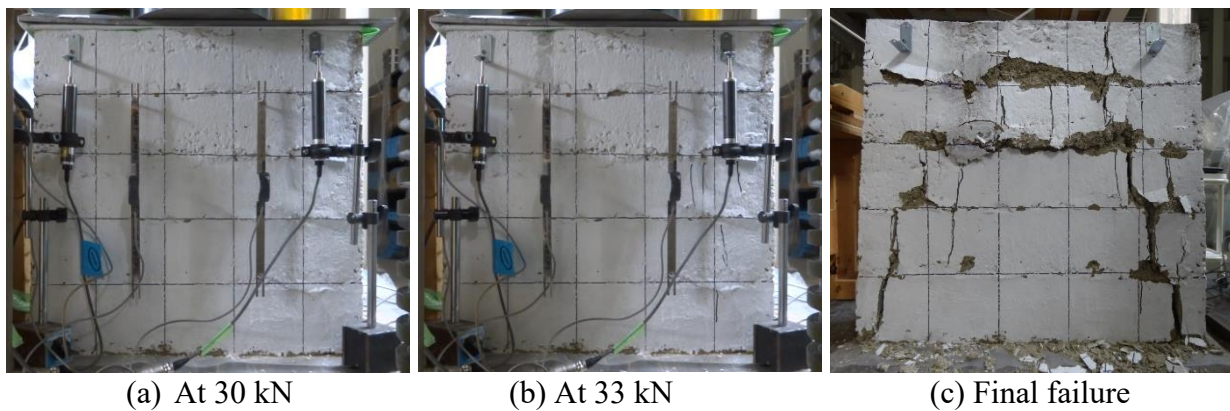


Figure 3.20 Failure pattern of U-100-C12-2.

### 3.6.2.2 50mm layer thickness

#### *Three months dried specimen*

Two wall samples were prepared, and they were named U-50-C3-1 for first wall sample and U-50-C3-2 for second wall sample. The strain-stress relationship of the wallettes is presented in Figure

3.21. The failure pattern for specimen U-50-C3-1 and U-50-C3-2 is presented in Figure 3.22 and Figure 3.23, respectively. For U-50-C3-1, there was crushing at the topmost layer of the specimen when the applied load was around 10 kN. There was no additional deformation found until when the applied load was around 55 kN. The first vertical crack appeared, as shown in Figure 3.22(b). It was followed by many other vertical cracks at various location of the specimen which was then followed by the horizontal crack between 7<sup>th</sup> and 8<sup>th</sup> layer. At the final failure, there was diagonal shear crack originating beneath the loaded region and a curve like crack is also observed at left-hand corner of the specimen. The failure mode of U-50-C3-2 is presented in Figure 3.23. The first vertical crack appeared at load 35 kN and is propagated in both upward and downward. Multiple minor cracks developed when the load reached 60 kN. At the final failure, there were curve-like cracks at both edges of the specimen, forming cone-like shaped at the top and bottom.

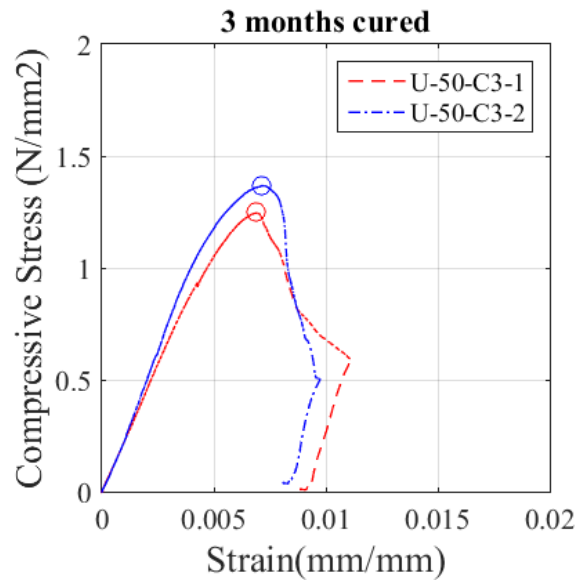


Figure 3.21 Compressive stress vs strain of 50 mm wallettes dried for three months.

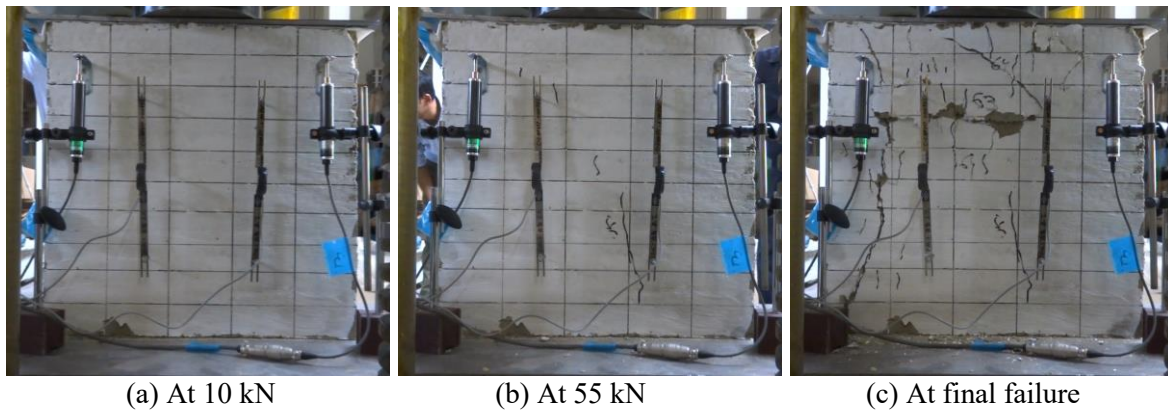


Figure 3.22 Failure pattern of U-50-C3-1.

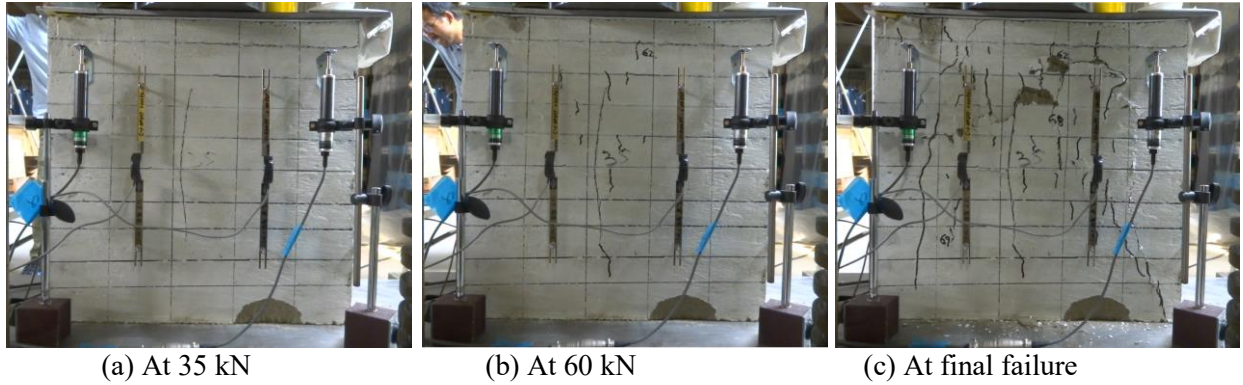


Figure 3.23 Failure pattern of U-50-C3-2.

***Twelve months dried specimen***

Here, only one specimen was tested since the other one was broken during transportation to the testing area. The stress-strain curve of the present wall U-50-C12-1 is similar to rest of the wallettes where it was almost linear in the initial phase and slight decrease in slope till it reaches the ultimate strength followed by a sharp decrement in its strength (Figure 3.24). Figure 3.25 shows the wall failure at different load application. The wall U-50-C12-1 did not show any deformation until when there was crashing at the toe at the right side of the specimen when the applied load was 40 kN. On the further application of the load, a spalling of white plaster was noticed, and when the load was around 83 kN, a thin curve like crack appeared on the right side of the wall. The final failure was characterized by falling of a portion of the earth.

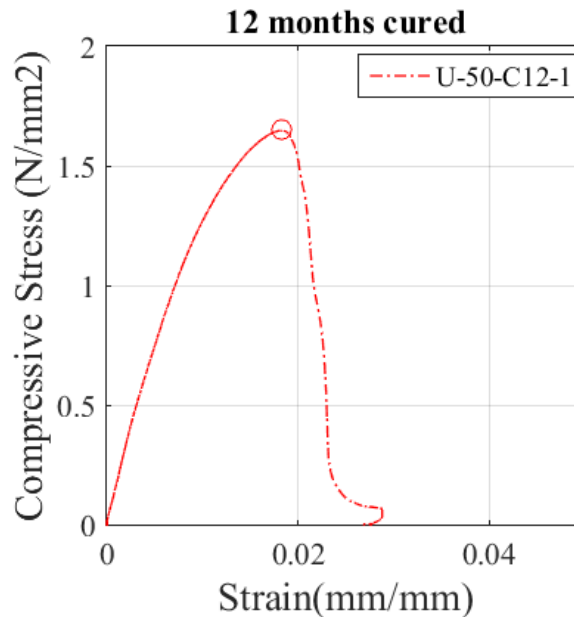


Figure 3.24 Compressive stress vs strain of 50 mm wallettes dried for twelve months.

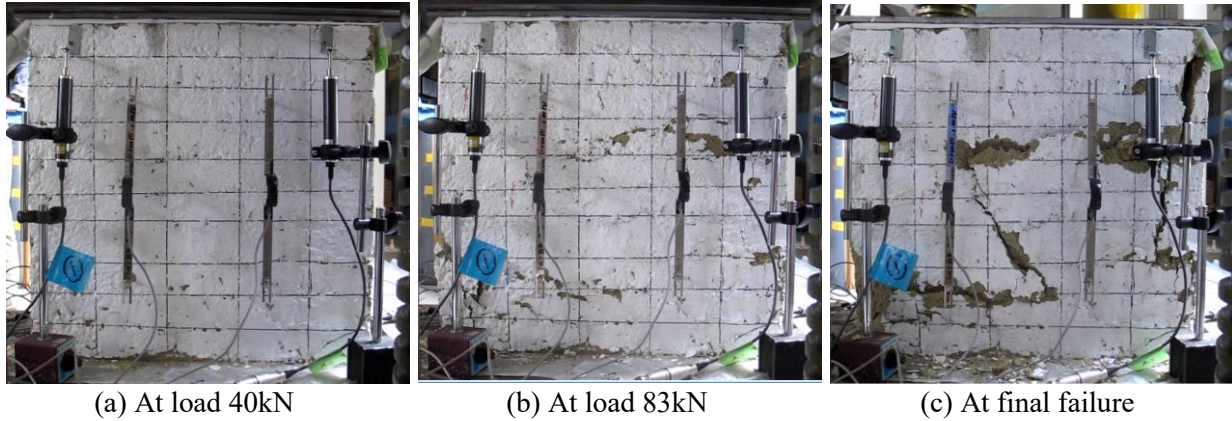


Figure 3.25 Failure pattern of U-50-C12-1.

A summary of the element test under compression loading results is given in Table 3.6, showing the peak load, compressive strength and Young's modulus. The minimum compressive strength recorded for 100 mm layer specimen is 0.55 MPa, and the maximum is 1.17 MPa. For the 50 mm layer wall, the minimum compressive strength of 1.25 MPa was observed, and the maximum value observed was 1.65 MPa. These values are more significant than the design values recommended by New Zealand code (recommends a compressive value of 0.5 MPa) and Australian Handbook (recommends a compressive value of 0.4 to 0.6 MPa). However, the New Mexico code recommends a compressive strength of 2.07 MPa. The young modulus of each specimen is calculated from a linear part of the stress-strain curve, taking the slope of the tangent line with the stress-deformation curve. Figure 3.26 illustrates an example of calculating the young modulus following the ASTM standard for thermal insulation material through uniaxial compression [25].

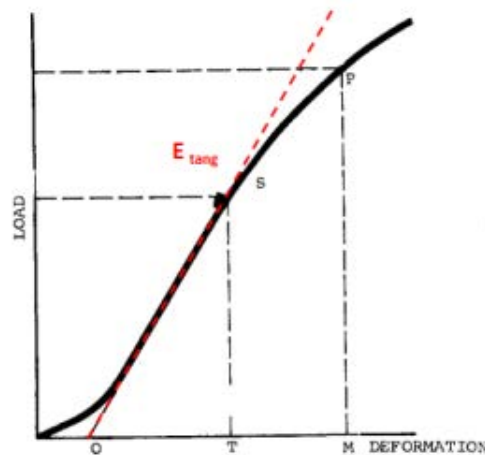


Figure 3.26 ASTM standard of calculating young's modulus for thermal insulation material [25].

The young modulus recorded ranges from 83.70 MPa to 118.62 MPa for 100 mm layered wall and these values for 50 mm layered wall ranges from 157.71 MPa to 265.64 MPa. The recommended design values by New Zealand code is 150 MPa and by the Australian Handbook is 500 MPa.

Table 3.6 Summary of compression test results.

Layer Thickness (mm)	Specimen ID	Peak load (kN)	Stress (MPa)	Average Stress (MPa)	Young Modulus (MPa)
100 mm layer	U-100-C1	30.42	0.55	0.55	83.70
	U-100-C3-1	43.96	0.897	0.91	118.62
	U-100-C3-2	47.3	0.92		104.61
	U-100-C12-1	50.64	0.99	0.98	95.79
	U-100-C12-2	40.32	0.79		109.13
	U-100-C12-3	62.16	1.17		100.97
50 mm layer	U-50-C3-1	64.16	1.25	1.31	232.76
	U-50-C3-2	70.36	1.37		265.64
	U-50-C12-1	86.80	1.65	1.65	157.71
	R-50-C3-1	115.5	2.01	1.74	953.20
	R-50-C3-2	85.4	1.46		612.61
	R-50-C12	105.2	1.79	1.79	693.23

Figure 3.27 summarizes the typical failure observed under compression loading. The general failure patterns are characterised by the appearance of inclined cracks originating below the applied load and extending towards the corners (Figure 3.27(a)), curve like cracks at wall sides (Figure 3.27(b)), vertical cracks mostly in the central parts of the specimen (Figure 3.27(c)), and crushing between the layer interface losing soil particles (Figure 3.27(d)). The rammed earth wall specimen under compression loading is observed having any one of these failure patterns or combination of them. When the wall does not achieve enough drying, the wall crushes at the bottom under compression loading.

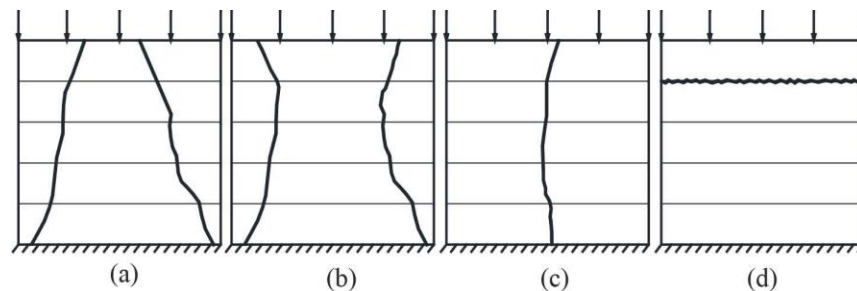


Figure 3.27 Typical failure patterns of RE wallettes observed under compression loading.



### 3.6.4 Effect of Drying Period

This section analyzes the possible effect of drying period on the compressive strength and young modulus of unstabilized rammed earth wallettes. For this reason, two specimen types with 50 mm and 100 mm layer thickness were considered, which were allowed to dry for one month, three months and twelve months. The peak compressive strength of all the rammed earth wallettes is plotted against the drying period, as shown in Figure 3.28. The peak strength values are the mean of samples tested for each specimen type except for specimen tested after one month (U-100-C1) and 50 mm layer specimen tested after twelve months of the drying period (U-50-C12). An increase in the compressive strength was observed with increasing drying period for both specimen type with 50 mm and 100 mm layer thickness. The average strength of U-100-C3 was 65.45% higher than U-100-C1, and the average strength of U-100-C12 was 7.69% higher in comparison to U-100-C3. In the case of RE wallettes with a 50 mm layer thickness, the peak strength value of U-50-C12 was 25.95% higher than U-50-C3 specimens. The percentage increase in strength was observed more significant for 50 mm layer wall, possibly due to the ramming process involved. As already mentioned, it was more difficult to achieve uniform compaction level within the layer of 100 mm layer wall. The lower part of the wall constituted prominent honeycombs, consequently reduced the dry density of the wall and thus resulting in lower strength of 100 mm layer wall. The compressive strength of earth block is proportional to its dry density, and this relationship is already proven in previous studies [2, 26-27].

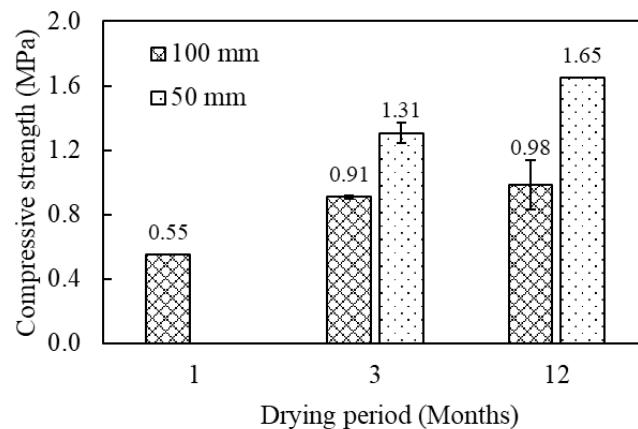


Figure 3.28 Effects of drying period in compressive strength.

The elastic modulus of rammed earth with higher drying period is lower than the rammed earth wallettes with lower drying period, for both 50 mm and 100 mm layer thickness despite having

higher compressive strength. The elastic modulus of each specimen is presented in Table 3.4. The reduction in elastic modulus of twelve months' specimens is due to the formation of cracks and small voids during drying, resulted as a consequence of the ageing phenomenon. A similar trend of having higher elastic modulus in new specimens was reported by Bui et al. [28]. The adopted test specimen is 110 mm thick, which allows complete drying over the cross-section of the wall, which is unlikely to happen in case of real scale RE wall of 600-1000 mm thickness.

### 3.6.5 Effect of Layer Thickness of Rammed Earth

Here, the author aims to evaluate the effect of layer thickness on the mechanical characteristic of rammed earth, in particular the compressive strength. For this purpose, the plot for the compressive stress-strain relationships for different RE layer is presented in Figure 3.29(a) and Figure 3.29(b) dried for three months and twelve months, respectively. In both cases of the drying period, 50 mm layer wall showed better strength against the 100 mm layer RE wall. This test result relates to the compaction achieved with the layer thickness. As mentioned earlier, 50 mm layer wall achieved better compaction, and it was denser in appearance than the 100 mm layer wall. There was 44% increment in average compressive stress for 50mm layer wall dried for three months and 68.37% for 50 mm layer wall dried for twelve months. The average elastic modulus of the thinner layer (50 mm) is found higher compared to the thicker layer (100 mm). For 50 mm layer RE wall dried for three months, the average elastic modulus found is 249.20 MPa, which is 123.27% higher than the 100 mm layer RE wall having the same drying period. Similarly, for 50 mm layer RE wall dried for twelve months, elastic modulus found is 157.71 MPa, which is 54.67% higher than 100 mm layer RE wall dried for twelve months.

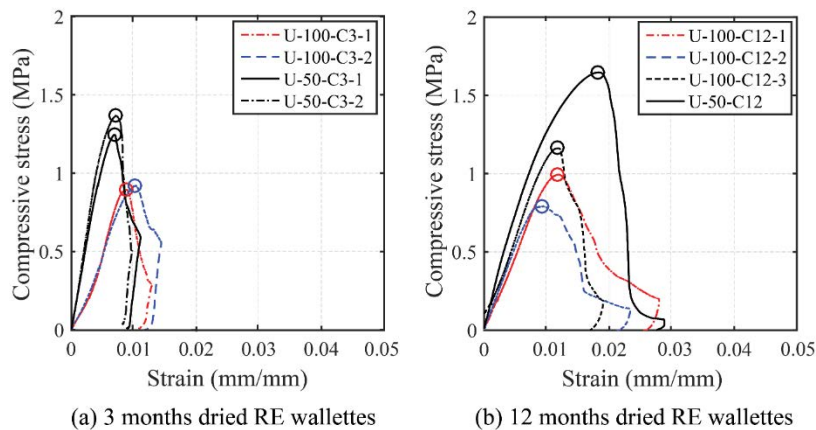


Figure 3.29 Relationship between stress and strain.

### 3.6.6 Effect of Mesh-Wrap Retrofitting Technique

The plot for the compressive stress-strain relationships for unreinforced and retrofitted specimens is presented in Figure 3.30(a) and Figure 3.30(b) dried for three months and twelve months, respectively. It is noted that with the use of mesh-wrap retrofitting technique, the compressive strength of RE wallettes has improved for both drying periods. For the RE wallettes dried for three months, the average compressive strength of RE wallettes has increased from 1.31 MPa to 1.74 MPa, which is 32.82% of the unreinforced one. For RE wall with 12 month drying period, only one sample each was tested. The result shows the compressive strength of the retrofitted RE wall (R-50-C12) is 1.79 MPa, and the strength of the unreinforced RE wall is 1.65 MPa. The percentage increment achieved in strength due to mesh-wrap technique is 8.48%. The mesh-wrap retrofitting technique is also observed to be effective in controlling the deformation on the RE wallettes. The crack appearances on the retrofitted RE wallettes are comparatively smaller than the unreinforced RE wallettes (Figure 3.31), which is evident in the stress-strain curve in Figure 3.30. The deformation of the retrofitted wall was lesser than the deformation observed on the unreinforced wall. It is worth noting here that the first compression test was conducted on specimen R-50-C12. This wall was retrofitted without shear connectors between mesh composite and the wall. The wall failed with the failure of an inner main wall without any traces of cracks on mesh composite. While inspecting, delamination of mesh composite from the main wallet was observed, as seen in Figure 3.31(c). Thus, the later prepared specimens were provided with screws to avoid such failure. The wall retrofitted using shear connectors had better strength than the wall retrofitted without shear connectors.

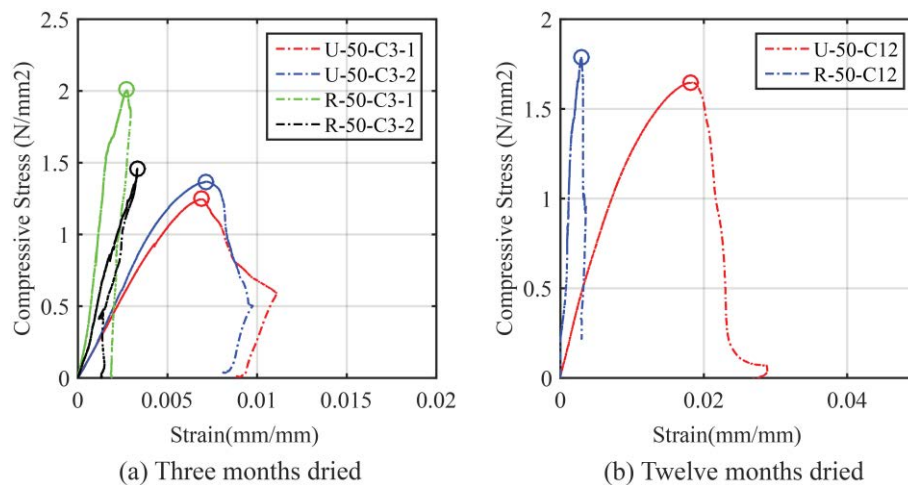


Figure 3.30 Relationship between stress and strain.

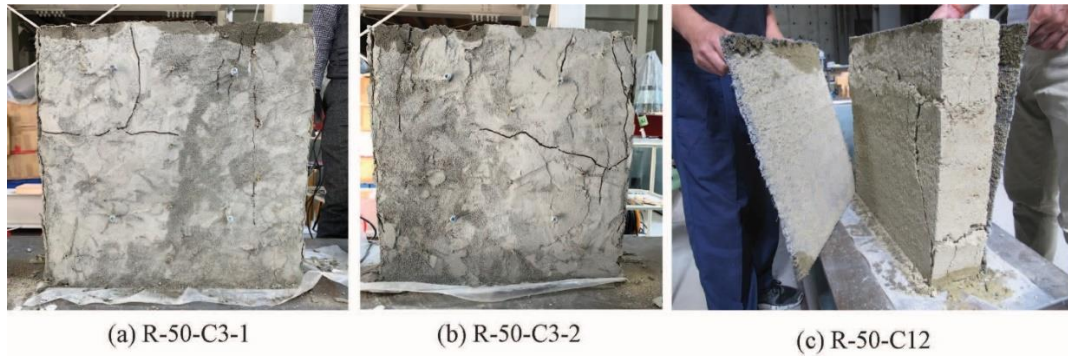


Figure 3.31 Failure observed in retrofitted RE wallttes.

### 3.7 Shear Test

#### 3.7.1 Test Matrix and Setup

Table 3.7 presents the details of test matrix for the element test conducted under shear loading. The effect of vertical stress in the shear strength of RE wall is also assessed by applying different stress values. The identified vertical stress values were 0.1 MPa, 0.15 MPa, 0.2 MPa, which closely represent the stresses at the roof, second, and first floor levels of typical Bhutanese RE buildings, respectively. However, for the 50 mm layer RE wall, there was excessive rocking behaviour exhibited at 0.1 MPa. Therefore, the vertical stress values for the 50 mm layered RE wall was limited to 0.15 MPa and 0.2 MPa. For naming the specimens, it follows similar patters as for the specimens tested under compression loading, except that the vertical stress values are included in the end. For example, “R-50-S12-0.2” stands retrofitted RE wall having 50 mm layer thickness

Table 3.7 Test matrix for element test under shear.

Specimen ID	Layer thickness (mm)	Drying period (months)	Vertical stress (MPa)	Unreinforced/ Retrofitted	
U-100-S3-0.1	100	3	0.1	Unreinforced	
U-100-S3-0.15			0.15		
U-100-S3-0.2			0.2		
U-100-S12-0.1		12	0.1		
U-100-S12-0.15			0.15		
U-100-S12-0.2			0.2		
U-50-S3-0.15	50	3	0.15		Retrofitted
U-50-S3-0.2			0.2		
U-50-S12-0.15		12	0.15		
U-50-S12-0.2			0.2		
R-50-S3-0.15	50	3	0.15		
R-50-S3-0.2			0.2		
R-50-S12-0.2		12	0.2		

tested under shear loading after twelve months of drying period and subjected to vertical stress of 0.2 MPa. The test setup and instrumentation details are shown in Figure 3.32(a) and Figure 3.32(b).

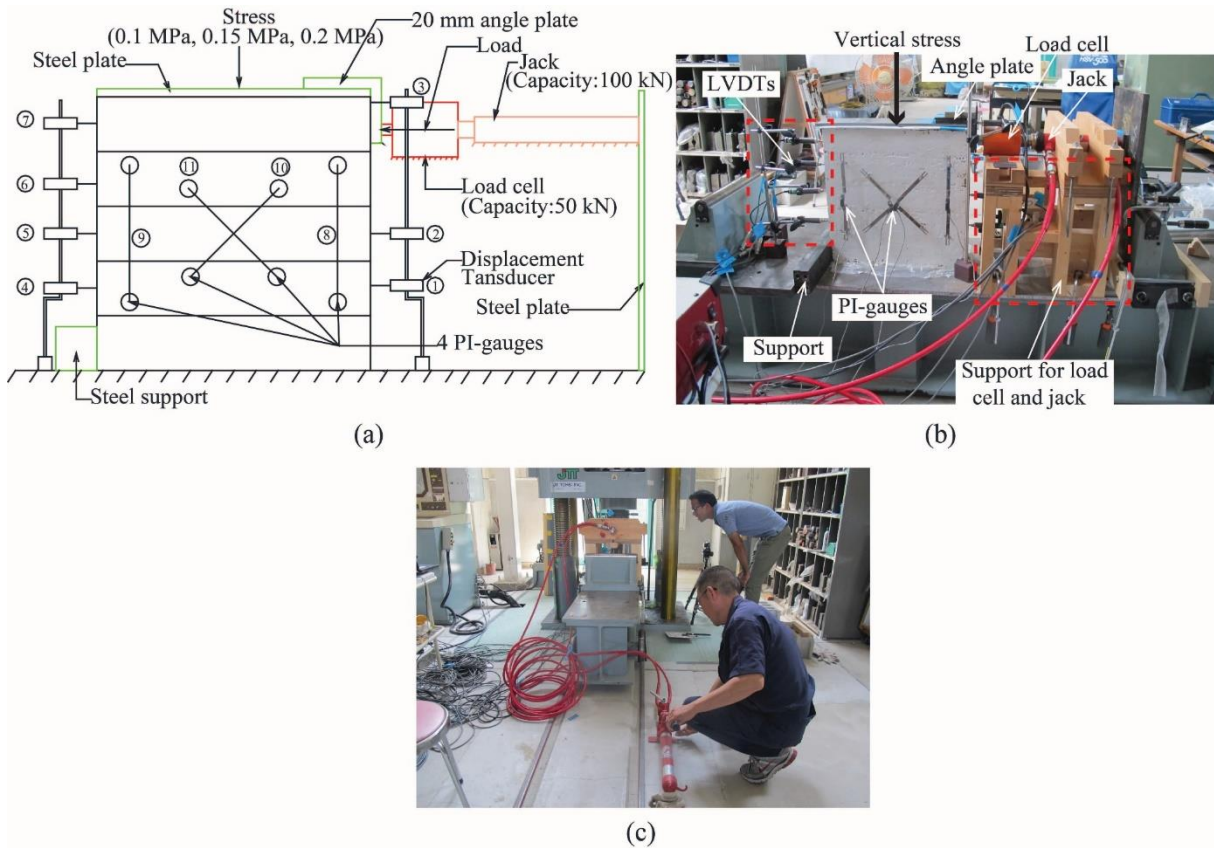


Figure 3.32 Shear test setup and instrumentation.

As in case of the specimens tested under compression, the specimens here are also capped with the white cement to have smooth finishes at the top. The specimens were also whitewashed and marked with the gridlines in one of the faces of the wall to locate cracks during the test. Four pi-gauges having a gauge length of 250 mm were fixed on the other face of the wall, where two were positioned diagonally to record cracks during the shear loading, and two were placed vertically to record the vertical displacement due to vertical load. A seven displacement transducers were placed both in the opposite (four numbers) and along the direction (three numbers) of horizontal load applied. They were fixed at different layers of rammed earth wall to record the horizontal displacement during the loading. A slow and consistent horizontal load was applied until the failure through load cell (capacity 500 kN) with manually operated jack having a stroke of 150 mm, as shown in Figure 3.32(c). At the same time, vertical stress is kept constant throughout the test. The different vertical stresses applied for each specimen were 0.2 MPa, 0.1 MPa and 0.04 MPa

representing the first storey, the second storey and the roof respectively. The normal stresses are calculated from the typical two-storied Bhutanese rammed earth houses.

### 3.7.2 Results and Discussion

#### 3.7.2.1 100 mm layer thickness

##### *Three months dried specimen*

Three rammed earth wallettes were prepared using the same material composition and ramming process as in case of the specimen tested under compression loading. The applied vertical stress differed from one another, which represented the stresses at the ground floor, first floor and roof floor of Bhutanese rammed earth building. The wallettes are named U-100-S3-0.1, U-100-S3-0.15 and U-100-S3-0.2 respectively for wall with vertical stress 0.1 MPa, 0.15 MPa and 0.2 MPa. The shear load-displacement relationship of three unreinforced rammed earth wallettes is plotted in Figure 3.33. Two wallettes U-100-S3-0.15 and U-100-S3-0.2 exhibited similar behaviour where the slope of the initial stage was very steep, and the load recorded till this point was 2.7 kN for U-100-S3-0.15 and 4 kN for U-100-S3-0.2. Both the curves were quasi-constant between the maximum load and the final failure. The wallettes failed with a combination of a horizontal crack along with the weaker layer and shear crack along the diagonal. For wall U-100-S3-0.1, the slope was steep up to load 1.35 kN and the slope decrease with the appearance of hairline crack at lower loading point as seen in Figure 3.34(a). There was a sudden drop of the slope when the horizontal crack between 4<sup>th</sup> and 5<sup>th</sup> layer appeared (Figure 3.34(b)). Unlike the wallettes with higher vertical stress, the top layer slipped along the bed joint at the final failure, and the maximum load recorded was 4.33 kN. The progression of failure patterns of specimen U-100-S3-0.15 and U-100-S3-0.2 are presented in Figure 3.35 and Figure 3.36, respectively.

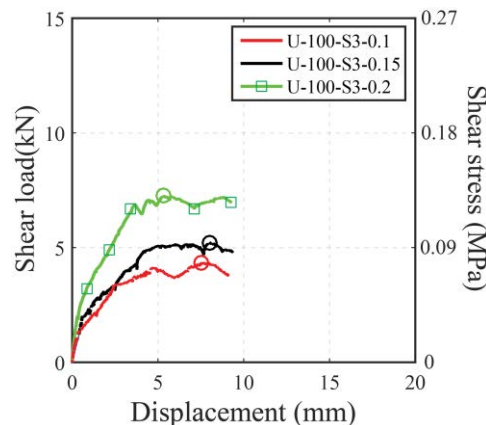
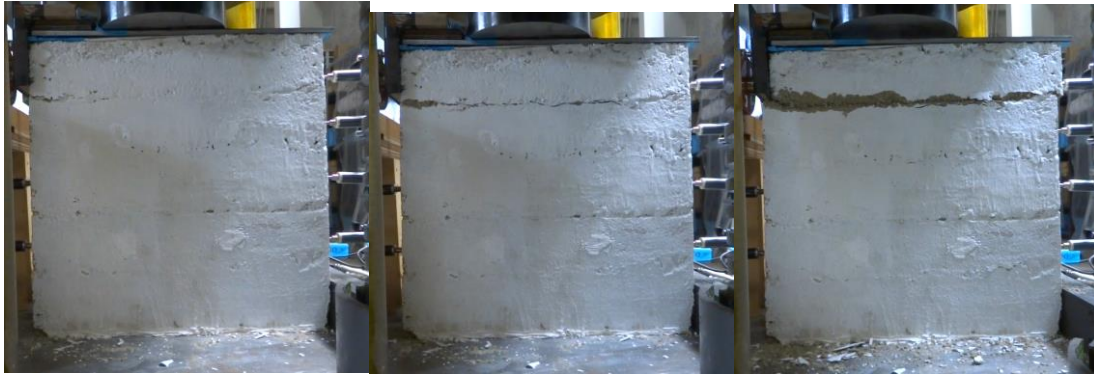


Figure 3.33 Shear load vs displacement of 100 mm wallettes dried for three months.



(a) At 2 kN (b) At 3.2 kN (c) At final failure

Figure 3.34 Failure pattern of U-100-S3-0.1.



(a) At 5 kN (b) At 5.89 kN (c) At final failure

Figure 3.35 Failure pattern of U-100-S3-0.15.



(a) At 2 kN (b) At 8.5kN (c) At final failure

Figure 3.36 Failure pattern of U-100-S3-0.2.

***Twelve months dried specimen***

All three wallettes exhibited similar behaviour as in case of the rammed earth wallettes dried for three months were in the initial behaved linearly up to and after which the behaviour became non-linear and almost plateau. The relationship between the shear load and displacement of each specimen wall are presented in Figure 3.37.

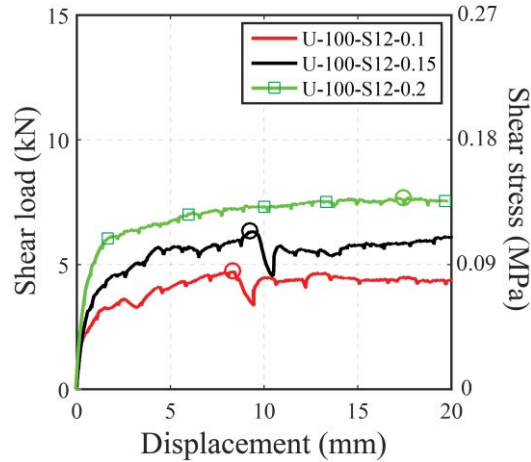


Figure 3.37 Shear load vs displacement of 100 mm wallettes dried for twelve months.

The mode of failure observed in each specimen is presented in Figure 3.38 for U-100-S12-0.1, Figure 3.39 for U-100-S12-0.15 and Figure 3.40 for U-100-S12-0.2. For specimen U-100-S12-0.1, a rocking was observed in the initial stage. The first horizontal crack appeared between 4<sup>th</sup> and 5<sup>th</sup> layer at 3.7 kN. Around 4.5 kN, a horizontal crack between 1<sup>st</sup> and 2<sup>nd</sup> layer was also noted. The wall failed with sliding along the weakest layer (the layer between 1<sup>st</sup> and 2<sup>nd</sup>). A similar failure mode was observed in U-100-S12-0.15 with rocking at the initial. Parts of earth started falling between 4<sup>th</sup> and 5<sup>th</sup> layer interface when the horizontal load was around 5.5 kN. A tension cracking was observed between 1<sup>st</sup> and 2<sup>nd</sup> layer at 6.2 kN followed by the horizontal crack between 2<sup>nd</sup> and 3<sup>rd</sup> layer. The wall failed with a slip of layer and forming a diagonal crack. For specimen U-100-S12-0.2, there was crushing between layers (4<sup>th</sup> and 5<sup>th</sup> followed by at 2<sup>nd</sup> and 3<sup>rd</sup> layer) due to vertical stress applied. A diagonal crack was formed at the final failure.

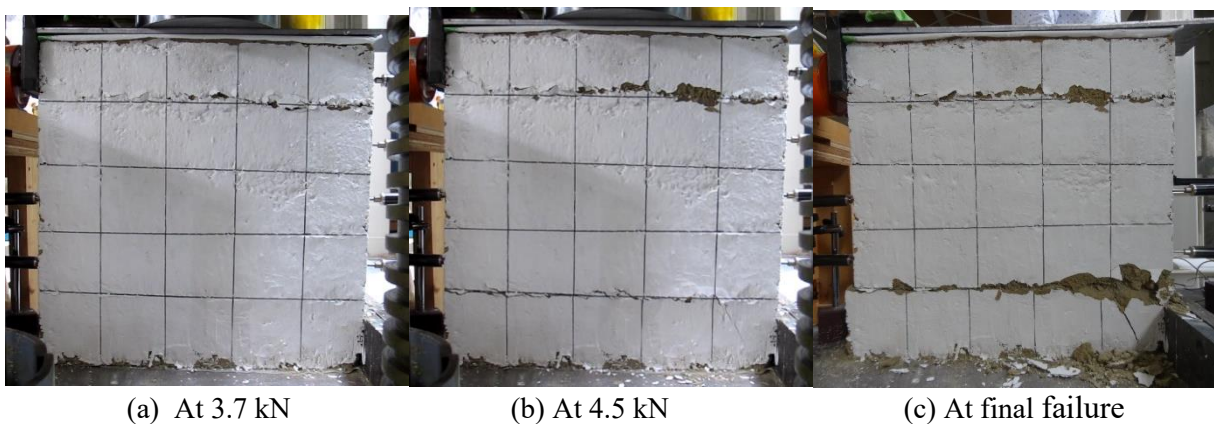


Figure 3.38 Failure pattern of U-100-S12-0.1.



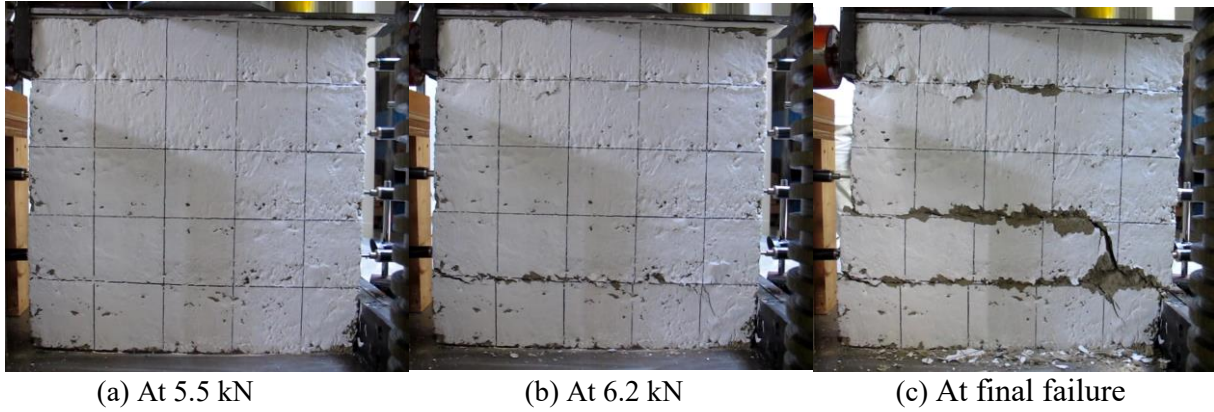


Figure 3.39 Failure pattern of U-100-S12-0.15.

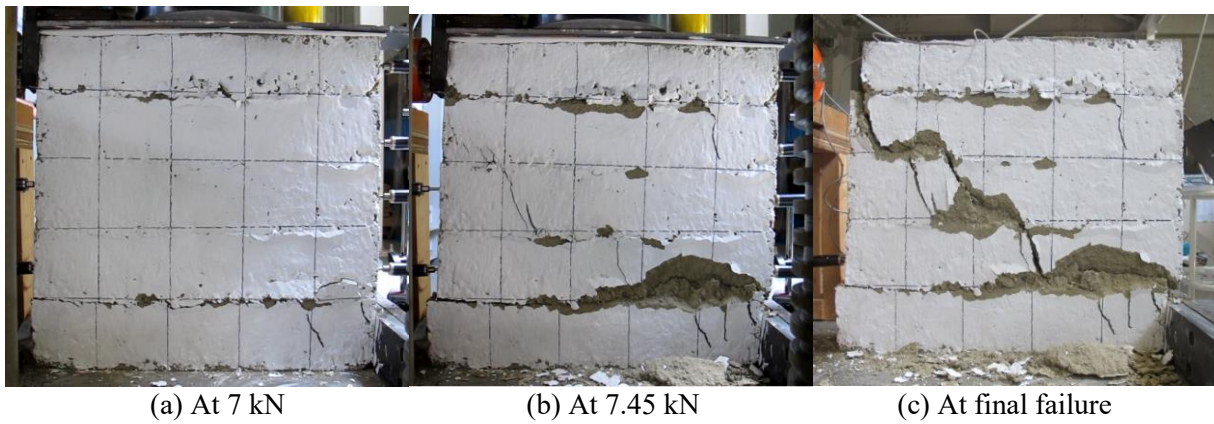


Figure 3.40 Failure pattern of U-100-S12-0.2.

### 3.7.2.2 50 mm layer thickness

#### *Three months dried specimen*

Figure 3.41 presents the load-displacement relationship of unreinforced rammed earth wallettes dried for three months. As reported earlier, the vertical stress was challenging to maintain constant in this case too during the experiment. The maximum vertical stress recorded in this experiment was 0.36 MPa. The slope of the load-displacement curve is almost vertical to a shear load of 2 kN, and the top layer of the wall was displaced about 1 mm. There was a sudden decrease in the slope when there was rocking at the base (Figure 3.42(a)). The slope is almost linear up to 13 kN followed by a sudden decrement in the load. Precisely at this point, the shear crack appeared along the diagonal, as shown in Figure 3.42(b). The crack widened on further application of load, and at the final failure, there was additional tensile cracking at the heel of the wall. The peak load recorded was 13.99 kN.

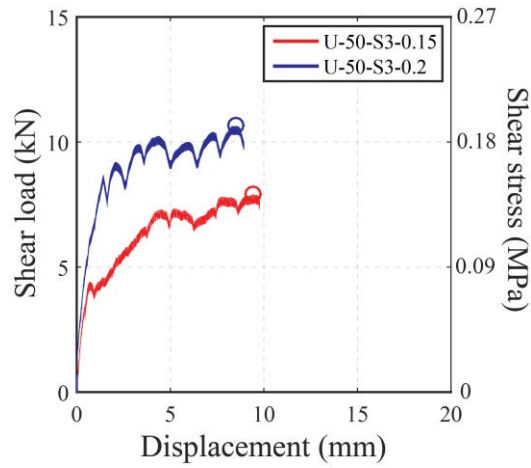


Figure 3.41 Shear load vs displacement of 50 mm wallette dried for three months.

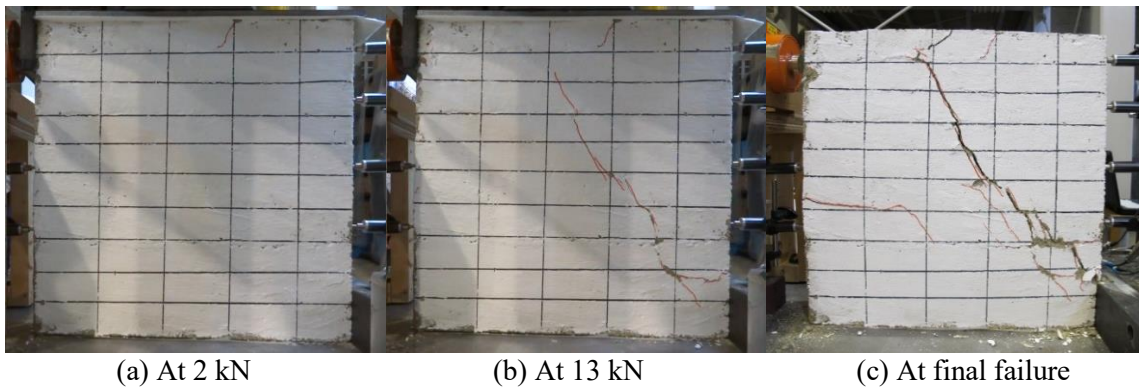


Figure 3.42 Failure pattern of U-50-S3-0.15.

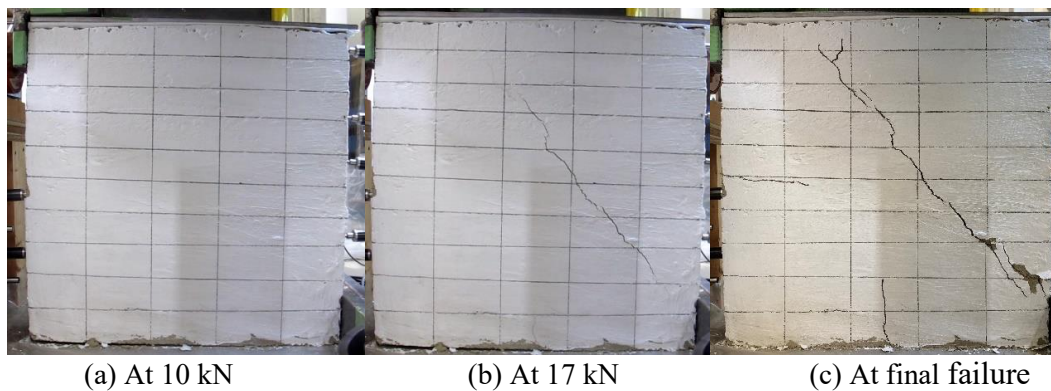


Figure 3.43 Failure mode of U-50-S3-0.2.

***Twelve months dried specimen***

The relationship between the shear load and displacement is shown in Figure 3.44. Both the specimens showed similar failure mechanisms with rocking at the base in the initial loading, and did not show any cracks until the maximum load. Both the wallettes failed with the formation of

diagonal crack. Figure 3.45 and Figure 3.46 presents the failure mode of U-50-S12-0.15 and U-S12-0.2, respectively.

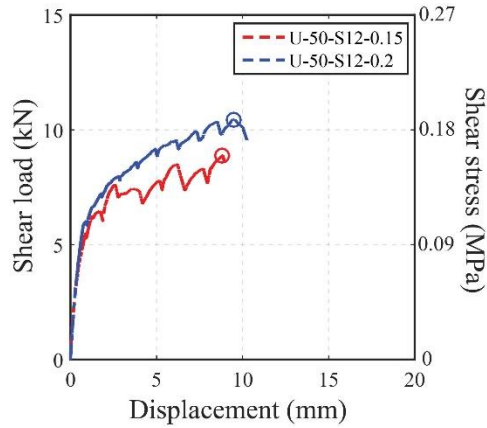


Figure 3.44 Shear load vs displacement of 50 mm wallettes dried for twelve months.



(a) At 5 kN (b) At 10 kN (c) At final failure

Figure 3.45 Failure pattern of U-50-S12-0.15.



(a) At 5 kN (b) At 7.5 kN (c) At final failure

Figure 3.46 Failure pattern of U-50-S12-0.2.

The results from the shear test have been summarized in Table 3.8 presenting peak horizontal load, shear stress, energy absorption and ductility index. The energy absorption ( $\Psi$ ), here, is defined as

the area under the maximum shear load and the corresponding horizontal displacement, represented by the shaded region in Figure 3.47(a). The ductility index ( $\mu$ ) is defined as the ratio of the corresponding displacement at maximum shear load ( $\Delta_{max}$ ) to the displacement at the yielding point ( $\Delta_y$ ). The yielding point here is considered to a point from a non-linear region right after the almost linear region of the load-displacement curve. The corresponding displacements at maximum load and yield point load are illustrated in Figure 3.47(b). The energy absorption and ductility index here are calculated for comparison of unreinforced and retrofitted rammed earth wallets, which is discussed more in later.

Table 3.8 Shear test summary.

Specimen Type	Specimen ID	Peak load (kN)	Shear strength (MPa)	$\Psi$ (kN–mm)	$\mu$
100mm layered	U-100-S3-0.1	4.327	0.084	30.14	25.66
	U-100-S3-0.15	5.896	0.117	38.06	11.33
	U-100-S3-0.2	8.703	0.167	35.15	13.00
	U-100-S12-0.1	4.744	0.091	31.11	18.35
	U-100-S12-0.15	6.374	0.122	46.54	10.45
	U-100-S12-0.2	7.686	0.148	121.98	14.18
50mm layered	U-50-S3-0.36	13.99	0.275	93.95	32.65
	U-50-S12-0.15	14.317	0.281	92.86	13.03
	U-50-S12-0.2	19.086	0.384	181.00	22.95

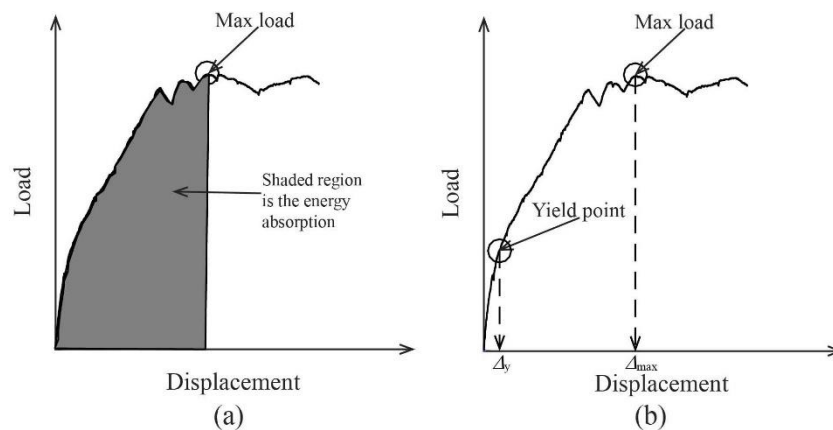


Figure 3.47 Illustration showing the calculation of: (a) Energy absorption; (b) Ductility from the load-displacement curve.

Figure 3.48 summarises the typical failure patterns observed under in-plane loading. They are characterised by rocking at the base (Figure 3.48(a)), diagonal crack (Figure 3.48(b)) and sliding between the layer interface (Figure 3.48(c)). These failure patterns were also reported in previous studies, as listed in Table 3.2. Rocking failure occurs due to overturning caused by the low axial load. In the present test, rocking behaviour occurred in the beginning of the test, and it was generally observed for those wallettes applied with 0.1 MPa vertical stress.

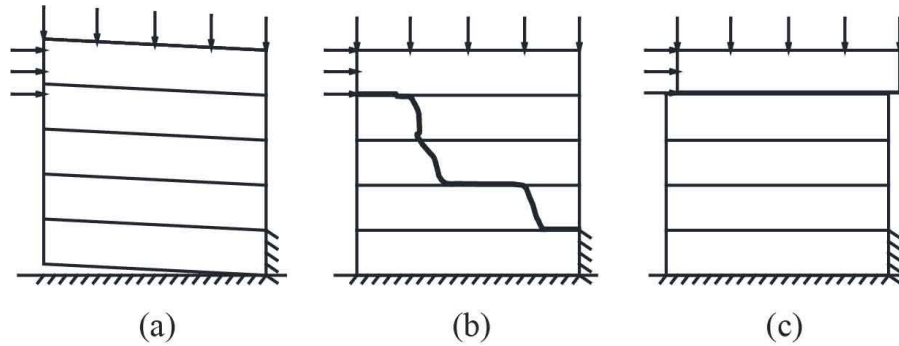


Figure 3.48 Typical failure mode of RE wallettes observed under shear loading.

### 3.7.3 Effect of Drying Period

Figure 3.49(a) presents the recorded shear strength for 100 mm layer RE wall with drying period of three months and twelve months subjected to vertical stress 0.1 MPa, 0.15 MPa, and 0.2 MPa. These values for 50 mm layer RE wallettes are presented in Figure 3.49(b). However, the vertical stresses for 50 mm layer RE wallettes are limited to 0.15 MPa and 0.2 MPa since rocking behaviour was noted at lower vertical stress of 0.1 MPa. For 100 mm layer RE wall, the shear strength increases with the increase in the drying period; however, the percentage increase varies with the

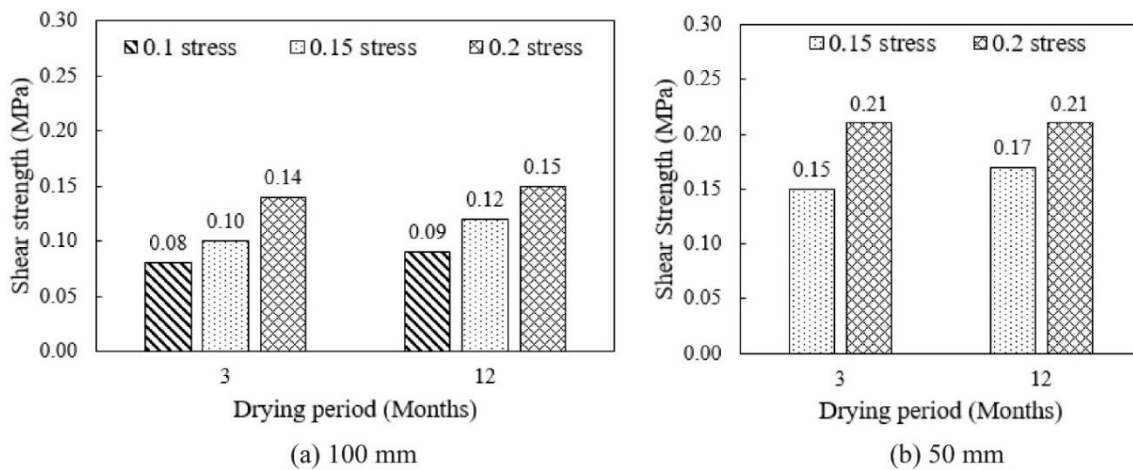


Figure 3.49 Shear strength of RE wallettes with varying drying periods.

individual specimens. The shear strength of U-100-S12-0.1 is observed at 0.09 MPa, which is 12.5% higher than U-100-S3-0.1. For U-100-S12-0.15, the shear strength is found significantly higher (20%) than its counterpart RE wall U-100-S3-0.15. However, the shear strength of U-100-S12-0.2 is found 7.14% higher than U-100-S3-0.2. For the RE wall with a 50 mm layer thickness, the increase in shear strength of twelve months dried specimen (U-50-S12-0.15) was observed 13.33% higher than the three months dried specimen (U-50-S3-0.15). However, the shear strength of U-50-S12-0.2 was observed 1.45% higher than U-50-S3-0.2. This shows the minimal effect of drying period in shear for 50 mm layer specimen with vertical stress of 0.2 MPa.

### 3.7.4 Effect of Layer Thickness

The relationship between the peak shear load and the horizontal displacement is illustrated in Figure 3.50. The figure also presents shear stress, calculated as the ratio of peak load to the cross-sectional area. Figure 3.50(a) and Figure 3.50(b) present the peak load recorded for RE wallettes dried for three months and twelve months, respectively with different layers and subjected to vertical stress of 0.15 MPa and 0.2 MPa. In both cases, the RE wallettes with a thinner layer (50

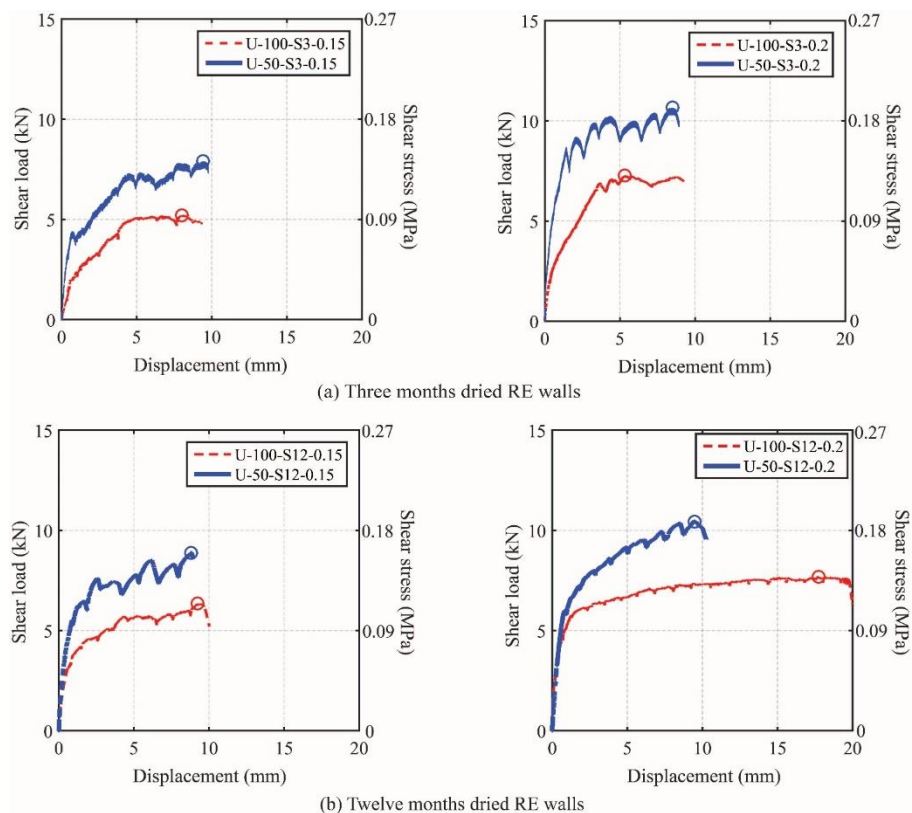


Figure 3.50 Shear load vs displacement of 100 mm and 50 mm layered RE wallettes.

mm) exhibited higher shear strength than the RE wallettes with a thicker RE layer (100 mm). The shear strength of U-50-S3-0.15 is 50% higher than U-100-S3-0.15, and the shear strength of U-50-S3-0.2 is also 50% higher in comparison to U-100-S3-0.2, as seen in Figure 3.50(a). A similar trend is witnessed for RE wallettes dried for twelve months with vertical stress of 0.15 MPa and 0.2 MPa, as seen in Figure 3.50(b). The shear strength of U-50-S12-0.15 and U-50-S12-0.2 exceeded 41.67% and 40%, respectively, with their counterparts RE wallettes with 100 mm layer thickness. The higher shear strength in the thinner wall can be again related to the dry density of the RE wallettes. The average dry density of 50 mm layered RE wall is 1895 kg/m<sup>3</sup>, and the average dry density of 100 mm layered RE wall is 1818 kg/m<sup>3</sup>; the percentage variation is 4.24%. The increase in shear strength of RE wall for the thinner layer compared to the thicker layer was also discussed in the authors' previous work, where the density of the thinner wall was 3.37% higher than the thicker wall [13].

### 3.7.5 Mohr-Coulomb Failure Envelopes

A Mohr-Coulomb failure envelope is derived through a linear fit for shear strength values at various vertical stresses. The plot for the maximum shear value obtained for each vertical stress is presented in Figure 3.51 for all specimen types to obtain the Mohr-Coulomb failure envelope. However, it should be noted that only one linear fit was developed each for 50 mm and 100 mm layer RE wall. Here, the effect of the drying period was ignored since it did not have much influence on the shear strength, as already discussed in the previous section. The acquired cohesion ( $c$ ) and frictional angle ( $\phi$ ) values are listed in Table 3.9 for 50 mm layer and 100 mm layer RE wall. It is noted that the cohesion value of RE wall with the thinner RE layer (50 mm) is slightly

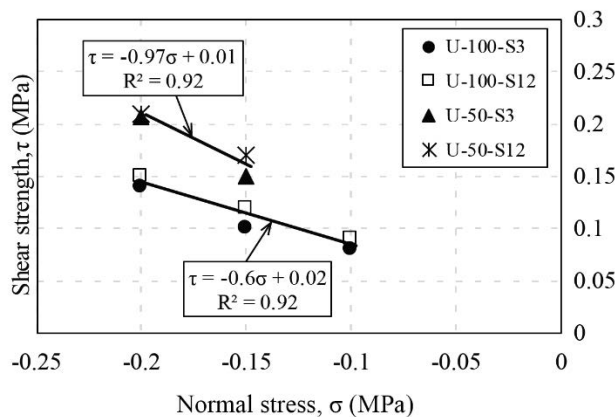


Figure 3.51 Mohr-Coulomb failure envelopes of rammed earth wall.

lower than the RE wall with a thicker RE layer (100 mm) despite having higher strength. The lower cohesion value and higher friction angle in 50 mm RE wall are possibly influenced by rocking behaviour during the initial stage. The cohesion values from these experimental results are almost the same as reported by El-Nabouch [9] and comparatively lower than those reported by Bui et al. [8], Pavan et al. [29] and Cheah et al. [30]. However, it should be noted that the cohesions reported in [29] and [30] are for cement stabilized RE.

Table 3.9 Mohr-Coulomb parameters of RE wallettes.

Parameters	Present work		Bui et al. [8]	Pavan et al. [29]	Cheah et al. [30]	El-Nabouch [9]
	10mm layer	50mm layer				
$c$ (MPa)	0.02	0.01	0.14	0.76-0.79	0.30, 0.72*	0.03
$\varphi$ (°)	30.96	44.13	51	26.15-49.28	45, 48*	35.3

$C$  – Cohesion,  $\varphi$  – frictional angel

Note: The first value under [30] is from triplet test, and the second value with an asterisk is from the triaxial test.

### 3.7.6 Effect of Mesh-Wrap Retrofitting Technique

The test results of retrofitted RE wallettes are presented in Figure 3.52. From the test results, it is seen that there is an improvement in shear capacity, energy absorption, and ultimate horizontal displacement for all the RE wallettes using the mesh-wrap retrofitting technique. For RE wall with vertical stress of 0.15 MPa and dried for three months, the peak shear capacity increased from 7.91 kN to 9.61 kN and ultimate horizontal displacement from 9.42 mm to 10.21 mm, which corresponds to the percentage increase of 21.49% and 8.4%, respectively. The energy absorption has increased from 58.38 kN-mm to 73.11 kN-mm corresponding to 25.23% increment. For the RE wall with 0.2 MPa and dried for three months, the peak load increased from 10.65 kN to 13.34 kN with a percentage increase of 25.26%. There is a significant improvement in energy absorption and the ultimate horizontal displacement, and the percentage increase is 131.21% and 99.65%, respectively. Even for the RE wallettes applied with 0.2 MPa and dried for twelve months, there is a significant improvement in shear strength, energy absorption and ultimate horizontal displacement. The percentage increment in shear strength, energy absorption and ultimate horizontal displacement is 43.35%, 116.16% and 55.77%, respectively. The mesh-wrap strengthening method contributed to the average shear load increment of 2.97 kN, which corresponds to around 0.3 MPa of shear strength. The tensile cracking strength of the mortar



composite is, however, a lot higher (around 3 MPa, as shown in Figure 8(b)), as compared to the increment in shear strength. This was possibly due to the non-uniformity of the plaster thickness as seen by rough surface seen in Figure 7(d), and the thickness of plaster applied on the wallete was less than the tensile coupon test samples. Furthermore, since the samples were free-standing walletes, the compaction pressure during plastering had to be reduced to avoid damages on the RE walletes. Consequently, the tensile strength of the mortar was reduced, resulting in lower participation in wall strengthening. Furthermore, the failure mode observed for the strengthened specimens showed an incipient rocking at the base of the wall, followed by diagonal shear cracking. The shear strength characteristic is primarily controlled by the post cracking strength of the composite characterized by the elongation of steel mesh and subsequent improvement in energy dissipation and ultimate horizontal displacement. All retrofitted RE walletes failed with the appearance of diagonal tension crack as in the case of unreinforced RE walletes with 50 mm layer thickness. The final failure mode of retrofitted RE walletes is shown in Figure 3.53.

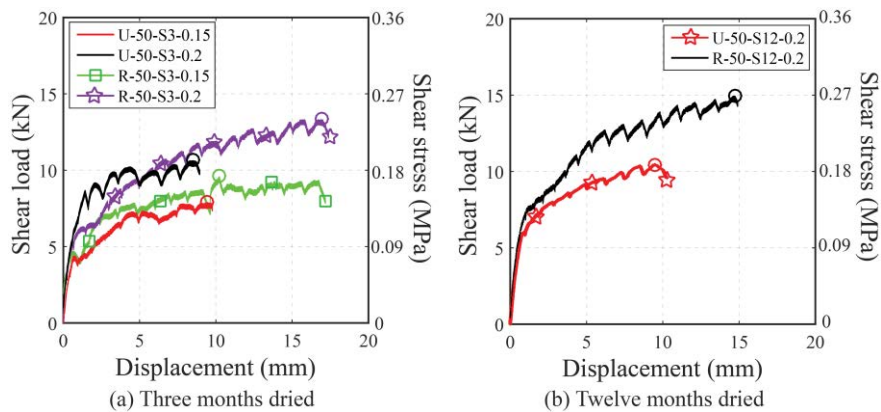


Figure 3.52. Shear load vs displacement of unreinforced and retrofitted RE walletes.



Figure 3.53 Final failure mode of RE walletes under in-plane shear loading.

### 3.8 Finite Element Modelling of In-Plane Loaded Rammed Earth Wall

#### 3.8.1 Modelling of Rammed Earth from Literature

Only limited references on the modelling of RE constructions are found in the literature. The behaviour of rammed earth is simulated using either Finite Element Method (FEM) or Discrete Element Method (DEM) with different damage models. Bui et al. [8] used FEM to simulate walls of  $1\text{ m} \times 1\text{ m} \times 0.3\text{ m}$  under compression loading with classical Mazars model. The comparison of load-displacements between the simulation and experiments of the study is shown in Figure 3.54. Clearly, the Mazars model was able to reproduce the initial stiffness and the peak load. However, the stiffness degradation (pre-peak) and post-peak behaviour was not reproduced correctly.

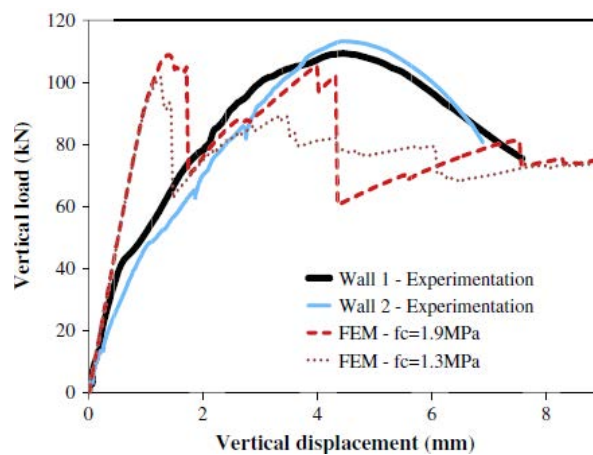


Figure 3.54 Comparison of the numerical and experimental results [8].

The first ever DEM was used by Bui et al. [31] to simulate wall ( $550 \times 550 \times 220\text{ mm}^3$ ) under compression as well as diagonal loading. Models were developed following both macro and micro approaches. The interfaces in case of micro model were modelled following Mohr-Coulomb model with a tension cut-off and post-peak softening. A comparison of the results is illustrated in Figure 3.55. For the wall under compression, both the models estimated the peak load 10% higher than the experimental result (Figure 3.55(a)). Further, the simulation of RE behaviour by both the models were similar which shows the presence of interface does not significantly affect the vertical loading. The model, however, predicted the failure patterns well. Figure 3.55(b) presents the comparison of the numerical and experimental results under diagonal shear without interface. The

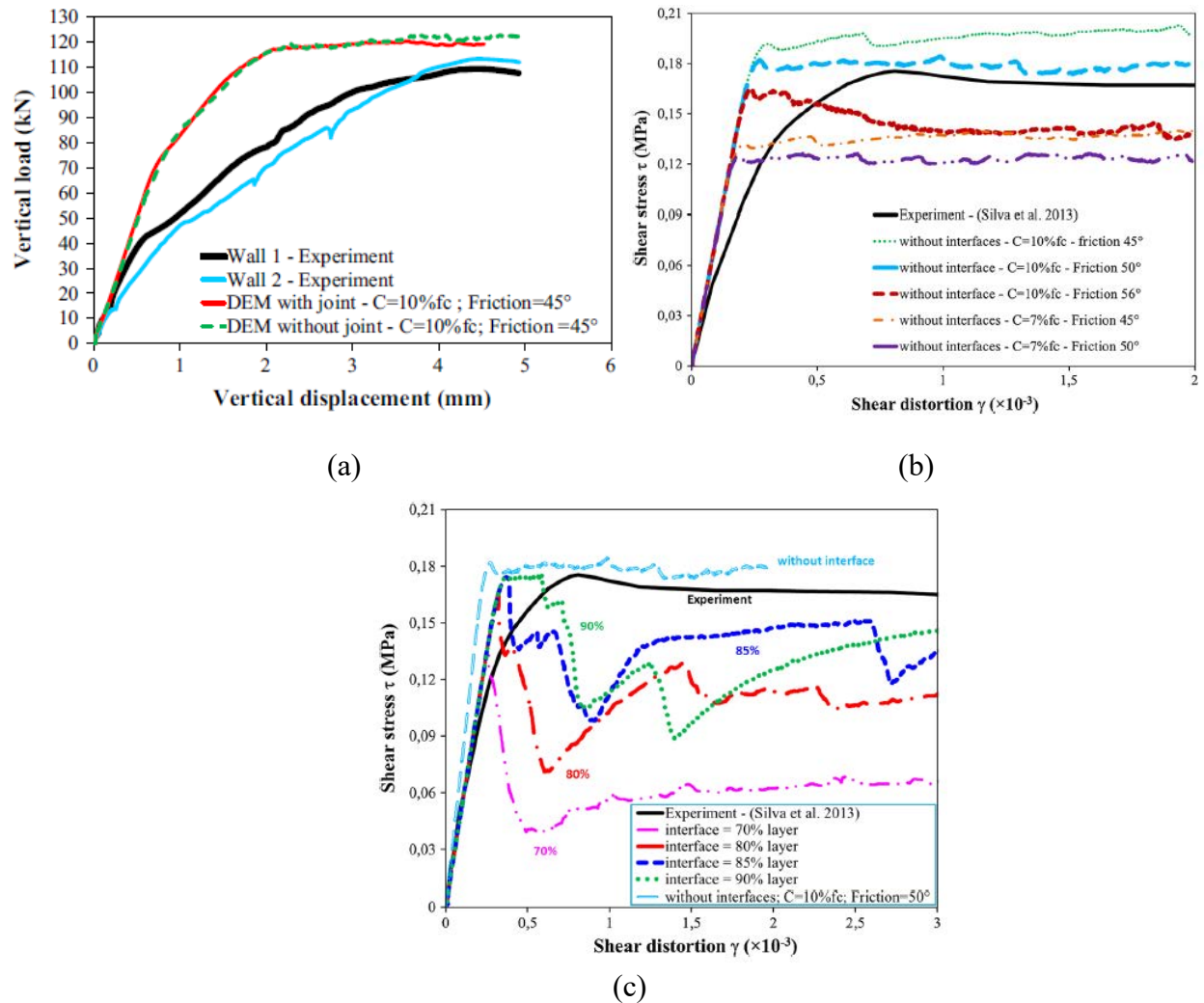


Figure 3.55 Comparison of the numerical and experimental results under: (a) Compression loading; (b) Diagonal shear without interface; (c) Diagonal shear with interface [31].

layer cohesion was 7 and 10 % of the compressive strength, and the friction angle varied from 45° to 56°. All models could reproduce the shear modulus of the wall, which was the slope of the first part of the test (until 20% of the ultimate shear stress) but could not reproduce the slope change after that. Amongst the models, the model with layer cohesion 10% of compressive strength and friction angle 50° gave the closest ultimate shear strength. Further, the model could reproduce the diagonal crack of the experiment but could not reproduce the horizontal crack. Thus, micro modelling approach was adopted with layer cohesion 10% of the compressive strength and friction angle 50° (the model that gave closest ultimate shear strength from the macro model list). Here, the interface cohesion and friction angles were assumed as 70, 80, 85 and 90% of the corresponding

parameters of the earth layer. The result is shown in Figure 3.55(c). Clearly, the model with interface could reproduce the first part of the experimental result (upto 50% of the ultimate stress) which is considered better than the macro models. However, none of the models were able to reproduce the nonlinear behaviour before the peak. Further, only model with interfaces at 85% of the layer's characteristics was able to reproduce the failure at the interface of the third layer. Rest of the models could only reproduce diagonal crack.

The Total Strain Rotating Crack Model (TSRCM) is another constitutive model based on damage which is induced by cracks. The TSRCM follow a smeared cracks approach for the fracture energy. It corresponds to a model of distributed and rotating cracks based on total strains, where the crack direction rotates with the principal strain axes [32]. This model is used in some works for rammed earth modelling under diagonal compression [15]. They used the TSRCM to model the behaviour of a rammed earth wallet throughout a diagonal compression test. The wallet was modelled as a homogeneous model (macro-model) and also as nonhomogeneous medium by introducing interfaces (micro-model) between compacted layers. The interface between layers was simulated using Mohr-Coulomb interface model. Figure 3.56 shows the comparison between experiments and simulations. The parameters in this models were not obtained by experiments, so they were estimated. Therefore, the model could not reproduce the experimental results (Figure 3.56(a)) and the calibration was required. The results after calibration (Figure 3.56(b)) were found within the average of the experiments envelope. After validating the model, the authors then simulated the shear behaviour of rammed earth walls under static lateral loading [10]. It was the first study that reported the simulation of rammed earth walls under in-plane loading. The results of the simulation was satisfactory and the model could reproduce the diagonal crack obtained experimentally. The authors recommended values for the numerical analysis for rammed earth with TSRCM and the Coulomb friction model as listed in Table 3.10 [10].

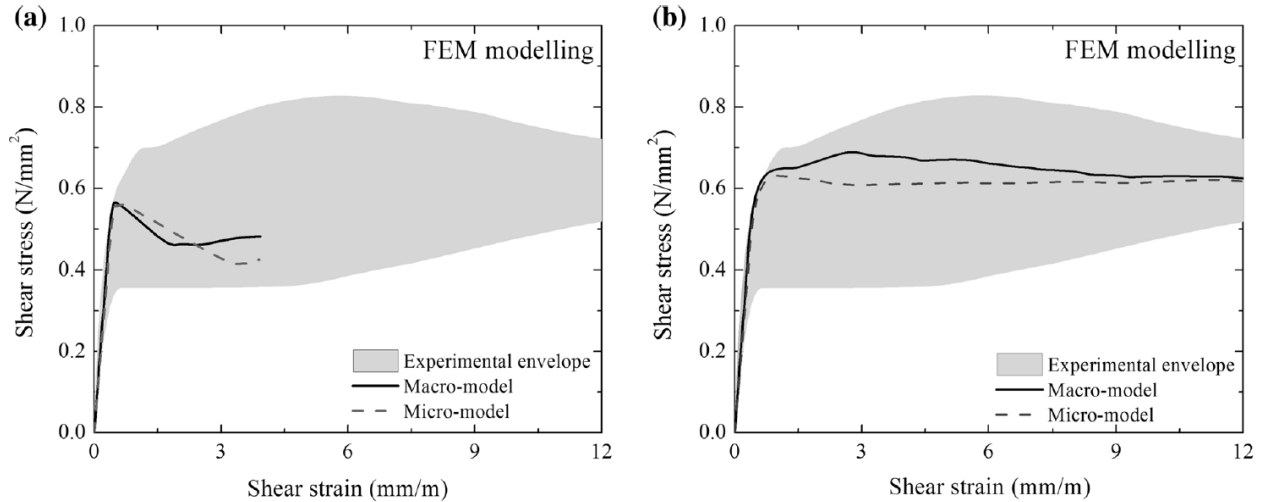


Figure 3.56 Behaviour of macro and micro models: (a) Using initial parameters; (b) After calibration [15].

Table 3.10 Recommended values for numerical analysis of rammed earth by Micoli et al [10].

Material	$E$ (N/mm <sup>2</sup> )	$\nu$	$f_c$ ((N/mm <sup>2</sup> ))	$G_c$	$f_t$ ((N/mm <sup>2</sup> ))	$G_f^I$ (N/mm)
TSRCM Rammed earth	a	a	Multi-linear relationship <sup>a</sup>	Multi-linear relationship <sup>a</sup>	$(0.08-0.12)f_c$	$(0.1-0.5)f_t$
Material	$k_n$ (N/mm <sup>3</sup> )	$k_s$ (N/mm <sup>3</sup> )	$c$ (N/mm <sup>2</sup> )	$\tan(\phi)$	$\tan(\psi)$	$f_t^I$ (N/mm)
Coulomb friction model Interfaces	$E/100$	$k_s=0.5*k_n/(1+\nu)$	$(1.5-2.0)f_t$	0.58-1.0	0	$(0.67-1)f_t$

<sup>a</sup> From testing;  $E$  – Young’s modulus;  $\nu$  – Poison ratio;  $f_c$  – compressive strength;  $f_t$  – tensile strength;  $G_c$  – Compressive fracture energy;  $G_f^I$  – Mode I tensile fracture energy;  $f_t^I$  – Interface tensile strength;  $c$  – cohesion;  $\tan(\phi)$  – friction angle;  $\tan(\psi)$  – Dilatancy angle.

The recent study by Shrestha et al. [13] also reported on the simulation of rammed earth wall under in-plane loading. Three walls having dimensions of  $1200 \times 1200 \times 600 \text{ mm}^3$  were tested: i) unreinforced with 120 mm layer thick, ii) reinforced with RC dowel with 120 mm layer thick, and iii) reinforced with rc dowel with 60 mm layer thick. A 3D FE model was developed for each wall specimen following TSRCM as a constitutive model. The parametric values for interface layers were assumed based on the values recommended by Miccoli et al. [10, 15]. Figure 3.57 shows the results of the simulation compared with the experimental results. The FE simulation predicted the peak shear force and failure pattern reasonably well for both unreinforced and reinforced walls.

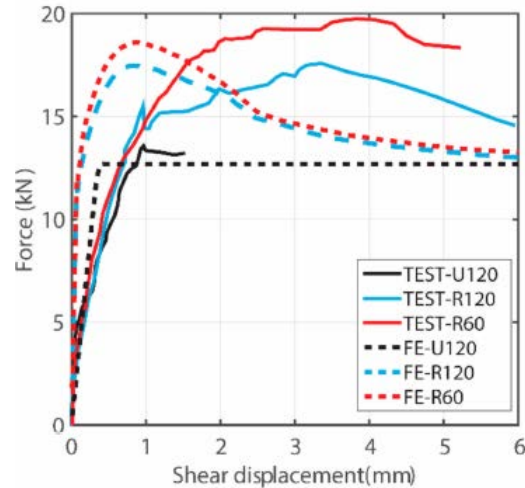


Figure 3.57 Shear force vs shear displacement for experimental and FE simulation [13].

The literature listed above mostly deal with finite modelling of the unreinforced RE wall, and only a few reported on strengthening elements [13]. In the present study, numerical modelling of RE wall tested under in-plane shear loading is carried out for both unreinforced and strengthened samples. The details on the modelling of mesh composite, used as strengthening technique in the present study, are discussed. The numerical analysis aims to reproduce the behaviour of rammed earth as observed during the experimentation. A sensitivity analysis is also carried out with different mechanical properties to analyze the effect of their variabilities on the shear strength of RE wall.

### 3.8.2 Modelling Strategy

Modelling strategy for masonry are classified into three depending on the level of accuracy and simplicity desired, as shown in Figure 3.58.

- i. Micro-modeling focuses on clearly defining all the components of the masonry separately as a unit and joint, connected using interface elements.
- ii. Simplified micro-modelling involves strategy where continuum elements represent the expanded units, and discontinuous interface elements represent the lumped joint mortar and unit-mortar interface.
- iii. The macro-modeling technique involves smearing of units, mortar, and unit-mortar interfaces out in a continuum. This method treats masonry as an anisotropic composite material. Thereby, a complete macro model should reproduce an orthotropic material with

different tensile and compressive strengths as well as different inelastic behavior along each material axes.

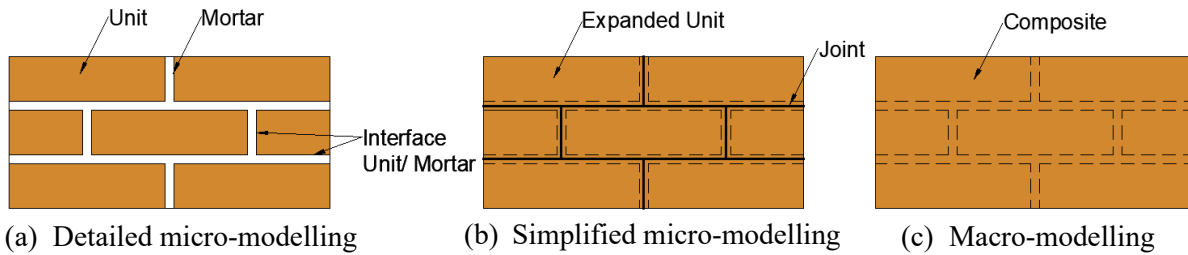


Figure 3.58 Modeling strategies for masonry structures.

The choice of the modelling strategy largely depends on the application field and requirement of accuracy in the study, and the preference of one modelling strategy over the other is generally not considered. Micro-modelling can provide a better understanding of the local behaviour of masonry structures. In contrast, macro-modelling is applicable to study structures composed of solid wallettes with sufficiently large dimensions, about uniform stress distribution along the macro-length. Moreover, macro-modelling is more practice-oriented due to reduced computational time and memory requirements. In the present study, two-dimensional finite element (FE) model was developed for the representative RE wallettes with FE program DIANA [32] following the simplified micro-modelling and macro-modelling strategies.

### 3.8.3 Geometry, Boundary and Loading Conditions

#### 3.8.3.1 Geometry

Five representatives RE wallettes from unreinforced (U-100-S12-0.2, U-100-S12-0.15, U-100-S12-0.1, U-50-S12-0.2, and U-50-S12-0.15) and two representatives RE wallettes from strengthened (R-50-S3-0.2 and R-50-S3-0.15) were considered for the numerical modeling. The dimensions of the FE model were considered the same as the tested RE wallettes' dimensions,  $500 \times 500 \times 110 \text{ mm}^3$ . The material properties adopted for the FE models, both for unreinforced and strengthened, are listed in Table 3.11. The values of density ( $\rho_r$ ), compressive strength ( $f_{cr}$ ) and elastic modulus ( $E_r$ ) in Table 3.11 follow the average value of the representative RE wall tested under compression loading. CQ16M (an eight-node quadrilateral isoparametric plane stress element) element with element size 20 mm was considered to generate the mesh for RE in both macro and micro models, and CL12I (six-noded interface element) to simulate the interface between RE layers. For FE-R-RE, the mesh-wrap strengthening element was added using an eight-node quadrilateral isoparametric plane stress element (CQ16M) with mesh element size 20 mm.

The thickness provided for mesh composite in the model was 20 mm, considering mesh composite of 10 mm thickness was provided in both faces of RE wall. Here, the plaster element and steel wire mesh were modelled as a single mesh composite element. The details of material properties adopted for mesh composite are given in Table 3.11. The compressive characteristics for the mesh composite are based on the cylindrical compression tests, and the tensile characteristics are from the tensile coupon test of the mesh composite.

Table 3.11 Material properties for FE model.

	Material properties	100 mm layer	50 mm layer
Rammed earth block	Mass density, $\rho_r$ (kg/m <sup>3</sup> )	1818	1895
	Poisson's ratio, $\nu$	0.15	0.15
	Elastic modulus, $E_r$ (MPa)	102	250
	Tensile strength, $f_{tr}$ (MPa)	0.05	0.07
	Mode-I tensile fracture energy, $G_{fr}$ (N/mm)	0.006	0.0084
	Compressive strength, $f_{cr}$ (MPa)	0.98	1.31
	Compressive fracture energy, $G_{cr}$ (N/mm)	1.47	1.965
	Interface between rammed earth layers	Normal stiffness, $K_n$ (N/mm <sup>3</sup> )	10200
Shear stiffness, $K_s$ (N/mm <sup>3</sup> )		4435	10870
Cohesion, $c_i$ (MPa)		0.1	0.14
Friction angle, $\tan\phi$ (rad)		0.6	0.6
Dilantancy angle, $\tan\phi$ (rad)		0	0
Interface tensile strength, $f_{ti}$ (MPa)		0.04	0.056
Mesh composite	Mass density, $\rho_m$ (kg/m <sup>3</sup> )	N/A	1979
	Poisson's ratio, $\nu$	N/A	0.15
	Elastic modulus, $E_m$ (MPa)	N/A	1000
	Tensile strength, $f_{tm}$ (MPa)	N/A	User supplied (Figure22(c))
	Compressive strength, $f_{cm}$ (MPa)	N/A	17.38
	Compressive fracture energy, $G_{cm}$ (N/mm)	N/A	0.001

N/A – Not applicable

### 3.8.3.2 Boundary and Loading Conditions

The vertical stress in the model was applied by imposing uniformly distributed force in the y-direction at the top edge of the model. The distributed horizontal load was applied by imposing prescribed deformation in the x-direction at the node (410 mm from the bottom) with multiple points constraints. Few nodes parallel to loading point had to be constrained to the master node (node at loading point) for partial fixation to simulate the experimental observation. Without providing this boundary condition, local failure was observed at the loading point, and this does not represent the actual experimental result. The nodes near the loading point of the wall were



constrained to the master node (node at loading point) to represent the angle section at the loaded portion. For boundary conditions, the bottom of the wall was supported in the y-direction, and the 1<sup>st</sup> layer at the bottom right corner was supported in the x-direction.

### 3.8.4 Constitutive Laws

The adopted constitutive model for rammed earth was a total strain-based rotating crack model. The tensile strength value ( $f_{tr}$ ) was calibrated, which closely represented the experimental result. The compressive fracture energy ( $G_{cr}$ ) was assumed as  $1.5f_{cr}$ , mode-I tensile fracture energy ( $G_{fr}$ ) as  $0.12f_{tr}$  [13,15]. The stress-strain relationship is based on previous literature for similar rammed earth wall [10,15]. The constitutive model for RE adopts an exponential tension-softening for the tensile behaviour (Figure 3.59(a)) and parabolic hardening with subsequent softening for the compressive behaviour (Figure 3.59(b)). The tensile behaviour of mesh composite is represented by a multilinear tensile stress-strain curve, representing the tensile coupon test of the mesh composite, shown in Figure 3.59(c). However, the initial cracking tensile strength of the plaster has been excluded since its participation in strengthening wall was reduced for the reasons stated under section 3.5.6.

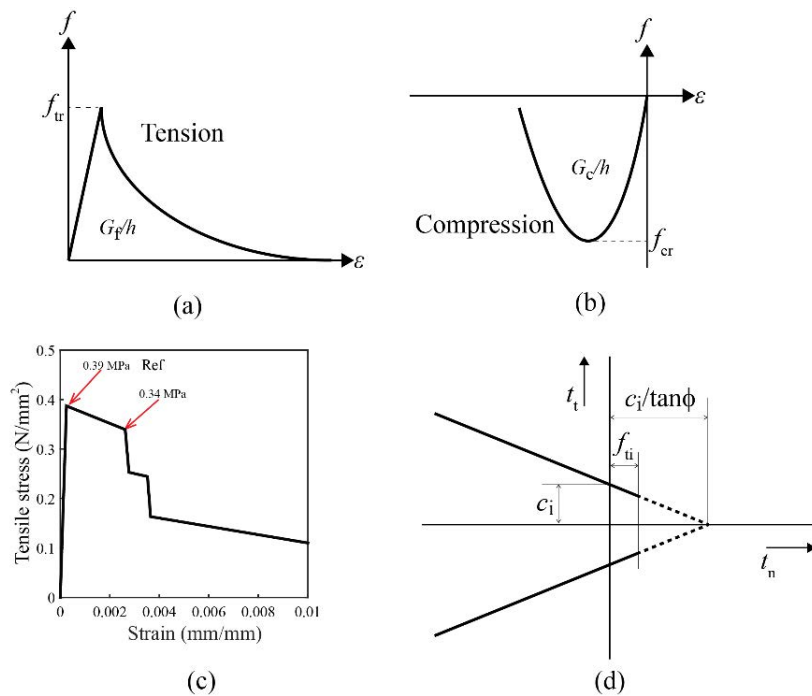


Figure 3.59 Material model adopted for FE.

For the micro model, the interface layer between RE layers was modelled with nonlinear Coulomb friction model (Figure 3.59(d)). The linear normal stiffness of interface layer,  $K_n$ , is taken 100 times that of the rammed earth [10,15], and the shear stiffness,  $K_s$ , was considered as  $[K_n/2(1+\nu)]$ . The interface cohesion ( $c_i$ ), tensile strength ( $f_{ti}$ ) and friction angle ( $\tan\phi$ ) are calibrated with the recommended values from the previous study [10, 15, 33] were considered in the micro modelling. CQ16M (an eight-node quadrilateral isoparametric plane stress element) element with element size 20 mm was considered to generate the mesh for RE in both macro and micro models, and CL12I (six-noded interface element) to simulate the interface between RE layers. Figure 3.60(a) and Figure 3.60(b) show the mesh generated for the FE macro and micro model, respectively.

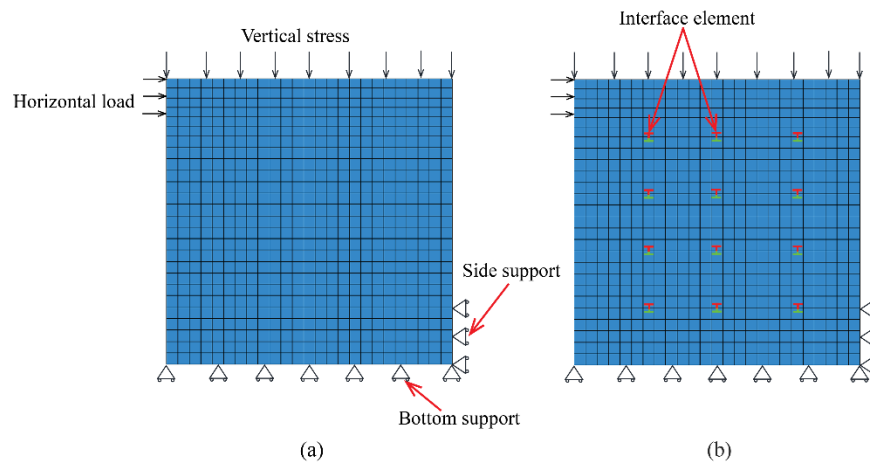


Figure 3.60 FE model: (a) Mesh for macro model; (b) Mesh for micro model of 100 mm layer.

### 3.8.2 Results and Discussion

The FE analysis results are compared with the experimental observations in terms of load-displacement relationship and failure mode. Table 3.12 presents the summary of FE simulation

Table 3.12 Experimental and FE results.

Specimen ID	Peak load $H_{max}$ (kN)			Energy absorption $\Psi$ (kN-mm)		
	Exp	FE-macro	FE-micro	Exp	FE-macro	FE-micro
U-100-S12-0.2	7.69	7.32	6.57	121.98	92.91	32.05
U-100-S12-0.15	6.34	6.37	5.37	46.54	67.72	17.97
U-100-S12-0.1	4.73	5.51	4.39	31.15	85.66	24.66
U-50-S3-0.2	10.65	10.22	6.88	75.20	115.12	17.19
U-50-S3-0.15	7.91	9.22	5.61	58.38	102.58	11.23
R-50-S3-0.2	13.34	13.09	10.08	173.87	112.2	23.66
R-50-S3-0.15	9.61	11.63	8.78	73.11	113.64	37.90

and experimental program for both unreinforced and strengthened RE wallettes in terms of peak load and energy absorption. The peak load values estimated by FE simulation are satisfactory with micro model predicting slightly lower than the macro model for both wall types. However, discrepancies in energy absorption are noted between the experimental and the FE models. Moreover, the energy absorption of the FE micro is comparatively lower than the FE macro. This is due to a sudden drop in load and subsequent divergence of the solution in FE micro models caused by shear slip along the bed joints. Figure 3.61 and Figure 3.62 presents the results from both experimental and FE simulation for 100 mm layer and 50 mm layer RE wallettes, respectively. Both FE micro and FE macro are able to reproduce the experimental load-displacement curve. The stiffness in the load-displacement response predicted by the FE model is slightly lower than the experimental results. This is possibly due to excessive rocking in FE model at the initial loading; however, in the experimental test set up, this initial rocking behaviour was not seen due to the partial fixity provided by the loading platen at the top of the RE wall (Figure 3.32).

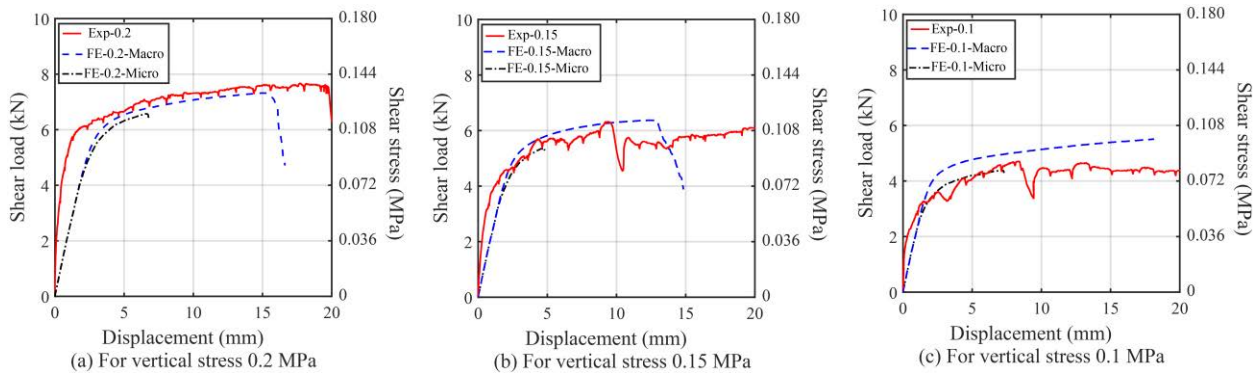


Figure 3.61 Experimental and FE results of unreinforced RE wallettes of 100 mm layer.

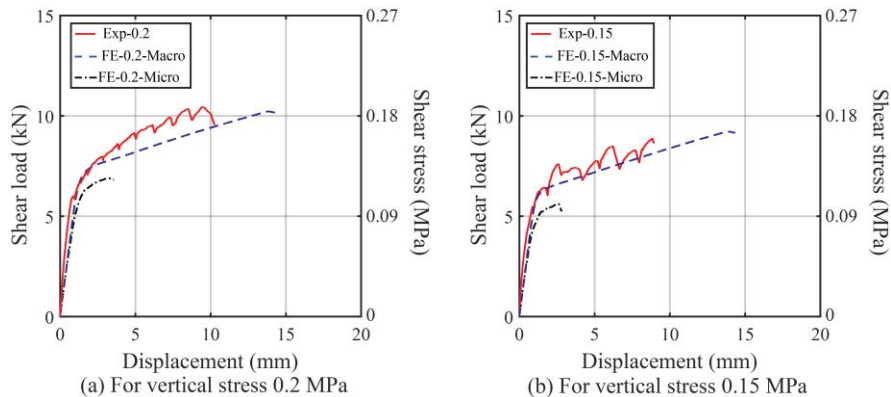


Figure 3.62 Experimental and FE results of unreinforced RE wallettes of 50 mm layer.

The crack patterns observed in macro and micro models for unreinforced RE wallettes are presented in Figure 3.63 and Figure 3.64 for 100 mm and 50 mm layer wall, respectively at various vertical stresses. The FE deformed shape is illustrated in terms of maximum principal strain at the final load step of micromodel. For both layers, the macro model is able to simulate initial rocking at the base followed by diagonal shear crack. At higher vertical stress (0.2 MPa), the rocking behaviour is reduced. The micro model, on the other hand is able to simulate a diagonal cracking with bed-joint opening at interface level.

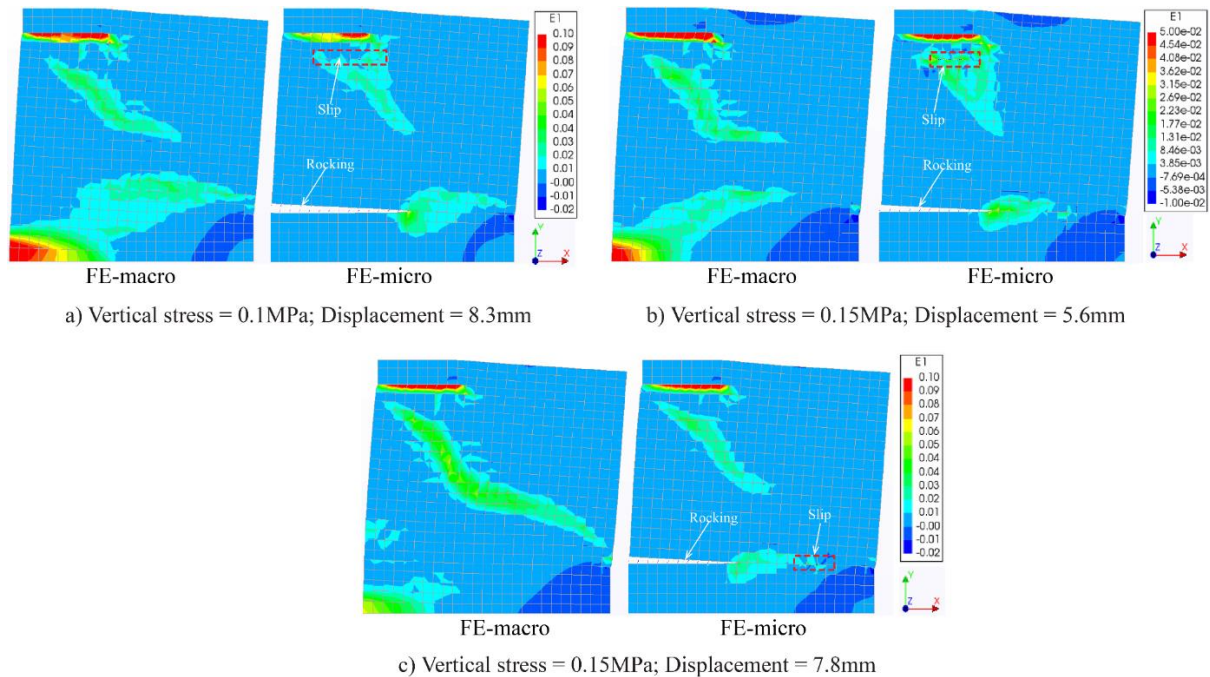


Figure 3.63 Failure mode observed in FE model of unreinforced RE wall of 100 mm layer.

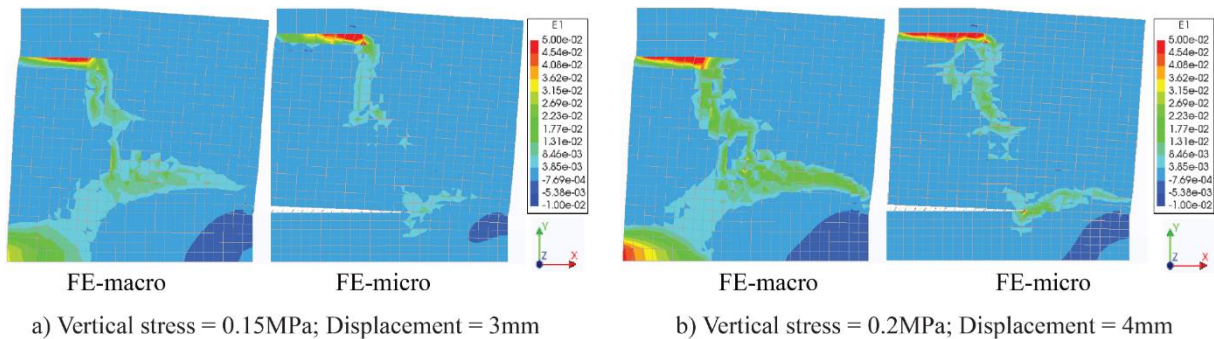


Figure 3.64 Failure mode observed in FE model of unreinforced RE wall of 50 mm layer.

Figure 3.65 presents the load-displacement relationship of the strengthened RE wallettes obtained from the experimental and numerical analysis. The peak shear load estimated by the macro model

for the RE wall with vertical stress at 0.2 MPa is close to the experimental value, as seen in Figure 3.65(b). However, for the RE wall with 0.15 MPa, the peak shear of the FE model is overestimated by 21% of the experimental value (Figure 3.65(a)). Even in this case, the initial stiffness predicted by the FE model is lower than the experimental, due to incipient rocking in FE model. The damages for strengthened RE wallettes predicted by both models at two different vertical stresses are presented in Figure 3.66 at different load steps represented by the maximum principal strain. In this case too, both the models were able to reproduce the shear cracks and diagonal cracks observed under the experimental program.

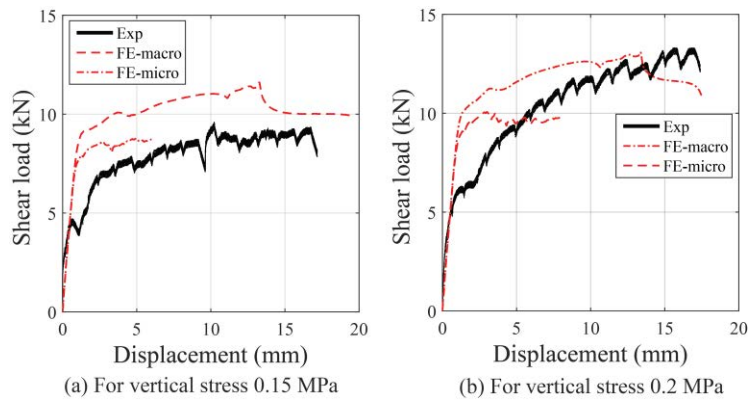


Figure 3.65 Experimental and FE results of strengthened wallettes of 50 mm layer.

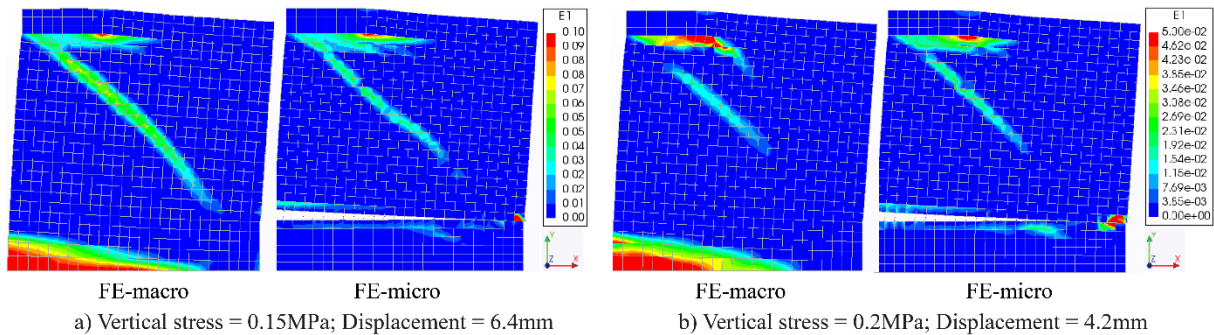


Figure 3.66 Failure mode observed in FE model of strengthened RE wall of 50 mm layer.

### 3.8.3 Sensitivity Analysis

A sensitivity analysis was carried out to assess the influence of different mechanical properties of the RE wall on their shear behaviour. The material properties values for the reference wall adopted in the sensitivity analysis are presented in Table 3.9. To this value, a variation of +20% to -20% was considered for each parameter involved to understand their effect on the shear response of the macro model. The list of parameters considered for the sensitivity analysis includes compression strength,  $f_{cr}$ , tensile strength,  $f_{tr}$ , vertical stresses,  $\sigma_r$ , elastic modulus,  $E_r$ , and density,  $\rho_r$ . The

individual variation for each parameter is presented in Table 3.13, along with their corresponding IDs. The interface parameters considered for sensitivity analysis is presented in Table 3.14.

Table 3.13 Parameters considered for sensitivity analysis and their corresponding FE-IDs.

Parameters	Compressive strength				Tensile strength				Vertical stress			
Change %	-20	-10	10	20	-20	-10	10	20	-20	-10	10	20
FE-ID	1	2	3	4	5	6	7	8	8	10	11	12
Parameters	Elastic Modulus				Density							
Change %	-20	-10	10	20	-20	-10	10	20				
FE-ID	13	14	15	16	17	18	19	20				

Table 3.14 Interface layer parameters for sensitivity analysis and their corresponding FE-IDs.

Parameters	$C_i, f_{ti}$				$K_n, K_s$				Tan $\phi$			
Change %	-20	-10	10	20	-20	-10	10	20	-20	-10	10	20
FE-ID	21	22	23	24	25	26	27	28	29	30	31	32

Figure 3.67 presents the shear load-displacement diagram showing the effect on the RE wall's shear response with the variability of each material characteristic. The effect of change in compressive strength Figure 3.58(a), tensile strength (Figure 3.63(b)), vertical stress (Figure 3.63(c)), and elastic modulus (Figure 3.63(d)) have a more significant influence on the in-plane shear strength of the RE wall. The shear strength of RE is observed to be improved with increased values for tensile strength, vertical stress, and elastic modulus. The influence of density on shear behaviour of RE wall is negligible pre-peak (Figure 3.63(e)). The other parameters that have the most significant influence on shear stress of rammed earth wall include cohesion, the Poisson's ratio and the tensile fracture energy as highlighted by Shrestha et al. [13] and Miccoli et al. [15]. The results from interface sensitivity analysis are presented in Figure 3.68 for a normalized peak horizontal load. Here, FE-micro was considered as the reference wall. Cohesion, tensile strength of interface layer and frictional angle had the most significant influence on the shear behaviour of the RE wallettes as well as on the peak shear load. When these values were reduced by 20%, there was a substantial drop in the maximum shear load, and the wallette failed with shear sliding. The variation of normal and shear stiffness modulus within the chosen range did not have much effect on the peak load and the behaviour of the RE wallette.

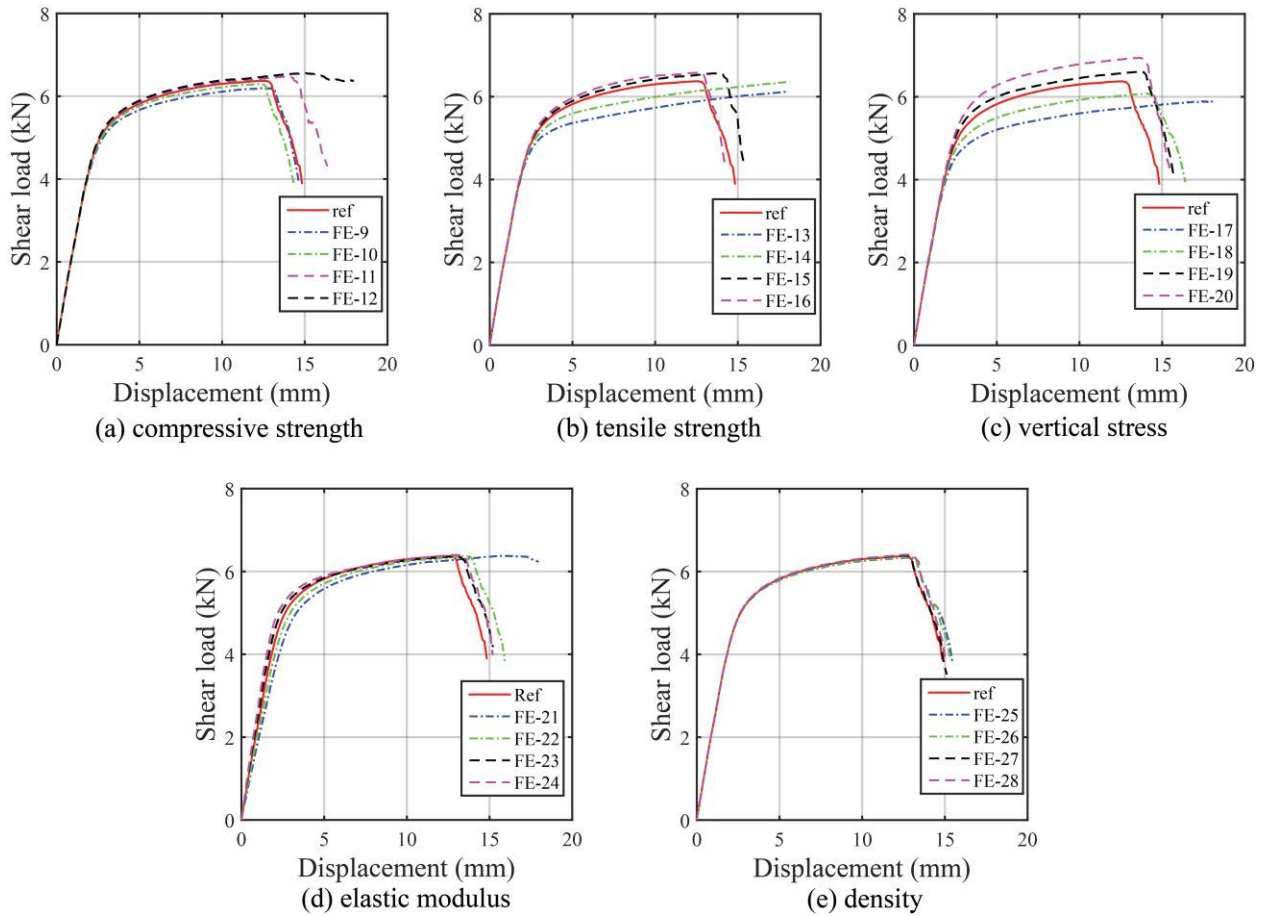


Figure 3.67 Results of sensitivity analysis showing shear load-displacement diagram under varying parameters considered.

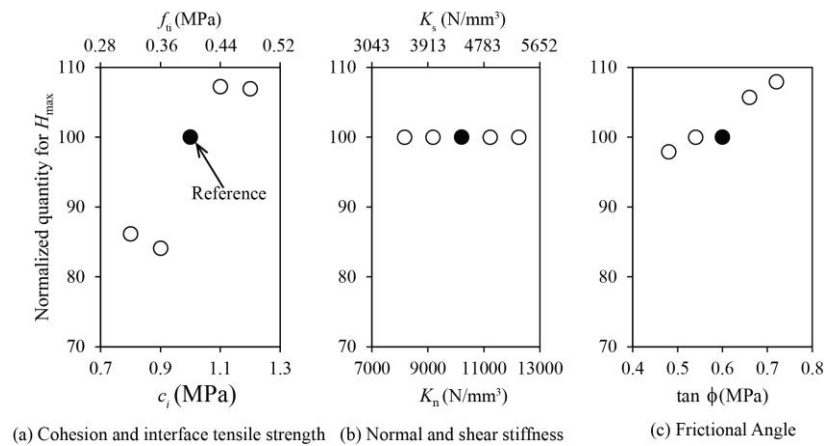


Figure 3.68 Results of sensitivity analysis for normalized peak horizontal load, under varying parameters considered.

For the retrofitted specimen, a tensile stress-strain curve of mesh composite was considered as a parameter to check its effect on the shear behaviour of the RE wallettes. The reference wall was modelled adopting the material properties listed in Table 3.10 for FE-R-RE with user-defined tensile stress-strain illustrated in Figure 3.55(c). Even here, a variation of -20% to +20% was adopted. The variation here applies to change in peak stress values while the tensile behaviour is maintained same, as shown in Figure 3.69(a). Table 3.15 presents the details of the variation percentage adopted for each specimen type and their corresponding FE IDs. The results of sensitivity analysis are presented in Figure 3.69(b) and Figure 3.69(c) in terms of the load-displacement curve for two specimen type having different vertical stress of 0.15 MPa and 0.2 MPa. In both cases, a slight improvement in shear strength of RE wall was noted with the increase in peak tensile stress value.

Table 3.15 Sensitivity analysis for retrofitted RE wall and their corresponding FE-IDs.

Parameters	Tensile stress-strain curve							
	FE-R-50-S3-0.15				FE-R-50-S3-0.2			
Change %	-20	-10	10	20	-20	-10	10	20
FE-ID	33	34	35	36	37	38	39	40

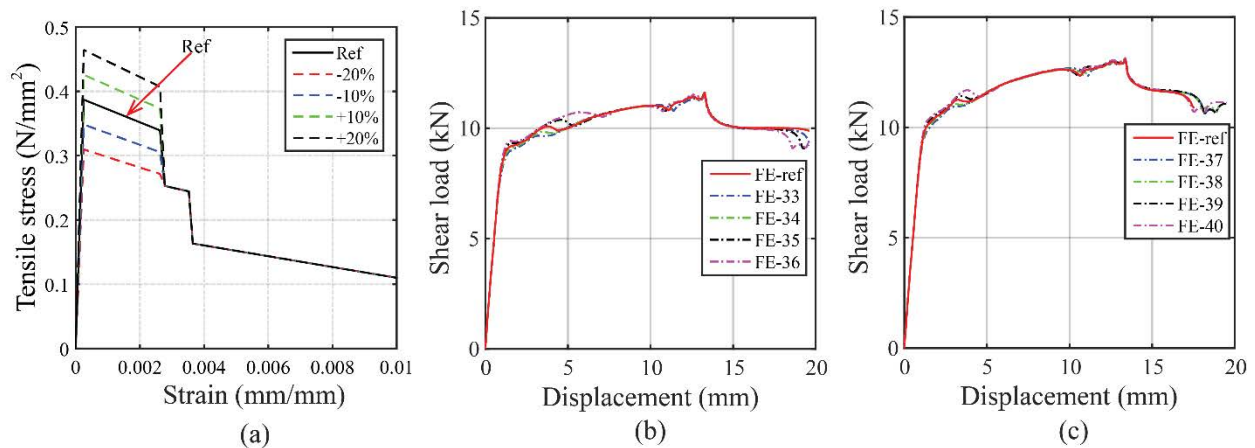


Figure 3.69 Results of sensitivity analysis showing shear load-displacement diagram under varying stress-strain curve of mesh composite: (a) User-defined tensile stress-strain curve of mesh composite; (b) 50 mm layer RE wall with vertical stress 0.15 MPa, (c) 50 mm layer RE wall with vertical stress 0.2 MPa.

### 3.7 Summary

The chapter reported on the experimental program conducted on rammed earth wall having dimensions  $500 \times 500 \times 110$  mm to assess their compressive strength and shear strength while examining the effect of different parameters on their strength. Two general parameters were



considered, namely the rammed earth layer and drying period for both the test type. For the shear test, in addition to the above parameters, the effect of vertical stresses is also examined. The vertical stresses considered for the test were 0.1 MPa, 0.15 MPa and 0.2 MPa, whose stresses closely represented the stresses of traditional Bhutanese houses in the roof floor, second floor and first floor, respectively. The test results have shown that the compressive strength and shear strength increases with the increase in drying period. The current work reflects only two drying periods at 3 months and 12 months. Through the current work, it is observed that the RE wallettes with a thinner layer (50 mm) required minimal effort to manufacture than the RE wallettes with a thicker layer (100 mm). The compaction achieved in 50 mm layered RE wallettes was better with slightly higher density compared to the 100 mm layered RE wallettes. The average compressive strength of 100mm layered RE wallettes with drying duration of 3 months and 12 months was 0.91 MPa and 0.98 MPa, respectively. For the 50 mm layered RE wallettes with drying duration 3 months and 12 months, the average compressive strength was 1.31 MPa and 1.65 MPa, respectively. For both cases of drying period, the strength for RE wallettes with a thinner layer are observed higher than the RE wallettes with a thicker layer. The better strength in a thinner layer is also observed for the RE wallettes tested under shear loading.

Moreover, it was also seen that the vertical stress influences the shear strength of the RE wallettes. The shear strength of 100 mm layered RE wallettes dried for three months with vertical stress 0.1 MPa, 0.15 MPa and 0.2 MPa are found 0.08 MPa, 0.1 MPa and 0.14 MPa, respectively. For 100 mm layered RE wallettes dried for 12 months with vertical stress 0.1 MPa, 0.15 MPa, 0.2 MPa, the shear strength was 0.09 MPa, 0.12 MPa and 0.15 MPa, respectively. A similar trend is observed in 50 mm layered RE wallettes, where the shear strength is seen increasing with an increase in vertical stress. The shear strength of 50 mm layered RE wallettes dried for 3 months with vertical stress is found 0.15 MPa and 0.21 MPa, respectively. In the case of the 50 mm layered dried for 12 months, the shear strength recorded are 0.21 MPa and 0.17 MPa, respectively. Furthermore, the shear strength values were ranging from 8.8%-11.45% of its average compressive strength.

The Mohr-Coulomb failure envelope was developed based on shear strength and vertical stress. The cohesion ( $c$ ) values obtained were 0.02 MPa for 100 mm layered RE wallettes and 0.01 MPa for 50 mm layered RE wallettes. The frictional angle ( $\phi$ ) computed for 100 mm layered RE wall is  $30.96^\circ$  and for 50 mm layered RE wallettes was  $44.13^\circ$ .

The efficacy of the mesh-wrap retrofitting technique was also assessed through compression and shear testing. Based on the experimental results, the proposed mesh-wrap retrofitting technique is found to be effective in strengthening the RE wallettes tested under all considered parameters. Further, the retrofitting technique also improved in controlling the failure mode of the RE wallettes. The energy absorption and ductility of the RE wallettes were also improved using the proposed retrofitting technique.

The numerical analysis for rammed earth wall under shear loading was performed by developing a two-dimensional finite element (FE) model following the macro-modelling approach. Total strain rotating crack model was used in modelling rammed earth layers and Mohr-Coulomb in layer interfaces. The peak shear load obtained from the FE models is found to have good agreement with the experimental values. A sensitivity analysis was also carried out with variability in the rammed earth wall's mechanical properties to understand their effect in shear strength. The tensile strength, vertical stress, and elastic modulus are found to have the most significant influence on the rammed earth wall's shear behaviour. However, the compressive strength and density have minimal effect on the rammed earth wall's shear strength. The tensile stress-strain curve of the mesh composite is also observed to have an effect on the shear strength of the rammed earth wall.

## References

- [1] P. Wangmo, K. C. Shrestha, and C. Affairs, "Exploratory study of rammed earth walls under static element test," *Constr. Build. Mater.*, 2020.
- [2] J. C. Morel, A. Pkla, and P. Walker, "Compressive strength testing of compressed earth blocks," *Constr. Build. Mater.*, 2007, doi: 10.1016/j.conbuildmat.2005.08.021.
- [3] Q. B. Bui, J. C. Morel, S. Hans, and N. Meunier, "Compression behaviour of non-industrial materials in civil engineering by three scale experiments: The case of rammed earth," *Mater. Struct. Constr.*, vol. 42, pp. 1101–1116, 2009, doi: 10.1617/s11527-008-9446-y.
- [4] M. Hall and Y. Djerbib, "Rammed earth sample production: Context, recommendations and consistency," *Constr. Build. Mater.*, 2004, doi: 10.1016/j.conbuildmat.2003.11.001.
- [5] D. M. Lilley and J. Robinson, "Ultimate strength of rammed earth walls with openings," *Proc. Inst. Civ. Eng. Struct. Build.*, 1995, doi: 10.1680/istbu.1995.27872.

- [6] V. Maniatidis and P. Walker, “Structural capacity of rammed earth in compression,” *J. Mater. Civ. Eng.*, 2008, doi: 10.1061/(ASCE)0899-1561(2008)20:3(230).
- [7] P. A. Jaquin, C. E. Augarde, and C. M. Gerrard, “Analysis of Historic Rammed Earth construction,” *Struct. Anal. Hist. Constr.*, 2006.
- [8] T. T. Bui, Q. B. Bui, A. Limam, and S. Maximilien, “Failure of rammed earth walls: From observations to quantifications,” *Constr. Build. Mater.*, vol. 51, pp. 295–302, 2014, doi: 10.1016/j.conbuildmat.2013.10.053.
- [9] R. El-Nabouch, “Mechanical behavior of rammed earth walls under Pushover tests,” 2017.
- [10] L. Miccoli, A. Drougkas, and U. Müller, “In-plane behaviour of rammed earth under cyclic loading: Experimental testing and finite element modelling,” *Eng. Struct.*, vol. 125, no. 15, pp. 144–152, 2016, doi: 10.1016/j.engstruct.2016.07.010.
- [11] K. Liu, M. Wang, and Y. Wang, “Seismic retrofitting of rural rammed earth buildings using externally bonded fibers,” *Constr. Build. Mater.*, vol. 100, pp. 91–101, 2015, doi: 10.1016/j.conbuildmat.2015.09.048.
- [12] R. El-Nabouch, Q. B. Bui, O. Plé, and P. Perrotin, “Assessing the in-plane seismic performance of rammed earth walls by using horizontal loading tests,” *Eng. Struct.*, 2017, doi: 10.1016/j.engstruct.2017.05.027.
- [13] K. C. Shrestha, T. Aoki, M. Miyamoto, P. Wangmo, and Pema, “In-plane shear resistance between the rammed earth blocks with simple interventions: Experimentation and finite element study,” *Buildings*, vol. 10, no. 3, pp. 1–13, 2020, doi: 10.3390/buildings10030057.
- [14] R. A. Silva, D. V. Oliveira, T. Miranda, N. Cristelo, M. C. Escobar, and E. Soares, “Rammed earth construction with granitic residual soils: The case study of northern Portugal,” *Constr. Build. Mater.*, vol. 47, no. May 2020, pp. 181–191, 2013, doi: 10.1016/j.conbuildmat.2013.05.047.
- [15] L. Miccoli, D. V. Oliveira, R. A. Silva, U. Müller, and L. Schueremans, “Static behaviour of rammed earth: experimental testing and finite element modelling,” *Mater. Struct. Constr.*, vol. 48, pp. 3443–3456, 2015, doi: 10.1617/s11527-014-0411-7.

- [16] L. Raju and B. V. V. Reddy, "Influence of layer thickness and plasticizers on the characteristics of cement-stabilized rammed earth," *J. Mater. Civ. Eng.*, vol. 30, no. 12, pp. 1–10, 2018, doi: 10.1061/(ASCE)MT.1943-5533.0002539.
- [17] DCHS, *Typology study on Bhutanese rammed earth buildings*. Thimphu: Division for Conservation of Heritage Sites, Department of Culture, Ministry of Home and Cultural Affairs, Royal Government of Bhutan, 2017.
- [18] M. Gernot, *Building with Earth: Design and Technology of a Sustainable Architecture*, Birkhauser. Basel, Berlin, Boston: Birkhäuser – Publishers for Architecture, 2006.
- [19] P. A. Jaquin, C. E. Augarde, D. Gallipoli, and D. G. Toll, "The strength of unstabilised rammed earth materials," *Geotechnique*, vol. 59, no. 5, pp. 487–490, 2009, doi: 10.1680/geot.2007.00129.
- [20] Q. B. Bui, J. C. Morel, S. Hans, and P. Walker, "Effect of moisture content on the mechanical characteristics of rammed earth," *Constr. Build. Mater.*, vol. 54, pp. 163–169, 2014, doi: 10.1016/j.conbuildmat.2013.12.067.
- [21] N. Yuasa *et al.*, "Study on earthquake resistance technology of composite masonry buildings in Bhutan, Part 2: Material strength of rammed earth.," in *Summaries of technical papers of Annual Meeting, Architectural Institute of Japan, Structures-IV*, 2018, pp. 905–906.
- [22] V. Maniatidis and P. Walker, "A review of rammed earth construction," in *Developing rammed earth for UK housing*, 2003.
- [23] M. Pang, S. Yang, and Y. Zhang, "Experimental study of cement mortar-steel fiber reinforced rammed earth wall," *Sustainability*, vol. 4, pp. 2630–2638, 2012, doi: 10.3390/su4102630.
- [24] ASTM Standard E8/E8M, "Tension Testing of Metallic Materials," *ASTM International*. 2016, doi: 10.1520/E0008\_E0008M-16A.
- [25] ASTM C165-07, "Standard Test Method for Measuring Compressive Properties of Thermal Insulations," *ASTM Int.*, 2011, doi: 10.1520/C0165-07R12.2.

- [26] C. H. Kouakou and J. C. Morel, “Strength and elasto-plastic properties of non-industrial building materials manufactured with clay as a natural binder,” *Appl. Clay Sci.*, vol. 44, no. 1–2, pp. 27–34, 2009, doi: 10.1016/j.clay.2008.12.019.
- [27] A. W. Bruno, D. Gallipoli, C. Perlot, and J. Mendes, “Mechanical behaviour of hypercompacted earth for building construction,” *Mater. Struct. Constr.*, vol. 50, no. 160, 2017, doi: 10.1617/s11527-017-1027-5.
- [28] Q. B. Bui and J. C. Morel, “First exploratory study on the ageing of rammed earth material,” *Materials (Basel)*, vol. 8, pp. 1–15, 2015, doi: 10.3390/ma8010001.
- [29] G. S. Pavan, S. N. Ullas, and K. S. Nanjunda Rao, “Shear behavior of cement stabilized rammed earth assemblages,” *J. Build. Eng.*, vol. 27, 2020, doi: 10.1016/j.jobbe.2019.100966.
- [30] J. S. J. Cheah, P. Walker, A. Heath, and T. K. K. B. Morgan, “Evaluating shear test methods for stabilised rammed earth,” *Proc. Inst. Civ. Eng. Constr. Mater.*, vol. 165, no. 6, pp. 325–334, 2012, doi: 10.1680/coma.10.00061.
- [31] T. T. Bui, Q. B. Bui, A. Limam, and J. C. Morel, “Modeling rammed earth wall using discrete element method,” *Contin. Mech. Thermodyn.*, vol. 28, no. 1–2, pp. 523–538, 2016, doi: 10.1007/s00161-015-0460-3.
- [32] DIANA. Fea, *DIANA Documentation*. 2019.
- [33] T. L. Bui, T. T. Bui, Q. B. Bui, X. H. Nguyen, and A. Limam, “Out-of-plane behavior of rammed earth walls under seismic loading: Finite element simulation,” *Structures*, vol. 24, pp. 191–208, 2020, doi: 10.1016/j.istruc.2020.01.009

*This chapter is written with reference to author's published paper titled "Assessment of out-of-plane behaviour of rammed earth walls by pull-down tests", 2019 [1], "Strengthening of rammed earth structures with simple interventions", 2020 [2], "Strengthening strategies for existing rammed earth walls subjected to out-of-plane loading", 2020 [3], and "In-plane shear resistance between the rammed earth blocks with simple interventions: experimentation and finite element study", 2020 [4]*

#### **4.1 Introduction**

The analysis of damages observed on rammed earth buildings after the earthquake events [5,6], has shown that the rammed earth wall fails by overturning outward. When the walls are slender, the out-of-plane failure mode dominates the structures. In most cases, such failure occurs without deformation, but the part of the structure separates from the rest and falls down. One or more wall detaches from the orthogonal walls losing its original configuration, which clearly shows the role of orthogonal walls as bracing elements as high importance. The out-of-plane failure can be classified into various type depending on the failure mechanism, as already discussed in Chapter 2. The literature is rich in studies contributing to behaviour of rammed earth wall under in-plane loading but the literature discussing the behaviour of rammed earth wall under out-of-plane loading is limited [1-3, 8-11]. So, this chapter will discuss the out-of-plane behaviour of rammed earth wall through the pull-down test in which the loading is statically applied in out-of-plane direction. Furthermore, the chapter also presents the in-plane shear test conducted on the 600 mm wall and the effect of RC dowels in improving the shear strength of rammed earth wall.

Several studies have been carried out on strengthening measures to improve the seismic performance of existing rammed earth structure. For examples, it includes using flax-fiber reinforcement [12], polyester fabric strips [13], cement mortar-steel fiber reinforcement [14], and canvas and tarpaulin as externally bonded fibers [5, 14]. All these strengthening measures were carried out for the undamaged walls. In the field of new construction techniques, Hamilton et al., 2006 [8] proposed use of the post-tensioned vertical rebar and Zhou et al., 2019 [10] used a thinner

section of reinforced concrete columns and beams. In both these studies, the reinforcements are embedded within the rammed earth wall, and the test results have shown their effectiveness in strengthening the rammed earth wall. Despite the availability of literature in improving the strength for both new and existing rammed earth, the discussion on the effectiveness of strengthening technique in out-of-plane is limited.

Furthermore, some of the strengthening technique proposed in the above studies cannot be applied to the rural homes of Bhutan mainly because some proposed measures are non-affordable while some materials are locally not available and not feasible. Therefore, feasible strengthening techniques are proposed, which is simple, cost-effective and material are available in the local market. In total, four strengthening techniques are chosen, two for new construction and another two for retrofitting purposes. The feasibility and effectiveness of the chosen strengthening techniques are examined through the pull-down test of one-storied full-scale wall.

The strengthening of the floor diaphragm and the interaction of the floor rigidity has not been discussed before. Therefore, another set of pull-down test is carried out for two-storied full-scale wall to assess the out-of-plane behaviour of rammed earth structures with floor beams. Apart from strengthening the rammed earth wall, a simple anchorage system for floor beams is also proposed to enhance the floor rigidity.

As a part of pull-down test, in-plane shear resistance between rammed earth blocks is also assessed. Here, the author intends to understand the in-plane shear characteristics of RE while assessing RC dowels' effects in strength increment within the RE blocks. In addition to this, the work also tries to analyze the effect of RE layer thickness on RE's strength characteristics.

## **4.2 Out-of-plane behaviour of rammed earth wall and their possible strengthening strategies**

### **4.2.1 Specimens and Materials**

Five rammed earth specimens were constructed by local masons using the soil from a nearby site. One of the walls was constructed without any strengthening measures as a reference wall representing the actual houses without seismic resilient features. Two of the specimens were reinforced with two different methods. Two other walls were constructed without reinforcement like the reference wall, but they were later strengthened with two different strengthening schemes. Based on their strengthening methods, the five walls were named as follows:

- a) One storied Unreinforced RE wall / Reference wall (U-RE)
- b) Mesh-wrap retrofitted RE wall (Mesh-RE)
- c) Timber frame retrofitted RE wall (Timber-RE)
- d) Reinforced RE wall with RC wedges and RC dowels (New-RE-A)
- e) Reinforced RE wall with RC wedges, RC posts and RC band (New-RE-B)

The details of each specimen are described in the following sections with the details on strengthening methods.

#### 4.2.1.1 Unreinforced Rammed Earth: Reference Wall

The unreinforced rammed earth wall (U-RE) was constructed following the construction procedure practised in Bhutan. The details of the dimension and configuration of U-RE wall considered for the test is presented in Figure 4.1. The wall had a total of five blocks in vertical, where each block had 600 mm thick in height. The wall's configuration follows the typical typology of traditional Bhutanese house where the first floor has a solid wall, and the second floor has a large opening in the front façade. In the present wall sample, first two layers' block represented the first floor, and three other blocks above them represented the second floor. Locally available red clay with small pebbles was used for the rammed earth wall construction. Before the construction of

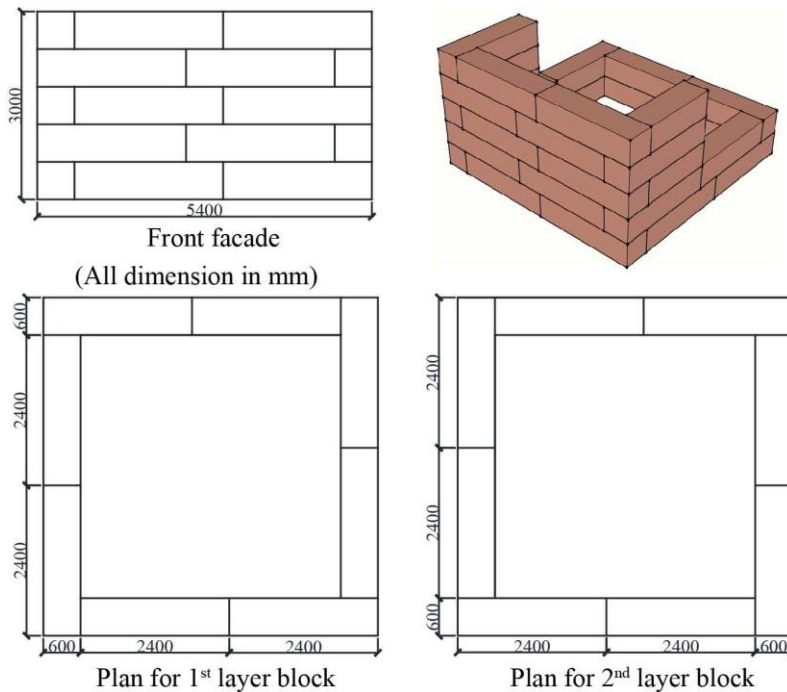


Figure 4.1 Details of U-RE.



rammed earth wall, a stone foundation is laid as generally seen in the traditional houses to avoid water ingress to the main wall. The process of construction is illustrated in Figure 4.2. The first step includes the installation of wooden formwork, as shown in Figure 4.2(a). The formwork consisted of i) shutter planks on both sides, ii) horizontal joining members on top and bottom, iii) vertical members to connect the shutter planks and horizontal members. Wedges were also inserted between the vertical members and shutter planks to keep the formwork stable, thus preventing wall bulging. This single formwork section gave a rammed earth block of around 250 cm length, 60–70 cm height and 60 cm thickness. Next, soil/red clay, brought on bags, was poured inside the space within the formwork, followed by manual ramming using ramming tools. The ramming usually lasted 30 minutes to 1-hour to complete one block. The final finished block looked smooth and shiny, indicating the sufficient hardness achieved. One block consisted of five layers, as shown in Detail A of Figure 4.2(c). Here, approximately 240 mm of soil was compacted to 120 mm for a single layer. After completing each section or block, the formwork was removed immediately and re-installed to construct the next section of the wall. Figure 4.2(c) shows the completion of the 1<sup>st</sup> block level. To prepare for the next block layer, a section from the lower block's top surface was cut to fit the bottom horizontal members of the formwork, as seen in Figure 4.2(d). And the process of installation of formwork and ramming the clay is repeated till the completion of specimen.

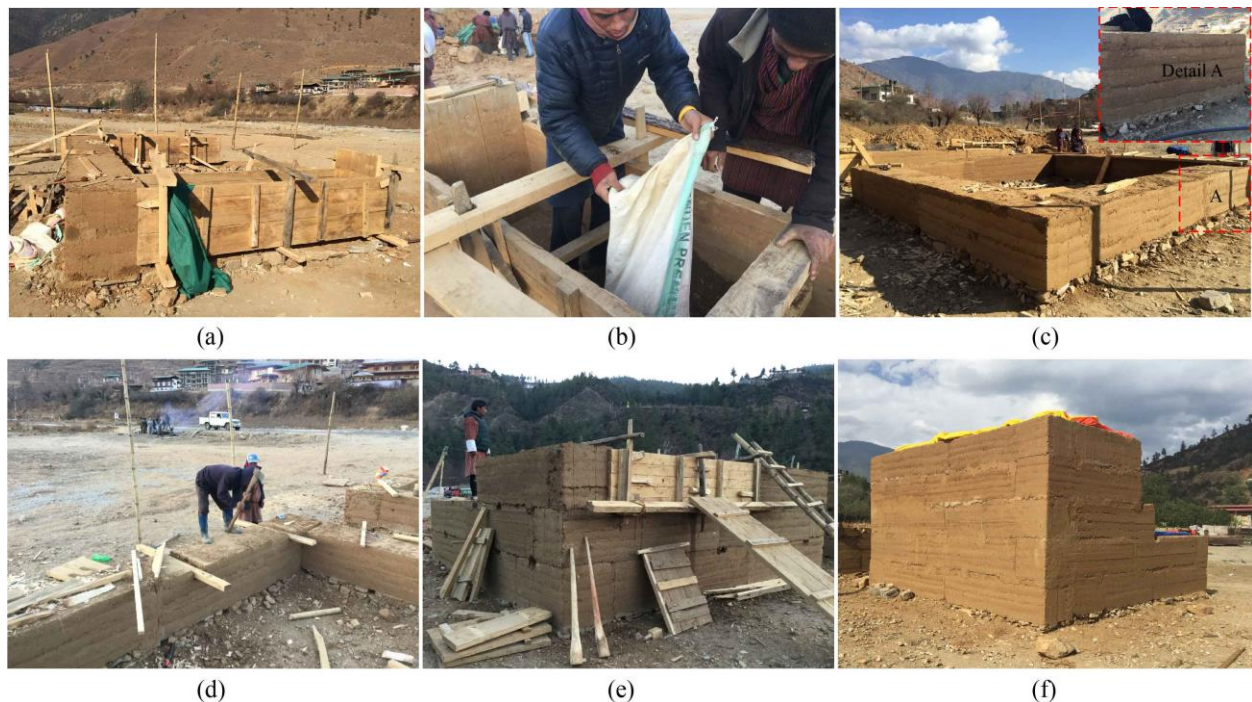


Figure 4.2 Construction process details of U-RE.

The blocks in corners were placed alternatively to avoid continuous head joint between the two rammed earth blocks. The sequence for placing the first layer block and the second level block is presented in Figure 4.1. This alternative arrangement of the block can be seen in Figure 4.2(e) as well as in Figure 4.2 (f) of the completed specimen. The grain size distribution for the soil used for the construction of the specimen is shown in Figure 4.3 with a particle size range of 0–10 mm. The construction of the test specimen was completed in January and tested in May after a drying period of four months. During drying, the test specimen was covered on top with tarpaulin to protect against snow and rain.

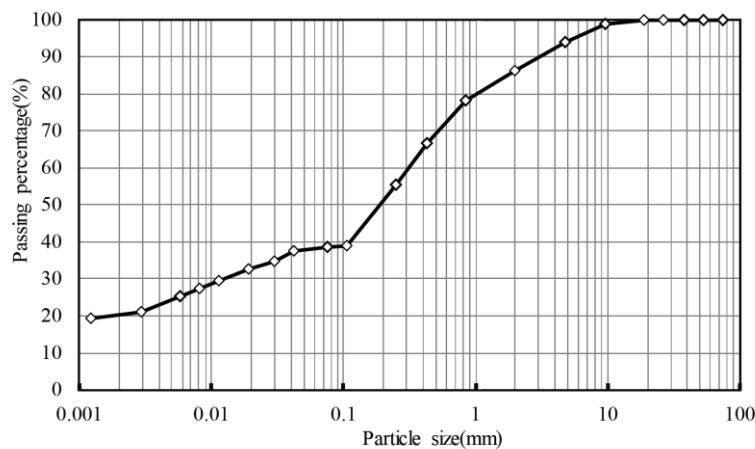


Figure 4.3 Grain size distribution of the soil used for specimens.

#### 4.2.1.2 Retrofitted Rammed Earth: For Existing Buildings

This section describes the two types of possible retrofitting techniques solely meant for the existing buildings. However, it should be noted that the proposed retrofitting technique here is provided for the new walls, and not for the damaged wall. Also, since the experimental was carried out in Bhutan, the retrofitting techniques were chosen based on the following guidelines:

- i) the materials are readily available within the local market;
- ii) the proposed retrofitting techniques are within the 20% of the actual cost of unreinforced rammed earth; and
- iii) the proposed technique is simple so that it can be constructed by the local artisans.

The two types of retrofitting techniques are described in detail in the following section.

#### 4.2.2.1 Mesh-wrap retrofitting (Mesh-RE)

The retrofitting technique is similar to the one presented in Chapter 3 for the element test. However, since this experimental program was conducted in Bhutan, the material selection was purely based on the availability in the local market. Therefore, the mesh sizes used here are slightly heavier than those used for element test; the details are described in the following.

##### *Retrofitting materials*

##### *Mesh*

After conducting a thorough market survey, a mesh with 16 gauge ( $\phi 1.5$  mm) was chosen as retrofitting material. It had a square pitch of 30 mm. The mechanical properties of the mesh used were derived on two samples, following the ASTM E8 2016 standards [15]. Figure 4.13(a) presents the test setup and Figure 4.13(b) presents the relationship between stress and time obtained from the test results. The mesh steel mesh has the yield and fracture stress of 355 MPa and 425 MPa, respectively.

##### *Plaster*

The covering to the mesh was provided with the mud plaster having cement mud ratio 1:4. The primary purpose of using stabilized mud plaster was to have a minimal visual impact on the rammed earth wall (Stabilized mud mortar looks like mud mortar at an instant glance).

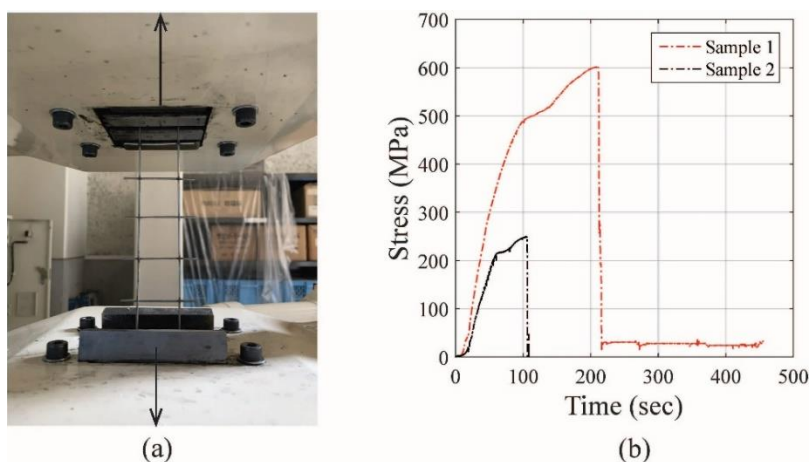
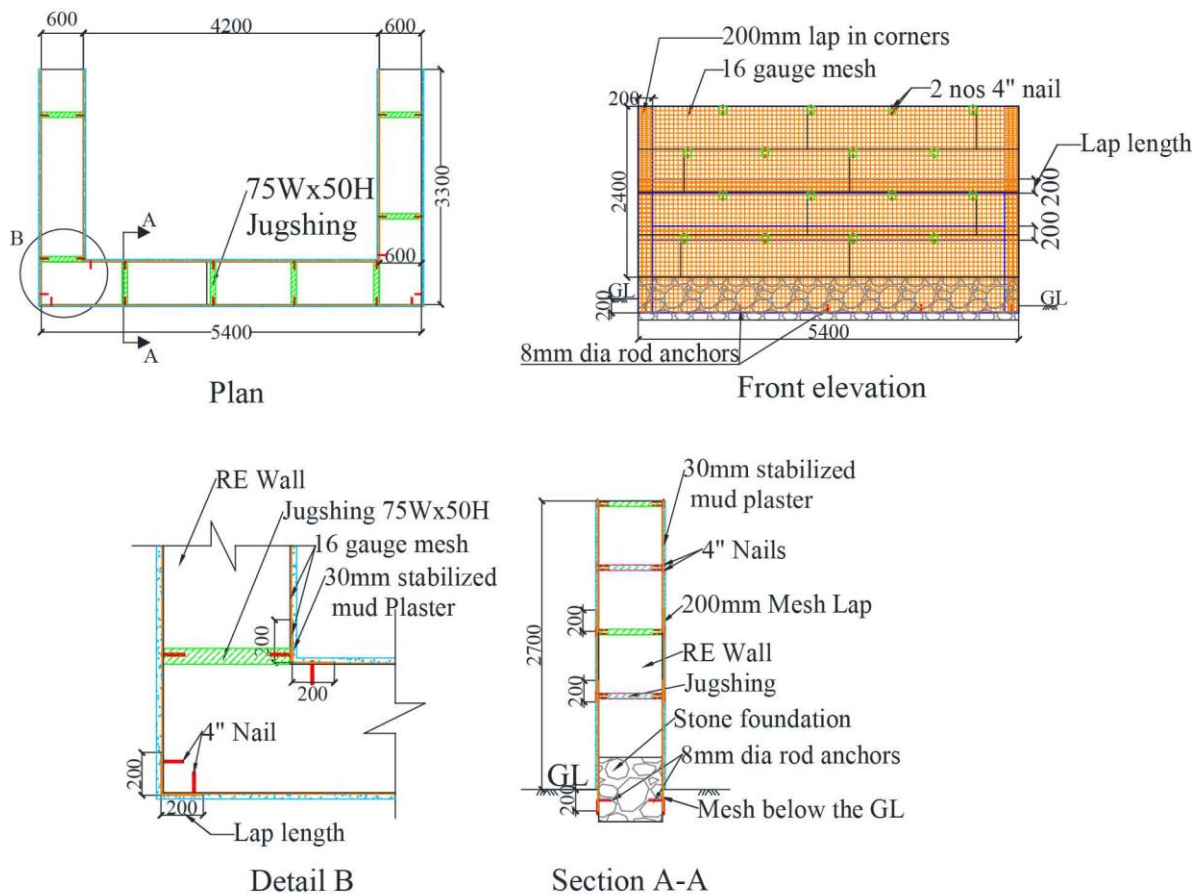


Figure 4.4 Material test: (a) test setup; (b) test results.

##### *Construction process*

Firstly, a U-shaped wall was constructed having the same configuration and dimensions as in case of New-RE. Even for this specimen, the soil properties are the same as reported for the

unreinforced RE wall. Also, the construction follows the same procedures as in the case of the unreinforced specimen (U-RE). The construction of the specimen was completed in the second week of July 2018. The wall was then kept undisturbed for two weeks for drying. The retrofitting work began precisely after two weeks. Figure 4.5 presents the retrofitted rammed earth specimen (Mesh-RE) details, showing the details and location of mesh and connectors. The retrofitting work was performed by placing mesh on both inside and outside faces of the wall. Figure 4.6(a) shows the specimen during the mesh layout. The meshes also covered the foundation, 430 mm from the ground level as detailed in Figure 4.5. To have these meshes at two face of the wall connected, a shear connector was required. In element test under Chapter 3, screws were provided.



ALL DIMENSIONS ARE IN MM

Figure 4.5 Details of mesh-wrap retrofitted rammed earth specimen (Mesh-RE).

But in this case, they were connected by the timber component (600 L x 75 W x 50 H) and nails (Figure 4.6(b)). It should be noted that the timber was inserted inside the hole before the mesh layout. As already mentioned in the previous section, the holes were created upon removing the

*jugshings* (lower horizontal member of formwork). To avoid local failure at the mesh joints, a lapping length of 200 mm was provided both in the horizontal and vertical direction. Before applying the mortar, the wall was adequately moistened with water, and dry cement powder was sprayed as illustrated in Figure 4.6(c). The final retrofitting work included plastering 30 mm thick stabilized mud plaster (1cement:4mud) over the mesh, as shown in Figure 4.6(d). The retrofitting work was completed in August 2018. The specimen was then allowed for curing for approximately one month after the mesh retrofitting work.

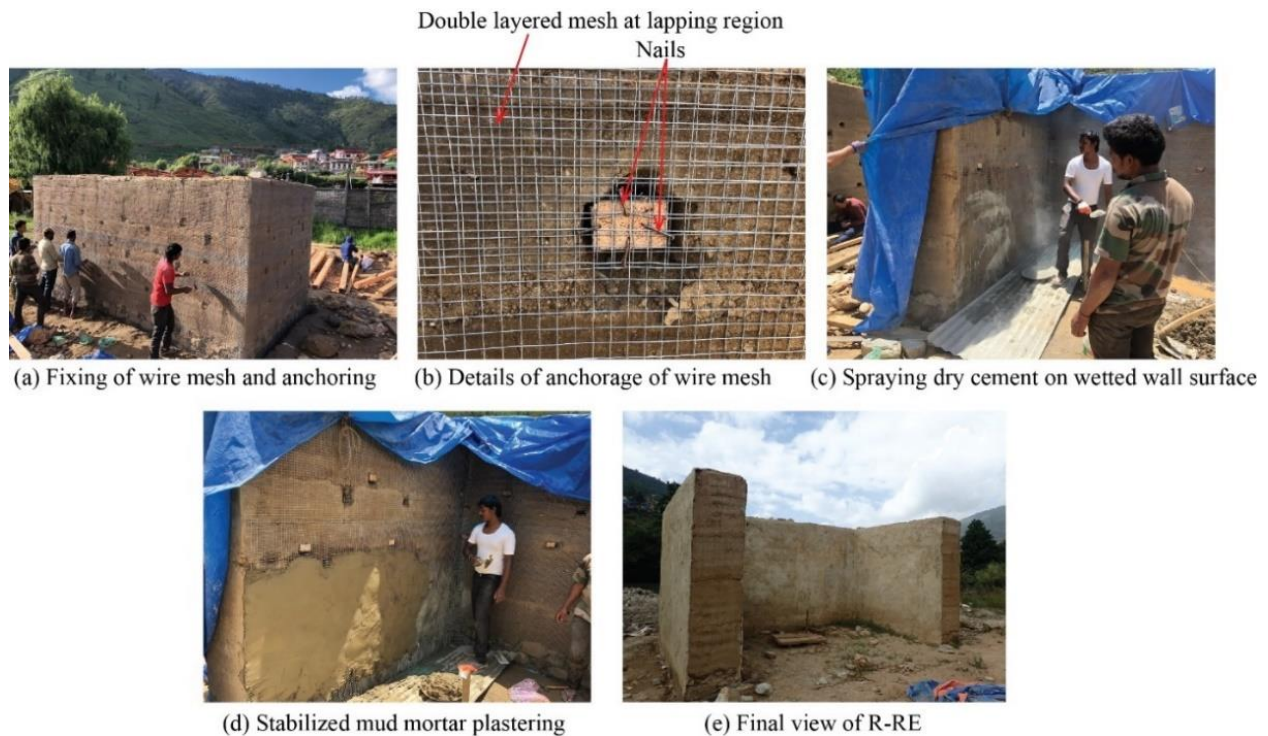


Figure 4.6 Construction details of retrofitted rammed earth specimen (Mesh-RE).

#### 4.2.2.2 Timber frame retrofitting (Timber-RE)

##### *Retrofitting material*

A timber frame consisting of vertical, horizontal and transverse members was used to retrofit the rammed earth wall, details in Figure 4.7(a). The vertical and horizontal members were installed on both faces of the wall, and they were connected by the transverse members forming a confined frame, as shown in Figure 4.7(b). The intersection of these members was joined by a timber wedge, as detailed in Figure 4.7(c). The proposed retrofit strategy increases the wall stiffness and strength for both in-plane and out-of-plane directions using vertical and horizontal timber elements installed on both faces, forming a confined frame.

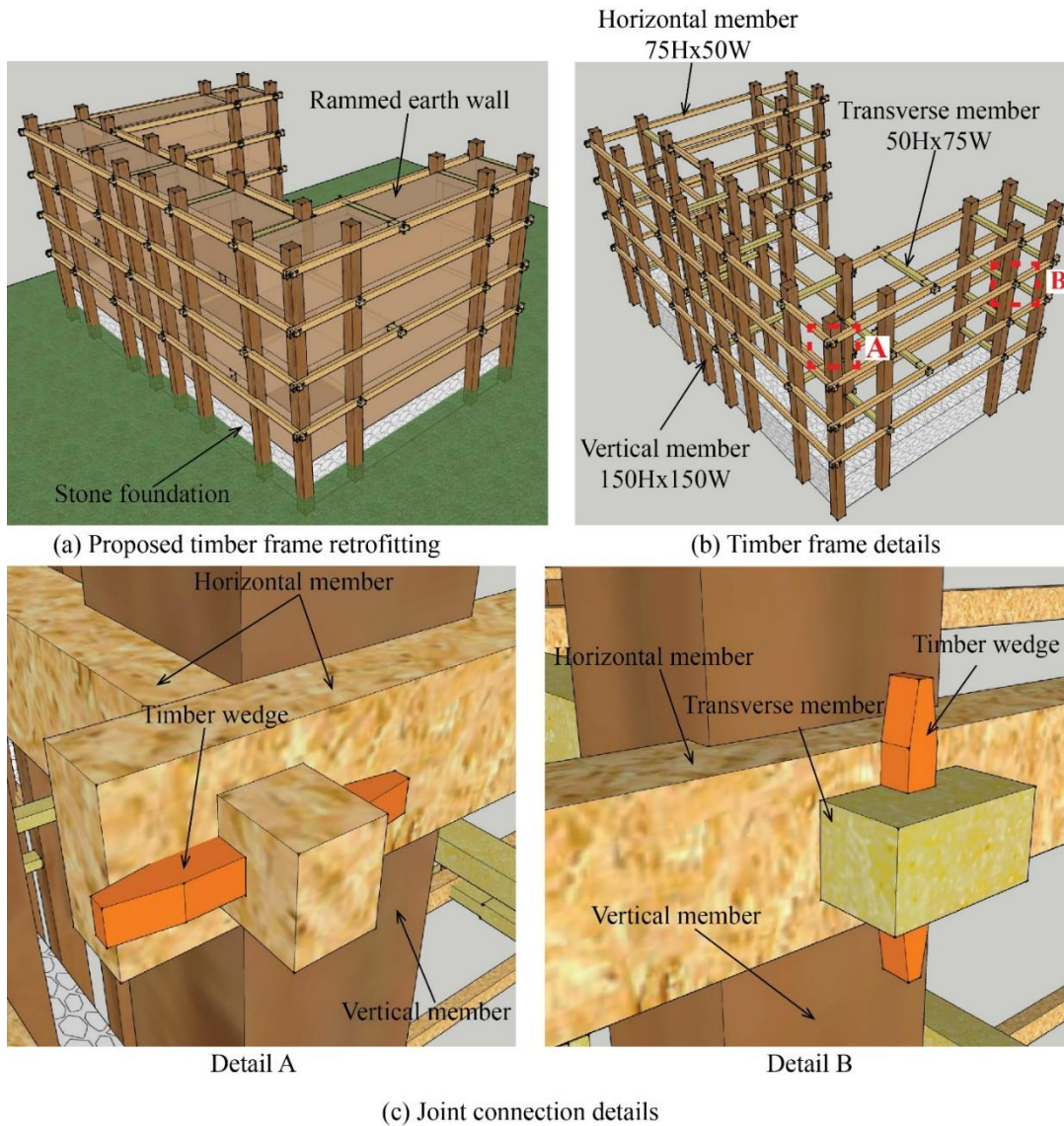


Figure 4.7 Details of timber frame retrofitting method.

### ***Construction process***

The specimen was first constructed following the same procedure described for U-RE. It also had the same material properties as the rest of the specimens. The retrofitting works were later carried out after the completion of the specimen. The retrofitting work included preparation of timber members and joineries, as seen in Figure 4.8(a). Firstly, vertical members were installed on both faces of the wall (Figure 4.8(b)), and later horizontal members were fixed over it, forming a frame-like system. Transverse members then connected these frames at both faces of the wall. The *jugshig* holes made it possible to insert the transverse members across the wall's cross-section, connecting the outer and inner frames. The intersection of these members was confined by a timber

wedge (Figure 4.8(c)). The view of the specimen after timber frame retrofitting is present in Figure 4.8(d).

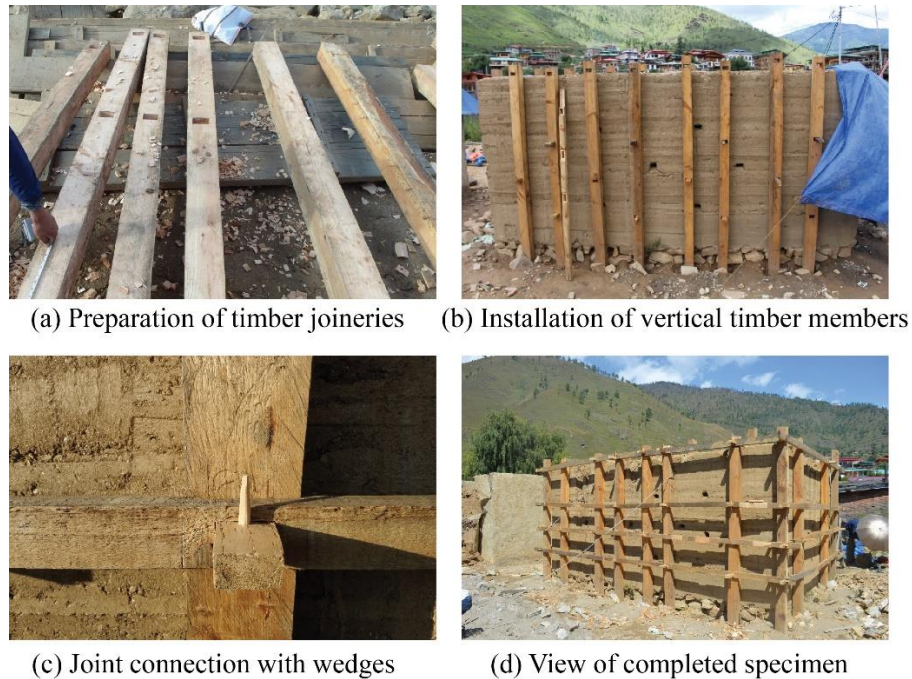


Figure 4.8 Construction details of Timber-RE.

#### 4.2.1.3 Reinforced Rammed Earth: For New Construction

This particular specimen was constructed aiming solely for the new construction to assess the possibility of reinforcing them with the reinforced concrete structures. Two reinforcing method are chosen:

- i) Method A: Reinforced with RC wedges and RC dowels
- ii) Method B: Reinforced with RC wedges, RC post and RC band

The specimen reinforced with method A is named “New-RE-A” and the one reinforced with method B is named “New-RE-B”. The details of each specimen and the reinforcing method used are discussed in the following section.

##### **Method A: RC wedges and dowels (NEW-RE-A)**

This specimen was constructed together with the unreinforced specimen (U-RE) having the same geometry with the same soil properties used for the unreinforced specimen (U-RE). It was also constructed by the same masons.

### Strengthening components

Two strengthening components were used here:

- i. RC wedges: They were precast on-site with M20 grade concrete before the wall construction. It was used to connect RE blocks in horizontally.
- ii. RC dowels: They were also precast with M20 grade concrete before the construction. It was used to connect the RE blocks vertically.

The RC wedges and RC dowels were introduced in between the blocks to improve the wall's integrity. The details of RC wedges and RC dowels are presented in Figure 4.9. The figure also presents the details of their placement on the wall. Such strengthening measures are inspired by the indigenous reinforcing method by placing horizontal reinforcement members like timber and flat stone over the joint blocks to avoid a vertical crack in weak areas like holes created by removal of Jugshing (Figure 4.10). A similar strengthening technique with floor anchorage system where wooden floor joist are anchored to the rammed earth wall is described in details elsewhere [4].

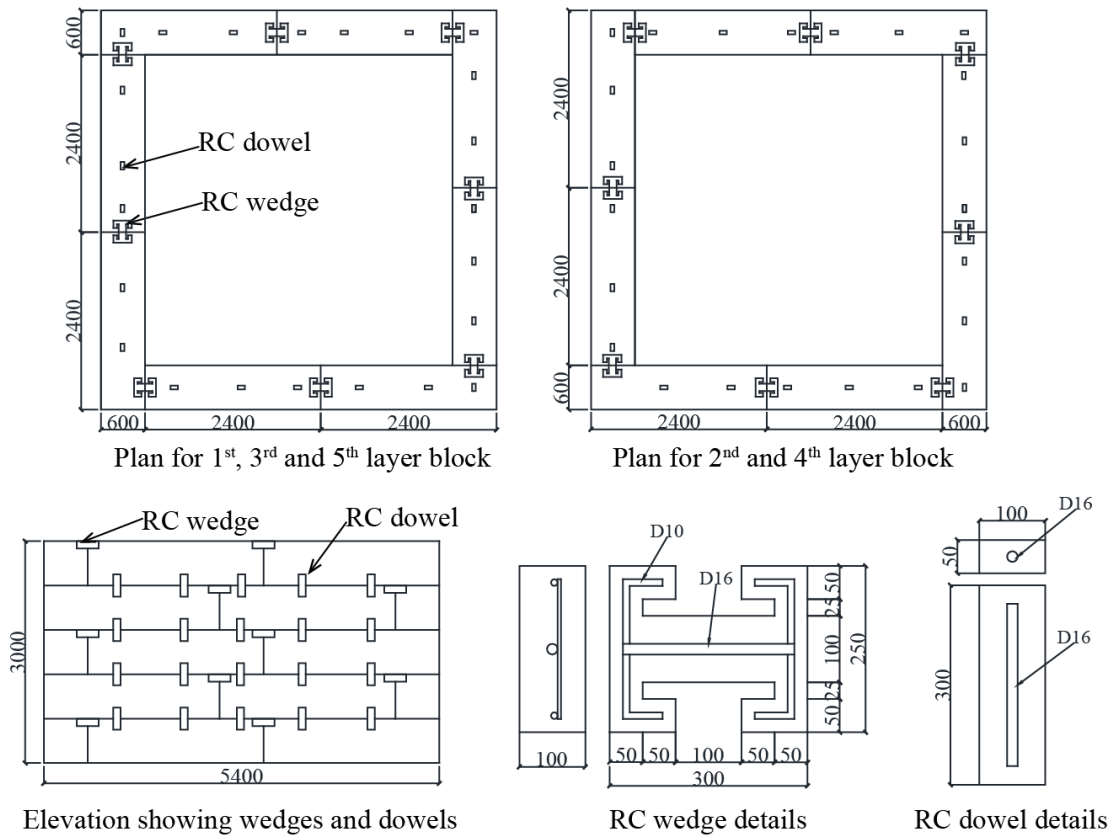


Figure 4.9 Details of reinforced rammed earth specimen of New-RE-A.





Figure 4.10 Reinforcing method practised in vernacular buildings in Bhutan.

### *Construction process*

The rammed earth wall's construction method is similar as already discussed for the unreinforced specimen (U-RE) in section 4.2.1. However, in the current specimen (New-RE-A) involved placing the RC elements during the wall construction. After completing one block and before constructing the next block, a hole was bored on the completed block to fit RC wedges and RC dowels. Figure 4.11(a) shows the borrowing the hole for RC dowel. RC wedges were fully embedded inside the block while the RC dowels were embedded half of its height, as seen in Figure 4.11(b). Next block was rammed over it, so it connected lower and upper block together. This

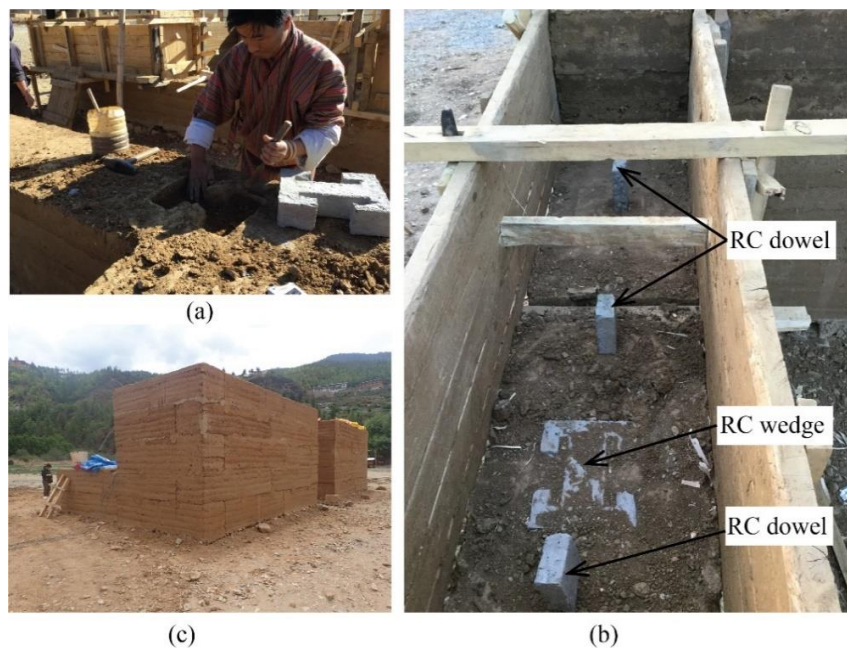


Figure 4.11 Construction details of New-RE-A.

completion can be seen in Figure 4.11(c). It is clear from Figure 4.11(c) that the blocks at the corners are interwoven, avoiding continuous head joint through the height. This ensures to prevent the corner cracks, which is usually found in the rammed earth walls. The same has been followed throughout the cross-section.

**Method B: RC post, RC wedges and RC band (NEW-RE-B)**

The specimen was constructed with the same soil properties used for the construction of the unreinforced specimen. However, the geometry of the current specimen is slightly modified from the previous specimens U-RE and New-RE-A. The wall has a U-shaped configuration, the front wall represent the main longitudinal wall, and two side walls represent the transverse wall. The wall has 5.4 m length, 2.4 m height and 0.6 m thickness, the average thickness found in traditional rammed earth houses in Bhutan. The wall consists of four layers of the block with each block having dimension 2.4 m length, 0.6 m height and 0.6 m thickness. Furthermore, within the block constituted five-layer having thickness ranging from 0.11-0.13 m. The details of the reinforced rammed earth specimen (New-RE-B) is presented in Figure 4.12, showing the reinforcing RC elements.

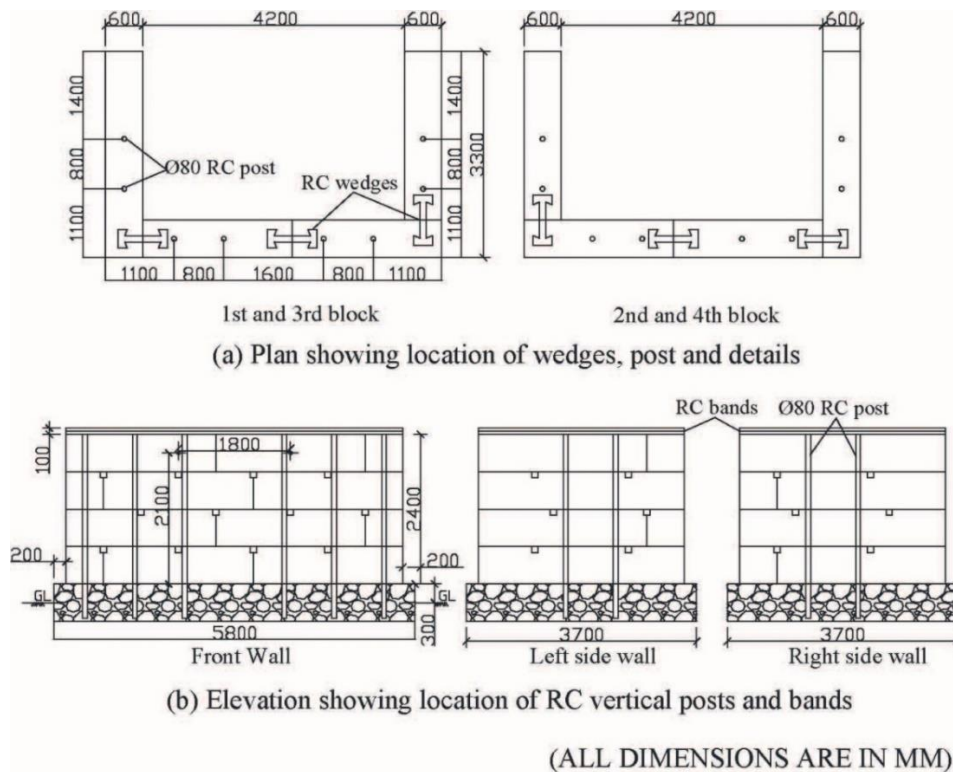


Figure 4.12 Details of reinforced rammed earth specimen (New-RE-B).

### Strengthening components

Three possible strengthening measures are incorporated, whose details are described below:

- i. Reinforced concrete post (RC post): The RC post was provided from foundation base till the top of the wall. The sole purpose in providing RC post was to connect all blocks together in a vertical direction. They were casted on site along with the rammed earth wall construction. The RC post had 80 mm in diameter with 16 mm rebar embedded inside. Figure 4.13 has the details of RC post and reinforcement used in it.

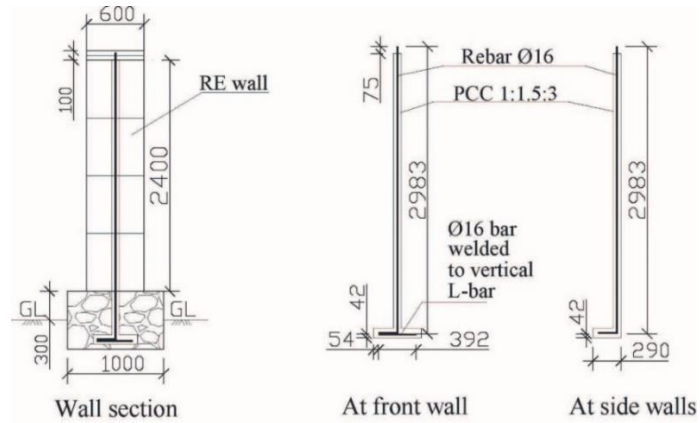


Figure 4.13 RC post and reinforcement details.

- ii. Reinforced concrete wedge (RC wedge): The rammed earth wall consists of several blocks. During an earthquake, there is a possibility to split one block from another just as in case of the rubble stone masonry. To avoid splitting, the I-shaped RC wedges having dimension 800 x 300 x 80 mm were provided at the block's joint interfaces but only in the horizontal direction. Unlike RC post, they were precast before the wall construction. The details of RC wedge are presented in Figure 4.14.

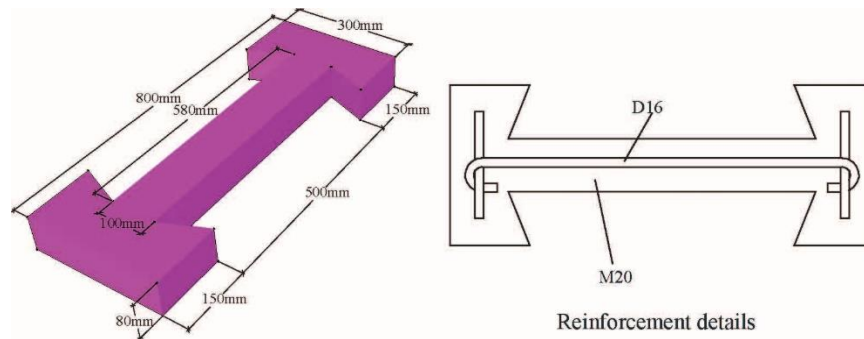


Figure 4.14 RC wedge and reinforcement details.

- iii. Reinforced concrete band (RC band): The resistance of a masonry building to lateral loads is provided by its integral box action. The building should behave like a box rather than individual walls during an earthquake. To achieve necessary box action in masonry building, RC band at plinth, lintel and roof level are recommended. This concept was replicated in the current rammed earth specimen having a U-shaped wall. The RC band was provided at the top of the wall. The band acted as a floor band integrating two side walls with the front wall and the RC post. The RC band had 600 mm width and 100 mm thickness. The detailing of the reinforcement used in the RC band is illustrated in Figure 4.15.

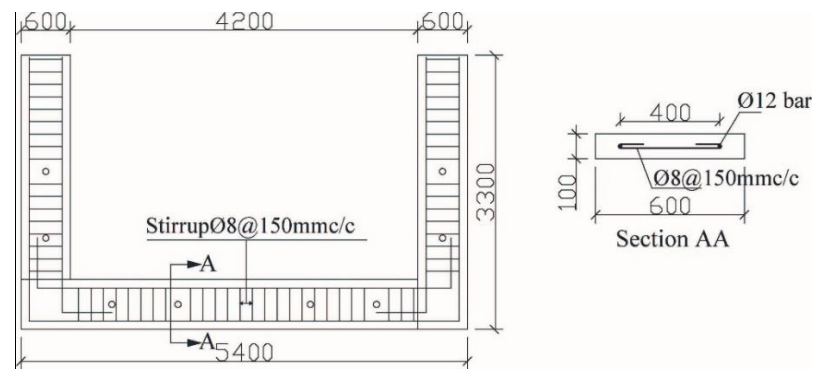


Figure 4.15 RC band and reinforcement details.

### ***Construction process***

The construction method of the rammed earth wall is similar as already discussed for the unreinforced specimen (U-RE) in section 4.2.1. However, in the current specimen (New-RE-B) involved placing the RC elements during the wall construction. Figure 4.16 highlights some of the details on the placement of RC posts, wedges and band. As in the case of the unreinforced specimen, the first step involved constructing a random rubble masonry foundation with 600 mm high and 1000 mm thickness. It should be noted that the reinforcement for RC post was already placed in its position along with the hollow pipe, which was just provided as a formwork. A plain cement concrete of (1cement:1.5sand:3aggregate) was poured from the top of the hollow pipe and compacted manually with rebar. The RC posts were casted to the foundation top. The hollow pipe formworks were removed immediately before the concrete set. Figure 4.16(a) shows the completion of the foundation with eight rebars projecting outside. The next process involved fixing the formwork for rammed earth wall, followed by ramming the first level block (Figure 4.16(b)).

The RC posts were again casted till the first block-level which again was followed by removal of pipe. The next procedure involved placing the RC wedges at every joint. To place the wedges, a hole was burrowed on the top surface of the finished RE block to precisely fit in the wedge (Figure

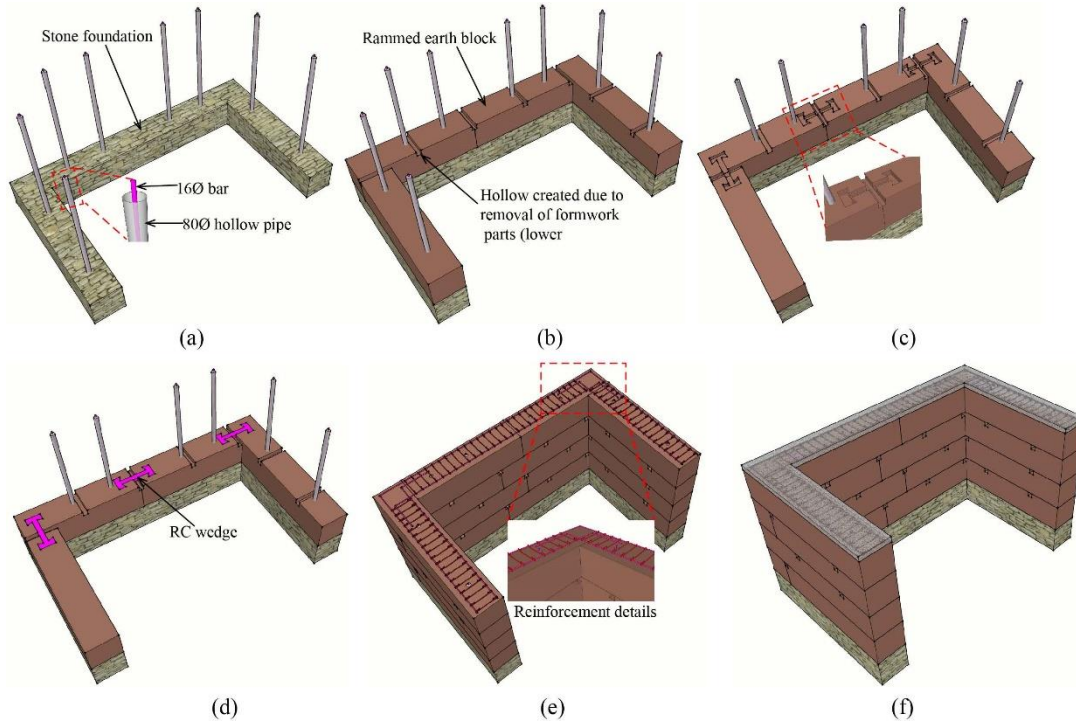


Figure 4.16 The sequence of placing strengthening components in New-RE-B.



Figure 4.17 Construction process details of New-RE-B.

4.16(c)), and this was followed by placing wedges at every joint (Figure 4.16(d)). Next, the new block was rammed over it. This process was repeated till the completion of the fourth block. Finally, reinforcements of RC band were laid (Figure 4.16(e)) followed by its casting (Figure 4.16(f)). The specimen's construction was completed on November 21, 2018, and it was tested on March 09, 2019. Figure 4.17 shows the construction process on-site.

## 4.2.3 Material Characterization

### 4.2.3.1 Rammed Earth Wall

#### *Core sampling*

In order to grasp the mechanical characteristics of the rammed earth samples, compressive and tensile strength testing was conducted on each rammed earth samples. Right after completion of the pull-down test, samples from the wall specimen were extracted using a core drill machine with a diameter 100 mm (DD120 Hilti Corporation), shown in Figure 4.18(a). Figure 4.18(b) shows the coring of sample from unreinforced rammed earth wall (U-RE). It can be observed from the figure that the direction of extraction was parallel to the rammed earth layer. At least six samples were extracted from each wall specimens, three each for compression and tension testing. The extracted



Figure 4.18 Sample collection for the material test.

specimens were around 100 mm in diameter, with the height ranging from 150 mm to 200 mm. A judgement was made on the suitability of samples to be used for compression and tensile testing based on their length and surface crack. The longer specimens, whose length was twice its diameter, were used for compressive strength testing while the shorter ones were used for tensile strength testing. The samples were irregular in shape due to processing difficulties on site; therefore, samples were firstly trimmed (Figure 4.18(c)) to ensure flat surface at both top and bottom of the specimen, the surfaces were further capped with white cement plaster (Figure 4.18(d)). All samples were capped to have a smooth contact surface at both ends.

### ***Test setup***

Figure 4.19(a) presents the tensile strength testing set up, and Figure 4.19(b) presents the test set up for compressive strength testing. The splitting tensile strength and compressive strength test on cylindrical rammed earth specimens were conducted according to the ASTM C496 [17] and ASTM C39 [18], respectively. The test was carried out in Bhutan Standard Bureau (BSB). For the tensile test, the specimen was placed in the universal testing machine, and the loading was in a direction perpendicular to the rammed earth layers. Here, the applied load was measured through the high accuracy compressive load cell (KCM-20KNA, Tokyo Sokki Kenkyujo Co., Ltd.), which was then recorded in a multi-channel dynamic strainmeter DS-50A with LAN interface setting (Figure

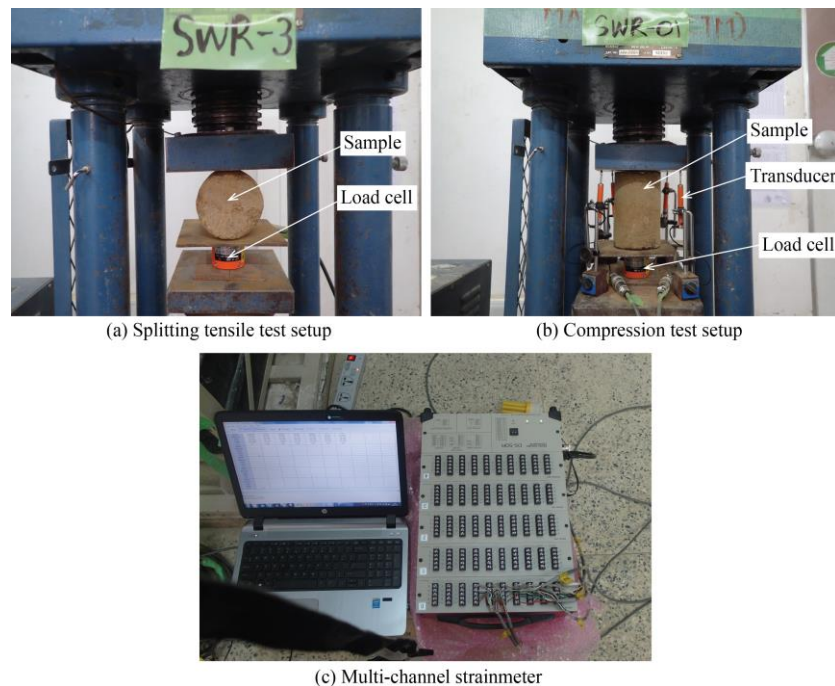


Figure 4.19 Material test setup and instrumentation.

4.19(c)). For the compressive strength testing, the applied load was measured using a compressive load cell with a higher capacity (KCM-200KNA, Tokyo Sokki Kenkyujo Co., Ltd.). The vertical displacement was recorded by four high-sensitive transducers (CDP-10MT, Tokyo Sokki Kenkyujo Co., Ltd.), placed at four corners.

### Results

Table 4.1 shows the summary of test results from material testing for all three rammed earth wall specimens. The test results show that the New-RE samples have higher compressive strength despite made of same material composition. The variation could have been affected by the ramming process involved and the place from where the samples are being extracted. The tensile strength of New-RE and R-RE are found same with strength value 0.17 MPa; however, the tensile strength of U-RE is found very low. Table 4.2 presents the mechanical characteristics of RE that are previously reported. It is noted that the mechanical reported in the thesis is comparatively lower than those reported in Table 4.2. Here, so many factors could have influenced the mechanical characteristics, for example, the grain size distribution of the soil, the ramming process and moisture content during the test. The relationship between material properties like density and young's modulus against compressive and tensile strength are presented in Figure 4.20. A relationship between tensile strength and compressive strength is also presented in the same figure, where the tensile strength ( $f_t$ ) is found 15% of the compressive strength ( $f_c$ ). The failure patterns observed were similar in all the test samples. However, only a few representatives are presented in Figure 4.21(a) for tensile strength and Figure 4.21(b) for the compressive strength test. All the test samples shown in Figure 4.21 are extracted from U-RE.

Table 4.1 Material characterization of rammed earth samples.

Specimen Type	$\rho_b$ (kg/m <sup>3</sup> )		$f_c$ (MPa)		$f_t$ (MPa)		$E$ (MPa)	
	Avg.	Std. dev.	Avg.	Std. dev.	Avg.	Std. dev.	Avg.	Std. dev.
U-RE	2033	282.79	0.52	0.14			22.34	20.45
New-RE-A	1840.1	75.08	0.41	0.04	0.07	0.01	37.69	15.39
New-RE-B/Timber-RE	2045.2	20.4	1.24	0.18	0.15	0.04	351.27	43.08
Mesh-RE	1925.9	19.2	0.68	0.05	0.17	0.01	358.27	22.21

$\rho_b$  - density;  $f_c$  - Compressive strength;  $f_t$  - Tensile strength;  $E$  - Young's modulus.



Table 4.2 Reported mechanical characteristics of rammed earth samples.

Specimen Type	$\rho_b$ (kg/m <sup>3</sup> )	$f_c$ (MPa)	$f_t$ (MPa)	$E$ (MPa)
Lilley and Robinson	1870-2170	1.8-2.0	-	-
Yamin et al.	1920	3.24	0.15	784.8
Bui and Morel	1800	1.0	-	90-105
Maniatidis et al.	1850	3.88	-	205
Miccoli et al.	-	3.73	-	4143

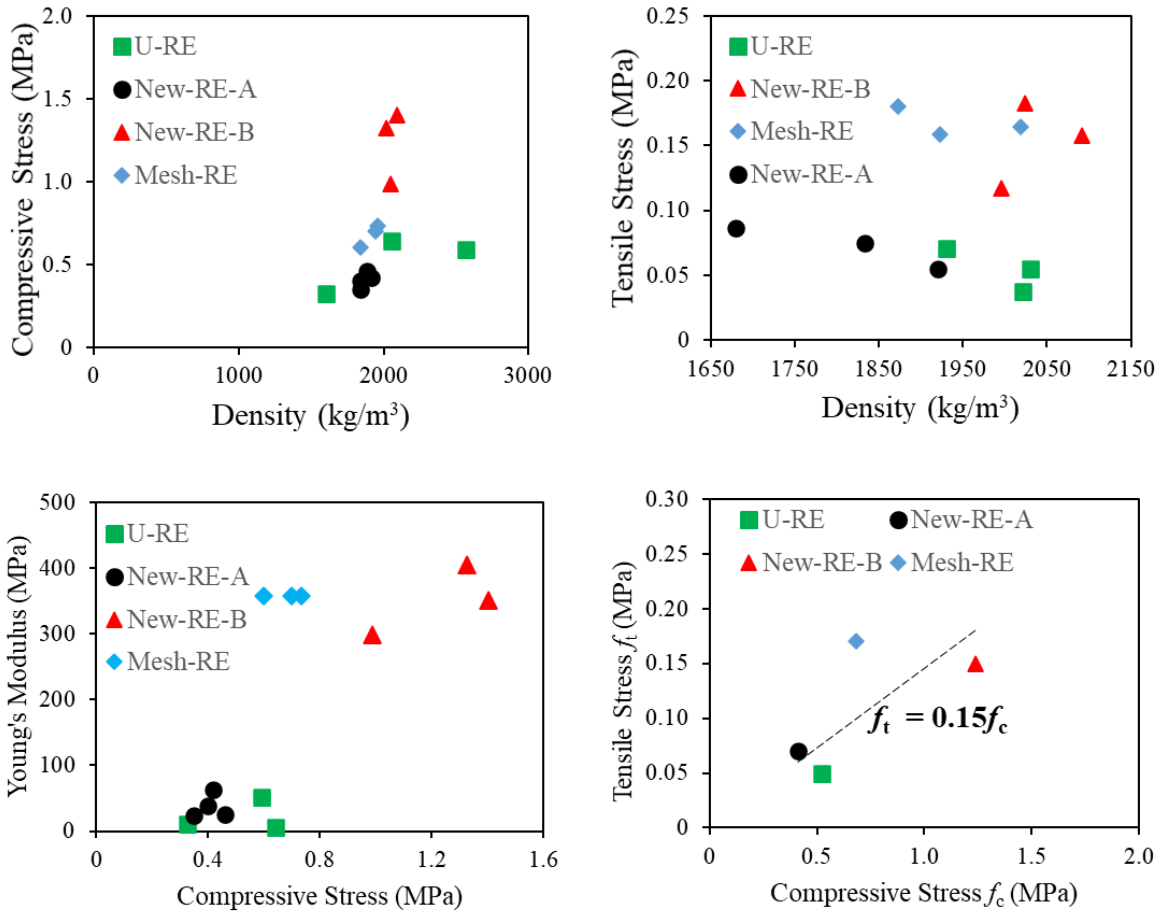


Figure 4.20 Material test results of rammed earth.

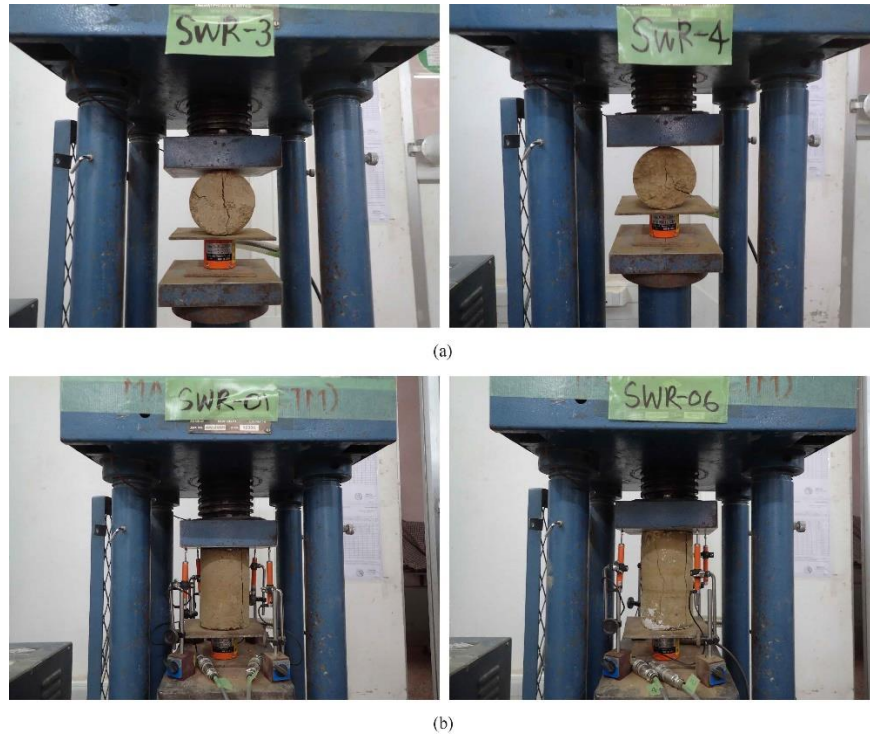


Figure 4.21 Failure patterns observed: (a) Tensile test; (b) Compression test.

#### 4.2.3.2 Plain Cement Concrete: Used in New-RE

The plain cement concrete (PCC) was used for casting RC vertical posts, wedges and band for the new rammed earth construction. As in the case of the stabilized mud mortar samples, six cylindrical samples were prepared with ratio 1 cement:1.5 sand: 3 gravel. The testing procedure was followed the same as the case of rammed earth wall samples. However, here, displacements were measured using compressometer (CM-10, Tokyo Sokki Kenkyujo Co., Ltd.) as shown in Figure 4.22. The results from the material test are presented in Table 4.3.



Figure 4.22 Test set up for material characterization of PCC.

Table 4.3 Result of a material test of PCC.

Specimen Type	Plain cement concrete		
	$\rho_b$ (kg/m <sup>3</sup> )	$f_c$ (MPa)	$E$ (MPa)
Average	2283.3	22.34	14318.46
Std. dev.	3.0	1.78	2397.26

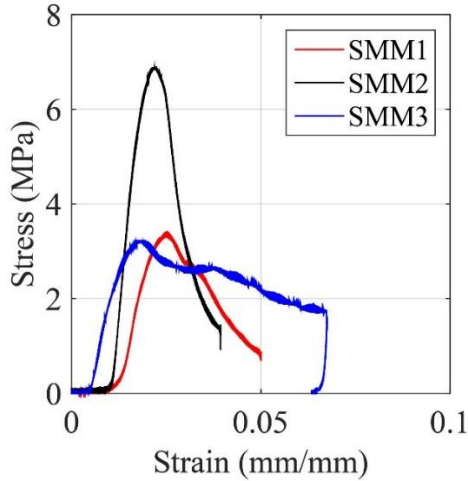
$\rho_b$  – Bulk density,  $f_c$  – Compressive strength,  $E$  – Young’s modulus

#### 4.2.3.3 Stabilized Mud Mortar: Used in Mesh-RE

The stabilized mud mortar was used as a plaster in retrofitting work for the R-RE wall. For material characterization, three cylindrical samples were prepared to have 100 mm diameter and 200 mm height using standardized moulds. The samples were tested only under compression loading. The test was carried out in Bhutan Standard Bureau. The material test set up and testing procedure followed the same as in case of plain cement concrete. However, here, in addition to four transducers, two Pi-shape displacement transducers (PI-5, gauge length 50 mm) were also used for displacement recording. The test set up and instrumentation are presented in Figure 4.23. The test results are summarized in Table 4.4. Figure 4.24(a) shows the relationship between compression stress and strain, and Figure 4.24 (b) presents the failure patterns observed in each test sample.



Figure 4.23 Test set up for material characterization of stabilized mud mortar.



(a) (b)  
Figure 4.24 Test results: (a) Stress-strain curve; (b) Failure patterns.

Table 4.4 Material properties of stabilized mud mortar.

Specimen Type	Stabilized Mud Plaster		
	$\rho_b$ (kg/m <sup>3</sup> )	$f_c$ (MPa)	$E$ (MPa)
Average	1809.1	4.48	
Std. dev.	31.5	1.7	

$\rho_b$  – Bulk density,  $f_c$  – Compressive strength,  $E$  – Young's modulus

#### 4.2.3.4 Three-Point Bending Test on Timber: Used in Timber-RE

Three-point bending test was conducted on thirteen timber samples having dimension 30 mm × 30 mm × 480 mm following the Japanese standard JIS Z 2241, 2011 [19]. Precision universal testing machine (AG-100kNIS-MS) was used for the loading. The test set up of three-point bending test is shown in Figure 4.25. The flexural strength of timber is calculated from the following Eq. (4.1)

$$\sigma = \frac{Fl}{4Z} \quad (4.1)$$

Where,

$\sigma$  is the flexural strength of the timber

$F$  is the peak load recorded during the experiment

$l$  is the effective length between the supports

$Z$  is the section modulus given by Eq. (4.2)

$$Z = \frac{bd^2}{6} \quad (4.2)$$

Here,  $b$  and  $d$  are width and depth of the timber specimen, respectively.

The elastic modulus of the three-point bending point is given by Eq. 4.3

$$E = \frac{l^3 \Delta F}{48I \Delta y} \quad (4.3)$$

Where,

$E$  is the elastic modulus

$\Delta F$  is the relative of peak load  $F$

$\Delta y$  is the relative bending deflection

$I$  is the moment of inertia given by Eq. (4.4)

$$I = \frac{bd^3}{12} \quad (4.4)$$

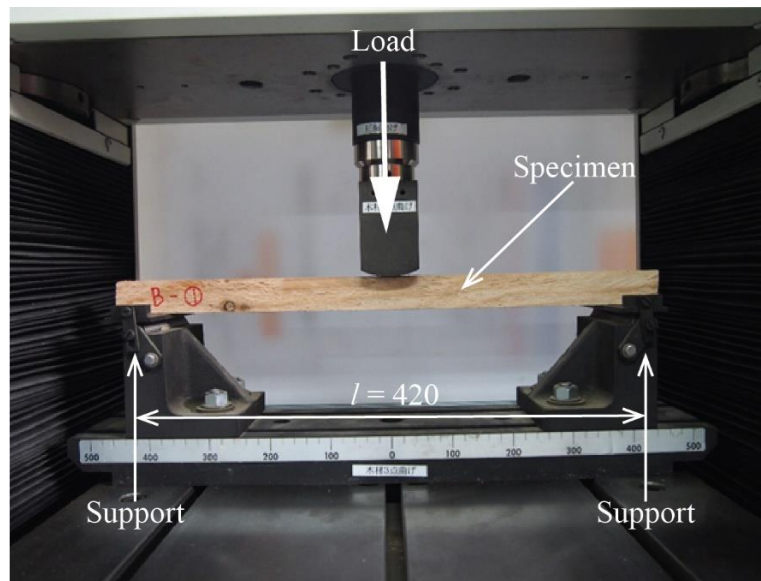


Figure 4.25 Test set up of 3-point bending test.

### **Results**

The test results from the three-point bending test are summarized in Table 4.5. The average flexural strength of the timber is 62.08 MPa, the average dry density is 446.96 kg/m<sup>3</sup>, and the average

elastic modulus is 7668.79 MPa. Figure 4.26 presents the relationship between bending strength, dry density and moisture content. The figure also presents the relationship between young's modulus, dry density and moisture content.

Table 4.5 Material properties of timber specimens.

Specimen Type	Timber specimen			
	$\rho_b$ (kg/m <sup>3</sup> )	Flexural strength (MPa)	$E$ (MPa)	Moisture content (%)
Average	446.96	62.08	7668.79	11.32
Std. dev.	28.68	11.67	980.55	0.43

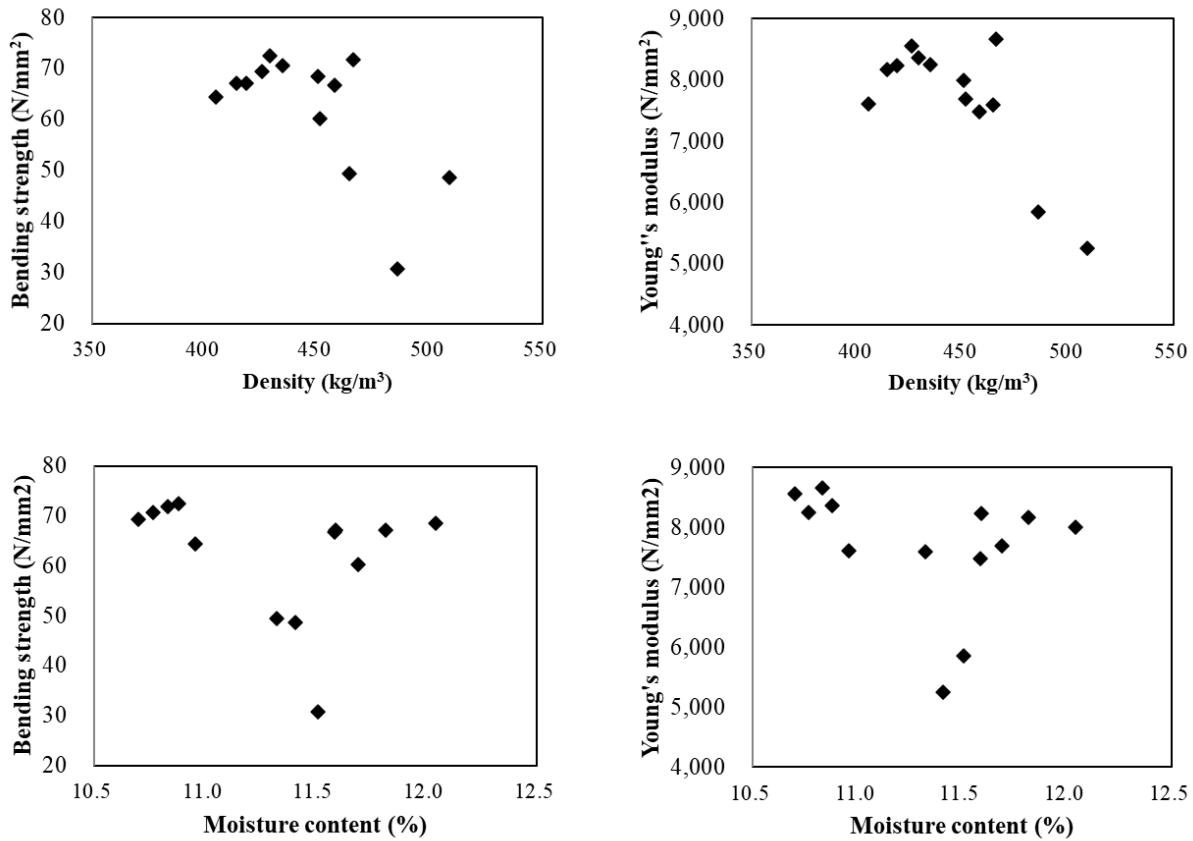


Figure 4.26 Test results from bending test.

#### 4.2.4 Test Setup

The post-earthquakes have shown that the wall mainly fails in out-of-plane, where the main longitudinal wall separates from the transverse walls. Thus, in the present experimental test, the test set up have been prepared to reproduce such behaviour during the horizontal loading. Figure

4.27 shows the experimental test set up for out-of-plane pull-down test. Due to non-availability of the testing facilities in the country, the pull-down load wall applied with Crane. The pull-down load was applied on the facade wall (longitudinal), 2100 mm from foundation top to excite the overturning mechanism. The facade wall was pulled in a horizontal direction with the backhoe of the crane with the loading point at 2100 mm from the foundation top. To distribute the uniform load to the wall, a 40 mm thick plank was fixed on two faces of the wall. Moreover, it helped to avoid local failure at the loading point. The planks together with front façade of the wall specimen were wrapped with the torsion wire (16 mm diameter) to apply the pulling force. The provision to insert torsion was kept during the wall construction, 2100 mm height from the foundation top. The load applied on the wall was measured by the tension load cell (TLP-200kNB), shown in Figure 4.27. The load cell had two shackles at both ends, where one end was connected to backhoe of crane and another end to the wall with the torsion wire's help. The load data were recorded in TML Multi-Channel Dynamic Strainmeter (DS-50A with 10-channel strain unit and 40-channel voltage unit) using LAN interface setting. The horizontal displacement of the wall was measured by displacement transducers (SDP-100C with 20 m cable), which is again connected to multi-channel

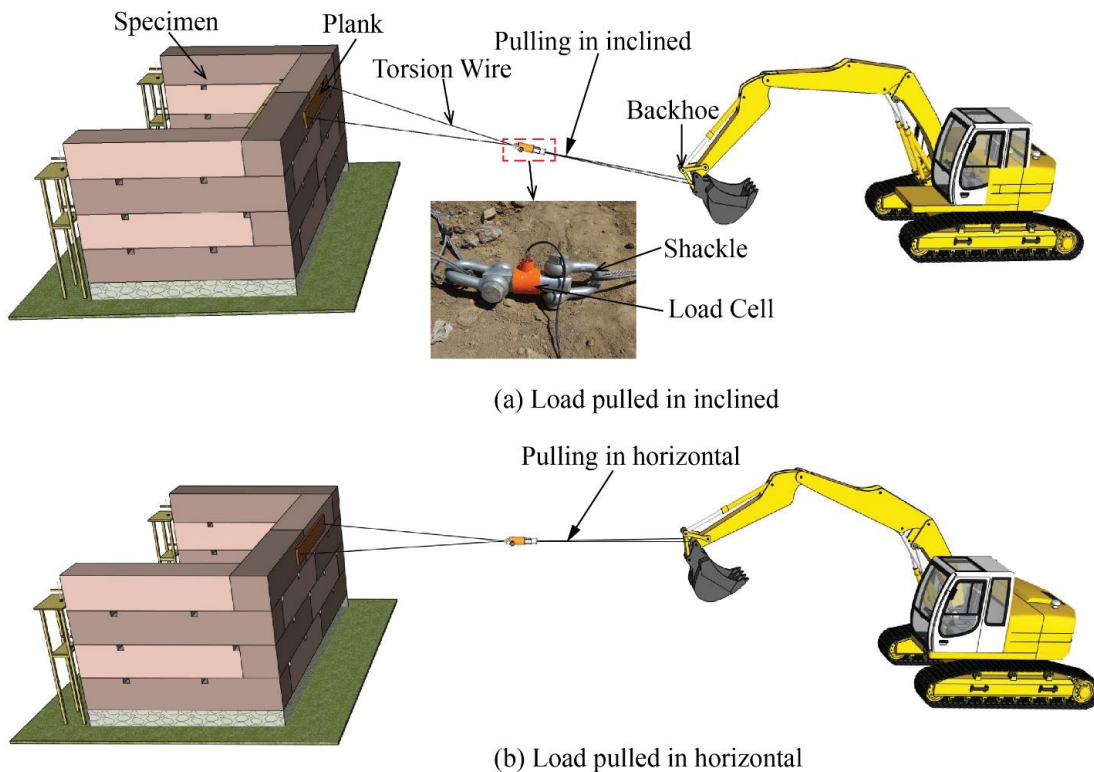


Figure 4.27 Overview of out-of-plane pull-down test.

dynamic strainmeter. Six of them were placed at the back of the front facade while the rest of the four transducers were placed to measure the side walls' deformation (Figure 4.28). The transducers at the top and mid-level were at 1900 mm and 1100 mm high from the foundation top respectively.

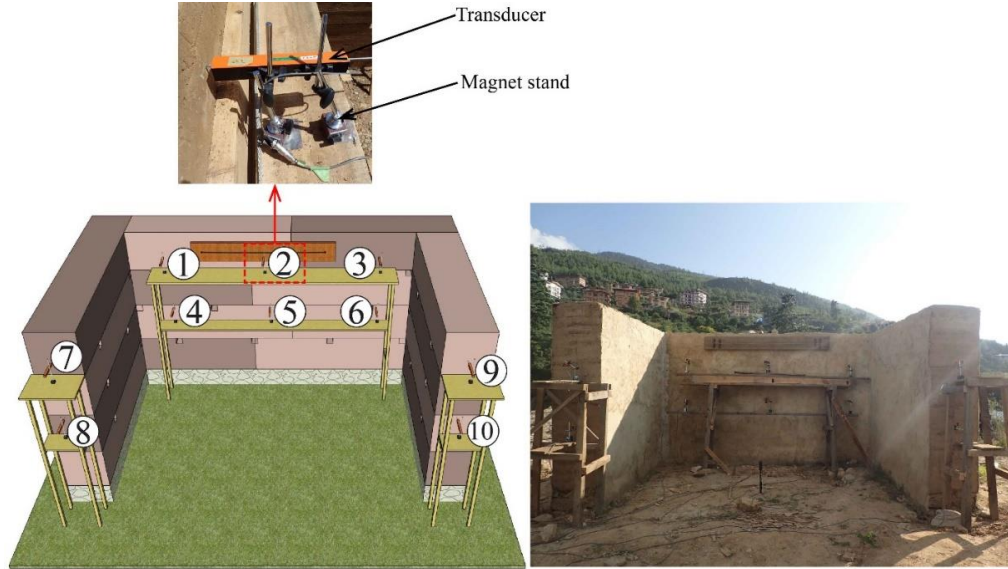


Figure 4.28 Location of transducers: 3D representation and on the field.

## 4.2.5 Results and Discussion

### 4.2.5.1 Unreinforced Rammed Earth Specimen: Reference Wall

Figure 4.29(a) shows the relationship between the pull-down force and horizontal displacement. The pull-down load is plotted against horizontal displacement recorded in all six sensors that were placed in front façade of the wall. From the load-displacement relationship graph, it is noted that there is a sharp increment in the until attaining the maximum pull load, and once it reached its peak load, the wall suddenly collapsed. The peak pull-load recorded was 29.99 kN, and its corresponding displacement for all the sensors are presented in Table 4.6. It is noted that the highest horizontal displacement was observed at 6.52 mm in the top-mid section of the wall, recorded by sensor number 2. Table 4.6 also presents the energy absorption ( $\Psi$ ) and ductility index for U-RE ( $\mu$ ). The energy absorption ( $\Psi$ ) is calculated as the area under the force-displacement curve until the 10% drop in the maximum load [1], measured by sensor 2. The ductility index here is defined as the ratio of the corresponding displacement at a 10% drop in the peak load ( $\Delta 0.9$ ) to the displacement at yielding ( $\Delta y$ ). The yield point is considered at the point on a non-linearity region where the first crack is initiated.  $\Delta 0.9$  and  $\Delta y$  for U-RE recorded by Sensor 2 is presented in Figure 4.29(b).



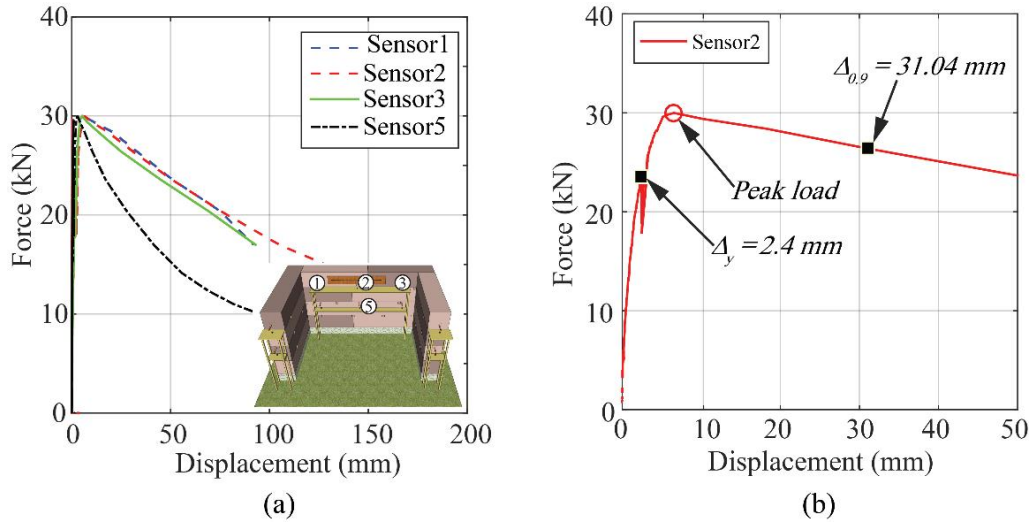


Figure 4.29 Load-displacement curve of U-RE: (a) Sensor 1,2,3 & 5; (b) Sensor 2.

Table 4.6 Maximum peak load and corresponding displacement in each sensor of U-RE.

Max. load (kN)	Corresponding displacement (mm)				$\Psi$ (kN-mm)	$\mu$ ( $\Delta_{0.9}/\Delta_y$ )
	sensor 1	sensor 2	sensor 3	sensor 5		
29.99	6.04	6.52	5.3	2.92	843	12.93

The failure mode is reported in Figure 4.30. The failure mode initiated with separation of facade wall from the two transverse walls at the top of the wall. The crack widened and extended downward with the rigid-body rocking of the front façade, shown in Figure 4.30(a). The front façade wall then overturned forming bed joint crack with the first layer block, shown in Figure 4.30(b). Figure 4.30(c) shows the final collapse of the wall. The separation of the facade wall from the side walls shows the lack of connection in the corner. The overturning behaviour with separation of the top block with the first block with the second block shows no connection between the blocks in a vertical direction.

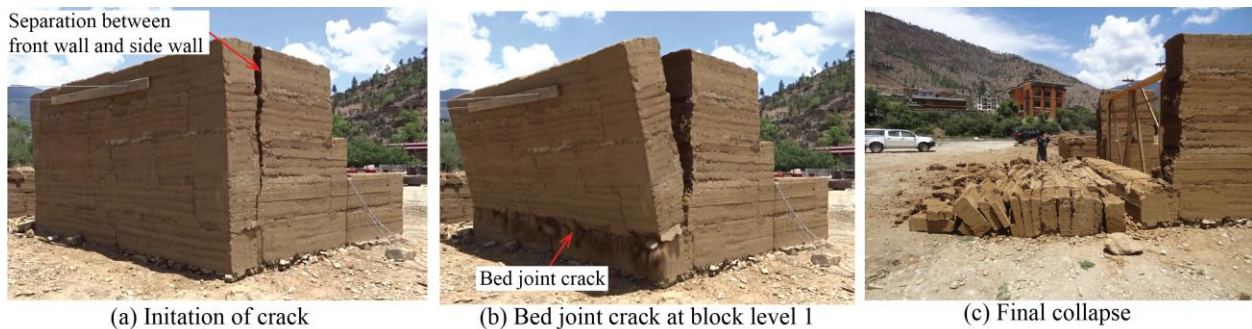


Figure 4.30 Failure mode of U-RE.

#### 4.2.5.2 Retrofitted Rammed Earth Specimen: For Existing Buildings

##### Mesh-RE

Figure 4.31 presents the pull-down load and horizontal displacement relationship for retrofitted RE specimen (Mesh-RE). The plot for load-displacement recorded at the top level of front facade, mid-level of the front facade and top level of transverse walls are presented in Figure 4.31(a), Figure 4.31(b) and Figure 4.31(c), respectively. The pull-down load-displacement curve of Mesh-RE is characterized by an early peak pull-down load followed by a hardening until the maximum pull down load. The post-peak behaviour is observed to be a plastic zone characterized by a quasi horizontal curve, which is then followed by a gradual softening behaviour. The experimental results of the Mesh-RE are summarized in Table 4.7, showing the peak pull-down load with the corresponding displacement recorded by all sensors, energy absorption and ductility. The mesh-wrap technique has improved the capacity of the wall by 1.72 times the unreinforced wall (U-RE). The Mesh-RE wall also showed better energy absorption and ductility than the U-RE wall. The corresponding displacement at a 10% drop in the peak load ( $\Delta_{0.9}$ ) and the displacement at yielding ( $\Delta_y$ ) is presented in Figure 4.31(d).

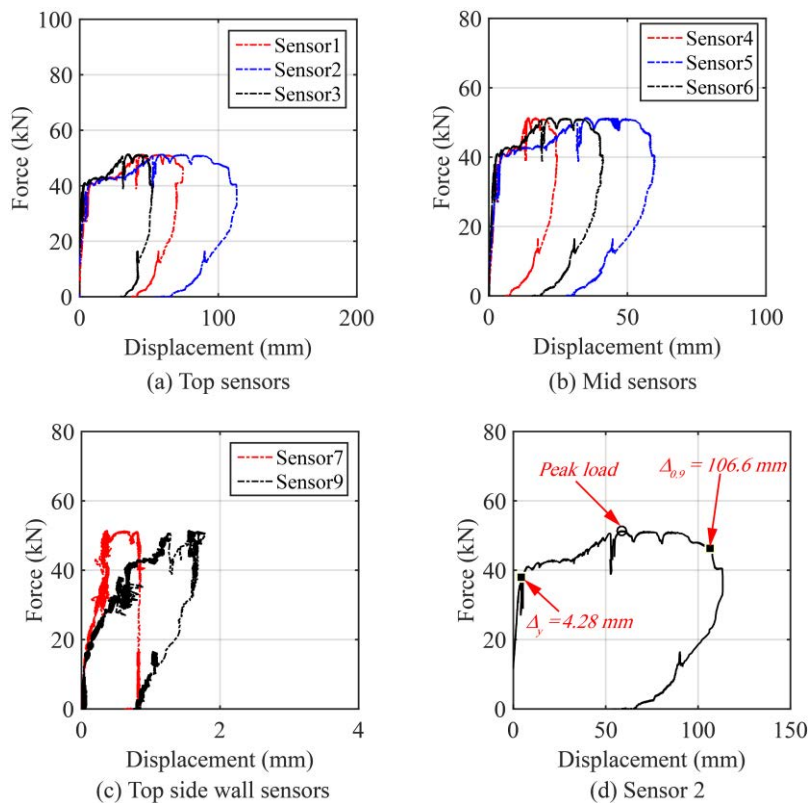


Figure 4.31 Relationship between pull-down load and horizontal displacement for Mesh-RE.

Table 4.7 Maximum peak load and corresponding displacement in each sensor of Mesh-RE.

Max. load (kN)	Corresponding displacement (mm)					$\psi$ (kN–mm)	$\mu$ ( $\Delta_{0.9}/\Delta_y$ )
	sensor 1	sensor 2	sensor 3	sensor 4	sensor 5		
51.47	44.7	58.66	35.16	14.22	34.90	4911	24.9
	sensor 6	sensor 7	sensor 8	sensor 9	sensor 10		
	21.66	0.37	0.28	1.54	0.63		

The failure of the Mesh-RE wall preceded by the appearance of the plaster cracks in the backside of the front facade near the loading point, as illustrated in Figure 4.32(a). In the next stage, plaster crack in the left corner of the wall initiated, and simultaneously, a plaster crack also emerged on the right side of the front wall away from the corner (Figure 4.32(b)). Till this stage, there were no traces of cracks from the front view of the facade wall. Upon further applying the load, the previously existing plaster cracks in the corners widened and propagated downward with clear visibility of the mesh inside. The bed joint crack also exhibited characterized by the bulging of the top block of the facade wall, as shown in Figure 4.32(c). The wall continued to displace until the wall's top block collapsed with tearing of mesh, as illustrated in Figure 4.32(d). Figure 4.32(e) and Figure 4.32(f) show the final view of Mesh-RE from the front and back, respectively. The final failure mode was local with sliding of the top RE block; however, before that, there was effective

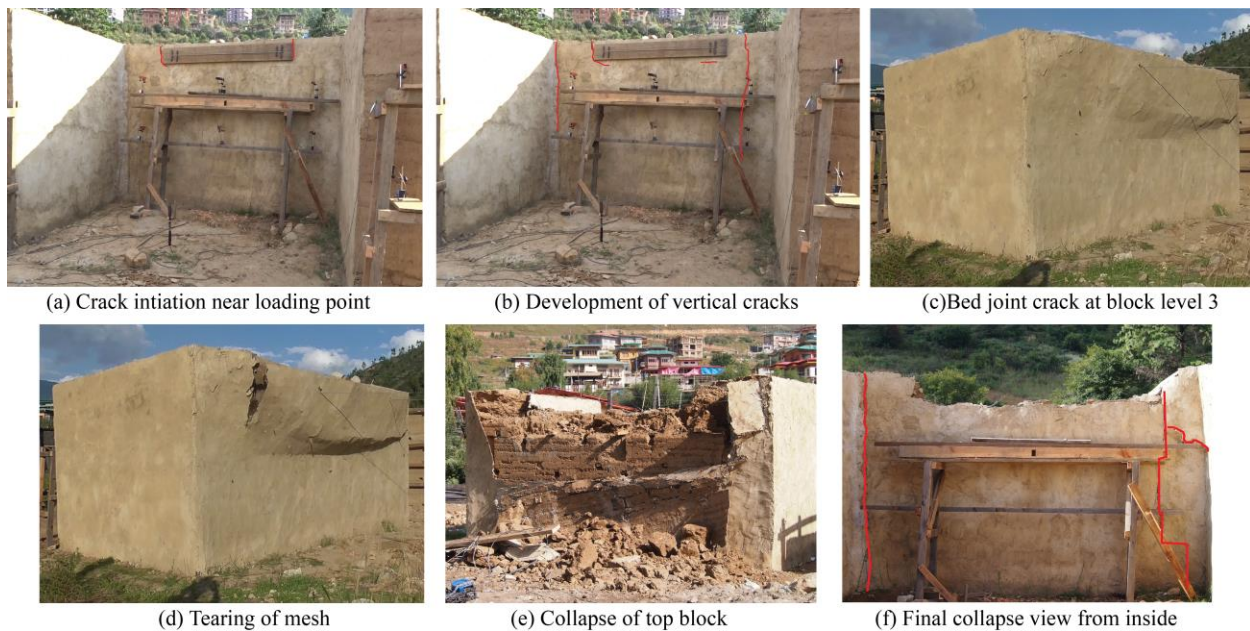


Figure 4.32 Failure mode of Mesh-RE.

load transfer over the wall's section through the mesh-wrap strengthening. Throughout the loading process, the cracks were seen within the mesh-plaster, and no delamination of plaster was seen. The delamination of mesh and plaster spalling at the front facade was observed only at the final failure. Further, the mesh strengthening retained a relatively large portion of the top block with controlled failure, preventing the crack at the bed joint and overturning of the entire facade as observed in case of U-RE. To achieve the optimum effect of the mesh-wrap retrofitting technique, it is recommended to use mesh of larger diameter. Furthermore, it is also recommended to provide longer lapping length to prevent mesh failure at this region.

### Timber-RE

The pull-down load-displacement behaviour of Timber-RE is observed similar to Mesh-RE, characterized by almost quasi-constant in a load before reaching the maximum pull-down load, as seen in Figure 4.33. Post peak is characterized by a gradual decrement in the load, but a sudden drop in load is observed as the wall collapse. The plot for load-displacement recorded at the top level of front façade, mid-level of front façade and top level of transverse walls are presented in Figure 4.33(a), Figure 4.33(b) and Figure 4.33(c), respectively. The maximum pull-down load recorded during the experiment is shown in Table 4.8, with the corresponding displacement recorded by all sensors. A comparative has been made for Timber-RE with U-RE in Figure 4.37(d). It is observed that the increment in pull-down load with the timber frame strengthening method is minimal (1.09 times the U-RE). However, there is a significant improvement in energy absorption. On the contrary, the ductility of Timber-RE is observed lower than the U-RE. The corresponding displacement at a 10% drop in the peak load ( $\Delta_{0.9}$ ) and the displacement at yielding ( $\Delta_y$ ) is presented in Figure 4.33(d). The lower ductility could have resulted as a consequence of the ramming process involved.

Table 4.8 Maximum peak load and corresponding displacement in each sensor of Timber-RE.

Max. load (kN)	Corresponding displacement (mm)					$\Psi$ (kN-mm)	$\mu$ ( $\Delta_{0.9}/\Delta_y$ )
	sensor 1	sensor 2	sensor 3	sensor 4	sensor 5		
32.64	77.02	88.58	71.26	60.22	13.85	3100	36.95
	sensor 6	sensor 7	sensor 8	sensor 9	sensor 10		
	68.24	0.62	N/A	0.32	0.32		

N/A- Not available

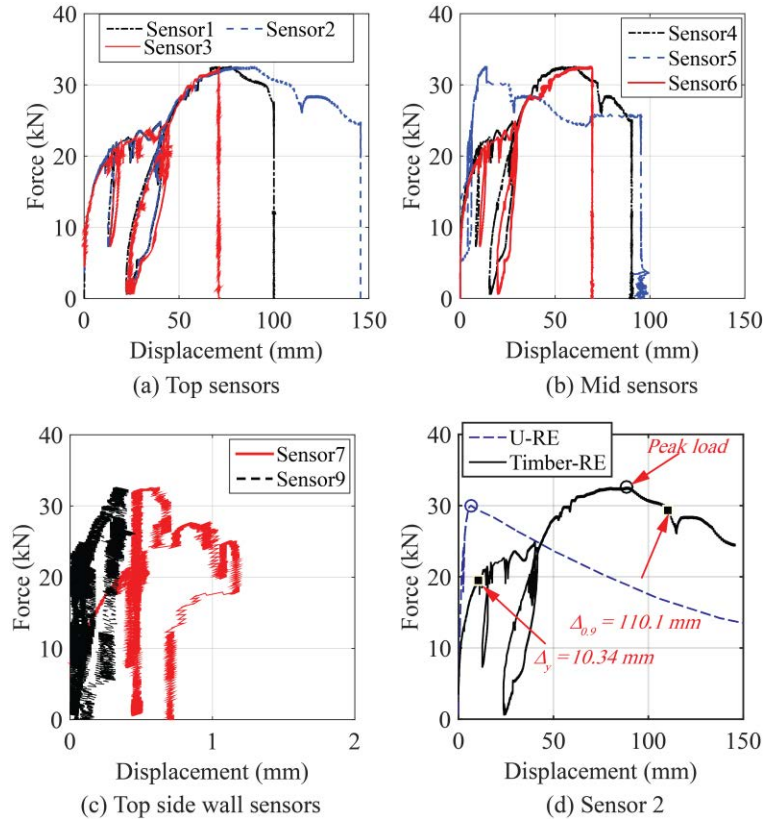


Figure 4.33 Relationship between pull-down load and horizontal displacement for Timber-RE.

Figure 4.34 presents the failure mode observed for Timber-RE. During the pull-down, a strong splitting sound of timber was heard, and the topmost transverse member near the right-hand corner of the facade wall split its connection with the other members. Following, the cracks initiated in rammed earth wall near the corner and loading point. The crack initiation can be seen in Figure 4.34(a) from the front and Figure 4.34(b) from the back. At this point, the rocking of the facade wall was also observed, as illustrated in Figure 4.34(b). The cracks then propagated downward as the pull-down continued. A vertical crack near another end of the loading point emerged, followed by a horizontal bed joint crack in between the 3<sup>rd</sup> and 4<sup>th</sup> block, as seen in Figure 4.34(c). The wall collapsed with overturning at the base. An apparent disconnection of the facade wall from the transverse walls was observed (Figure 4.38(d)). The vertical members at the back face of the facade wall overturned without any breakage but losing their connection from the foundation (Figure 4.34(d)). It shows the inadequacy of timbers' anchorage inside the foundation. Figure 4.34(e) and Figure 4.34(f) presents the overview of the final failure mode from front and back, respectively. From Figure 4.34(e), it is observed that the bottom portion of the facade wall was retained although there was a clear separation between the facade and transverse walls.

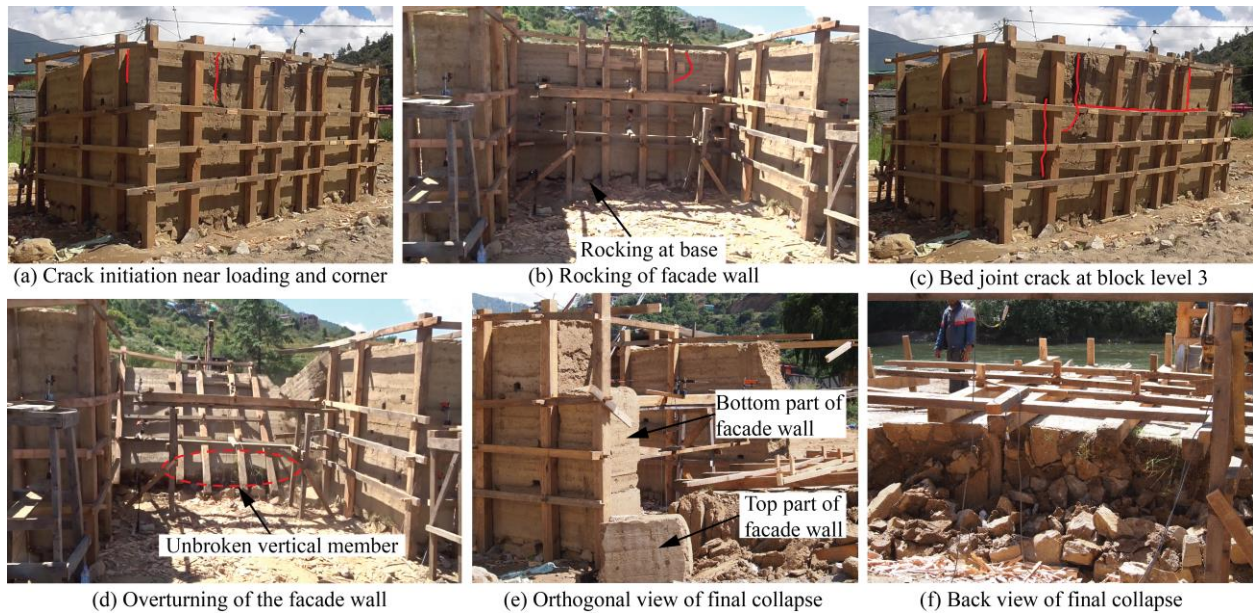


Figure 4.34 Failure mode observed for Timber-RE.

The importance of having enough embedded length and proper anchorage inside the foundation was clearly understood from the observations above. However, this may not be practical in the real building since the stone foundation's width is larger than the rammed earth walls; the vertical member cannot be embedded within the earth, but it can only be rested on top of the stone foundation. Furthermore, the use of timber-frame around the wall disrupts the visual aspects of the rammed earth wall.

#### 4.2.5.3 Reinforced Rammed Earth Specimen: For New Construction

##### New-RE-A

The load-displacement curve of rammed earth specimen reinforced with method A (New-RE-A) is shown in Figure 4.35. The load-displacement response of New-RE-A is slightly different from the U-RE before the peak load. The curve shows the first peak, and the load is almost constant before reaching the maximum pull down load. The post-peak behaviour is similar to the U-RE where the load significantly drops after attaining the maximum pulldown load. Table 4.9 shows the maximum pulldown load recorded and the corresponding displacement recorded by sensors placed at different locations. The maximum pull-down load recorded was 30.38 kN. The presence of RC wedges and RC dowels has not improved the wall strength in out-of-plane. Firstly, it would be due to the lower material characteristic strength than the U-RE. Secondly, it is assumed that the RC wedges and RC dowels do not enhance the wall's overall integrity. Therefore, it is felt

necessary to check the wall's strength by providing RC posts starting from foundation till wall top and RC band to connect the whole wall which is why the strengthening method B was adopted later. Figure 4.35(b) presents the load-displacement curve recorded by sensor 2 with showing the corresponding displacement at 10% drop in the peak load ( $\Delta_{0.9}$ ) to the displacement at yielding ( $\Delta_y$ ) to calculate the ductility. The value obtained for ductility and energy absorption is presented in Table 4.9. It is noted that there is an improvement in both ductility and energy absorption.

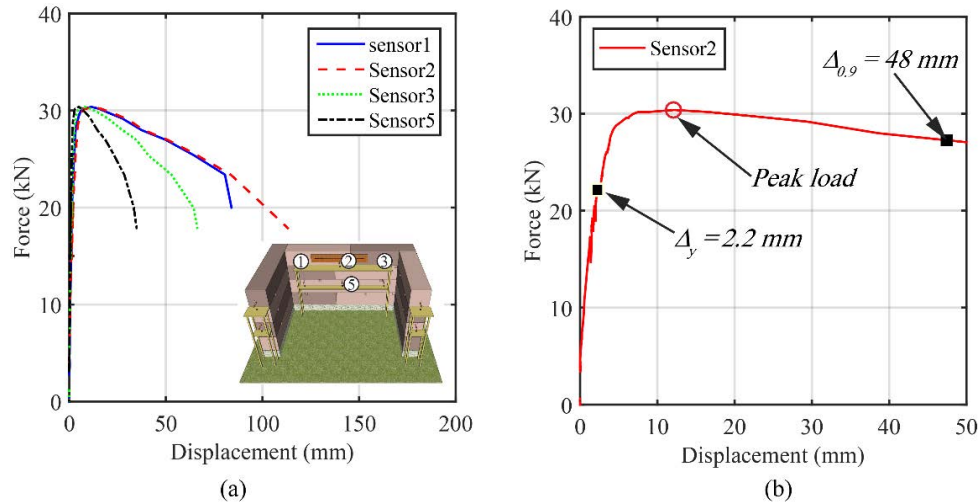


Figure 4.35 Load displacement relationship of New-RE-A: (a) Sensor 1,2,3 & 5; (b) Sensor 2.

Table 4.9 Maximum peak load and corresponding displacement in each sensor of New-RE-A.

Max. load (kN)	Corresponding displacement (mm)				$\Psi$ (kN–mm)	$\mu$ ( $\Delta_{0.9}/\Delta_y$ )
	sensor 1	sensor 2	sensor 3	sensor 5		
30.38	6.04	6.52	5.3	2.92	1434.6	21.82

The failure mode observed during the test is shown in Figure 4.36. The damage initiated with a vertical crack near corners and near the loading point, as seen in Figure 36(a). The vertical crack in the right side of the wall was a separation between the façade and the transverse wall, while the vertical crack in the left side of the wall was within the front faced wall. While closely examining, it was observed that these vertical cracks were initiated along the head joints of the RE blocks. On the further application of the pulldown load, an inclined crack was formed in facade, distributed along the bed joints (Figure 4.36(b)). Gradually, the upper part of the facade wall (Block 3<sup>rd</sup>, 4<sup>th</sup> and 5<sup>th</sup>) collapsed with bedding failure. Few layers of 3<sup>rd</sup> block remained intact without collapse (Figure 4.36(c)) due to the presence of RC dowels. Furthermore, 1<sup>st</sup> and 2<sup>nd</sup> block of façade wall

remained connected to the transverse wall, which means strengthening components used are effective in controlling the out-of-plane failure. Figure 4.36(d) shows the RC wedge inside the wall exposed after part of the facade wall connected by it was collapsed. Here, the effect of RC wedge to connect facade and the transverse wall was considered minimal. In some case, the concrete in RC wedges crushed, leaving steel bar exposed. It is worth noting here that casting of RC wedges was difficult since the length of the wedge was short, and the gap between the web and flange of the wedge was minimum. Therefore, the size of the RC wedge used in specimen New-RE-B was much longer and bigger.

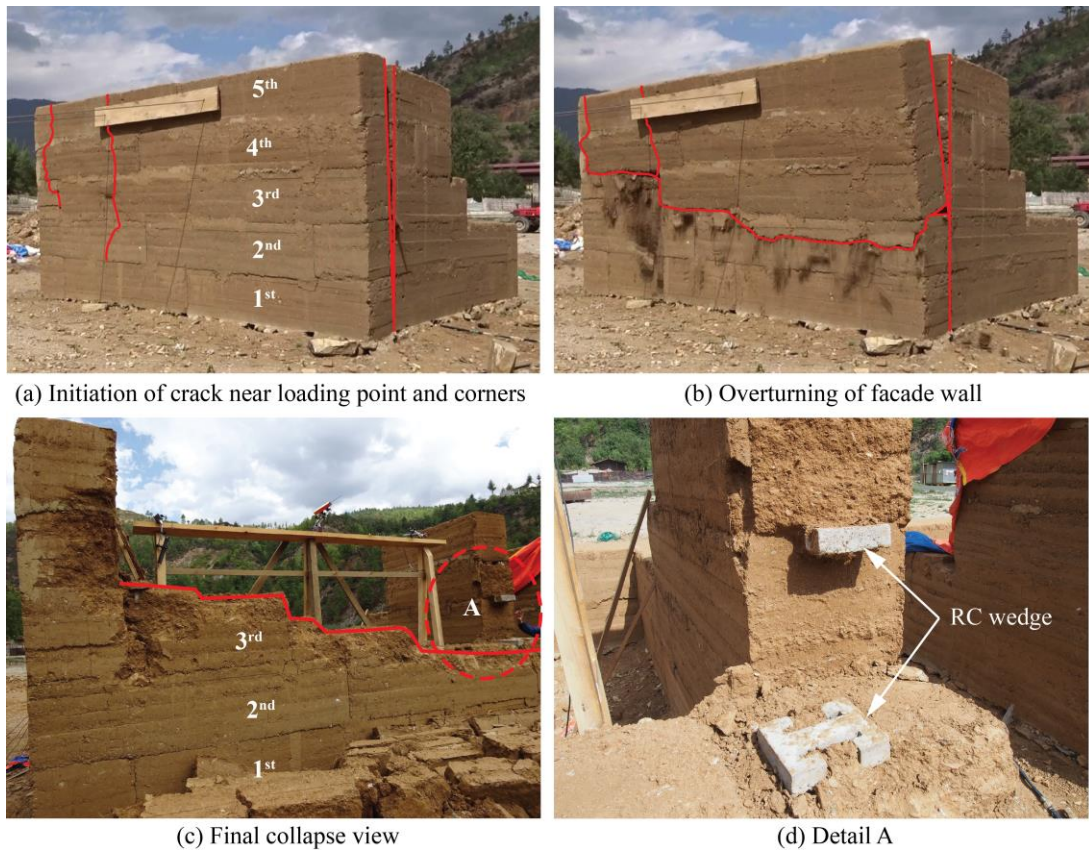


Figure 4.36 Failure modes of New-RE-A.

### ***New-RE-B***

The pull-down load and horizontal displacement relationship for reinforced rammed earth specimen (New-RE-B) are presented in Figure 4.37 with displacement recorded at various location of the specimen. The plot for load-displacement recorded at the top level of the front facade is presented in Figure 4.37(a) and mid-level in Figure 4.37(b). Figure 4.37(c) presents the load-displacement relationship recorded at the top level of transverse walls. The pull-down load versus



Table 4.10 Maximum peak load and corresponding displacement in each sensor of New-RE-B.

Max. load (kN)	Corresponding avg. displacement (mm)					$\psi$ (kN–mm)	$\mu$ ( $\Delta_{0.9}/\Delta_y$ )
	sensor 1	sensor 2	sensor 3	sensor 4	sensor 5		
95.55	13.89	23.63	21.53	9.72	15.26	9558	19.55
	sensor 6	sensor 7	sensor 8	sensor 9	sensor 10		
	10.14	3.89	16.58	4.51	4.51		

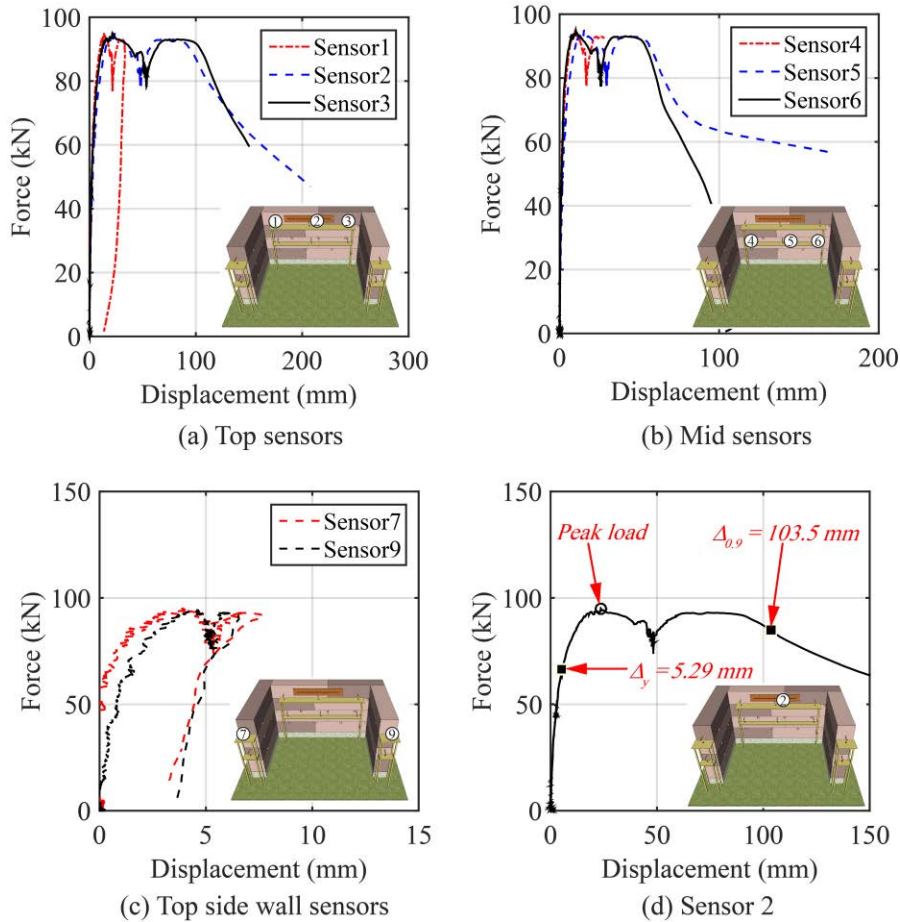


Figure 4.37 Relationship between pull-down load and horizontal displacement for New-RE-B.

displacement of New-RE-B is characterized by a steady rise in pulldown load until the peak load is reached. Within this region, both linear and non-linear behaviour is observed. The pull-down load-displacement curve is almost linear until pulldown load of 70 kN, and this is followed by non-linear hardening part. The post-peak was followed by a plastic zone, characterized by quasi horizontal curve, which is then followed by a gradual softening behaviour. The drop observed after the peak pull-down load is due to unloading during the experimentation caused by back and forth movement of the excavator. The peak pulldown load observed during the experimentation was

95.55 kN, and the corresponding displacement at peak load recorded in each sensor are presented in Table 4.10. As in the case of the unreinforced rammed earth specimen, the top mid part of the wall showed the highest horizontal displacement, which was recorded 23.63 mm. The strengthening RC components improved the wall's strength significantly, where its strength is found to be 3.19 times the unreinforced wall (U-RE). Furthermore, a significant improvement in ductility and energy absorption was also observed using strengthening components. The ductility and energy absorption of New-RE-B was 1.5 and 11 times the U-RE, respectively. The corresponding displacement at a 10% drop in the peak load ( $\Delta_{0.9}$ ) and the displacement at yielding ( $\Delta_y$ ) is presented in Figure 4.37(d). The drop in pull-down load at around 50 mm displacement is avoided since this drop was due to the back and forth movement of the excavator, and this drop does not represent the loss in capacity of the wall.

The presence of strengthening RC components have influenced the failure mechanism too. The

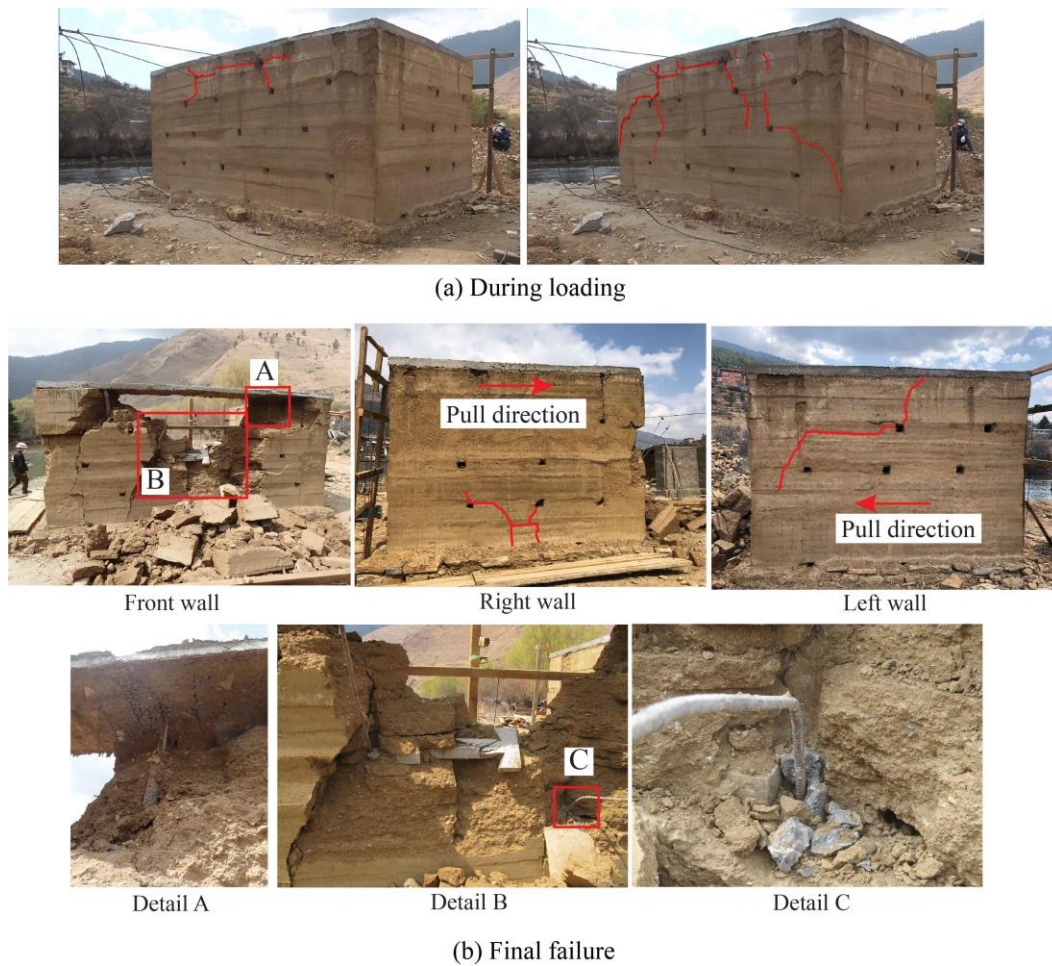


Figure 4.38 Failure mode for New-RE-B: (a) During loading; (b) Final failure.

crack initiated from the two ends of loading point and extended diagonally towards two extreme corners (Figure 4.38(a)). At the final failure mode, the concrete in vertical posts at the left side (Detail A and C), as well as the wedges (Detail B), were crushed (Figure 4.38(b)). No fracture of reinforcing bar was seen, with a slip of vertical rebar from the top band and crushing of concrete within the RC post. Unlike in the case of the U-RE, the damages in New-RE were distributed in the facade wall as well as in the transverse walls. The diagonal shear cracks observed in both the transverse walls (marked in red colour), is the effect of the RC band which enhanced to unite the whole wall together, creating box-like action between the front wall and the side walls. The RC band is found effective in transferring the pull load from the weaker wall (the front facade wall) to the stronger ones (two side walls). Thus, the proposed strengthening method can be adopted for the new rammed earth construction.

### **4.3 Finite Element Modelling**

#### **4.3.1 Geometry, Boundary and Loading Conditions**

Only the unreinforced wall (U-RE) is modelled using the finite element program DIANA. The rammed earth walls are modelled following both macro and micro modelling approaches. In macro model, the rammed earth material is treated as a homogeneous continuum medium, which allows obtaining models with lower complexity than those obtained from a micro-modelling approach [20]. In micro-model, the rammed earth material is treated as a set of stacked layers of finite elements to simulate the interface between rammed earth blocks. Further, it is also used to capture the gap opening between the blocks caused by out-of-plane loading.

The dimensions of the tested wall of U-RE is taken as the dimensions of the numerical model. However, the only half-length of sidewalls are considered here, since it did not contribute to the maximum pull-down load. In present work, macro-modelling approach used the eight-node isoparametric solid brick elements HX24L to model the rammed earth structure as a homogeneous continuum element. In micro-modelling, joint interfaces between the rammed blocks are also modelled. This micro-modelling strategy is used extensively in modelling mortar joint interfaces in masonry construction. The RE block interfaces were modelled using three-dimensional plane interface elements Q24IF between the faces of the HX24L brick elements. The finite element mesh of the macro-model constituted 520 solid bricks elements, while micro-model constituted 520 solid bricks elements and 240 interface elements. The element size for meshing was kept at 300 mm.

Figure 4.39 presents the mesh generated for micro-model and the locations of bed joints and head joints interfaces. The mesh for macro model same as Figure 4.39 without the interface elements. For the boundary conditions, the bottom of the wall was pinned, and the side walls were supported in the y-direction, as illustrated in Figure 4.39. The back walls were not included in the FE model since the two orthogonal side walls were sufficiently rigid in the in-plane direction. The red arrow line represents the displacement controlled load applied at the top of the wall. A multi-point constraint/tying, represented by red dots in Figure 4.39, was used at the level of application of load with the loaded point as a master node.

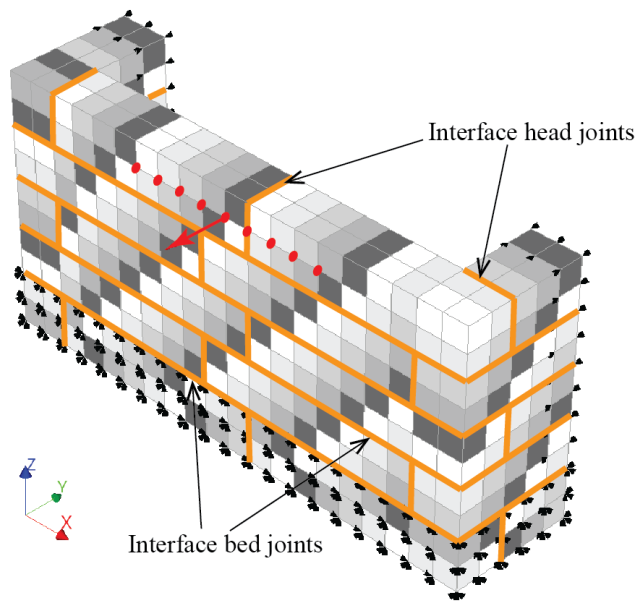


Figure 4.39 FE mesh generated for micro-model.

### 4.3.2 Constitutive Laws

The constitutive model adopted for the rammed earth is followed same as reported in Chapter 3, i.e. total strain based rotating crack model (TSRCM), which describes both the tensile and the compressive behaviour of the material with one stress-strain relation. Here, the fracture energy based exponential softening for the tensile cracking (Figure 4.40(a)) was assumed, and the wall's compressive characteristic was assumed as parabolic (Figure 4.40(b)). The compressive fracture energy,  $G_c$  was estimated as  $1.5f_c$  and mode-I tensile fracture energy,  $G_f^I$  as  $0.02f_t$ . The RE block interfaces were modelled using the non-linear Coulomb friction model with brittle cracking (Figure 4.40(c)). It should be noted that the interfaces along the bed joints and head joints of the RE blocks were modelled and the interfaces between the RE layers were not taken into account

for the present work. In the absence of detailed material characterization test for the interface properties, the values for interface material properties listed in Table 4.11 are assumed as follows:

- (i) the linear stiffness of the interface,  $k_{nz}$ , is considered 100 times of the rammed earth,
- (ii) the gap tensile strength of the interface is assumed 80% of the tensile strength of the rammed earth,
- (iii) cohesion is twice the gap tensile strength, and
- (iv) friction angle is assumed as 0.8.
- (v) The shear stiffnesses of the interface ( $k_{sx}$  and  $k_{sy}$ ) were estimated as  $[0.5 k_{nz}/(1+\nu)]$  where,  $\nu$  is the poisson's ratio.
- (vi) The gap tensile strength of the RE block interface,  $f_{ti}$  was assumed as 0.0432 MPa, which is 80% of the rammed earth tensile strength,  $f_t$ .

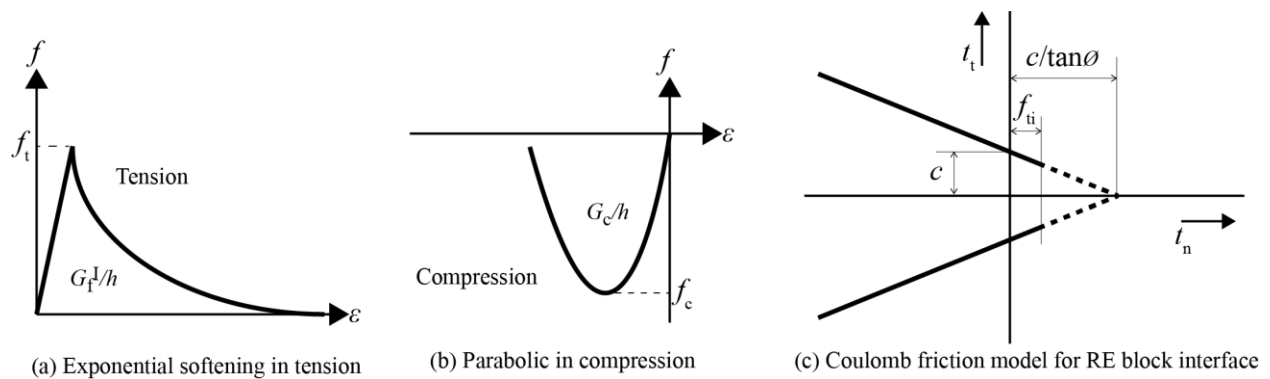


Figure 4.40 Material models adopted in FE.

The 20% decrement of interface gap tensile strength is based on preliminary FE analysis results, where micro-model with  $f_{ti}$  equal to  $f_t$  showed response similar to the macro-model with minimal influence of interfacial properties. Further, the interface material properties, namely the linear stiffness, cohesion, and friction angle, were calibrated based on the values recommended by Miccoli et al. [20].

The material properties used in the FE model are listed in Table 4.11. The values in Table 4.11 follow the material characterization tests of the extracted core samples, as illustrated in Table 4.1. However, the elastic modulus from the characterization tests of U-RE was very low due to the lack of proper extensometers to measure the strain. Therefore, its value was assumed based on calibration with the test result.

Table 4.11 Material properties for FE model.

Material properties		U-RE
Rammed earth properties	Mass density, $\rho_r$ (kg/m <sup>3</sup> )	2033
	Poisson's ratio, $\nu$	0.15
	Elastic modulus, $E_r$ (MPa)	220
	Tensile strength, $f_t$ (MPa)	0.054
	Mode-I tensile fracture energy, $G_f^I$ (N/mm)	0.01
	Compressive strength, $f_c$ (MPa)	0.52
	Compressive fracture energy, $G_c$ (N/mm)	0.78
Interface properties	Normal stiffness, $k_{nz}$ (N/mm <sup>3</sup> )	22000
	Shear stiffness, $k_{sx}$ (N/mm <sup>3</sup> )	9560
	Shear stiffness, $k_{sy}$ (N/mm <sup>3</sup> )	9560
	Cohesion, $c$ (MPa)	0.086
	Friction angle, $\tan\phi$	0.8
	Dilatancy angle, $\tan\psi$	0
	Tensile strength, $f_{ti}$ (MPa)	0.043

### 4.3.3 Results and Discussion

Table 4.12 presents the summary of FE results and the pull-down test. The results include the peak pull-down force, the initial stiffness of the force versus deflection curve,  $k_{ini}$ , and the energy absorption,  $\psi$  for each wall specimen. The peak force is well estimated by both the macro and micro-models. However, there are large variations for the initial stiffness and the energy absorption between the experiment and the FE results. The pull-down force vs displacement acquired from the FE results are plotted together with the experiment result in Figure 4.41. The rammed earth walls showed a typical out-of-plane characteristic with a sharp increment of the force in pre-cracking stage followed by a rapid decrement in the capacity in the post-cracking phase.

Table 4.12 Experimental and FE results for the pull-down tests.

Peak force (kN)			Initial stiffness, $k_{ini}$ (kN/mm)			Energy absorption, $\psi$ (kN-mm)		
Exp	FE-macro	FE-micro	Exp	FE-macro	FE-micro	Exp	FE-macro	FE-micro
29.9	30.6	30.1	9.6	16.2	15.5	1877	1143	971

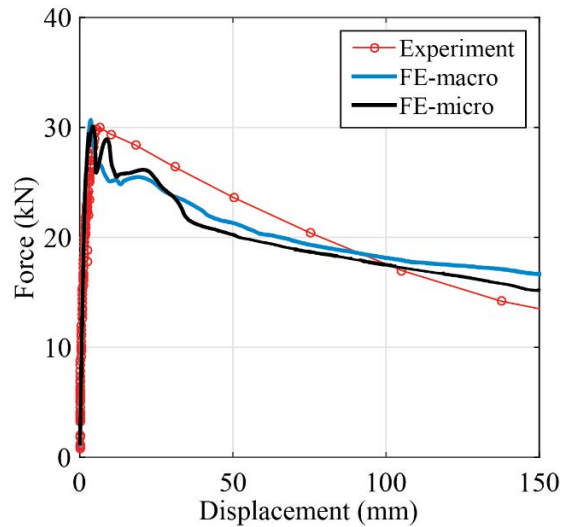


Figure 4.41 Experiment and FE results for pull-down test.

Figure 4.42 and Figure 4.43 illustrates the observed failure mechanism for the macro-model and micro-model, respectively. The experimentally observed failure mechanism was effectively predicted by the adopted FE models. The cracking mode for the FE models are presented for three displacement levels (i) 2 mm representing initial cracking phase, (ii) 5 mm, and (iii) 10 mm representing the final mode of failure. The FE-macro model in Figure 4.42 predicts the initial cracking at the RE block's head joint and the corner joint. The final failure mechanism was attributed by cracks at the corner joint and the bed joint near the bottom of the wall. The micro-model in Figure 4.43 showed clear delamination at the RE block interface bed joint and interface shear slip at the right corner and gap opening at the left corner joint. The macro-model, in contrary, did not show such delamination and did not differentiate the failure of rammed earth and the joint interface. Nevertheless, both the models were capable of predicting the failure zones and failure mechanisms under out-of-plane loading close to the experimental observations.

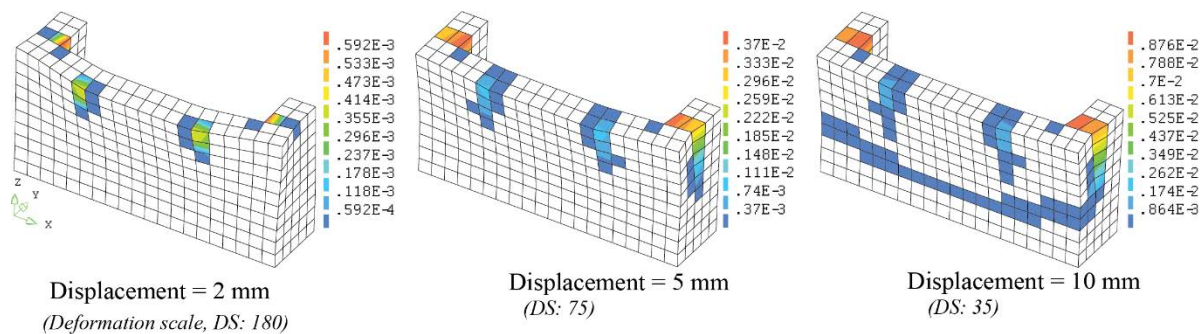


Figure 4.42 Failure modes observed for FE-macro.

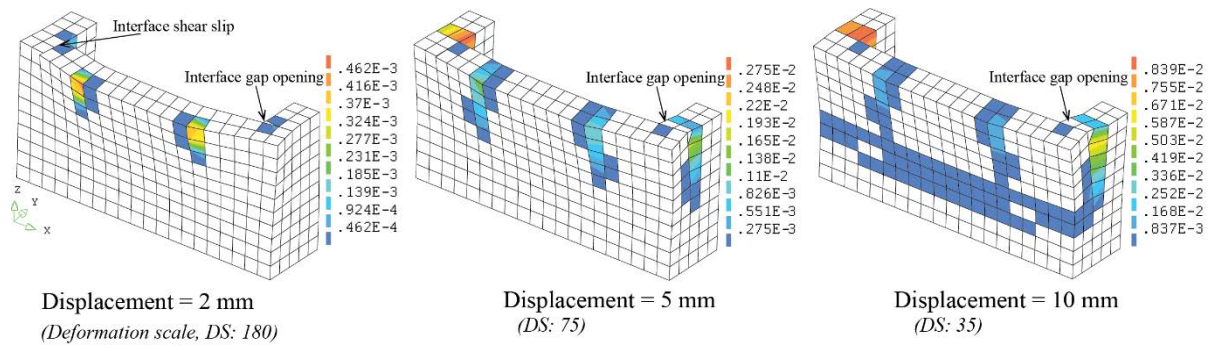


Figure 4.43 Failure modes observed for FE-micro.

### 4.3.4 Sensitivity Analysis

There is a strong variability in the material parameters, namely tensile strength, density and elastic modulus of the rammed earth within the test matrix as listed in Table 4.1. Therefore, a parametric sensitivity study is performed to assess the effect of changes in the material parameters and physical characteristics.

#### 4.3.4.1 Sensitivity analysis on interface properties

As mentioned earlier, the interface properties namely cohesion, frictional angle, linear stiffness and gap tensile strength are assumed and calibrated based on the previous study. Their influences on the out-of-plane behaviour of rammed earth wall are assessed. For this, seven different micro-models are developed, having different interface properties value as listed in Table 4.13. The corresponding name of the models is also listed in the Table 4.13.

Table 4.13 Details for parametric study of micro-model.

Specimen ID	Normal stiffness	Shear stiffness	Cohesion	Gap tensile strength	Friction angle
FE-micro	$k_{nz}$	$k_{sx}, k_{sy}$	$c$	$f_{ti}$	$\tan\phi$
FE-micro1	$k_{nz}$	$k_{sx}, k_{sy}$	$0.75 c$	$0.75 f_{ti}$	$\tan\phi$
FE-micro2	$k_{nz}$	$k_{sx}, k_{sy}$	$0.5 c$	$0.5 f_{ti}$	$\tan\phi$
FE-micro3	$k_{nz}$	$k_{sx}, k_{sy}$	$c$	$f_{ti}$	$0.8 \tan\phi$
FE-micro4	$k_{nz}$	$k_{sx}, k_{sy}$	$c$	$f_{ti}$	$0.6 \tan\phi$
FE-micro5	$0.1 k_{nz}$	$0.1 k_{sx}, 0.1 k_{sy}$	$c$	$f_{ti}$	$\tan\phi$
FE-micro6	$0.01 k_{nz}$	$0.01 k_{sx}, 0.01 k_{sy}$	$c$	$f_{ti}$	$\tan\phi$

The results of this sensitivity analysis are presented in terms of pull-down force vs displacement graphs in Figure 4.44. The influence of friction angle (Figure 4.44(b)) is minimal compared to the



effect of variation in gap tensile strength (Figure 4.44(a)) and linear stiffness (Figure 4.44(c)). Furthermore, the initial cracking mechanisms also change with the variation in gap tensile strength and stiffness, as shown in Figure 4.45, where Figure 4.45(a) is the crack pattern of FE-micro, which serves as the benchmark. The decrease in gap tensile strength results in gap openings at multiple bed joints for FE-micro2 (Figure 4.45(b)). Figure 4.45(c) shows that FE-micro6 with low linear stiffness values lead to excessive shear slipping and sliding at the right corner interface joints and multiple bed joint openings. Miccoli et al. [20] reported that the cohesion and friction angle of the interface were critical parameters for shear behaviour.

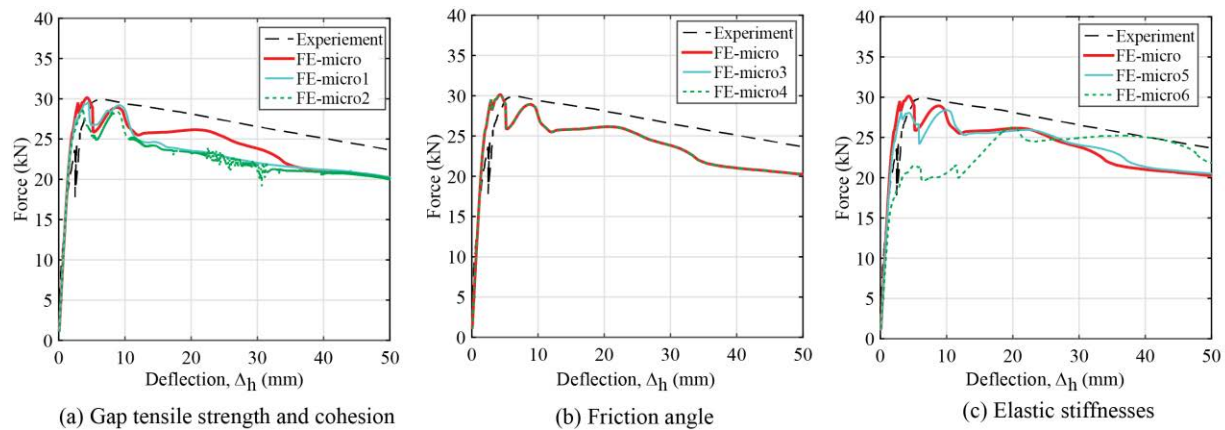


Figure 4.44 Pull-down force vs displacement for parametric study on micro models with variation in interface properties.

On the contrary, in the present study, the friction angle of interface does not play a significant role in out-of-plane behaviour. The bed joint interface gap opening and slipping of corner head joint interface is the predominant observed failure mode in out-of-plane mechanism. Hence, the gap tensile strength and the linear stiffnesses play a significant role in the failure mechanism and out-of-plane response of RE wall.

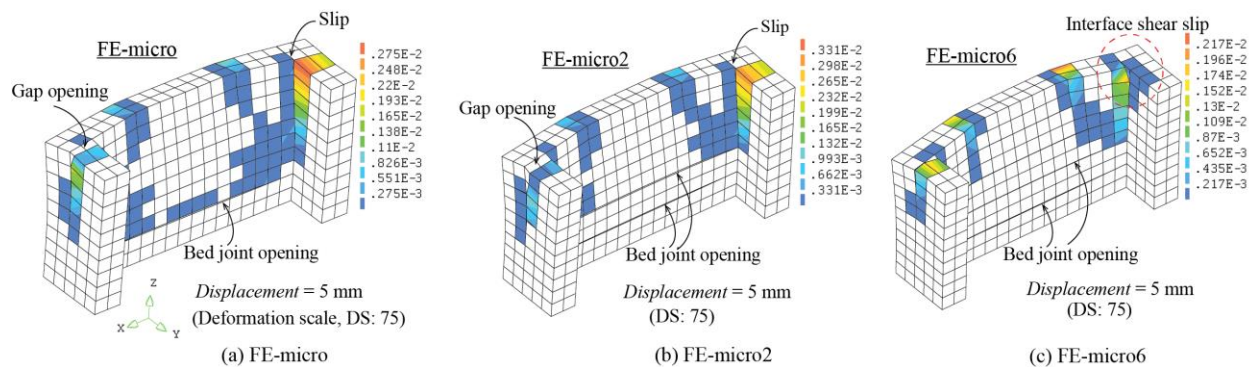


Figure 4.45 Failure patterns for FE models.

#### 4.3.4.2 Sensitivity analysis of material characteristics

The sensitivity analysis of different material characteristics of the rammed earth wall was carried out to assess their effect on the response and load-carrying capacity of the walls. Here, FE–macro was used as a benchmark for the sensitivity analysis. The macro model was selected over the micro model in sensitivity analysis for the two main reasons: (i) the material properties for the macro model were based on compressive and tensile characterization tests as reported in Table 4.1, whereas these values for micro model were assumed through calibration and recommended from the previous study, (ii) the failure mechanisms and pull–down force deformation characteristics for the macro and micro model were not significantly different and both the models closely simulated the experimental observations. The material parameters involved in the sensitivity study include the tensile strength,  $f_t$ , the bulk density,  $\rho_r$ , and the elastic modulus,  $E_r$ , of the rammed earth blocks.

Table 4.14 shows the lists of the parameters controlling the sensitivity analysis with their corresponding IDs. A variation of –30% to +30% was considered for the parameters involved, which represents a sufficiently wide range of material characteristics for rammed earth construction. The influence of material characteristics on the response of the rammed earth wall was assessed based on three response quantities; namely, the peak pull–down load, the initial stiffness,  $K_{ini}$ , and the energy absorption,  $\psi$ . Here, the energy absorption quantity is calculated as the area under the pull–down load versus deflection curve up to 30% decrement in the ultimate load.

Table 4.14 Material parameters for sensitivity study and corresponding FE model IDs.

	Tensile strength, $f_t$						Density, $\rho_r$						Elastic modulus, $E_r$					
Change (%)	–10	10	–20	20	–30	30	–10	10	–20	20	–30	30	–10	10	–20	20	–30	30
FE-ID	1	2	3	4	5	6	7	8	9	10	11	12	13	14	15	16	17	18

The results of the sensitivity analysis are shown in Figure 4.46 in terms of pull–down force versus displacement. The variation in tensile strength (Figure 4.46(a)) of the rammed earth block has relatively less effect on the pull–down load versus deflection characteristics. The effect of change in the density parameter showed a significant effect in the post–cracking behaviour under the pull–down load, as seen in Figure 4.46(b) while the change in elastic modulus was more significant in

the pre-cracking phase of the wall, as shown in Figure 4.46(c). Figure 4.47 presents a more precise effect of these material parameters in the selective response quantities. Here, the response quantities are presented as normalized values where each of the result is normalized with the value of the reference specimen, FE-macro. Figure 4.47(a) shows the effect of parameter changes in the peak pull-down force, Figure 4.47(b) for the initial stiffness,  $K_{ini}$ , and Figure 4.47(c) for the energy absorption,  $\psi$ . The effect of change in tensile strength,  $f_t$ , was clearly not significant for initial stiffness and energy absorption. The only effect of change in  $f_t$  was in peak pull-down force, in the pre-cracking phase, where increase in tensile strength resulted in rise in peak pull-down force. The effect of change in density,  $\rho_r$  of rammed earth was significant in peak pull-down force and energy absorption. Both the response quantities increased for denser systems with higher values of density. The initial stiffness,  $K_{ini}$  showed no change for variable parameters tensile strength and density. The material parameter, elastic modulus,  $E_r$ , was influential in all three response quantities, peak pull-down force, initial stiffness and energy absorption. The response quantities peak pull-down force and initial stiffness increased with increment of elastic modulus. The energy absorption,  $\psi$ , however, decreased with higher values of elastic modulus. The parametric study showed that the response characteristics of the out-of-plane loaded rammed earth wall were primarily influenced by the elastic modulus and the mass density of rammed earth blocks.

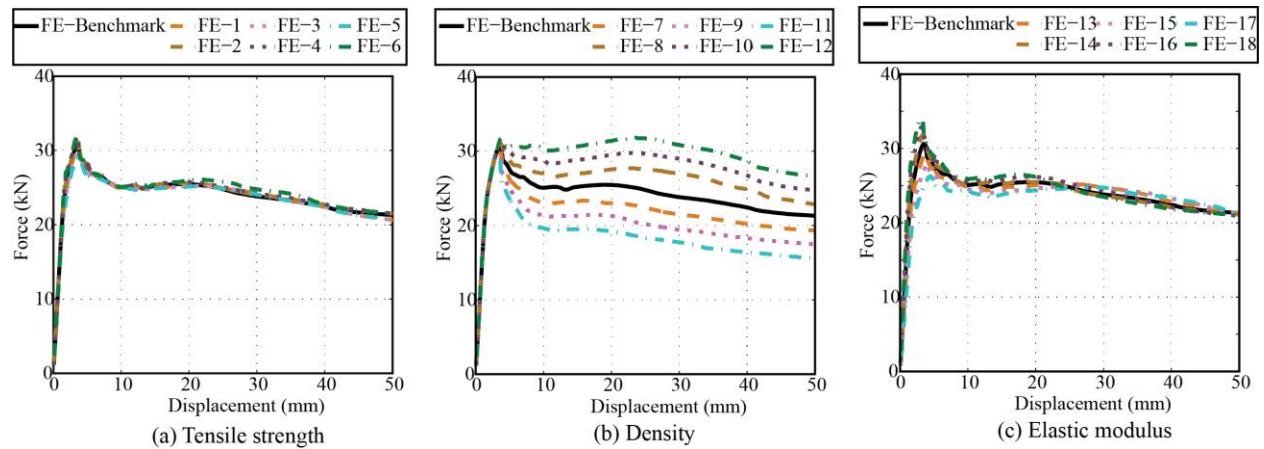


Figure 4.46 Pull-down force vs displacement for parametric study on micro models with variation in interface properties.

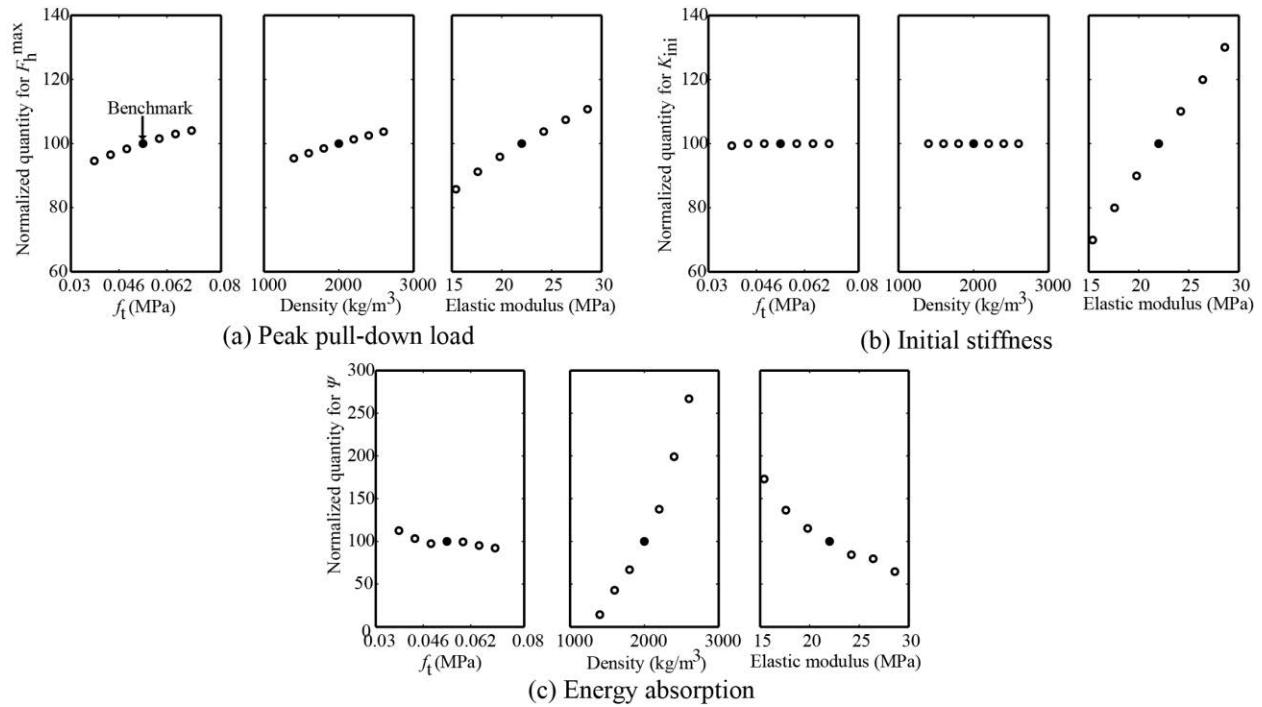


Figure 4.47 Comparison of parametric study for normalized response quantity.

#### 4.4 Assessment of effectiveness of strengthened rammed earth wall with rigid floor

##### 4.4.1 Specimens and Materials

In extension to work reported in section 4.2, this section tries to assess the behaviour of two-storied full-scale rammed earth structure to study out-of-plane characteristics of RE walls with possible effects of orthogonal back walls and also floor interaction with presence of the floor joists.

The tests involved two specimens: an unreinforced RE structure (U-RE) as a reference wall and an identical reinforced counterpart (R-RE). The soil properties and the construction process are same as already described under Section 4.2. However, the geometry of the current specimens is different from the previous specimens. Further, the current specimens have wooden floor beams. The test specimen here represents a typical two-storied rammed earth structure with a box-type plan with a single room. The length of the facade was 5.4 m, and the height of the structure was 2.4 m. For the ease of construction and test, the first storey level height was slightly reduced where the level of beam joists rested at 1.8 m. Figure 4.48 shows the details of the R-RE test specimen. U-RE details are not presented here for brevity and are similar without the strengthening interventions of reinforcement dowels, wedges and beam anchorages. The construction period

lasted for approximately two months from the month of September till November 2016. The tests were performed after a curing period of around nine months.

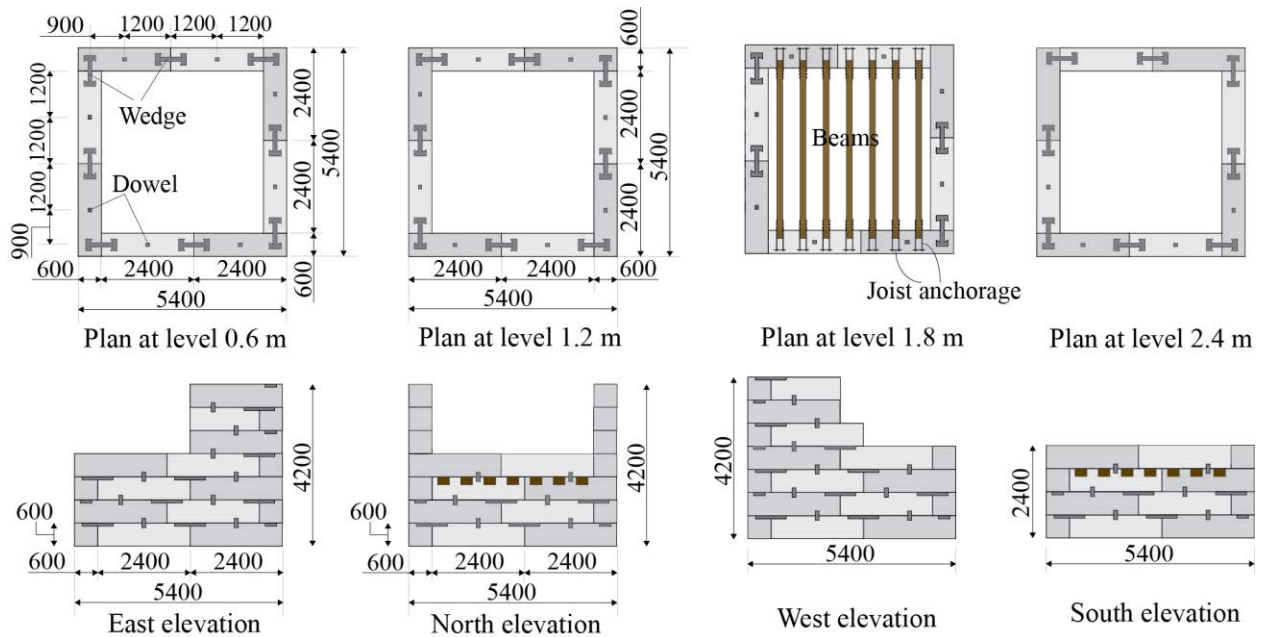


Figure 4.48 Details of reinforced rammed earth specimen (R-RE).

### ***Strengthening components used for R-RE***

RC wedges and dowels were provided within the rammed earth wall at the critical interfaces and joints of RE blocks. The dowels were placed vertically while the wedges were positioned horizontally at the RE joint interfaces, as shown in Figure 4.48. The vertically placed dowels restrain cracking along the RE blocks' bed joints, and the horizontally placed wedges provide strengthening at the corner joints and restrain the development of vertical cracks. The details of the RC dowel and wedge used are shown in Figure 4.49.

As a part of strengthening measures, wooden floor beams were anchored to the surrounding RE with steel plates attached at the ends of the beams which act as locks against the slippage, as illustrated in Figure 4.50. In addition to the strengthening of front and back walls, the anchorages of beams are also expected to make the floor relatively stronger and rigid compared to the unreinforced one. Such interventions looking into the improvement of floor diaphragm were never executed before. Figure 4.51 presents the schematic details for the strengthening interventions adopted for a wooden floor. The process of placing floor beams is same as followed for placing

the RC dowels and wedges described in the previous section. The holes were cut in the RE wall to precisely fit in the floor beam along with the steel plates. After the placement of beams, the holes in between beam and plates were filled up. This process is also being followed same for placement of the wooden beams in unreinforced RE specimen (U-RE).

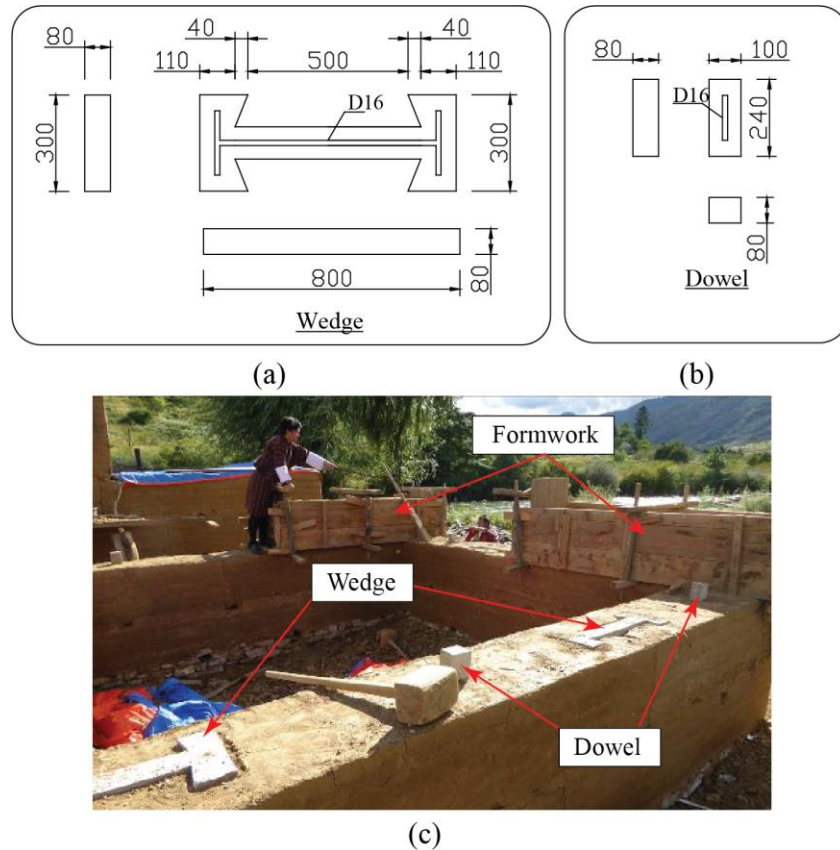


Figure 4.49 Details of: (a) Wedge; (b) Dowel; (c) Photo showing dowels and wedges at the site.

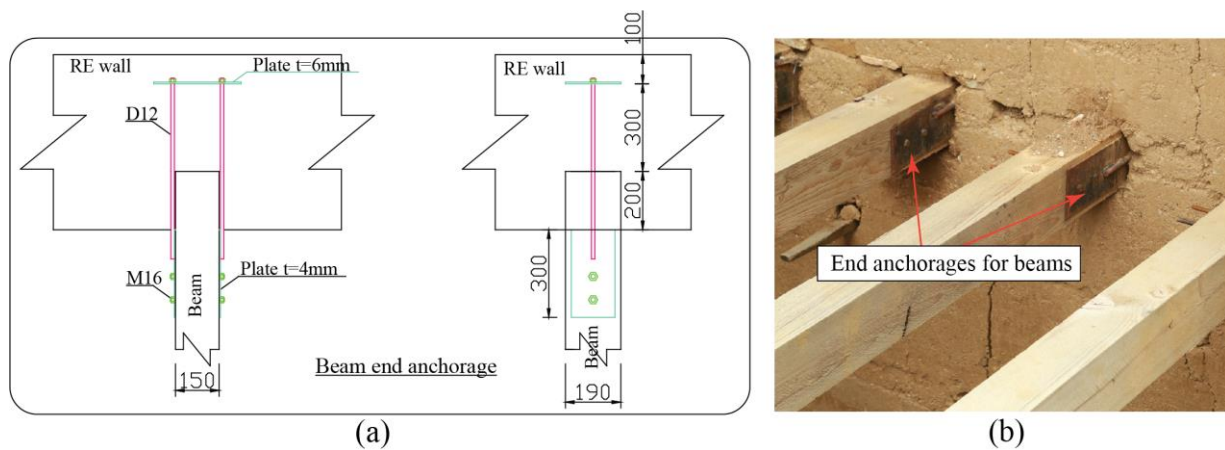


Figure 4.50 Details of: (a) Beam end anchorage; (b) Photo details of beam end anchorage at site.

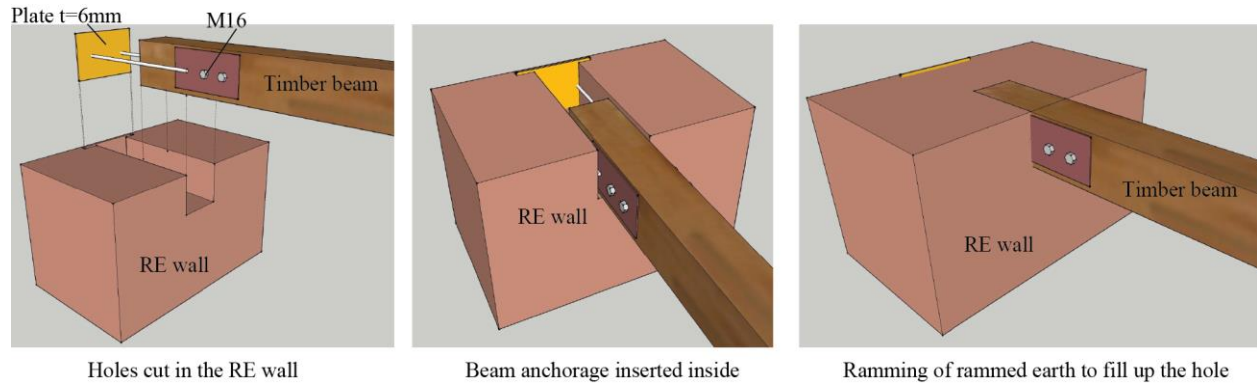


Figure 4.51 Process of floor beam placement within the RE wall.

#### 4.4.2 Material Characterization

The material characterization test result from the extracted samples are presented in Table 4.15. The material properties of wooden floor beam are same as listed in Table 4.5.

Table 4.15 Properties of rammed earth from material characterization tests.

Specimen ID	Bulk density (kg/m <sup>3</sup> )		Compressive strength (MPa)		Tensile strength (MPa)		Elastic modulus (MPa)	
	Mean	Std. dev.	Mean	Std. dev.	Mean	Std. dev.	Mean	Std. dev.
URE	2028	97	0.85	0.20	0.16	0.04	79.30	25.10
RRE	1927	98	0.49	0.10	0.12	0.04	35.80	17.50

#### 4.4.3 Test Setup

The set-up for the pull-down test is illustrated in Figure 4.52 (a). The backhoe of the excavator was connected to the one end of torsion wire, while the other end was connected to the load cell. The load cell in series was connected to another torsion wire which was wrapped around the test specimen. The test instrumentations involved the use of a tension load cell (TLP-200kNB) to measure pull-down load and nine displacement transducers to measure the deformation of test wall during the experimentation. The pull-down tests were done at two different levels on two opposite facades, first at the height of 3.9 m (*Pull-down-1*) followed by the second test at the height of 1.5 m (*Pull-down-2*) from the bottom. The two pull-down tests were done on two opposite facades of a test specimen, as illustrated in Figure 4.52 (a). The data sampling was done at a frequency of 100 Hz.

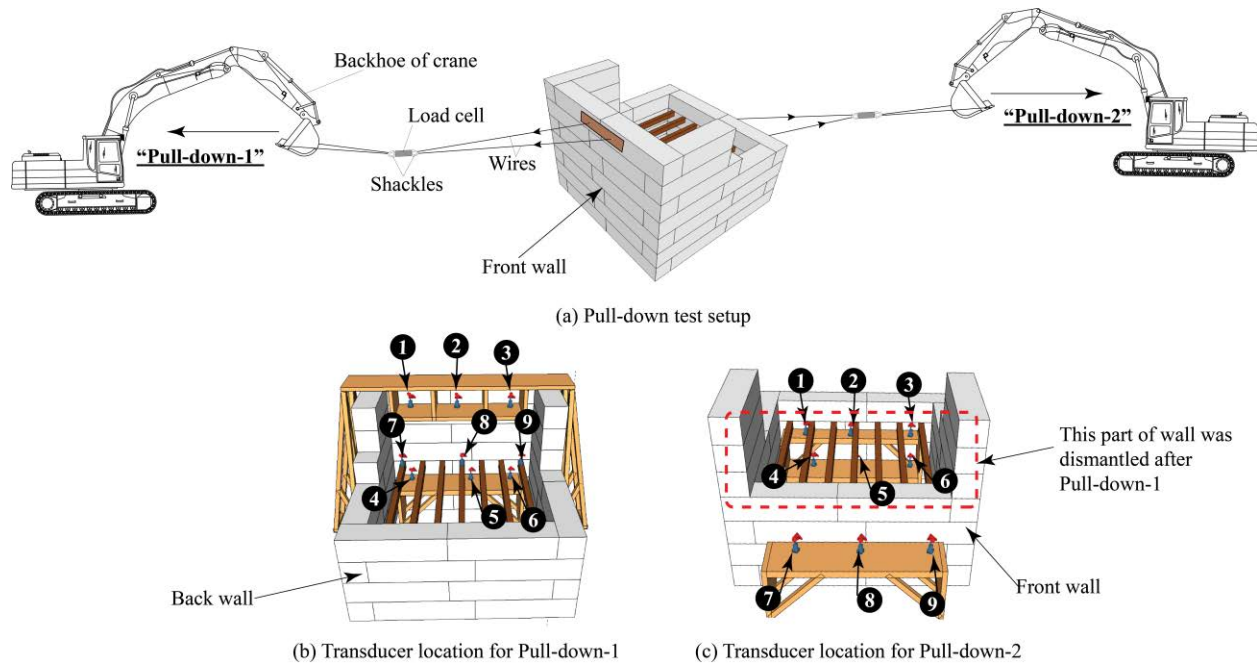


Figure 4.52 Pull-down test setup and location of displacement sensors.

### ***Pull-down-1***

The aim of Pull-down-1 was to observe the effectiveness of dowels and wedges as strengthening interventions to restrain the out-of-plane movement of wall's facade. Here, three transducers were positioned at 3.9 m level and the three others at 1.5 m level from the ground to measure the out-of-plane deformation of the façade (Figure 4.52(b)). The last three transducers were used to measure relative deformation of beam and wall at 2.1 m level.

### ***Pull-down-2***

The aim of the Pull-down-2 was to evaluate the strengthening at the floor level through beam end anchorages. Here, six displacement transducers were used to measure the deformation of pulled-down facade at two different levels (1.9 m and 0.8 m), and three transducers at the opposite facade at the level of 1.8 m (Figure 4.52(c)). The top part of the front wall indicated by red dotted line in Figure 4.52(c) was dismantled after pull-down-1 to have same floor level as the back wall.

## **4.4.4 Results and Discussion**

### ***Pull-down-1***



Pull-down-1 involved loading at the level of 3.9 m (seventh row of RE block) from the ground. The aim of Pull-down-1 was to observe the effectiveness of dowels and wedges as strengthening interventions to restrain the out-of-plane movement of wall's facade. Figure 4.53 shows the comparison of U-RE and R-RE test specimens in terms of pull-down force versus the deformation characteristics. The maximum pull-down load for U-RE was 30.1 kN and for R-RE it was 35.4 kN which corresponds to 18% increment. Both U-RE and R-RE specimens showed large displacements at the top-level transducers Figure 4.53(a). The bottom level transducers showed small displacement values as shown in Figure 4.53(b) was below the cracking plane, and therefore these transducers. The relative displacement transducer readings in Figure 4.53(c) showed comparatively large displacement for U-RE specimen, both at pre-cracking and post-cracking phase. The R-RE specimen showed minimal relative displacement of beam joist and wall, confirming the effectiveness of the adopted anchorage system.

The out-of-plane characteristics of the wall's facade was governed by cracking at the bed joint level of the RE block's joint interface and separation at the corner joints. The observation of collapse sequence of the U-RE as shown in Figure 4.54(a) involved cracking at both the left and right edge corners, with separation of the facade from both the side-walls followed by horizontal bed joint crack above the third and fourth row of RE block. There was also a horizontal crack at beam level, with the whole mass of RE wall above the beam level falling in out-of-plane direction. The damage pattern of U-RE showed clear vulnerability of unreinforced RE structure with damage to a larger mass of facade and failure of sidewalls from the corners.

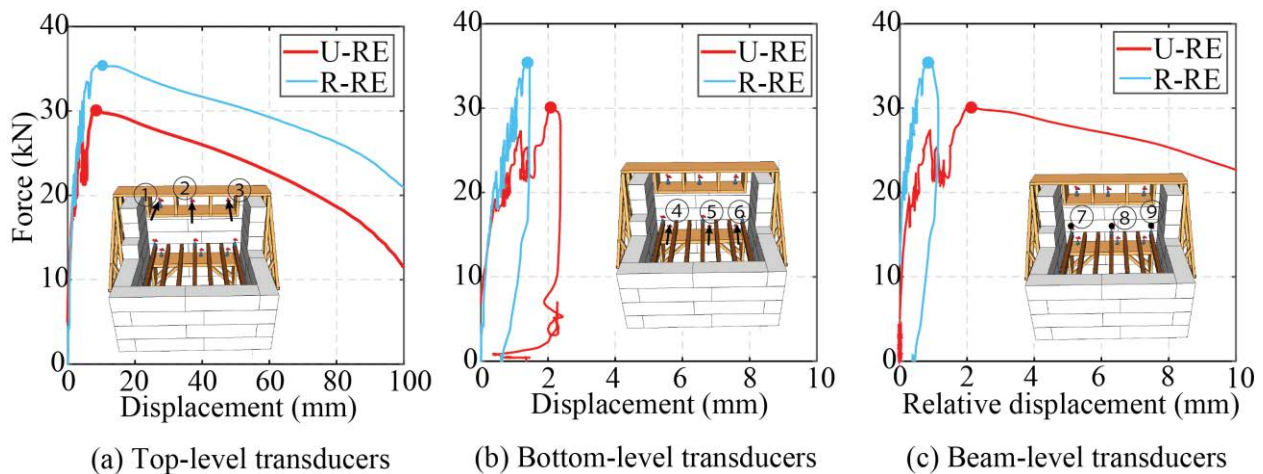


Figure 4.53 Pull-down force versus deformation characteristics for Pull-down-1 test.

The R-RE specimen as illustrated in Figure 4.54(b) showed different collapse phenomena with the sequence of collapse involving following observations: (1) relatively smaller mass of the facade fell in out-of-plane direction, (2) horizontal bed joint crack above the fifth row of RE block, (3) sidewall collapse at the left edge corner, but the right edge corner and the sidewall did not fall, (4) the strengthening intervention effectively controlled the out-of-plane failure mechanism and separation at the corners of the facade with the presence of dowels and wedges.



Figure 4.54 Damage of U-RE and R-RE specimens during “Pull-down-1” test.

### ***Pull-down-2***

Pull-down-2 test was conducted at the level of 1.5 m (third row of RE block) from the bottom after the completion of Pull-down-1. The primary aim of this test was to assess the effectiveness of the floor anchorage strengthening. Figure 4.55 shows the pull-down force versus the deformation plots for U-RE and R-RE specimens recorded by various sensors. A maximum pull-down force of 39.2 kN was observed for U-RE and 62.5 kN for R-RE showing 59% increment in pull-down load. Both the top and bottom level transducers showed large displacements for U-RE, whereas the R-RE did not show large displacement at the top-level transducers at the floor joists' level as shown in Figure 4.55(a) and (b). The deformations recorded for transducers placed at the opposite facade of R-RE showed the effectiveness of the floor anchorage for the reinforced specimen as shown in Figure 4.55(c). On the contrary, the U-RE showed no deformation of the opposite facade confirming minimal rigidity of the unreinforced specimen at the floor level. The failure mechanism of R-RE effectively avoided the slippage of floor joists and showed only the local failure of the rammed earth wall below the floor level. However, the whole floor level collapsed with slippage of all floor joists for U-RE specimen.

Figure 4.56 illustrates the failure mechanism for U-RE and R-RE test specimens. The unreinforced The failure sequence of U-RE initiated with appearance of crack at both corners and

near loading point. The whole back wall overturned with slippage of the floor joists from both side walls. On the other hand, the reinforced R-RE specimen with anchored floor beams showed different failure mechanism, as shown in Figure 4.56(b). The crack initiated within the back wall near the loading point. A relatively small portion of the facade failed in out-of-plane direction below the floor beam level. Cracks at the corner joints were also avoided in R-RE specimen. The connection system with steel plates achieved firm anchorage for the floor beams, which is seen in Detail A of Figure 4.56(b) where the steel plate at back wall was bent. There was no slippage of floor beams at the opposite wall (front wall).

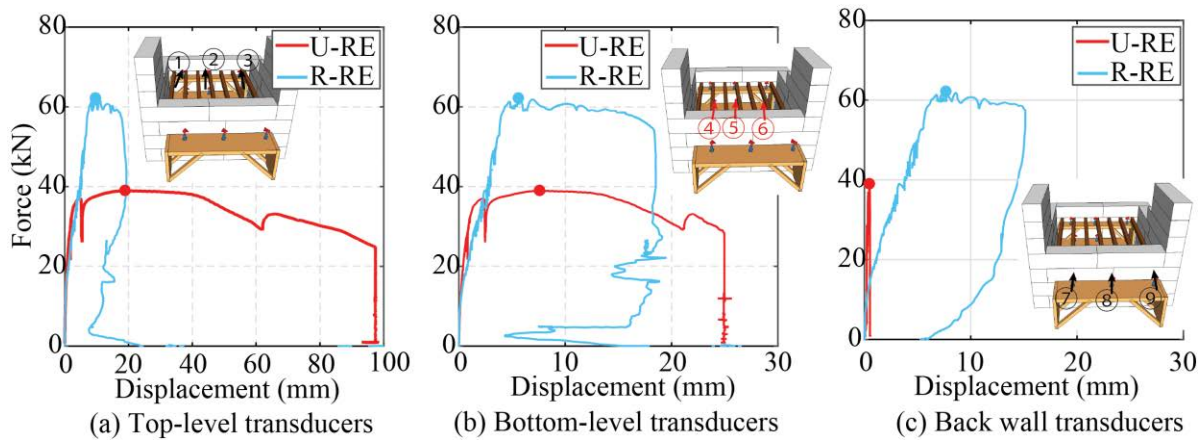


Figure 4.55 Pull-down force versus deformation characteristics for “Pull-down-2” test.

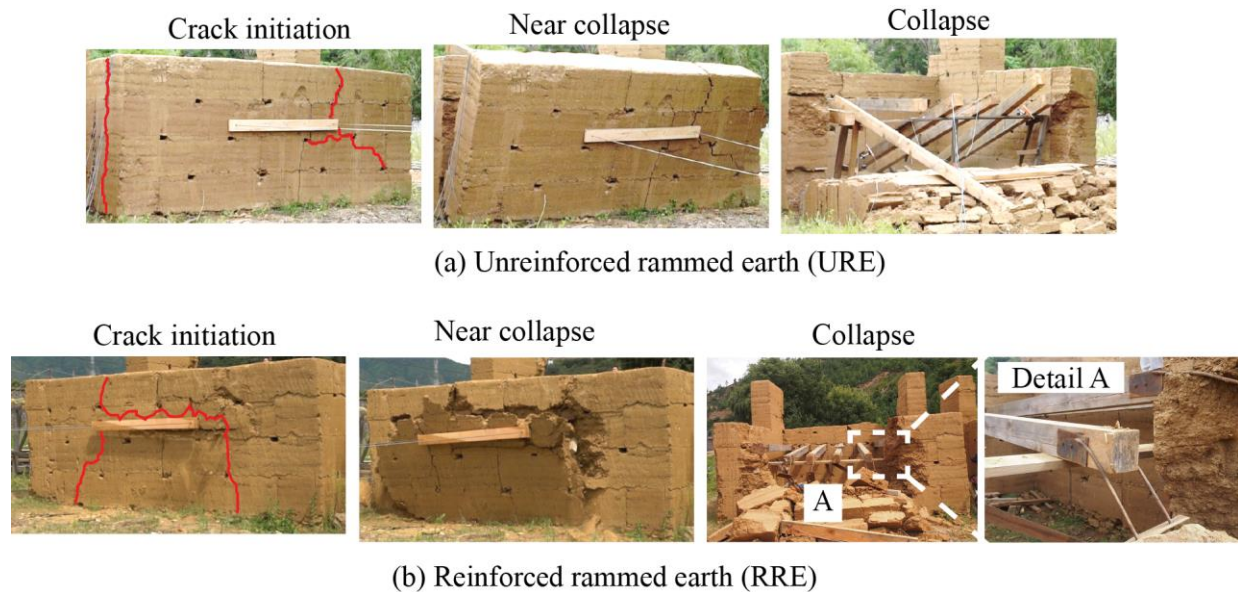


Figure 4.56 Damage of U-RE and R-RE specimens during “Pull-down-2” test.

#### **4.5 In-Plane Shear Resistance between the Rammed Earth Blocks offered by RC Dowels**

The RC dowels' effectiveness between the rammed earth blocks in resisting the out-of-plane behaviour is discussed in the previous section. Here, the author intends to understand the in-plane shear characteristics of RE while assessing the effects of RC dowels in strength increment within the RE blocks. In addition to this, the present work also tries to analyze the effect of RE layer thickness on the strength characteristics of RE. In chapter 3, the author chose two RE layer thickness, i.e. 50 mm and 100 mm. However, in this study, the author chose 60 mm and 120 mm layer thickness, which is also prevalent to the Bhutanese practice. In both cases, the compaction percentage is maintained the same at 50%.

##### **4.5.1 Specimen and Materials**

A total of three specimens were prepared to have size 1200 mm long, 600 mm thick, and 1200 mm high. The first specimen without dowel inside served as the reference wall have 120 mm layer thickness at its final compaction. The second specimen was reinforced with one dowel between the RE blocks; it also has 120 mm layer thickness on final compaction. The third specimen was also reinforced with RC dowels between the RE blocks, but it had 60 mm layer thickness at its final compaction. The specimens were labelled in “X-Y-Z” format. Here, “X” denotes the unreinforced (U) or reinforced (R) specimens. “Y” denotes the RE layer thickness either 60 mm or 120 mm. “Z” denotes the in-plane shear test (S). Thus, the three specimens are:

- i) U-120-S (Unreinforced and have 120 mm layer thickness/reference wall)
- ii) R-120-S (Reinforced and have 120 mm layer thickness)
- iii) R-60-S (Reinforced and have 60 mm layer thickness)

The details of specimens R-120-S and R-60-S are presented in Figure 4.57. The specimen U-120-S has the same details as the specimen R-120-S but without the dowel inside.

The specimens were constructed by the local craftsmen using the same soil used for constructing the U-shaped wall for pull-down test. The method for constructing the unreinforced wall also follows the same procedure discussed in previous sections, which includes: i) installation of wooden formwork, ii) Boarding the moist soil inside the formwork, and the quantity boarded depended on the layer thickness of the wall, ii) Manual compaction until the desired thickness with wooden ramming tools, and iv) Removal of formwork when one block (lower block in this case)

is completed. The preparation of the upper block included repeating the processes i) to iv). For the reinforced specimen (R-120-S and R-60-S), after completion of the lower block, a rectangular hole of size 100 mm x 80 mm with 120 mm depth was cut from the top of the lower block to place the RC dowel, as shown in Figure 4.58. Following, the processes from i) to iv) is repeated to complete the whole specimen. The specimens' construction started on 30<sup>th</sup> July, and it was completed on 10<sup>th</sup> August. The shear test on all specimens was conducted in September 2017 after a drying period of one month. Details of placement of reinforced concrete dowels (240×100×80 mm) in reinforced RE specimens are shown in Figure 4.58.

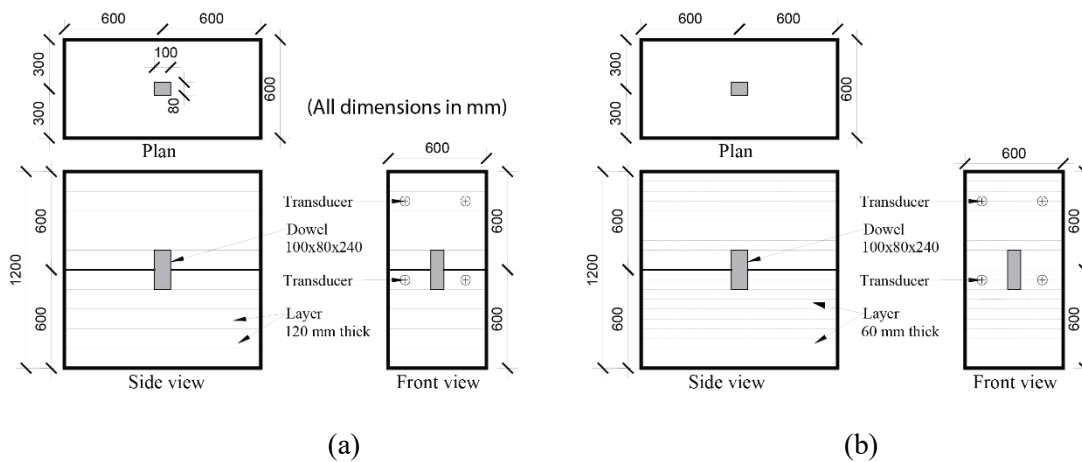


Figure 4.57 Test specimen details and measuring points: (a) R-120-S; (b) R-60-S.

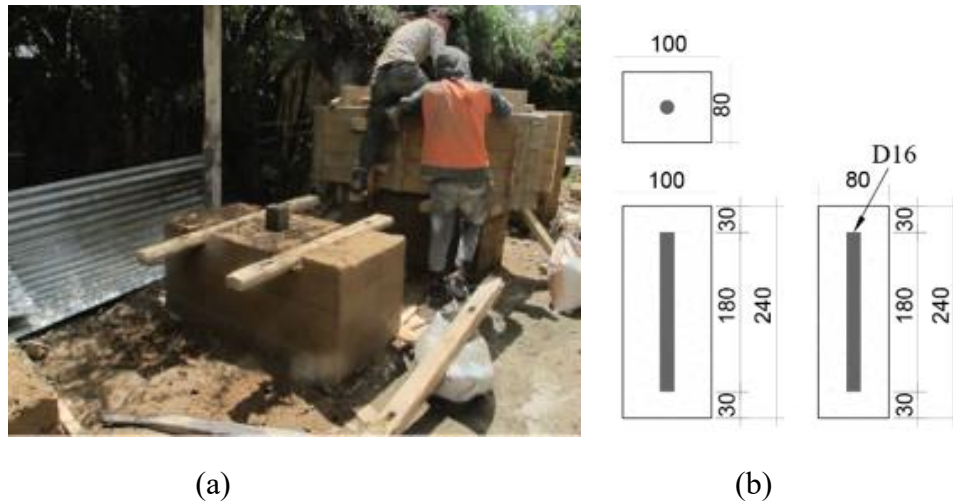
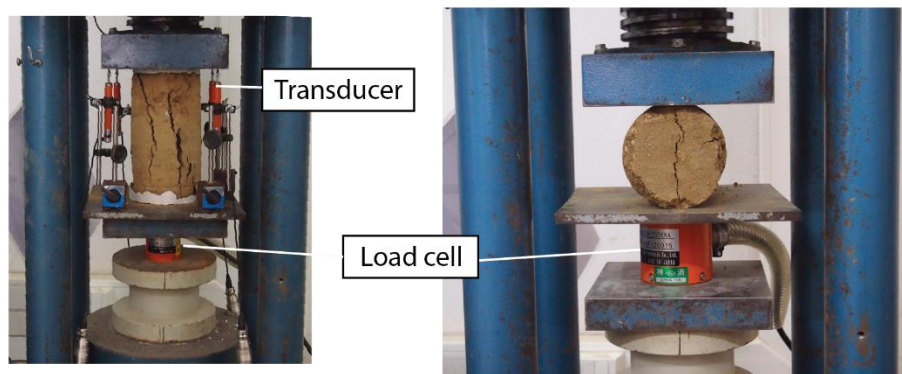


Figure 4.58 Specimen construction: (a) Insertion of RC dowel; (b) RC dowel details.

#### 4.5.2 Material Characterization

After the completion of the shear test, a total of eighteen RE cylindrical core samples were extracted from the test specimens using core drilling machine with diamond core bits to evaluate

the splitting tensile strength [18] and compressive strength [19]. The samples had 92–96 mm in diameter and 163–200 mm length. The core samples were left for drying under the room temperature, and they were tested after one month and six months of the drying period. Figure 4.59 shows the test set-up for the compressive and tensile test. Load cell (KCM–20kNA) was used to record both compression and tension load and four displacement transducers (CDP–10MT), fixed at four corners, recorded the displacement. The test matrix for the material characterization tests involved two parameters, first rammed earth type based on two rammed earth layer thicknesses and second the drying time.



(a) Compressive test

(b) Tensile splitting test

Figure 4.59 Material characterization test.

Table 4.16 shows the results of the material characterization tests performed on the specimens. For 120 mm RE layer thickness, the average cylinder compressive strength was 0.5 MPa at one month drying and 1.15 MPa at six months drying. Similarly, this was 0.56 MPa at one month drying and 1.18 MPa at six months drying for 60 mm RE layer. There is around 120% increment in compressive strength on average with the sample dried between 1 month and six months. The RE layer of 60 mm thickness has slightly higher strength characteristics compared to 120 mm thickness. The average splitting tensile strengths were 0.06 MPa and 0.11 MPa for the RE layer of 120 mm and 60 mm respectively at a one month drying period. The result observed from the material characterization tests is consistent as reported in Chapter 3, where, both RE layer and drying period improves the shear strength of the RE wall. Figure 4.60 shows typical stress–strain curves for the RE under compression at 6 months drying. It should be noted that the strain values shown in Figure 4.60 could possibly be overestimated due to the linear displacement measurements within the specimen height. As a result, the elastic modulus reported in Table 4.16 may be less than the actual values.

Table 4.16 Material properties of rammed earth from material characterization tests.

Rammed earth layer thickness – Drying period	Bulk density (kg/m <sup>3</sup> )		Compressive strength (MPa)		Tensile strength (MPa)		Elastic modulus (MPa)	
	Mean	Std. dev.	Mean	Std. dev.	Mean	Std. dev.	Mean	Std. dev.
120 mm – 1 month	1918	50	0.50	0.07	0.06	0.006	59.96	8.6
60 mm – 1 month	1985	32	0.56	0.04	0.11	0.006	66.76	27.2
120 mm – 6 months	2060	10	1.15	0.05	–	–	255.5	47.1
60 mm – 6 months	2080	17	1.18	0.08	–	–	186.5	74.5

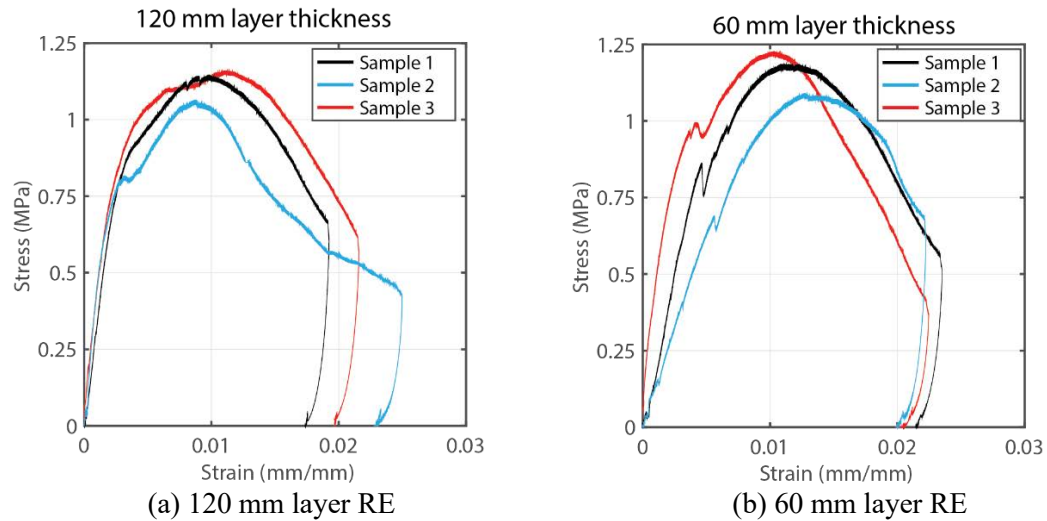


Figure 4.60 Compressive test results on cylindrical core samples at 6 months drying period.

#### 4.5.3 Test Setup and Instrumentation

Figure 4.61 shows the experimental test set up for specimen tested in shear. The wall was pulled in a horizontal direction with the help of a chain block. To apply uniform load on the wall, two planks were placed on two faces of the wall, and they are tied with nuts and bolts of 16 mm diameter. Torsion wire was then inserted through the holes in planks to wrap whole wall block. The load applied on the wall is recorded by a load cell (TLP-200kNB) which is placed in between connecting chain block and torsion wire wrapping the wall. The load was applied at the height of 720 mm from the base of the lower RE block. Displacement transducers were placed at the back of the specimens at a different height to measure the displacement. Four displacement transducer, two at the bottom and two at the top were placed. The data were recorded at a frequency of 100 Hz.

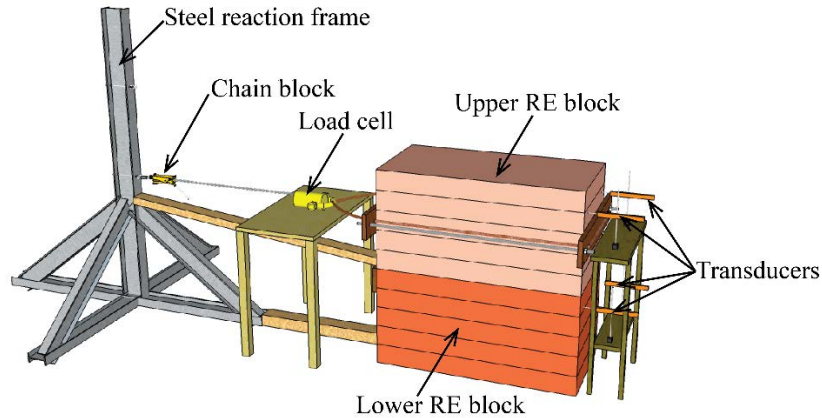


Figure 4.61 Test set up and instrumentation for R-120-S.

#### 4.5.4 Result and Discussion

Figure 4.62 presents the shear force versus shear displacement plots for all the test specimens tested in in-plane shear loading. Mean of two transducers at the top level is taken for displacement plots. The maximum shear load recorded was 13.55 kN for unreinforced specimen U-120-S, 17.57 kN for reinforced specimen R-120-S, and 19.73 kN for R-60-S. There was a 28.2% increment in in-plane shear strength for reinforced specimen R-120-S over the unreinforced one U-120-S. The increment in the strength of around 3.98 kN was contributed by the presence of dowel. The reinforced specimen with thinner (60 mm) rammed earth layer R-60-S showed 15% increment in strength over the reinforced specimen with thicker (120 mm) rammed earth layer R-120-S, contributed by denser and higher strength characteristics for rammed earth of R-60-S.

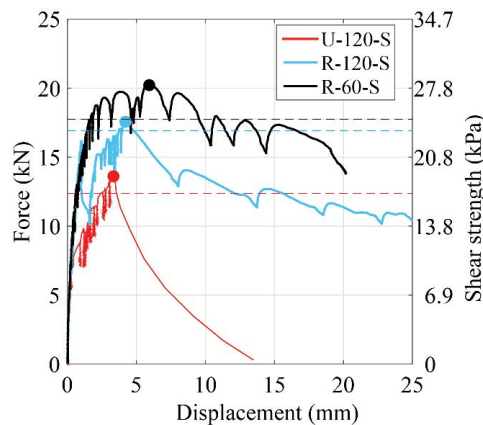


Figure 4.62 Shear force vs shear displacement: Experimental and Theoretical.

To study the strengthening effect of the dowel, the theoretical bearing strength of dowel,  $F_{dow}$ , is calculated given by the product of bearing resistance offered by rammed earth in compression ( $f_{bear}=0.5$  MPa) and cross-sectional bearing area of rammed earth ( $A_{bear}=120\times 80$  mm). The above



formulation gives theoretical  $F_{\text{dow}}$  equals 4.8 kN, which is relatively close to the experimentally observed value of 3.98 kN.  $F_{\text{dow}}$ , for experimental data, is slightly lower possibly because of the relatively softer inner section of rammed earth which is not well dried as the outer part from where the samples were extracted to get the compressive strength.

The theoretical shear strength of the tested specimens is assumed with a theoretical formulation given by Eq. (4.5):

$$F_{\text{th}} = F_s + F_{\text{dow}} \quad (4.5)$$

Where,

$F_{\text{th}}$  is the theoretical shear strength of the specimen;

$F_s$  is the shear strength of the unreinforced RE block interface computed by following equation Eq. (4.6):

$$F_s = (c + f_n \tan\phi) A_{\text{block}} \quad (4.6)$$

where

$c$  is the cohesion of the interface;

$f_n$  is the normal stress at the interface (based on mass density and geometry);

$\tan\phi$  is the friction coefficient; and

$A_{\text{block}}$  is the RE block cross-sectional area (1200 mm × 600 mm).

The straight dashed line in Figure 4.62 presents the theoretically computed shear strength for each specimen.

Figure 4.63 shows the failure patterns for all the specimens tested in shear. The specimens U-120-S failed with upper block sliding over the lower block. It should be noted that the diagonal crack in the lower block resulted when testing for the second time and the load was applied at that point. For R-120-S and R-60-S, the wall failed in a similar way as the unreinforced counterpart where the top block slide over the lower block. A shear crack was also observed below the RC dowel in case of R-120-S. In general, the specimen tested in shear showed similar cracking mechanism, where sliding failure was observed along the interface between the two rammed earth blocks.

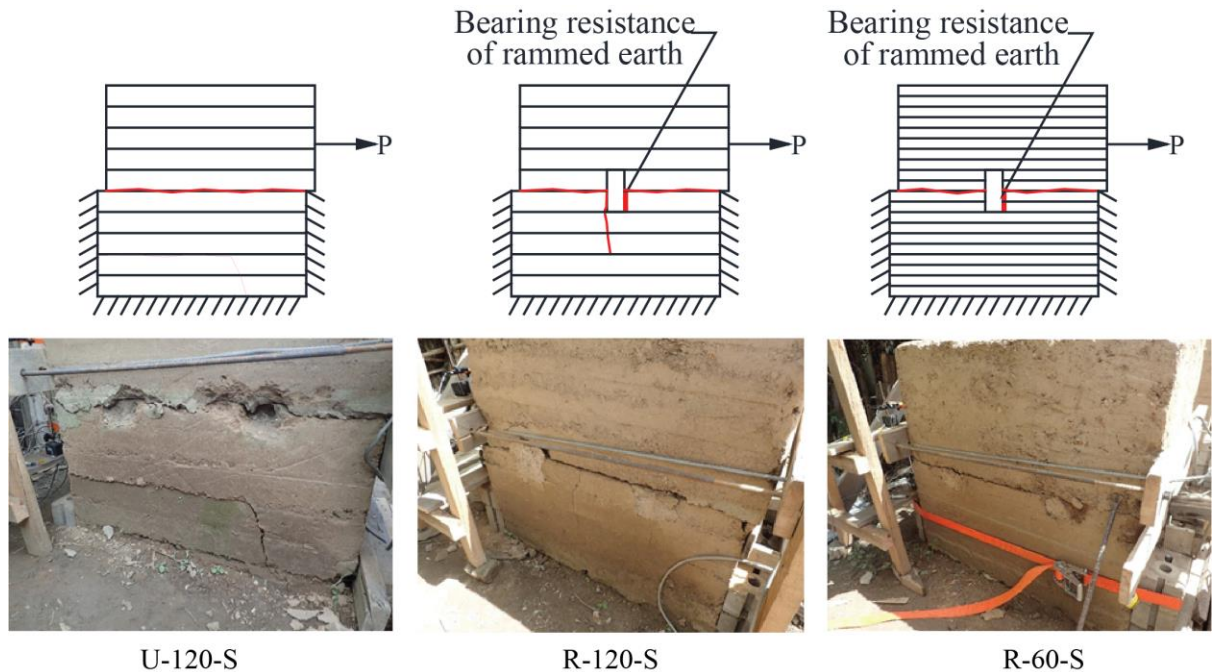


Figure 4.63 Failure pattern observed for U-120-S, R-120-S and R-60-S.

#### 4.6 Conclusions

The out-of-plane behaviour of rammed earth wall is studied while examining the effectiveness of various strengthening measures proposed for new construction and retrofitting the old house. A mesh-wrap retrofitting technique (Mesh-RE) and timber-framed (Timber-RE) retrofitting technique are chosen as a potential strengthening technique for existing rammed earth buildings. For the new construction, two strengthening technique are chosen where the first one involved use of reinforced concrete (RC) dowels and wedges (New-RE-A) and the second method involved use of RC wedges, posts and band (New-RE-B). Their feasibility and effectiveness were assessed by conducting a pull-down test on a one-storied full-scale wall with U-shape in plan. The loading was statically applied in out-of-plane direction with the excavator to excite the overturning mechanism. The use of mesh-wrapped and timber-framed retrofitting technique improved the load-carrying capacity by 1.72 and 1.09 times, respectively. The strength increment contributed by timber-framed retrofitting technique was minimal. For the new construction, the first strengthening technique, i.e., using RC dowels and wedges (New-RE-A) did not improve the strength, and its strength was 1.01 times the unreinforced. However, the second strengthening technique with the use of RC wedges, posts and band improved the strength significantly, and its strength was 3.19 times the unreinforced wall. The unreinforced failed with typical rocking characteristics and

collapse of the whole front facade wall, representing the vulnerability of rammed earth wall in out-of-plane. The use of all strengthening measures delayed the wall collapse and reduce the damage to the facade wall with a controlled failure mechanism.

A strengthening system for floor diaphragm was proposed where floor joists were anchored to the surrounding rammed earth wall with steel plates. To evaluate the efficiency of this system, pull-down test was carried out for two-storied full-scale wall with box-type in plan. This proposed system resulted in strong floor mechanism where the pull-down resistance of the wall was improved by 1.59 times the unreinforced counterpart.

The chapter also presented on the effectiveness of RC dowel in improving the shear strength of RE wall having different layer thickness (120 mm and 60 mm). The RC dowel was embedded vertically within the wall connecting two RE blocks. The use of RC dowel enhanced the load carrying capacity by 1.29 times the unreinforced counterpart. And comparing the strength of 120 mm layer thickness wall and 60 mm layer thickness wall, it was observed that the strength of thinner layer (60 mm) was 1.12 times the thicker layer wall (120 mm).

Based on the test observations, simple RC components like wedges, posts and bands are proposed for the new construction while the composite mesh-wrap technique is proposed for strengthening the existing buildings. As already mentioned, it is recommended to use a mesh of larger diameter to have the optimum effect of a proposed mesh-wrap retrofitting technique. Also, it is necessary to provide enough lapping length to avoid failure in the lapping region. The proposed strengthening measures are further verified through the full-scale test, which is discussed in Chapter 5.

## References

- [1] P. Wangmo, K. C. Shrestha, M. Miyamoto, and T. Aoki, "Assessment of out-of-plane behavior of rammed earth walls by pull-down tests," *Int. J. Archit. Herit.*, vol. 13, no. 2, pp. 273–287, 2019, doi: 10.1080/15583058.2018.1433903.
- [2] K. C. Shrestha *et al.*, "Strengthening of rammed earth structures with simple interventions," *J. Build. Eng.*, vol. 29, p. 101179, 2020, doi: 10.1016/j.jobee.2020.101179.
- [3] Wangmo, P.; Shrestha, K.C.; Aoki, T.; Miyamoto, M. Strengthening Strategies for Existing Rammed Earth Walls Subjected to Out-of-Plane Loading. **2020**, *1(3)*, 229–242,

doi:<https://doi.org/10.3390/civileng1030014>.

- [4] K. C. Shrestha, T. Aoki, M. Miyamoto, P. Wangmo, and Pema, “In-plane shear resistance between the rammed earth blocks with simple interventions: Experimentation and finite element study,” *Buildings*, vol. 10, no. 3, pp. 1–13, 2020, doi: 10.3390/buildings10030057.
- [5] DCHS, *Damage Assessment of Rammed Earth Buildings-After the September 18,2011 Earthquake*. Division for Conservation of Heritage Sites, Department of Culture, Ministry of Home and Cultural Affairs, Royal government of Bhutan, 2011.
- [6] K. Liu, M. Wang, and Y. Wang, “Seismic retrofitting of rural rammed earth buildings using externally bonded fibers,” *Constr. Build. Mater.*, vol. 100, pp. 91–101, 2015, doi: 10.1016/j.conbuildmat.2015.09.048.
- [7] M. Miyamoto, Pema, T. Aoki, and Y. Tominaga, “Pull-down test of the rammed earth walls at Paga Lhakhang in the Kingdom of Bhutan,” *Int. J. Sustain. Constr.*, vol. 2, no. 1, pp. 51–59, 2014, doi: 10.14575/gl/rehab2014/033.
- [8] H. R. Hamilton, J. McBride, and J. Grill, “Cyclic testing of rammed-earth walls containing post-tensioned reinforcement,” *Earthq. Spectra*, 2006, doi: 10.1193/1.2358382.
- [9] T. Konishi, M. Miyamoto, T. Aoki, N. Ehara, Pema, and P. Wangmo, “An experimental study on seismic strengthening method for traditional houses in the Kingdom of Bhutan,” *J. Struct. Eng.*, vol. 64B, 2017.
- [10] T. Zhou and B. Liu, “Experimental study on the shaking table tests of a modern inner-reinforced rammed earth structure,” *Constr. Build. Mater.*, 2019, doi: 10.1016/j.conbuildmat.2019.01.070.
- [11] T. L. Bui, T. T. Bui, Q. B. Bui, X. H. Nguyen, and A. Limam, “Out-of-plane behavior of rammed earth walls under seismic loading: Finite element simulation,” *Structures*, vol. 24, pp. 191–208, 2020, doi: 10.1016/j.istruc.2020.01.009.
- [12] J. S. J. Cheah, P. Walker, A. Heath, and T. K. K. B. Morgan, “Evaluating shear test methods for stabilised rammed earth,” *Proc. Inst. Civ. Eng. Constr. Mater.*, vol. 165, no. 6, pp. 325–334, 2012, doi: 10.1680/coma.10.00061.

- [13] L. Miccoli, U. Müller, and S. Pospíšil, “Rammed earth walls strengthened with polyester fabric strips: Experimental analysis under in-plane cyclic loading,” *Constr. Build. Mater.*, vol. 149, 2017, doi: 10.1016/j.conbuildmat.2017.05.115.
- [14] M. Pang, S. Yang, and Y. Zhang, “Experimental study of cement mortar-steel fiber reinforced rammed earth wall,” *Sustainability*, vol. 4, pp. 2630–2638, 2012, doi: 10.3390/su4102630.
- [15] Y. Wang, M. Wang, K. Liu, W. Pan, and X. Yang, “Shaking table tests on seismic retrofitting of rammed-earth structures,” *Bull. Earthq. Eng.*, vol. 15, no. 3, pp. 1037–1055, 2017, doi: 10.1007/s10518-016-9996-2.
- [16] ASTM Standard E8/E8M, “Tension Testing of Metallic Materials,” *ASTM International*. 2016, doi: 10.1520/E0008\_E0008M-16A.
- [17] ASTM C496, “Standard Test Method for Splitting Tensile Strength of Cylindrical Concrete Specimens,” *ASTM Int.*, 2011, doi: 10.1520/C0496.
- [18] ASTM C39, “Standard Test Method for Compressive Strength of Cylindrical Concrete Specimens: C39/C39M-18,” *American Society for Testing and Materials*. 2018.
- [19] J.I.S. Z2101, “Methods of Test for Woods,” *Japan Wood Res. Soc.* 2009.
- [20] Miccoli, L.; Oliveira, D. V.; Silva, R.A.; Müller, U.; Schueremans, L. Static behaviour of rammed earth: experimental testing and finite element modelling. *Mater. Struct. Constr.* 2015, 48, 3443–3456, doi:10.1617/s11527-014-0411-7.

# FULL-SCALE QUASI-STATIC TEST: ASSESSMENT OF SEISMIC PERFORMANCE OF RAMMED EARTH STRUCTURES

## CHAPTER 5

*This chapter is written with reference to a published paper titled “Influence of Traditional Building Practices in Seismic Vulnerability of Bhutanese Vernacular Rammed Earth Architecture”, 2020 [1], conference paper titled “Full–Scale Pull–Down Tests on a Two–Storeyed Rammed Earth Building with Possible Strengthening Interventions, 2019 [2] and “Mesh –wrap retrofitting for rammed earth buildings-Test results of full-scale static tests”, 2020 [3].*

### 5.1 Introduction

Rammed earth has been used as a traditional building technique throughout many parts of the world by humankind. The major centres for earthen structures include Asia (China, India, Nepal, Bhutan), North Africa, Australia, regions of North and South America, and Europe (France, Germany, and Spain).

Bhutan, in particular, the western region, has large numbers of rammed earth structures from rural homes to heritage buildings. The survey [4] has classified rural homes in five categories (Figure 5.1) based on the architectural style and configuration as following:

- a) **Type A:** It has rammed earth outer walls on all four sides on both upper and lower floors. There are few openings apart from some on the front. On the first floor, a wooden projecting floor (balcony) is added. This projecting part made of wood is supported by colonnades that have foundation stones or cantilevers projecting from a wall.
- b) **Type B:** It has rammed earth outer walls on all four sides on both upper and lower floors and also sidewalls made of rammed earth projecting towards the front. The balcony is constructed on the front face of the first floor between the sidewalls. On the front side of the balcony, a wooden structure (window or half-timber wall) is installed between pillars and supported by colonnades that have foundation stones.
- c) **Type C:** It has rammed earth outer walls on all four sides only on the lower floor. On the upper floor, only on the front face, a wooden structure (window or half-timber wall) is installed, between pillars, instead of a rammed earth wall.

- d) **Type D:** It has rammed earth outer walls on all four sides only on the lower floor. On the upper floor, on the front face and in front of both side faces, a wooden structure (*Rabsel*) is installed between pillars. At the front end position of both sidewalls on the upper floor, partition walls made of rammed earth are installed on both upper and lower floors.
- e) **Type E:** It has rammed earth outer walls on all four sides only on the lower floor. On the upper floor, on the front face and in front of both side faces, a wooden structure (*Rabsel*) is installed between pillars. There is no partition wall on both upper and lower floors.

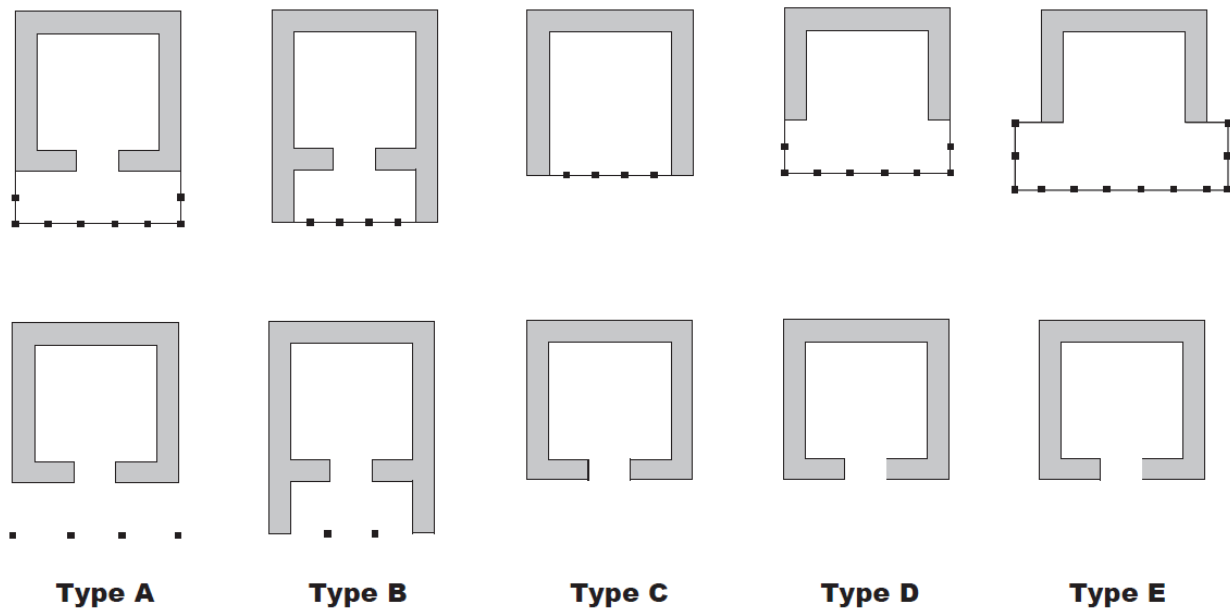


Figure 5.1 Classification of traditional houses based on the plans [4].

It was observed that the Type D plan was most popular and dominant amongst others as per the building typology study conducted by the Division for Conservation of Heritage Sites [5]. Therefore, the building specimens assessed in this study has the same plan as in Type D. Figure 5.2 shows one of the houses with type D.

The chapter will discuss the series of full-scale test conducted on a prototype rammed earth building specimens to understand their response under quasi-static loading. The strengthening techniques proposed in Chapter 4 is implemented, and their feasibility and effective is further verified. This chapter will also present the seismic evaluation of the rammed earth building with Type D plan following the existing general guidelines for rammed earth in Bhutan [6]. The limit states for the rammed earth buildings are proposed based on the capacity curve from the

experimental program. Further, a conventional fragility curve is developed using the capacity spectrum methods (CSM).



Figure 5.2 Rammed earth house with type D plan (Photo credit: NRICPT and DOC).

## 5.2 Seismic Evaluation of Rammed Earth Building

The regularity of stiffness and strength, and symmetry of configuration are the most critical factors governing the seismic performance of the building. The traditional Bhutanese rammed earth buildings are usually irregular in mass along the height as well as in the plan. To assess the weaknesses and the potential fragilities to seismic action, a detailed plan, sections and elevations of type D plan are prepared as shown in Figure 5.3, Figure 5.4 and Figure 5.5. For simplicity, the architectural features of the window are excluded in the design. In Figure 5.3, it is clear that the building shows a regular and compact plan in the first floor (1FL) but the presence of traditional window (rabsel) in the second floor (2FL) affects the overall symmetry of the building. The past earthquakes have proved poor performance of such structures [2, 7-10]. To clearly understand its vulnerability, a seismic evaluation is carried out based on the only available guideline for rammed earth buildings in Bhutan [6]. The guideline is developed based on the Indian standard codes, Eurocodes and building standard law of Japan. In the first part, a seismic design for new rammed earth construction is presented. The second part of the evaluation covers the evaluation for the existing rammed earth buildings.



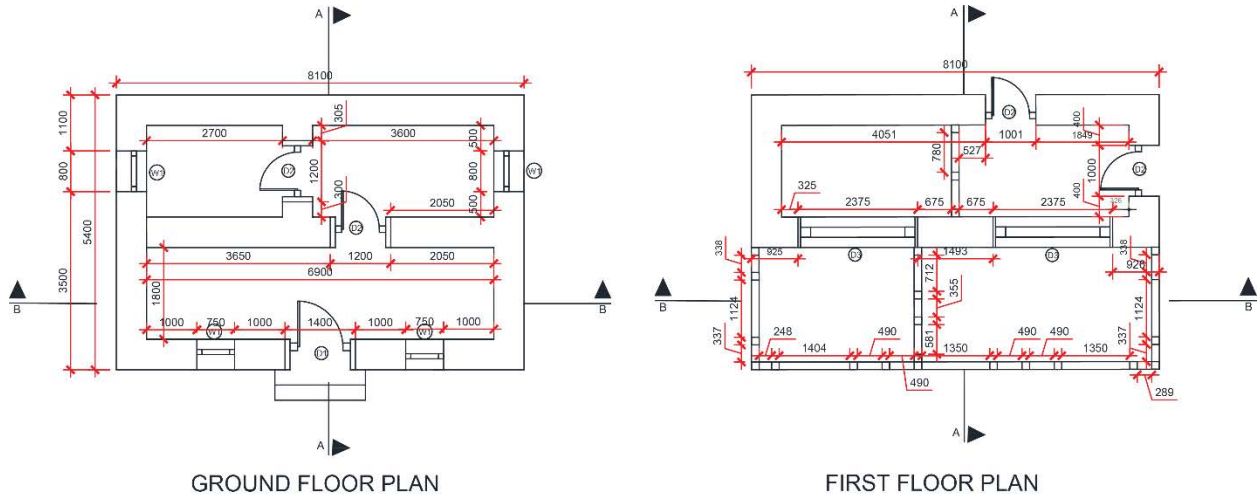


Figure 5.3 Plans of U-RE-SHORT.

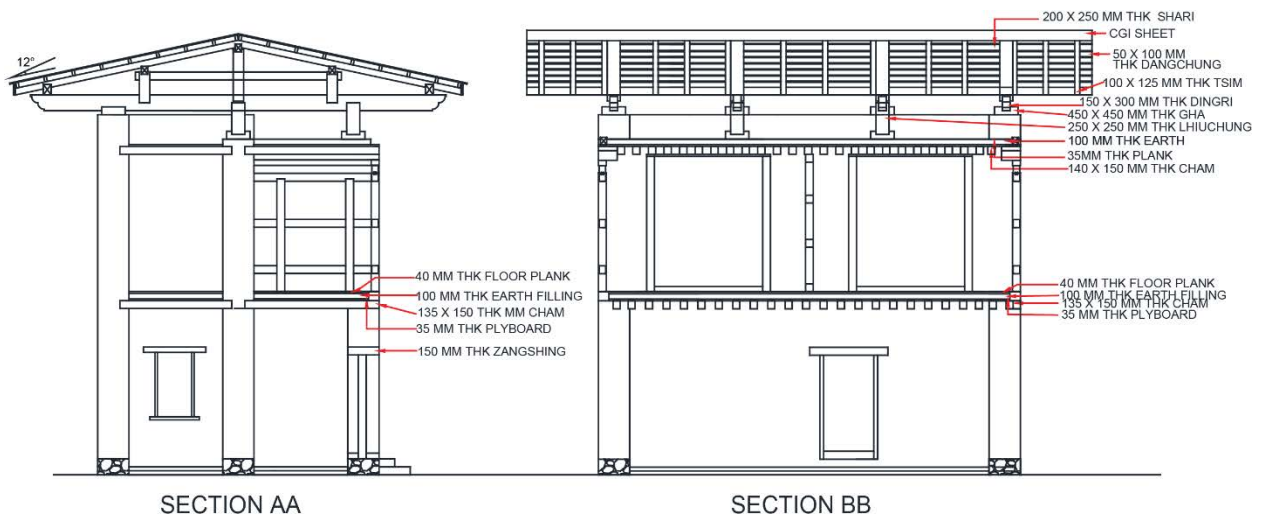


Figure 5.4 Sections of U-RE-SHORT.

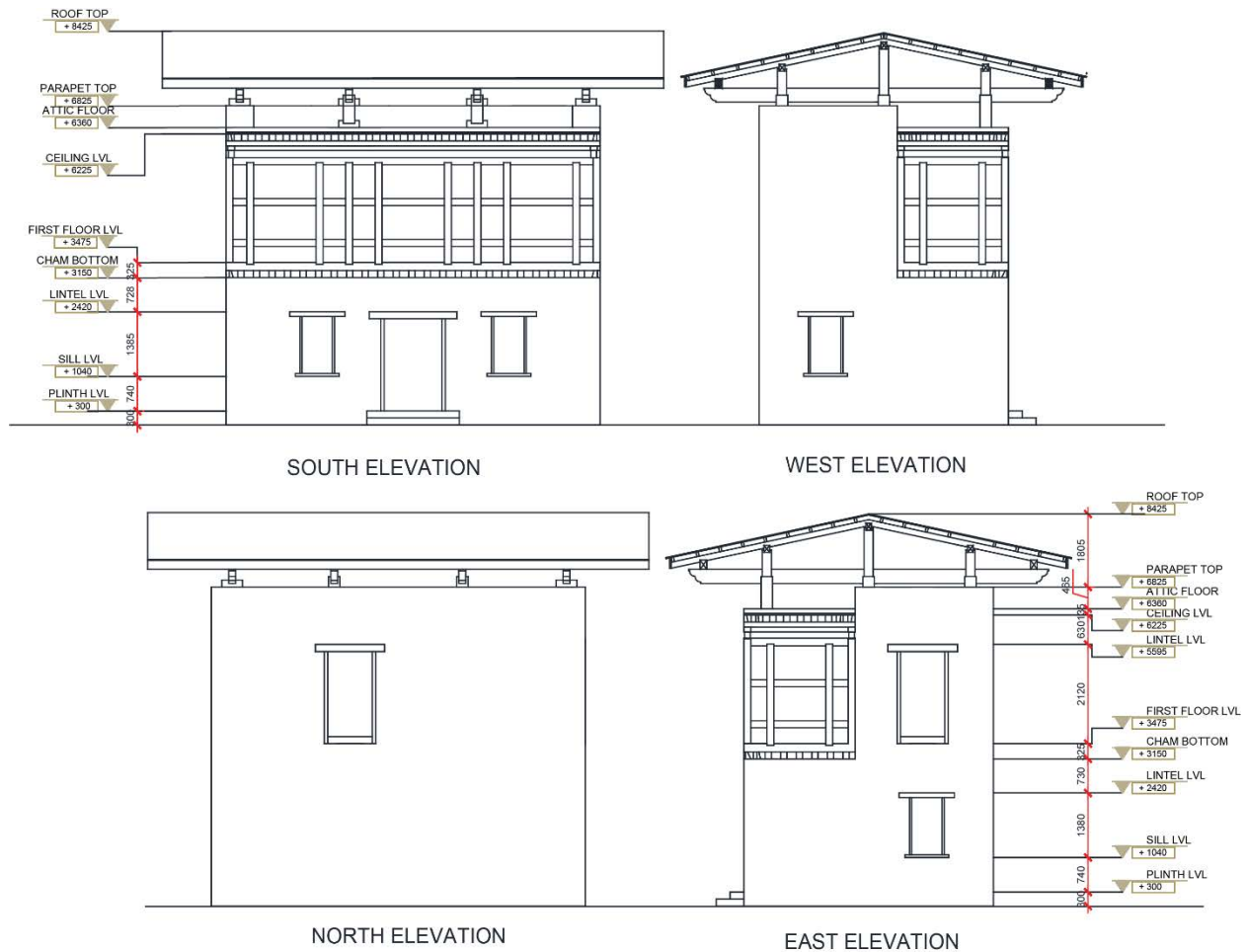


Figure 5.5 Elevations of U-RE-SHORT.

The guideline [6] proposes three phases of seismic design as follows:

- a) First phase of seismic design: Specification code
- b) Second phase of seismic design: Allowable Unit Stress calculation
- c) Third phase of seismic design: Horizontal load-carrying capacity

### 5.2.1. First phase of seismic design: specification code

#### *Material Properties*

The material properties used for the current evaluations are from the material characterization test, which is described in detail in later sections. The value used for each material properties are given below:

- i. Density of rammed earth:  $18.93 \text{ kN/m}^3$
- ii. Density of timber:  $4.38 \text{ kN/m}^3$
- iii. Compressive strength of RE,  $f_c$ :  $1.3 \text{ MPa}$

- iv. Tensile strength of RE,  $f_t = 0.15$  MPa

### ***Physical Properties***

1. Foundation structure: The traditional rammed earth buildings are constructed on top of the stone masonry wall. The height of the stone foundation varies from 300 mm to 900 mm, with an average value of 600 mm [5]. The height of the foundation is adequate as per the guideline.
2. Wall length: The maximum wall length must be less than 600 mm. The maximum wall length measured for each floor is given in Table 5.1. It exceeds the recommended value.

Table 5.1 Maximum wall length in each floor level.

Floor level	Maximum wall length $l$	Recommended value $(l_{max})$	Judgment
First floor	6900	6000	NG
Second floor	6900	6000	NG

3. Wall thickness: The adopted wall thickness is 600 mm, which is within the limit 580 and 900 mm.
4. Floor height: The floor height in both the floor level exceeds the limits.

Table 5.2 Floor height in each floor level.

Floor level	Maximum wall length $H$	Recommended value $(h_{max})$	Judgment
First floor	3300	2400-3000	NG
Second floor	3525	3000	NG

5. Aspect ratio: The aspect ratio is calculated as the ratio between wall height to the wall thickness. Table 5.3 shows the aspect ratio of the considered building exceeds the limit.

Table 5.3 Aspect ratio in each floor level.

Floor level	Wall height (h)	Wall thickness (t)	Aspect ratio	Recommended value	Judgment
First floor	3300	600	5500	5000	NG
Second floor	3525	600	5875	5000	NG

6. Shear span ratio: The shear span is the ratio between wall length and wall height. Table 5.4 shows that the shear span is within limits.

Table 5.4 Shear span ratio in each floor level.

Floor level	Wall length ( <i>l</i> )	Wall height ( <i>h</i> )	Shear-span ratio	Judgment
First floor				
<i>Longitudinal wall</i>	2700	3300	1.22	OK
<i>Transverse wall</i>	3600	3300	0.92	OK
<i>Longitudinal wall</i>	6900	3300	0.48	OK
<i>Transverse wall</i>	1800	3300	1.83	OK
Second floor				
<i>Longitudinal wall</i>	6900	3525	0.51	OK
<i>Transverse wall</i>	1800	3525	1.96	OK

The guideline indicates that the necessary length of the wall will depend on the material properties. In the absence of the data, the condition, as per Table 5.5, may apply.

The wall quantity is given by Eq.(5.1):

$$\text{Wall quantity, } L = \frac{\text{Total length of wall}}{\text{Floor Area}} \quad (5.1)$$

Necessary length,  $L_{om} = F_o L_o = 400\text{mm/m}^2$

$$\text{Condition, } L \geq L_{om} \quad (5.2)$$

Where,

L: wall quantity on each floor in each direction ( $\text{mm/m}^2$ )

$F_o$ : the seismic zone factor (1.0). This value should be derived from seismography.

$L_o$ : standard wall amount determined in Table 10 ( $\text{mm/m}^2$ )

$L_{om}$ : minimum wall amount determined in Table 10 ( $\text{mm/m}^2$ )

Table 5.5 Standard and minimum wall length ( $\text{mm/m}^2$ ).

Floor	Standard wall amount ( $L_o$ )	Minimum wall amount ( $L_{om}$ )
One storey or top floor	400	300
Second storey from the top floor	400	300
Third floor from the top floor	500	400

Table 5.6 Judgment for wall length (mm/m<sup>2</sup>).

	Wall length (mm)	Floor area			Wall Quantity, L (mm/m <sup>2</sup> )	Judgment
		Length (m)	Width (m)	Area (m <sup>2</sup> )		
First floor						
<i>Longitudinal wall</i>	19000	6.9	4.2	28.98	655.62	OK
<i>Transverse wall</i>	9800	6.9	4.2	28.98	338.16	NG
Second floor						
<i>Longitudinal wall</i>	10250	6.9	1.8	31.86	321.72	NG
<i>Transverse wall</i>	4800	8.1	2.4		150.66	NG

Note: Wall length should not include the openings and floor area refers to the area inside the exterior walls.

### 5.2.2 Second phase of seismic design: Allowable unit stress calculation

#### *Weight of the building*

The earthquake force is an inertia force that acts on each mass of the structure and acts throughout the structure. It is proportional to the mass and the acceleration. In a real structure, the mass is distributed throughout the structure; however, for the current analysis, the masses are lumped at the centre of the floor, as shown in Figure 5.6 for convenience. The mass of the structure is lumped at a floor level. The mass of the roof floor (RFL) includes the mass of the whole roof structure, roof floor and upper part of the second floor (2FL). The mass of the 2FL includes half of the storey above and half of the storey below. The force  $Q_i$  and  $M_i$  is the lateral force and lumped masses, respectively acting on individual floor level.

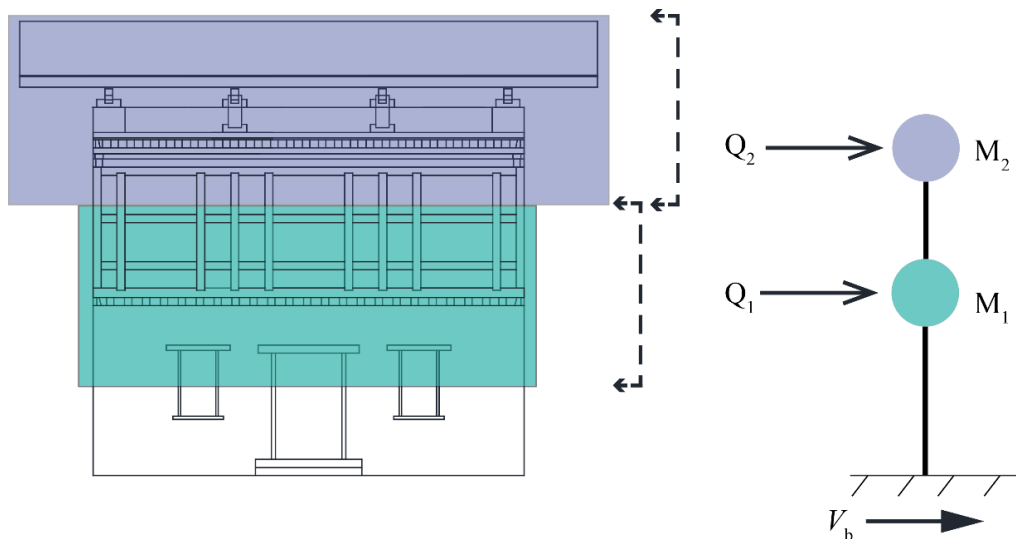


Figure 5.6 Lumped mass on the floor level.

Seismic weight  $W$  is calculated as the sum of the dead load and live load. Here, the dead load is calculated as the product of material volume and the density of each material. The densities are obtained from the material test reported in Chapter 4 and Chapter 5. The live load associated with the use of floor is considered  $2 \text{ kN/m}^2$  as per Indian standard code for residential buildings [11]. However, only 25% of the live load is considered for live load less than  $3 \text{ kN/m}^2$  based on the IS 1893 (Part-I):2000 [12]. The summary of loads on each floor is presented in Table 5.7.

Table 5.7 Dead load and live load.

Floor	Total Dead Load (kN)	Live load (kN)	Seismic weight (kN)
2FL	912.7	14.36	947.16
RFL	393.89	11.88	422.41
Total seismic weight ( $W$ )			<b>1333 kN</b>

### ***Seismic Force***

The seismic force is computed based on building standard law of Japan and IS codes.

#### *a. Following Building Standard Law of Japan*

The lateral seismic force of the  $i$ -th storey,  $Q_i$  above the ground level shall be determined as follows:

$$Q_i = C_i W_i \quad (5.3)$$

Where,

$C_i$  is the seismic shear coefficient of the  $i$ -th storey; and

$W_i$  is the weight of the building above the  $i$ -th storey.

$$C_i = Z R_t A_i \alpha_h \quad (5.4)$$

Where,

$Z$  is the zone factor. Since the country does not have the seismography, the zone factor here is assumed as 1.

$R_t$  is the vibrational characteristic factor derived based on Table 5.8 and Table 5.9. For  $T < T_c$ ,  $R_t = 1.0$ .

Vertical Distribution Factor ( $A_i$ ) is calculated using Eq. (5.5):

$$A_i = 1 + \left( \frac{1}{\sqrt{\alpha_i}} - \alpha_1 \right) \frac{2T}{1+3T} \quad (5.5)$$

Where,

$\alpha_i$  is the normalized weight of the  $i^{\text{th}}$  storey, which is calculated as the weight above the  $i^{\text{th}}$  storey divided by the weight above the ground level as follows:

$$\alpha_i = \frac{\sum_{j=i}^n w_j}{\sum_{j=1}^n w_j} = \frac{W_i}{W} \quad (5.6)$$

$$\alpha_i = \frac{\text{Total permanent load added to imposed load above story } i}{\text{Total permanent load added to imposed load}}$$

The design values of the horizontal seismic coefficient,  $\alpha_h$

$$\alpha_h = \beta I \alpha_o \quad (5.7)$$

Where,

$\beta$  value of the soil-foundation system is derived from Table 5.10.

$\alpha_o$  is the basic horizontal seismic coefficient, given as follows:

- Allowable unit stress limit (Medium earthquake) = 0.08
- Horizontal load carrying capacity (Severe earthquake) = 0.40

Table 5.8 Vibration Characteristics Factor.

T	$T < T_c$	$T_c \leq T < 2T_c$	$T \geq 2T_c$
$R_t$	1.0	$R_t = 1 - 0.2 \left( \frac{T}{T_c} - 1 \right)^2$	$\frac{1.6T_c}{T}$

Where, T: Fundamental natural period(s) of the building (0.19 sec)

T<sub>c</sub>: Critical period(s) of the soil (0.6 from Table 5.9)

Table 5.9 Classification of soil.

Soil profile	Ground characteristics	T <sub>c</sub> (sec)
Type-I (Hard soil)	Ground consisting of rock, hard sandy gravel, etc., classified as tertiary or older, or Ground whose period, estimated by calculation or by other investigations, is equivalent to that of the above.	0.4
Type-II (Medium soil)	Other than Type I and Type III	0.6
Type-III (Soft soil)	Aluminum consisting of soft delta deposits, topsoil, mud, or the like (including fills if any), whose depth is 30m or more, land obtained by reclamation of marsh, muddy sea bottom, etc., where the depth of the reclaimed ground is 3m or more and where 30years have not yet elapsed since the time of reclamation, or Ground whose period, estimated by calculation or by other investigations, is equivalent to that of the above.	0.8

Table 5.10 Value of  $\beta$  for different soil foundation systems.

Type of soil mainly constituting the foundation	Piles passing through any soil but resting on soil type I	Piles not covered under column 3	Raft foundation	Combined or isolated RCC footing with tie beams	Isolated RCC footing without tie beams or unreinforced strip foundations	Well foundations	Stone foundation of rammed earth and random stone masonry
Type-I: Rock or Hard soils	1.0		1.0	1.0	1.0	1.0	1.0
Type-II: Medium Soil	1.0	1.0	1.0	1.0	1.2	1.2	<b>2.0</b>
Type-III: Soft Soil	1.0	1.2	1.0	1.2	1.5	1.5	2.5



Based on the above mentioned criterias, the values for each parameters considered are presented in table 5.11 for calculations. The summary of the calculation is shown in Table 5.12. The table also presents the base shear value,  $V_b$ , calculated as the summation of the lateral seismic forces.

Table 5.11 Parameters for the structural calculations.

Particulars	Specifications	Values
Type of soil	Type II (Medium)	
Soil-Foundation System, $\beta$	Stone foundation	2.00
Type of structure, I	Importance factor	1.00
Design Fundamental time-period, T (sec)	From microtremor measurement. The “T” is also calculated with empirical formula = $0.03*H$ , where H is the height of the building	0.19
Seismic Zone factor, Z	Need to be derived from seismography	1.00
Shear factor, $C_o$	Serviceability Limit state- SLS	0.20
	Ultimate Limit State- ULS	1.00
Basic horizontal seismic coefficient, $\alpha_o$	Allowable unit stress limit (Medium earthquake)	0.08
	Horizontal load carrying capacity (Severe earthquake)	0.40
Vibration Characteristic factor, $R_t$	Derived from observation of surface layer of ground	1.00

Table 5.12 Summary of structural calculation for seismic shear force.

Design	Floor level	$W_i$ (kN)	$\alpha_i = \frac{W_i}{\sum W_i}$	$A_i$	$\alpha_h$	$C_i$	$Q_i$ (kN)	$V_b$ (kN)
Allowable unit stress limit (Medium EQ)	RFL	405.77	0.31	1.36	0.16	0.22	89.27	302.52
	2FL	1332.83	1.00	1.00	0.16	0.16	213.25	
Horizontal load carrying capacity (Large EQ)	RFL	405.77	0.31	1.36	0.80	1.09	443.09	1509.36
	2FL	1332.83	1.00	1.00	0.80	0.80	1066.26	

b. As per IS 1893 (Part 1):2002, the lateral force,  $Q_i$ , along each floor is calculated from the Eq. (5.8) as following:

$$Q_i = V_b \frac{W_i h_i^2}{\sum_{i=1}^n W_i h_i^2} \quad (5.8)$$

Where,

$V_b$  is the design lateral base shear, obtained from Eq. (5.9)

$$V_b = A_h W_t \quad (5.9)$$

Where,

$V_b$  is the design base shear

$W_t$  is the seismic weight of the building (1333 kN from Table 5.7)

$A_h$  is the design horizontal base shear coefficient given by Eq. (5.10)

$$A_h = \frac{ZI S_a}{2R g} \quad (5.10)$$

Where,

$Z$  is the zone factor taken as 0.36 for very severe seismic zone,

$I$  is the importance factor taken as 1 for a residential building,

$S_a/g$  is the spectral acceleration coefficient taken as 2.5 for a natural time period of approximately 0.2 seconds for a two-storied masonry building, and

$R$  is the response reduction factor taken as 1.5 for an unreinforced load-bearing masonry wall building [13].

The lateral force distribution in each floor is presented in Table 5.13.

Table 5.13 Lateral Force distribution in each floor.

Floor	$W_i$	$h_i$	$h_i^2$	$W_i h_i^2$	$V_b$	$Q_i$
RFL	405.77	6.168	38.05	15437.20	399.85	241.00
2FL	927.06	3.313	10.98	10175.38	399.85	158.85
			$\sum W_i h_i^2$	76467.91		

### ***Shear stress verification***

It is necessary to confirm that stresses acting upon the sections of wall elements necessary for medium-scale earthquake motion do not exceed the allowable stress, as shown in Table 5.14. The confirmation results are tabulated in Table 5.15 and 5.16 for a medium level and large earthquake, respectively.

Table 5.14 Allowable unit stress.

Design	Compression	Tension (Shear)	
		Allowable unit stress calculation	$2f_c/3$
Horizontal load-carrying capacity calculation	$f_c$	$f_c/10$	0.13 N/mm <sup>2</sup>

$f_c = 1.3 \text{ N/mm}^2$  from material characterization test

Table 5.15 Confirmation results of shear stress for medium-level EQ.

Floor	Direction	$Q_i$ (kN)	A (m <sup>2</sup> )	$\tau$ (N/mm <sup>2</sup> )	Allowable Unit Stress (N/mm <sup>2</sup> )	Judge
RFL	Longitudinal	89.27	6.15	0.01	0.09	OK
	Transverse	89.27	2.88	0.03	0.09	OK
2FL	Longitudinal	213.25	11.4	0.02	0.09	OK
	Transverse	213.25	5.88	0.04	0.09	OK

Table 5.16 Allowable shear stress for a large-level earthquake.

Floor	Direction	$Q_i$ (kN)	A (m <sup>2</sup> )	$\tau$ (N/mm <sup>2</sup> )	Allowable Unit Stress (N/mm <sup>2</sup> )	Judgement
RFL	Longitudinal	443.09	6.15	0.07	0.13	OK
	Transverse	443.09	2.88	0.15	0.13	NG
SFL	Longitudinal	1066.26	11.4	0.09	0.13	OK
	Transverse	1066.26	5.88	0.18	0.13	NG

### ***Allowable storey drift angle verification***

The allowable storey drift angle,  $\gamma_i$  is given by Eq. (5.11). This value is based on the experimental results where the building undergoes only moderate damages without detachment of any building components within the specified storey drift angle.

$$\gamma_i \leq \frac{1}{500} \quad (5.11)$$

Here,

$$\gamma = \frac{\tau}{G} \quad (5.12)$$

$$G = \frac{E}{2(1+\nu)} \quad (5.13)$$

Where,

$\tau$  = shear stress

G = Shear modulus

$\nu$  = Poison's ratio (Take as 0.15)

Table 5.17 Storey drift angle verification.

Floor	Direction	$\tau$ (N/mm <sup>2</sup> )	G (N/mm <sup>2</sup> )	$\gamma=\tau/G$	Allowable storey drift angle	Judgment
RFL	Longitudinal	0.07	210.59	0.0003	0.002	OK
	Transverse	0.15	210.59	0.0007	0.002	OK
SFL	Longitudinal	0.09	210.59	0.0004	0.002	OK
	Transverse	0.18	210.59	0.0009	0.002	OK

### ***Stiffness ratio and eccentricity ratio***

The stiffness ratio is the indicator of the balance of vertical hardness on each floor of the building, and the eccentricity ratio is the indicator of the balance of horizontal hardness on each floor.

The stiffness ratio,  $R_i$  is given by:

$$R_i = \frac{r_i}{\bar{r}} \quad (5.14)$$

Where,

Storey stiffness,  $r_i = \frac{1}{\gamma_i}$

$\bar{r} = \text{Average of } r_i$

Condition:  $R_i \geq 0.6$  (5.15)

Table 5.18 Stiffness ratio verification.

Floor	Direction	$r_i$	$\bar{r}$	$R_i$	Judgement
RFL	Longitudinal	2922.88	2587.19	1.13	OK
	Transverse	1368.76	1265.03	1.08	OK
SFL	Longitudinal	2251.50	2587.19	0.87	OK
	Transverse	1161.30	1265.03	0.92	OK

The eccentricity ratio,  $R_e$  is given by Eq. (5.18), and the summary is shown in Table 5.19.

$$R_i = \frac{e}{r_e} \quad (5.16)$$

Where,

$e$  is the eccentric distance

$r_e$  is the elasticity radius.

$$r_e = \sqrt{\frac{K_r}{\Sigma K}} \quad (5.17)$$

$K_r$  is the torsional stiffness, and  $\Sigma K$  is the sum of horizontal stiffness.

Condition:  $R_e \leq 0.6$  (5.18)

Table 5.19 Eccentricity ratio verification.

Floor	Direction	$e$ (m)	$r_e$ (m)	$R_e$	Judgement	$F_{es}$
RFL	Longitudinal	0.38	3.10	0.12	OK	1.00
	Transverse	0.08	0.05	1.59	NG	1.50
SFL	Longitudinal	0.02	3.22	0.01	OK	1.00
	Transverse	0.15	0.07	2.16	NG	1.50

### 5.2.3 Third phase of seismic design: Horizontal load-carrying capacity

The horizontal load carrying capacity calculations is carried as follows, and the results are tabulated in Table 5.20.

$$Q_u \geq Q_{un} \quad (5.19)$$

$$Q_{un} = D_s F_{es} Q_{ud} \quad (5.20)$$

Where,

$Q_u$ : Horizontal load-carrying capacity of each storey (in kN)

$Q_{un}$ : Required value of horizontal load-carrying capacity of each storey (in kN)

$D_s$ : Structural characteristics factor, considering damping characteristics and ductility of each storey. Here,  $D_s = 1$ .

$F_{es}$ : Shape factor, representing stiffness ratio and eccentricity ratio (up to 3.0 for irregular structure).

$$F_{es} = F_e F_s \quad (5.21)$$

$F_s$ : Shape factor by stiffness ratio

$F_e$ : Shape factor by eccentricity ratio

$Q_{ud}$ : Horizontal force acting upon each storey due to seismic force ( $\alpha_o \geq 0.4$ ) (in kN)

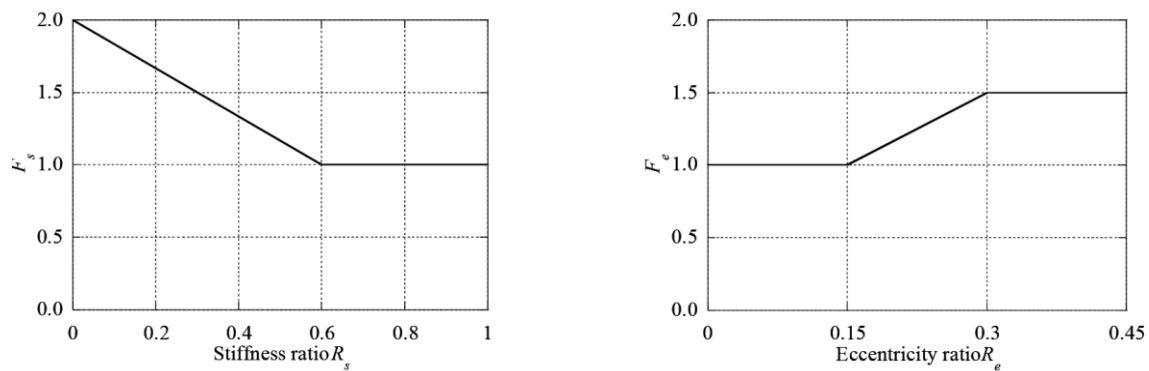


Figure 5.7 Shape factor by stiffness ratio and Shape factor by eccentricity ratio.

Table 5.20 Confirmation results for third phase of seismic design.

Floor	Direction	$Q_{un}$ (kN)	$Q_u$ (kN)	Judgement
RFL	Longitudinal	443.1	799.5	OK
	Transverse	664.6	374.4	NG
SFL	Longitudinal	1066.3	1482.0	OK
	Transverse	1599.4	764.4	NG

Based on the structural analysis carried in this section, it is confirmed that the building is not safe under a severe earthquake. Therefore, it is necessary to carry out the strengthening measures for such building type. However, it should be noted that these buildings (rural rammed earth houses) are preserved and promoted as the heritage buildings in Bhutan. Therefore, in the present chapter, the rectifications of eccentricity are not carried out, respecting the associated heritage values of such building typology. The chapter only explores the strengthening methods based on the

recommendations from chapter four for both new construction and old existing buildings. The details of the strengthening methods carried out are discussed in detail in section 5.3.

### 5.3 Specimens and Materials

Five full-scale rammed earth buildings having the same geometry and architectural plan are considered for the test. The details of the specimen showing plans, sections and elevations are already presented in Figure 5.3, Figure 5.4 and Figure 5.5, respectively. The specimens were the replication of the Bhutanese rammed earth building with dominating typology having two stories, where the ground floor has solid walls with small openings for doors and windows, and the first floor has a large opening in the front façade. The building specimen had a floor area of 8.1 m × 5.4 m and 6.83 m height excluding the roof. The thickness of the wall was maintained 600 mm throughout the height, as seen in the traditional houses. The plan in ground floor consists two external and one internal longitudinal load-bearing walls, linking east and west walls, and two external transverse walls and the short inner transverse wall which connected internal longitudinal wall with the north wall (Figure 5.3). However, in the first-floor plan, the whole south wall and part of the east and west wall are covered by the traditional window called *Rabsel* (Figure 5.3 and Figure 5.5).

Two buildings were constructed without any seismic features, representing the actual rural homes in Bhutan, and they served as the reference building. However, they were loading differently during experimentation. One of the building was loaded in its short span while other was loaded in the long span. The same set of buildings were later retrofitted after the first phase of the test. They were tested again under the same loading conditions, and the direction of loading was maintained the same as in the initial phase of testing. Another building was constructed with reinforcement, and it was loaded in a shorter span. The numerology of the specimens is based on the strengthening technique used and the loading direction as following:

- a) Unreinforced RE loaded in short span (U-RE-SHORT)
- b) Unreinforced RE loaded in long span (U-RE-LONG)
- c) Retrofitted RE loaded in short span (R-RE-SHORT)
- d) Retrofitted loaded in long span (R-RE-LONG)
- e) Reinforced RE loaded in short span (New-RE-SHORT)

The details of each specimen are described in the following sections with the details on strengthening methods.

### **5.3.1 Unreinforced RE Loaded in the Short Span (U-RE-SHORT)**

The construction technique of rammed earth wall follows the same pattern as detailed in Chapter 4. The soil used for the specimen was selected from the nearby site and then stocked near the construction site. Larger pebbles were removed from the soil; however, smaller pebbles were left unremoved. Following, the soil was prepared to get a suitable mixture by checking the right amount of water content through a traditional field test. A handful of moist earth is squeezed and tossed up in the air, about a meter away from the ground; the mixture is considered suitable if falling back on the ground, breaks into two or three major pieces [13]. Here, the building specimen was directly constructed on the strong RC floor without laying the stone foundation. The wooden formwork was set consisting of all member as described in Chapter 2. The moistened soil was then laid in layers inside a formwork; the layer thickness was about 200 mm. The soil was compacted manually by ramming tools till the layer thickness was about 100 mm. Two different types of rammers were used here, having different base shapes. A rammer with hammerhead was used for normal compaction, and smooth finishing at the edges was achieved using a rammer with wedge head. One completed rammed earth block consisted of 600 mm height and 600 mm thickness, and the length of each block differed depending on the location of the openings like door and windows. Each block comprised six rammed earth layers whose thickness was 100 mm at its final compaction. The blocks at the corners and junctions are interwoven to avoid continuous head joint, as seen in Figure 5.8. The plastic at the plinth level was provided to protect the wall from rainwater. The construction of the test specimen was completed in September 2018 and tested in December 2018 after a drying period of three months. Shrinkage cracks were observed during the drying period, which is generally observed for rammed earth walls. The shrinkage cracks were documented before the test, and they are marked in Figure 5.9 with the approximate crack widths observed in millimetre (marked by red ink). The cracks appeared along the joints and openings.





Figure 5.8 Isometric view of U-RE-SHORT.

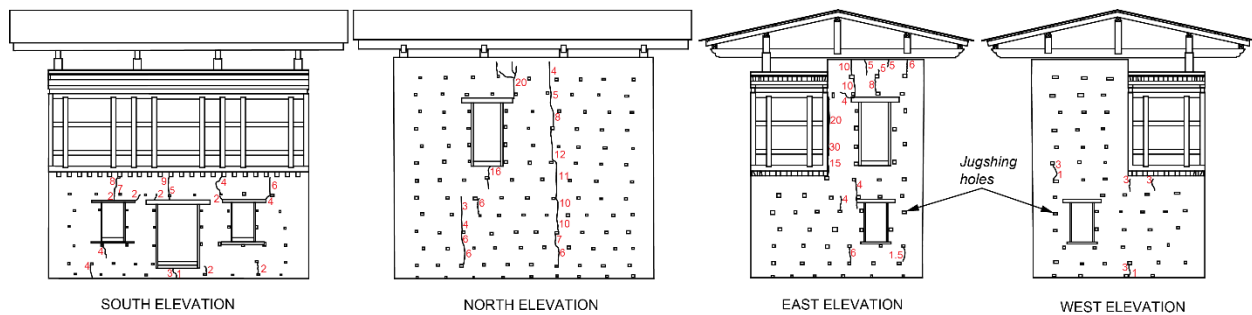


Figure 5.9 Shrinkage cracks observed in U-RE-SHORT during the drying period.

### 5.3.2 Unreinforced RE Loaded in Long Span (U-RE-LONG)

The specimen U-RE-LONG is constructed following the same procedure followed in U-RE-SHORT. It also had the same geometry and dimension, as already mentioned. The specimen was constructed simultaneously along with the U-RE-SHORT. So, the construction of U-RE-LONG was also completed in September 2018 and tested in December 2018 after three months of the drying period. The only difference between the U-RE-SHORT and U-RE-LONG is the direction of loading placed during the experiment, which is discussed in detail in the later section. Figure 5.10 presents the isometric view of U-RE-LONG. Even for this specimen, shrinkage cracks were observed during the drying period, and the detail is presented in Figure 5.11, showing its location and crack widths in mm.



Figure 5.10 Isometric view of U-RE-LONG.

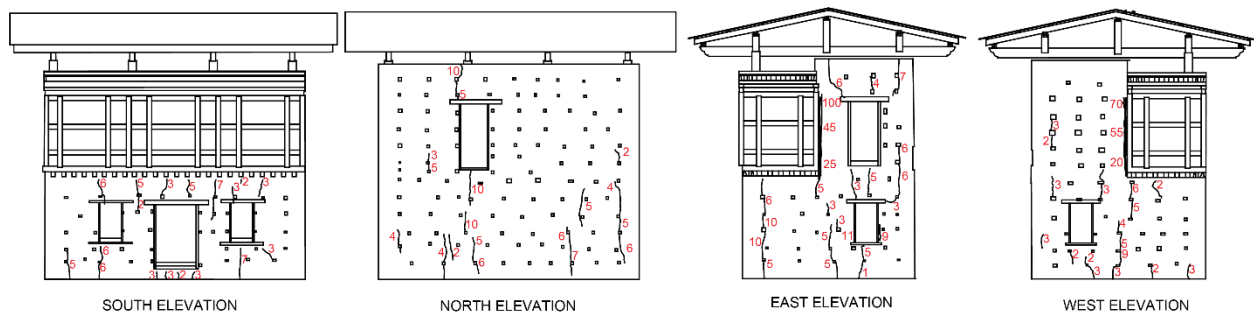


Figure 5.11 Shrinkage cracks observed in U-RE-LONG during the drying period.

### 5.3.3 Retrofitted RE Loaded in Short Span (R-RE-SHORT)

As previously mentioned, immediately after the first phase of testing the unreinforced buildings RE-U-SHORT, the retrofitting works were carried out, and it was renamed as RE-R-SHORT. The retrofitting work began in late December 2018. The retrofitting procedures are followed the same as detailed in Chapter 4. However, a stronger mesh is used here, as recommended in Chapter 4 to have the optimum effect of the proposed mesh-wrap retrofitting technique. Furthermore, here, longer lapping length is provided to prevent the mesh failure at the lapping regions. Even here, the selection of the mesh and other materials were based on the availability in the local market. The material used here is described in detail in the following.

#### 5.3.3.1 Retrofitting material

##### *Mesh*

Based on the recommendations from the previous chapter, a stronger mesh with larger diameter was chosen to strengthen the wall. The chosen mesh was 12 gauge ( $\phi 1.83$  mm) with  $34 \times 34$  mm<sup>2</sup>

openings. It served as the main mesh (M-mesh), provided in the entire wall from both inside and outside. Due to its size limitation, lapping was unavoidable. At least 600 mm overlap was provided in both horizontal and vertical directions. As a further intervention and to prevent the creation of weak joints at the lapping regions, another mesh, which was more flexible and easier to bend was necessary. It was provided as a lapping mesh (L-mesh) over the M-mesh at their joints, corners and junctions. L-mesh comprised 1.45mm diameter and an opening of 28x28 mm<sup>2</sup>. It was the same mesh used to retrofit the U-shaped wall in chapter 4. The mesh steel mesh has the yield and fracture stress of 355 MPa and 425 MPa, respectively, for L-mesh, derived as per the ASTM E8 2016 standards [15]. These values for M-mesh are 335.65 MPa and 517.4 MPa, respectively. The tensile test set up is presented in Figure 5.12, along with the results.

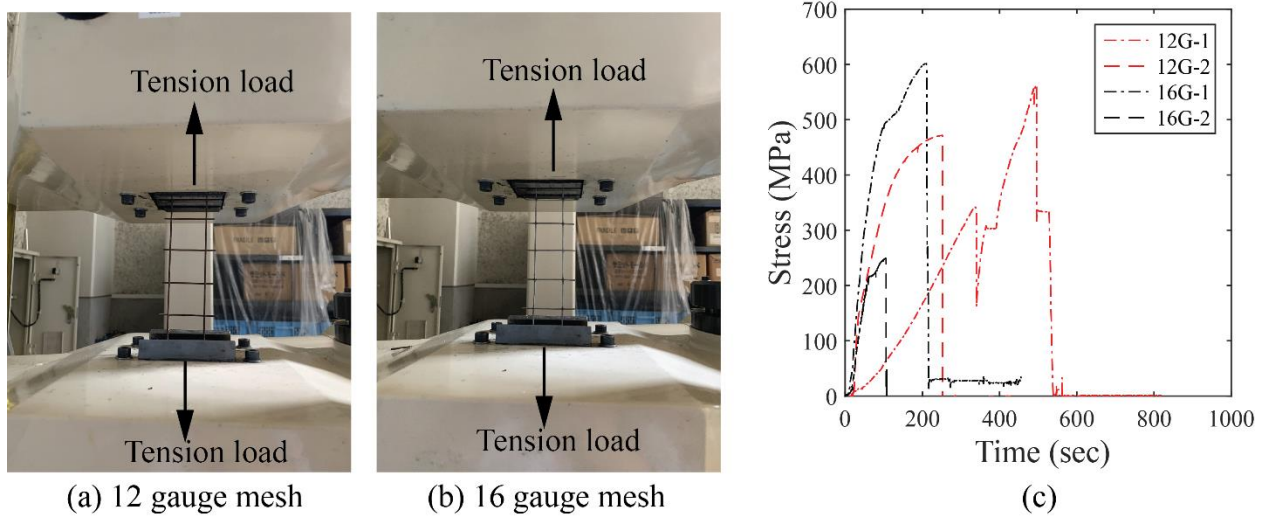


Figure 5.12 Material test set up: (a) and (b); (c) test results.

### ***U-hook and anchor rod***

Firstly, U-hooks were used to affix the meshes to the walls. Anchor rods with nuts were later used to connect the meshes at two faces of the wall firmly. Threaded bars were fabricated depending on the wall thickness. It had 600 mm length with 12 mm diameter. These threaded bars were inserted through the *jugshing* holes, an opening created upon removal of *jugshing*. Figure 5.13 shows the U-hook and threaded bar used for anchoring and connecting the meshes together.



(a)



(b)

Figure 5.13 Fastener and anchorage: (a) U-hook; (b) Anchor rod.

### ***Cement mortar plaster***

The covering to the mesh was provided with the cement plaster having cement sand ratio 1:3. Cement mortar was applied over the mesh to provide good bonding between the wall and the mesh. The cement plaster also enhanced the aesthetic view of the wall surface with smooth finishing. Two governing criteria were considered for the selection of mortar: (1) availability in the local market and (2) affordability. Based on these guidelines, cement mortar with cement and sand ratio of 1:3 was chosen.

### **5.3.3.2 Retrofitting process**

The U-RE-SHORT, after its first phase of testing, underwent several damages. The retrofitting works were carried out immediately in late December 2018. The retrofitting technique here involved the use of locally available mesh, wrapped around the building on both faces, and they were connected by the threaded bars. The mesh-wrap retrofitting technique was provided only for the in-plane walls in both faces of the walls. After retrofitting, the specimen was renamed R-RE-SHORT. The details of the mesh layout are presented in Figure 5.14. The area shaded by green colour in elevations represents the area where M-mesh are fixed, whereas the area shaded by pink represents the area where L-mesh were provided. As seen in the figure, the M-mesh were fixed throughout the in-plane walls, i.e. east and west elevations only. However, for the out-of-plane walls, the M-mesh was provided at the floor levels where the loading was applied (shown in north elevation). It should be noted that the L-mesh was provided over the M-mesh, therefore the mesh

at loading levels in north elevations appear pink in colour. The mesh at a loading level of south elevation was avoided due to the presence of timber elements. The L-mesh were provided over the joints of M-mesh both in horizontal and vertical directions to avoid the local failure of M-mesh. Furthermore, they were also provided in the corners and wall junctions. The mesh layout in exterior and interior wall can be seen in plans of Figure 5.14. The cross-section of the wall shows the details of anchor rods and mesh-wrap retrofitting details.

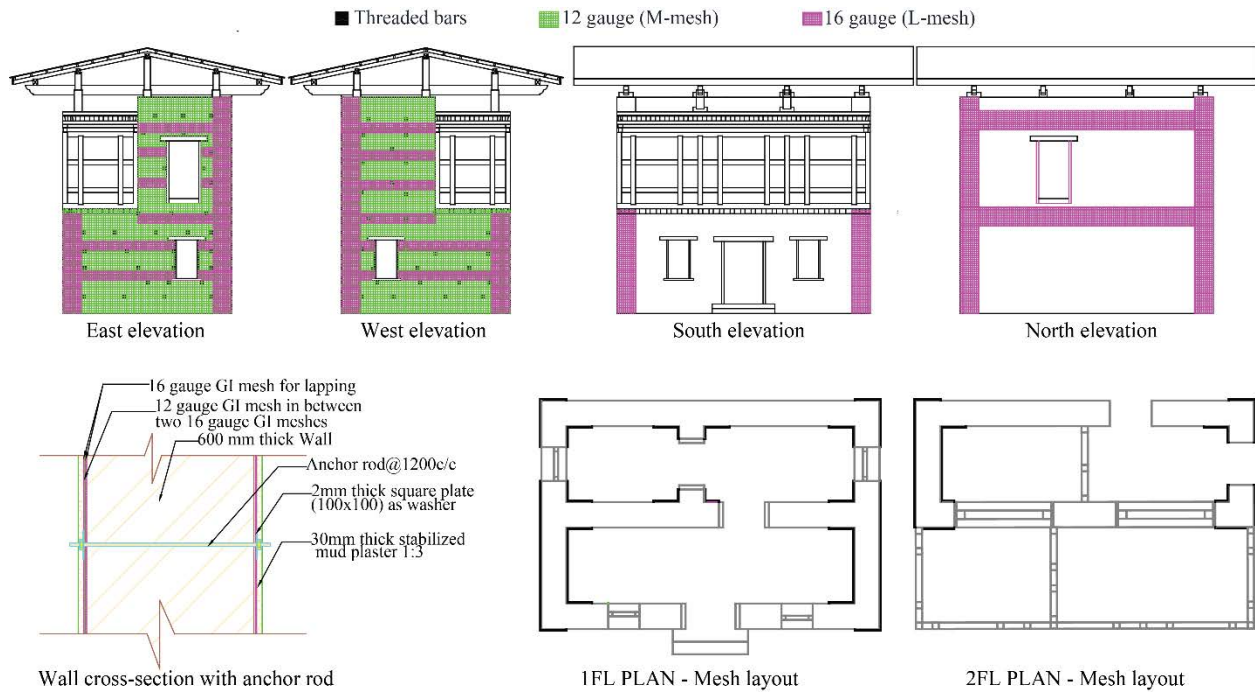


Figure 5. 14 Details of mesh–layout in U-RE-SHORT.

The first step of mesh-wrap retrofitting technique involved fixing M-mesh on both faces of the wall using U-hook fasteners, shown in Figure 5.15(a) and Figure 5.15(b). However, in the corners and wall junctions, L-mesh was provided first, which means the M-mesh was sandwiched between the L-mesh. Following, the L-mesh were provided over the joints of M-mesh in horizontal with lapping length of 300 mm. The L-mesh were also fixed on wall corners and intersection of longitudinal and transverse walls, providing a lapping length of 600 mm. To unite the meshes at two faces of the wall, they were connected by anchor rods having nuts and washer plate, as shown in Figure 5.15(c). The next step involved providing cover to those meshes with cement plaster. Before plasterwork, the wall surface was firstly moistened by applying cement slurry, as seen in Figure 5.15(d). Following, the cement plaster was applied, providing cover to the mesh (Figure 5.15(e)). The total thickness of the cement plaster provided was 30 mm. As a part of retrofitting

measures, timber bracing was also provided under the floor joists for all floor levels. Figure 5.15(f) shows the timber bracing provided in SFL. The entire retrofitting work was completed within three weeks. The specimen RE-R-SHORT was tested in March 2019 after two months of curing period. Figure 5.15(g) shows the specimen after completion of the retrofitting work.

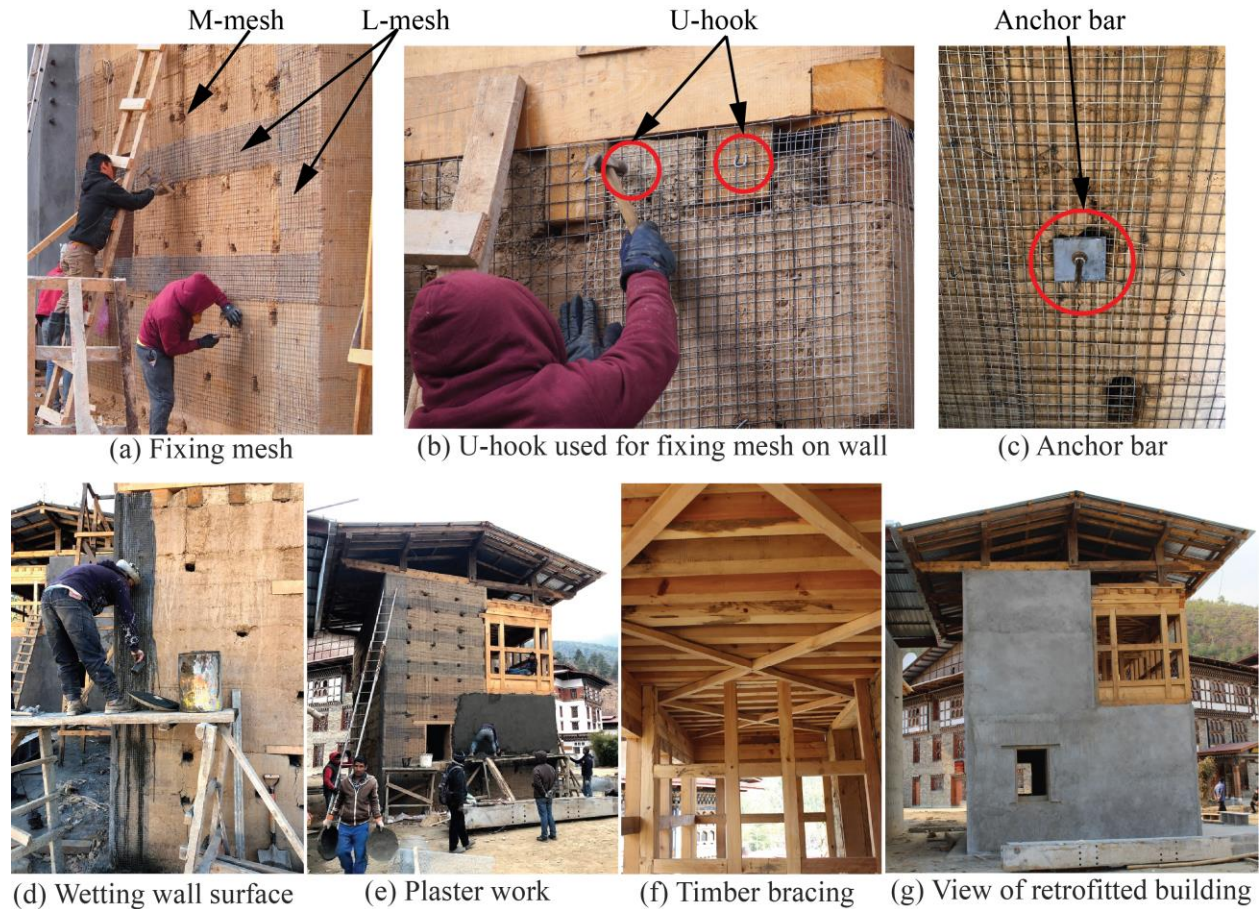


Figure 5.15 Retrofitting details of R-RE-SHORT.

### 5.3.4 Retrofitted RE Loaded in Long Span (R-RE-LONG)

The U-RE-LONG was retrofitted in a similar way described in section 5.2.3 after its initial testing. The specimen was then named R-RE-LONG. The retrofitting technique here involved the repetition of the same process followed for R-RE-SHORT and using the same materials like M-mesh, L-mesh, U-hooks and anchor bars. Since the loading, in this case, was applied in the longer span, the meshes were provided in south and north elevations (in-plane walls), shown in Figure 5.16. Similar to the U-RE-SHORT, the meshes were also provided at the loading levels, i.e. first-floor level and second-floor level, as can be seen in east and west elevations of Figure 5.16.

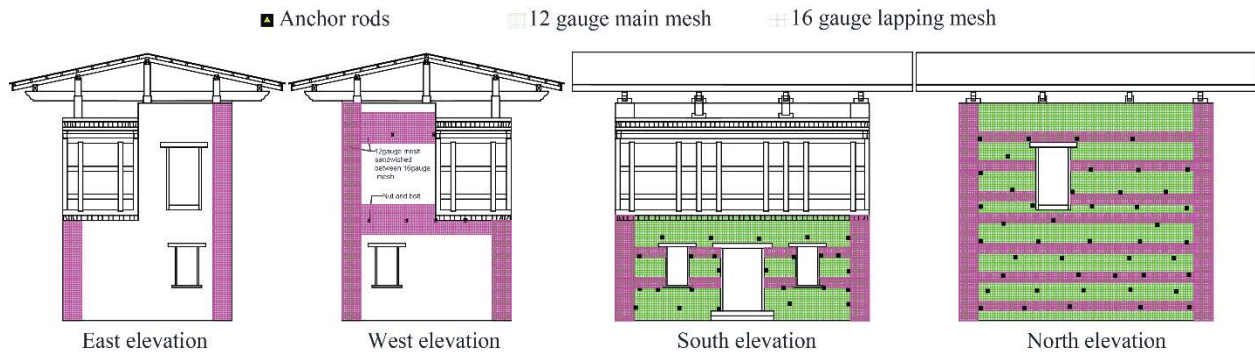


Figure 5.16 Details of mesh-layout in U-RE-LONG.

The chronology of mesh-wrap retrofitting technique followed the same process as described in previous section. Meshes were fixed to walls in both faces using U-hooks, and meshes at two faces were connected by the anchor rods (Figure 5.17(a)-(c)). As mentioned already, M-mesh were fixed first except at the corners and intersections of two walls. In corners and intersections of two walls, the L-mesh were provided first in both faces of the wall. Over it, M-mesh was provided, and again the L-mesh was provided to make the joints stronger. So, in corners and wall junctions, M-mesh was sandwiched between the two L-mesh. In other parts of the wall, L-mesh were provided only



Figure 5.17 Retrofitting details of R-RE-LONG.

at the joints of the M-mesh. The meshes at two faces of the wall were firmly connected by the anchor rods (Figure 5.17(c)). The next step involved providing cover to meshes by cement plaster, as shown in Figure 5.17(d). Timber braces were also provided under the floor joist at both a first-floor and second-floor levels as a strengthening measure (Figure 5.17(e)). Figure 5.17(f) shows the final view of the specimen R-RE-LONG after completion of retrofitting works. The specimen was left for curing for two months before the testing.

### 5.3.5 Reinforced RE Loaded in Short Span (New-RE-SHORT)

The specimen New-RE-SHORT was newly constructed with strengthening components proposed in Chapter 4 for new constructions. The specimen was constructed with the same soil properties used for the construction of unreinforced specimens. Even here, the geometry and plan were maintained the same as the unreinforced specimen. The details of the reinforced rammed earth loaded in a short span is presented in Figure 5.18. The figure shows the plans with location of RC posts and sections with various bands.

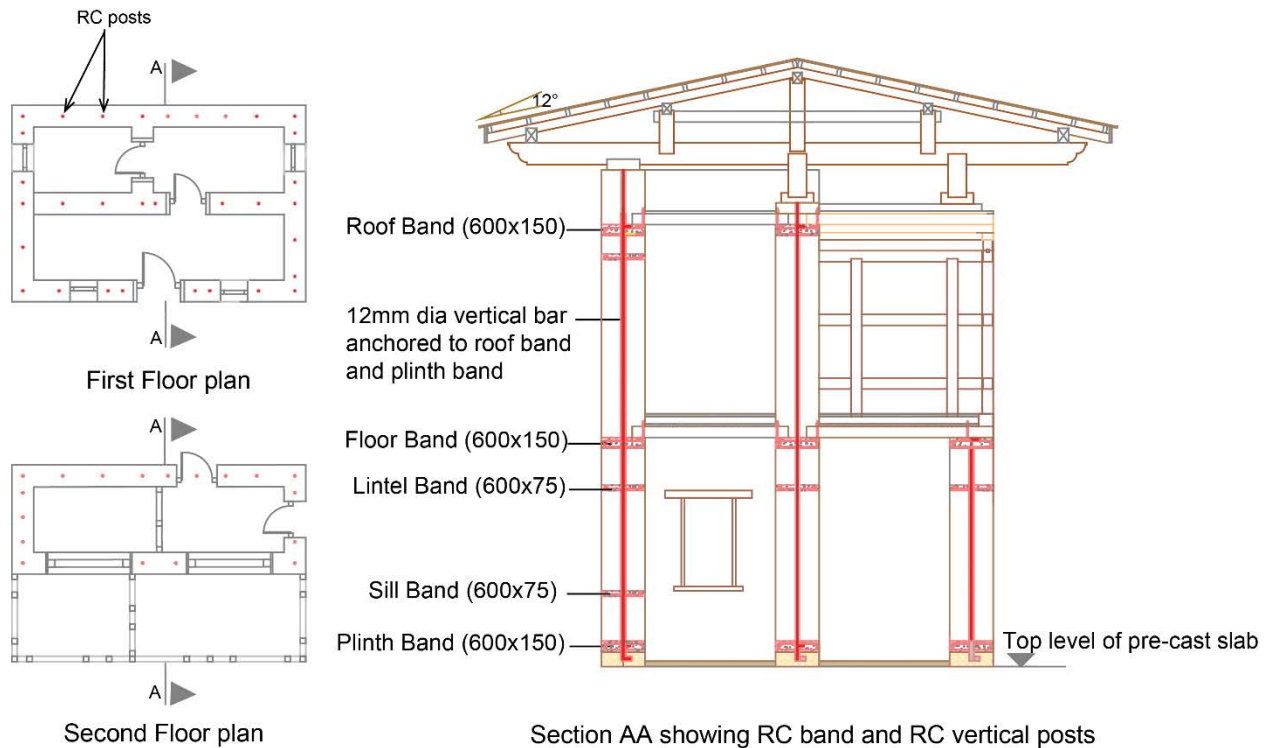


Figure 5.18 Details of reinforced rammed earth specimen (New-RE-SHORT).



### 5.3.5.1 Reinforcing components

Rammed earth, as described in Chapter 1 is the most traditional construction technique practised in Bhutan. They are non-engineered construction built by the local masons without any seismic resistance measures. The rammed earth material being brittle, low tensile strength and heavy wall mass [15-17] is susceptible to seismic forces. Further, the past earthquakes have revealed that earthen building is vulnerable to earthquake forces because of i) lack of integral action, ii) lack of connections between walls, roof element and foundation, iii) inadequate strength for out-of-plane forces, iv) low tensile and shear strength, v) high in-plane stiffness of wall, vi) low ductility and deformability capacity and vii) heavy mass. In view of the highlighted reasons, three possible strengthening measures are incorporated to increase the seismic resistance of rammed earth building.

The details of three possible strengthening measures incorporated are described below:

- i) Reinforced concrete post (RC post): The RC post was provided from foundation base till the top of the wall. The sole purpose in providing RC post was to connect all blocks together in a vertical direction to improve the tensile strength of the building. They were casted on site along with the rammed earth wall construction. The RC post had 80 mm in diameter with 12 mm rebar embedded inside. The rebar of RC post was embedded inside the RC bands floor/ roof levels and foundation, to integrate the whole structure. Figure 5.19 has the details of RC post and reinforcement used in it. The figure also shows J-hook (16 mm in diameter) used to anchor floor joist with the RC band.

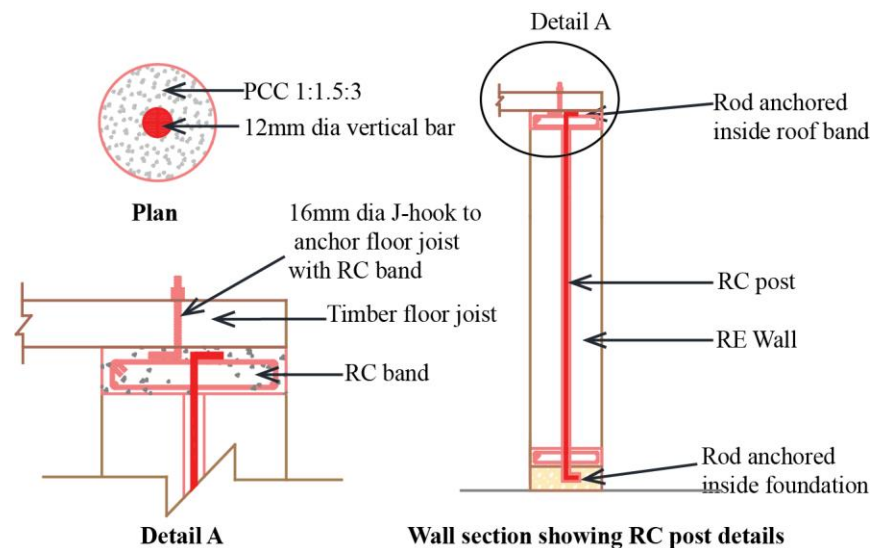


Figure 5.19 RC post and reinforcement details.

- ii) Reinforced concrete band (RC band): In this specimen, RC bands were provided at different levels, i.e. at plinth, lintel, sill and roof level to achieve integral box action in the building. The sizes of bands varied according to its use at different levels. The roof band, floor band and plinth band had same dimension and reinforcement details, while the lintel and sill band had the same dimensions. RC band at the roof, floor and plinth had 600 mm width and 150 mm thickness, and RC band at sill and lintel level had 600 mm width and 75 mm thickness. The detailing of the reinforcement used in the RC band is illustrated in Figure 5.20. The figure also shows the detailing of RC bands at L-junctions and T-junctions.

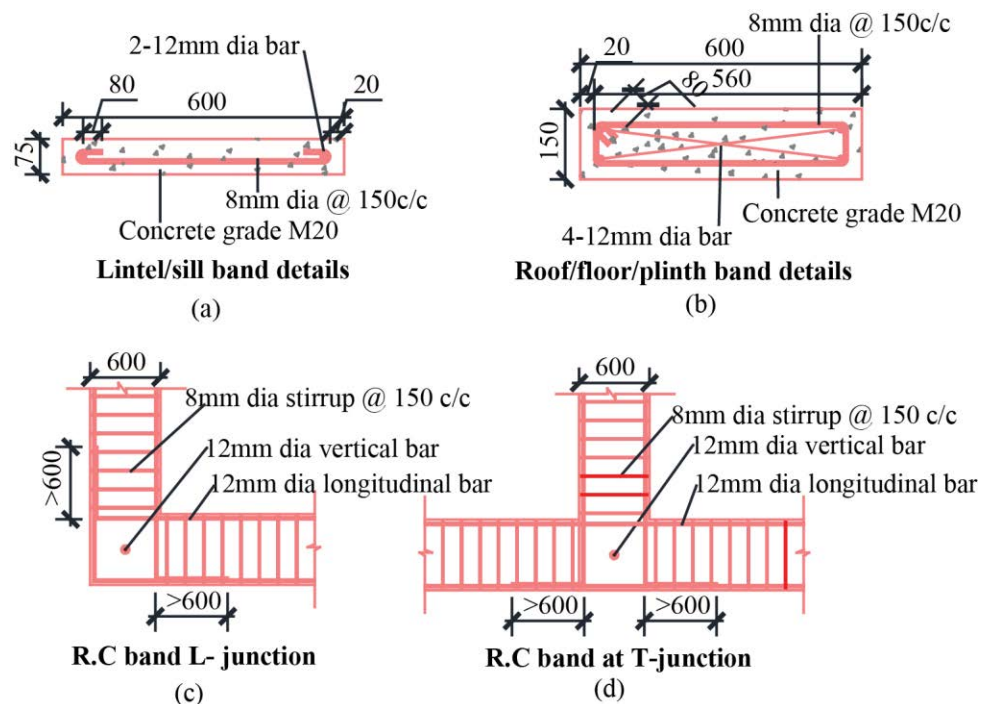


Figure 5.20 RC band and reinforcement details.

### 5.3.5.2 Construction process

The lack of stone foundation in case of unreinforced specimens resulted in exposure to rising damp and water run-off. Therefore, here, a random rubble masonry foundation with enough height of 200 mm high was constructed, and its thickness was maintained the same as the rammed earth wall, i.e. 600 mm. The reinforcement bar of RC posts was centred together with the foundation, as seen in Figure 5.21(a). RC posts were provided from the foundation base till the wall top to connect the rammed earth blocks vertically (Details in Figure 5.18 and Figure 5.19). It was followed by reinforcement layout for plinth band and providing formwork for RC post (Black

HDPE pipe in Figure 5.21(b)). Subsequently, the plinth band and RC posts were casted together with M20 grade concrete (1 cement:1.5 sand:3 aggregate) as seen in Figure 5.21(c). It should be noted that the RC posts were casted till the height of plinth band, and their formwork pipes were removed immediately before concrete sets. The next process involved in fixing formworks for both rammed earth walls and RC posts, followed by pouring the moist soil and ramming manually until the desired height was achieved (Figure 5.21(d)). The average height of the block was 600 mm. The RC post till this height was casted again. Before ramming the next block, RC band at sill level was casted (Figure 5.21(e)). These processes were repeated till the completion of the main wall. Finally, a traditional roof structure was provided to shield it from the rain. To strengthen the floor joist connections, J-hooks were provided for every joist, and they were embedded within the RC band (Figure 5.21(f)). Figure 5.21(g) presents the overall view of New-RE-SHORT showing RC bands at different levels. The specimen was tested in October 2019 after three months of drying.



Figure 5.21 Construction process of New-RE-SHORT.

## 5.4 Material Characterization

### 5.4.1 Rammed Earth Wall

#### *Core sampling*

In order to grasp the mechanical characteristics of the rammed earth samples, compressive and tensile strength testing was conducted on each rammed earth samples. Right after completion of the pull-down test, samples from the wall specimen were extracted using a core drill machine with a diameter 100 mm (DD120 Hilti Corporation), shown in Figure 5.22(a). Figure 5.22(b) shows the coring of a sample from the unreinforced rammed earth wall (U-RE). It can be observed from the figure that the direction of extraction was parallel to the rammed earth layer. At least six samples were extracted from each wall specimens, three each for compression and tension testing. The extracted specimens were around 100 mm in diameter, with the height almost close to 200 mm.

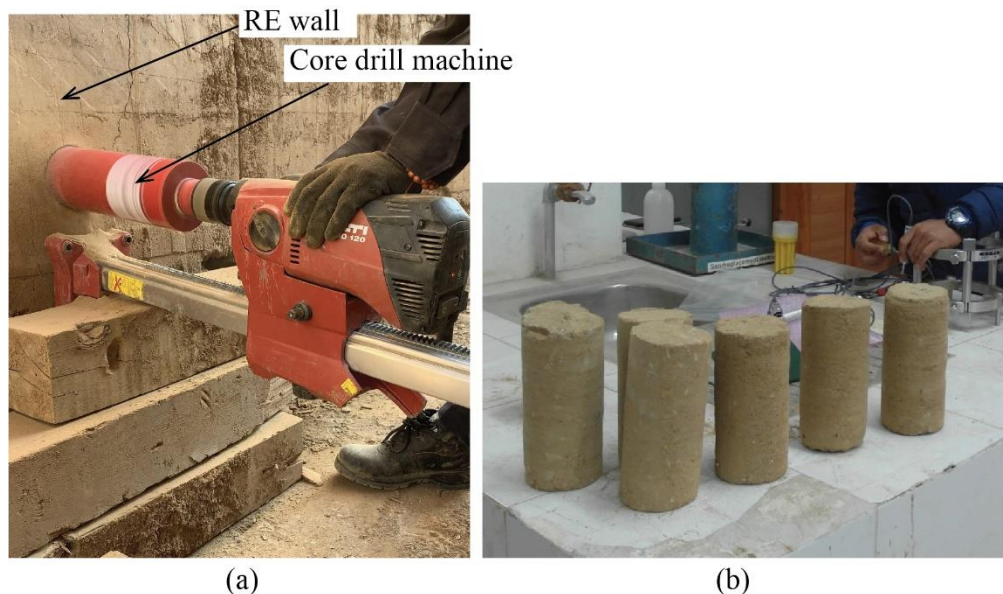


Figure 5.22 Sample extractions from wall: (a) Core sampling; (b) Extracted samples.

### ***Test Setup***

Figure 5.23(a) presents the compressive strength testing setup, and Figure 5.23(b) presents the test setup for tensile strength testing. The splitting tensile strength and compressive strength test on cylindrical rammed earth specimens were conducted according to the ASTM C496 [18] and ASTM C39 [19], respectively. The test was carried out in Bhutan Standard Bureau (BSB). For the tensile test, the specimen was placed in a universal testing machine, and the loading was in a direction perpendicular to the rammed earth layers. Here, the applied load was measured through the high accuracy compressive load cell (KCM-200KNA, Tokyo Sokki Kenkyujo Co., Ltd.), which was then recorded in a multi-channel dynamic strainmeter DS-50A with LAN interface setting. The vertical displacement was recorded by high-sensitivity strain gauge installed within the compressometer (CM-10, Tokyo Sokki Kenkyujo Co., Ltd.).

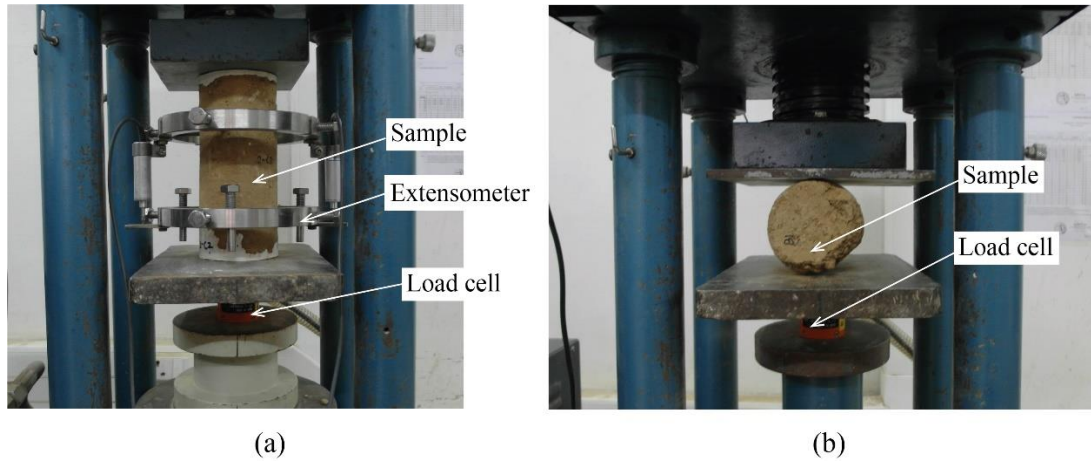


Figure 5.23 Test setup: (a) Compression test; (b) Tensile test.

### Results

Table 5.21 shows the summary of test results from material testing for all three rammed earth wall specimens. The test results show that the RE-LONG samples have higher compressive strength, while compressive strength of RE-SHORT and New-RE are almost the same. The variation could have been affected by the ramming process involved and the place from where the samples are being extracted. For example, the samples for RE-LONG were extracted from a wall face that received enough sunlight for drying, and therefore the strength is higher. However, the samples for RE-SHORT and New-RE were extracted from the back wall (north elevation), which did not receive sunlight as it was blocked by the building specimen itself. Therefore, the strength is lower than the RE-LONG. Figure 5.24 shows some of the failure patterns observed for these tested samples under compression and tensile strength testing.

Table 5.21 Material characterization of rammed earth samples.

Specimen Type	RE-SHORT				RE-LONG				New-RE-SHORT		
	$\rho_b$ (kg/m <sup>3</sup> )	$f_c$ (MPa)	$f_t$ (MPa)	$E$ (MPa)	$\rho_b$ (kg/m <sup>3</sup> )	$f_c$ (MPa)	$f_t$ (MPa)	$E$ (MPa)	$f_c$ (MPa)	$f_t$ (MPa)	$E$ (MPa)
Average	1836.7	0.94	0.12	275.70	2023.7	1.65	0.17	693	0.96	0.17	60.58
Std. dev.	32.9	0.12	0.02	21.49	12.92	0.15	0.03	107.81	0.18	0.03	12.27

$\rho_b$  – density;  $f_c$  – Compressive strength;  $f_t$  – Tensile strength;  $E$  – Young's modulus.

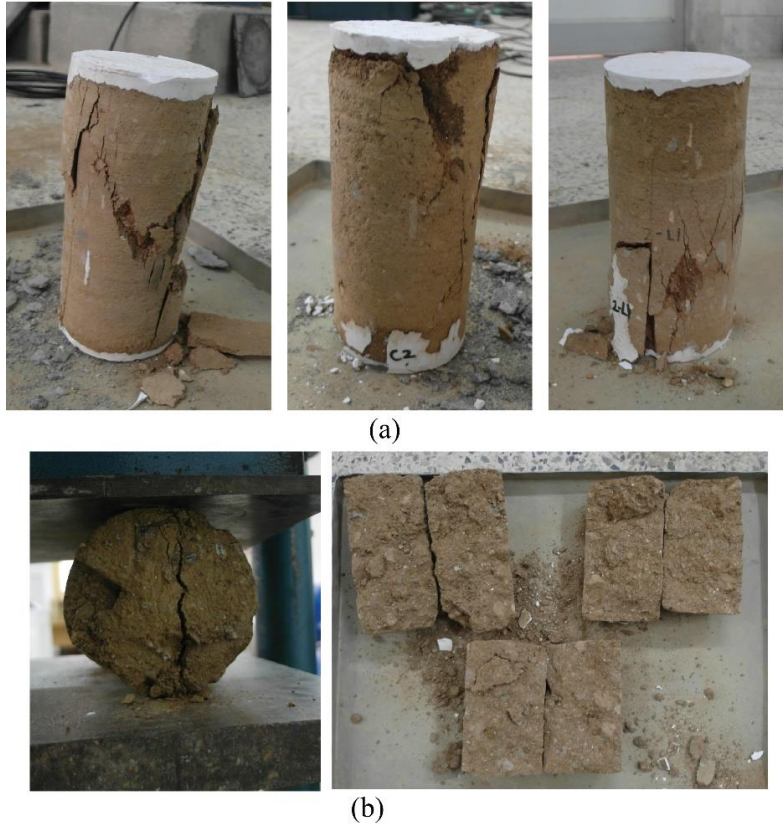


Figure 5.24 Failure patterns observed: (a) Compression test; (b) Tensile test.

#### 5.4.2 Plain Cement Concrete

The plain cement concrete (PCC) was used for casting RC vertical posts and bands for the New-RE-SHORT. Three cylindrical samples were prepared with ratio 1 cement:1.5 sand: 3 gravel. The testing procedure was followed the same as the case of rammed earth wall samples (Figure 5.25). The results from the material test are presented in Table 5.22. Figure 5.26 shows the failure patterns of samples tested under compression loading.



Figure 5.25 Test setup for plain cement concrete.

Table 5.22 Result of a material test of PCC.

Specimen Type	Plain cement concrete		
	$\rho_b$ (kg/m <sup>3</sup> )	$f_c$ (MPa)	$E$ (MPa)
Average	2283.3	22.34	14318.46
Std. dev.	3.0	1.78	2397.26

$\rho_b$  – Bulk density,  $f_c$  – Compressive strength,  $E$  – Young’s modulus

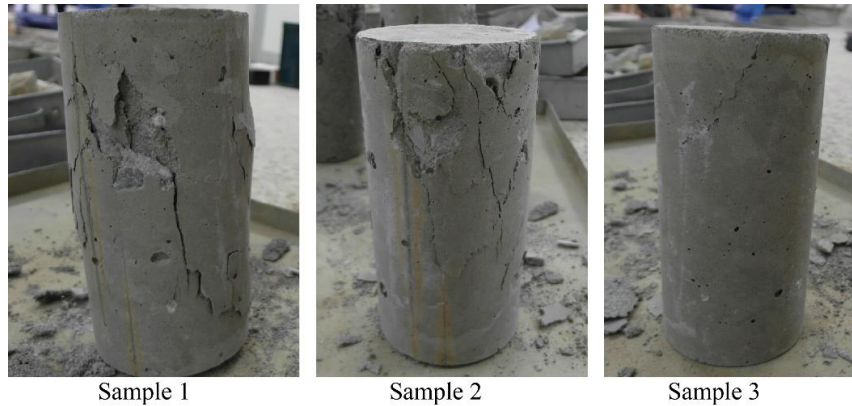


Figure 5.26 Failure patterns observed under compression test.

### 5.4.3 Cement Mortar

The cement mortar was used as a plaster in retrofitting work for the R-RE-SHORT and R-RE-LONG. For material characterization, three cylindrical samples were prepared to have 100 mm diameter and 200 mm height using standardized moulds. The test was carried out in Bhutan Standard Bureau. The material test setup and testing procedure followed the same as in case of plain cement concrete. The test setup and instrumentation are presented in Figure 5.27.

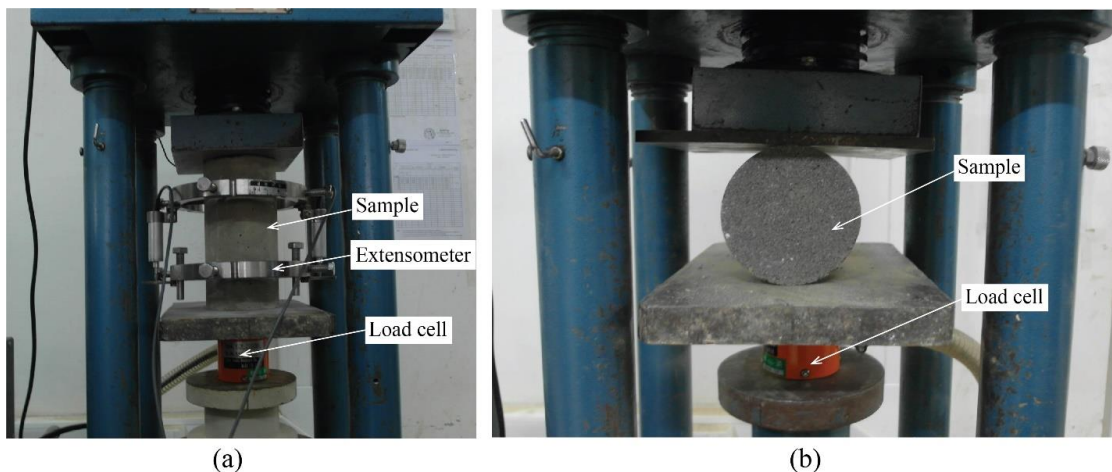


Figure 5.27 Test setup: (a) Compression test; (b) Tensile test.

## Results

The test results are summarized in Table 5.23. The failure patterns observed under compression and tensile strength testing are presented in Figure 5.28(a) and Figure 5.28(b), respectively.

Table 5.23 Result of a material test of cement mortar.

	Material properties			
	$\rho_b$ (kg/m <sup>3</sup> )	$f_c$ (MPa)	$f_t$ (MPa)	$E$ (MPa)
Average	1979.3	17.38	-	1.59
Std. dev.	20.4	2.1	-	0.18

$\rho_b$  – Bulk density,  $f_c$  – Compressive strength,  $f_t$  – Tensile strength,  $E$  – Young's modulus



Figure 5.28 Failure patterns observed: (a) Compression test; (b) Tensile test.

### 5.4.4 Tensile Coupon Test for Mesh Composite

A tensile coupon test was conducted on mesh composite samples as per the AC434 [21] to acquire their tensile strength. Samples were prepared with dimensions 200 mm long, 50 mm wide, and 30 mm thick on a wooden formwork (Figure 5.29(a)). The mesh was sandwiched between the cement plaster with cement-sand ratio 1:3. The samples were left for 28 days curing period. Before testing, both face ends of the samples were bonded to the metal plates using epoxy, with bonding length 75mm (Figure 5.29(b)).



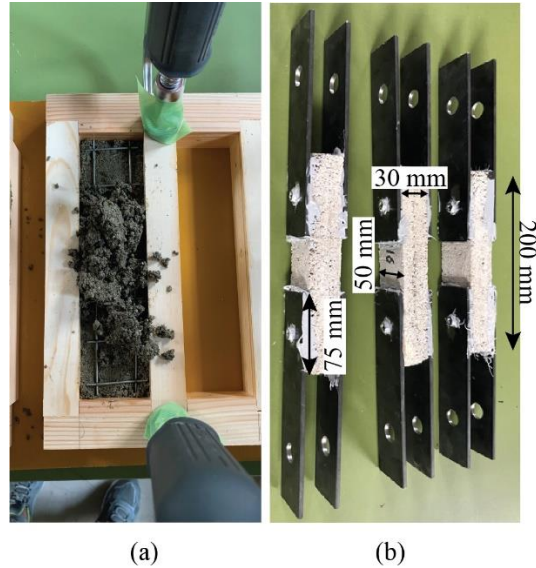


Figure 5.29 Sample preparation for tensile coupon test.

The test setup for the tensile coupon test is illustrated in Figure 5.30. A tension load was applied to a sample through a clevis type grips. PI-gauges were fixed at two faces as seen in the figure to measure the displacements. The results from the coupon test are presented in the stress-strain curve in Figure 5.31(a). It is observed that there is initially high stiffness and drops in load at around 0.6-1MPa stress. The initial peak and drop represent the initial cracking of the mortar. The stiffness reduces significantly afterwards, and at around 1.7-1.9 MPa, another drop in load is observed, representing the initiation of bond-slip between the mesh and plaster. Post that, there was an increase in crack width with further slip along the length of the coupon. No samples failed due to

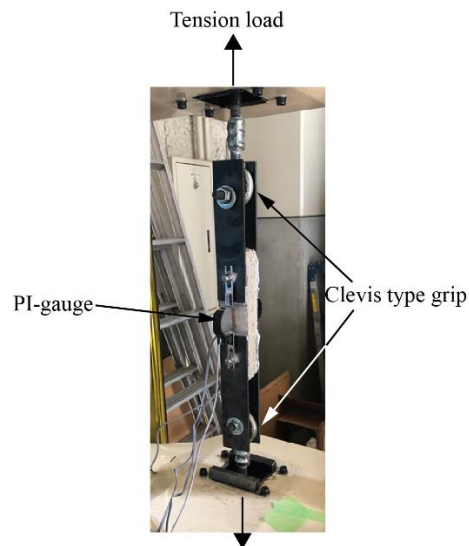


Figure 5.30 Tensile coupon test set up with clevis type grip.

debonding of samples and metal plates. A typical failure of the mesh composite is presented in Figure 5.31(b).

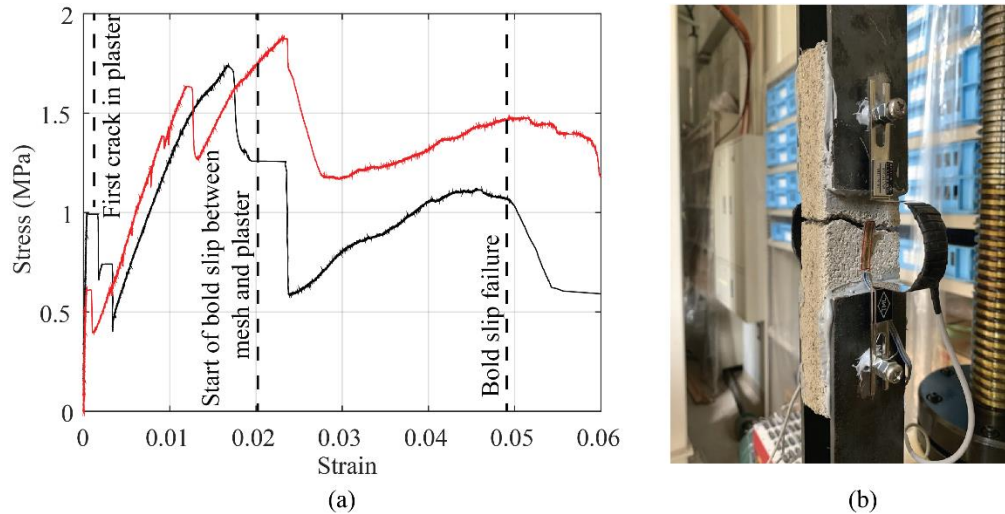


Figure 5.31 Tensile coupon test results: (a) Stress-strain curve; (b) Failure pattern.

### 5.5 Test Setup

Figure 5.32 presents an overview of the test facility and the specimens loaded in two spans. It is observed that while the specimen is loaded in long-span, the in-plane walls are south and north walls and the out-of-plane walls are east and west walls. When the loading is in sort-span, the in-plane walls are east and west walls, and out-of-plane walls are south and north walls. The test setup and instrumentations for specimen loaded in short-span and in long-span are illustrated in Figure

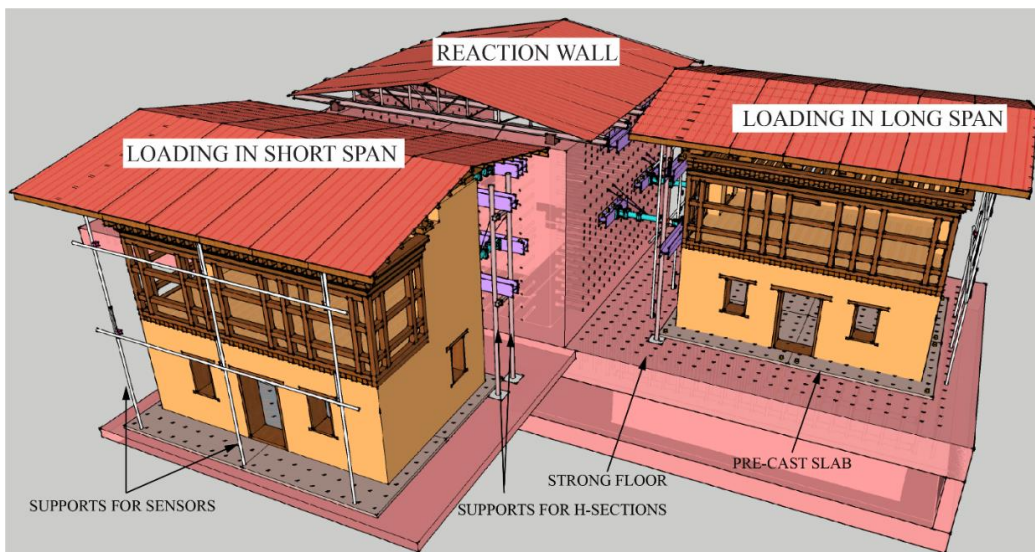


Figure 5.32 Overview of the fullscale test.

5.33(a) and Figure 5.33(b), respectively. The test setup utilizes four static jacks having the capacity of 1000 kN and 500 kN to apply the horizontal load at respective floors. Two 500 kN capacity jacks were positioned on the second floor (2FL), and the other two of 1000 kN capacity were placed at the roof floor (RFL). One end of the static jack was connected to reaction wall through the built-up section and another end to building specimen through a 9.5 m long H-section. There were two H-sections at 2FL and RFL, resting on support systems (Figure 5.32 and Figure 5.34), that allowed them to slide along the support with the jacks. The static jacks were operated manually with the hydraulic pumps to apply and release load (Figure 5.34). The setup helps to transfer the uniform load to all the walls, and the distribution of load in each wall is assumed to be based on their respective stiffness. Here, only a monotonic static loading is applied, and cyclic loading was avoided due to brittle nature of rammed earth. Each floor level of the building was subjected to displacement controlled loading to a specified target storey-drift. The load applied in 2FL and RFL were controlled to have the same storey-drift during the loading process. Here, the storey-drift,  $\theta$ , is defined as the ratio of the lateral displacement to the floor height. Cracks and damage observed

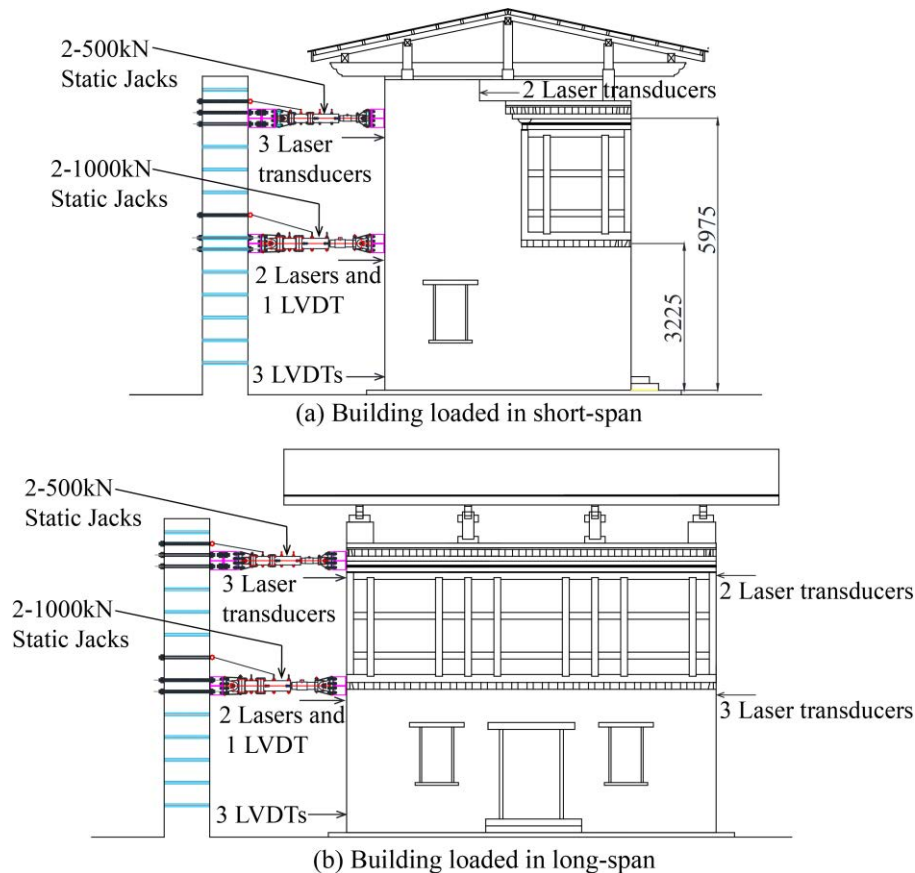


Figure 5.33 The test setup and instrumentations.

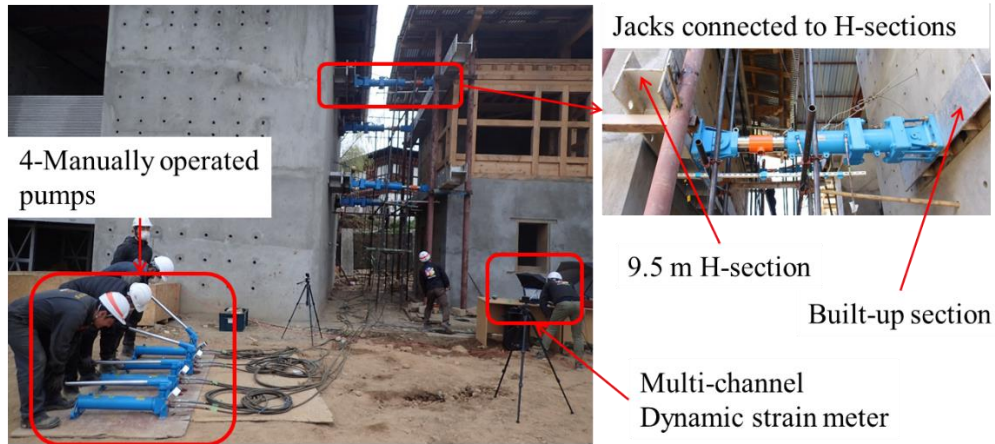


Figure 5.34 Test set up and instrumentation on the field (R-RE-LONG).

were documented at the storey-drift: 1/2000 (0.05%), 1/1000 (0.1%), 1/750 (0.13%), 1/500 (0.2%) for unreinforced rammed earth specimens. For retrofitted buildings, in addition to the above drift values, the buildings were subjected to storey-drift of 0.4%, 0.67%, 1.0% and 1.13%. The reinforced building (New-RE-SHORT) was further subjected to storey-drift of 2.0% and 3.33%. The horizontal displacements during loading were recorded by 14 displacement transducers (Figure 5.35); 10 laser transducers (Keyence, IL-300) and 4 linear variable displacement transducers

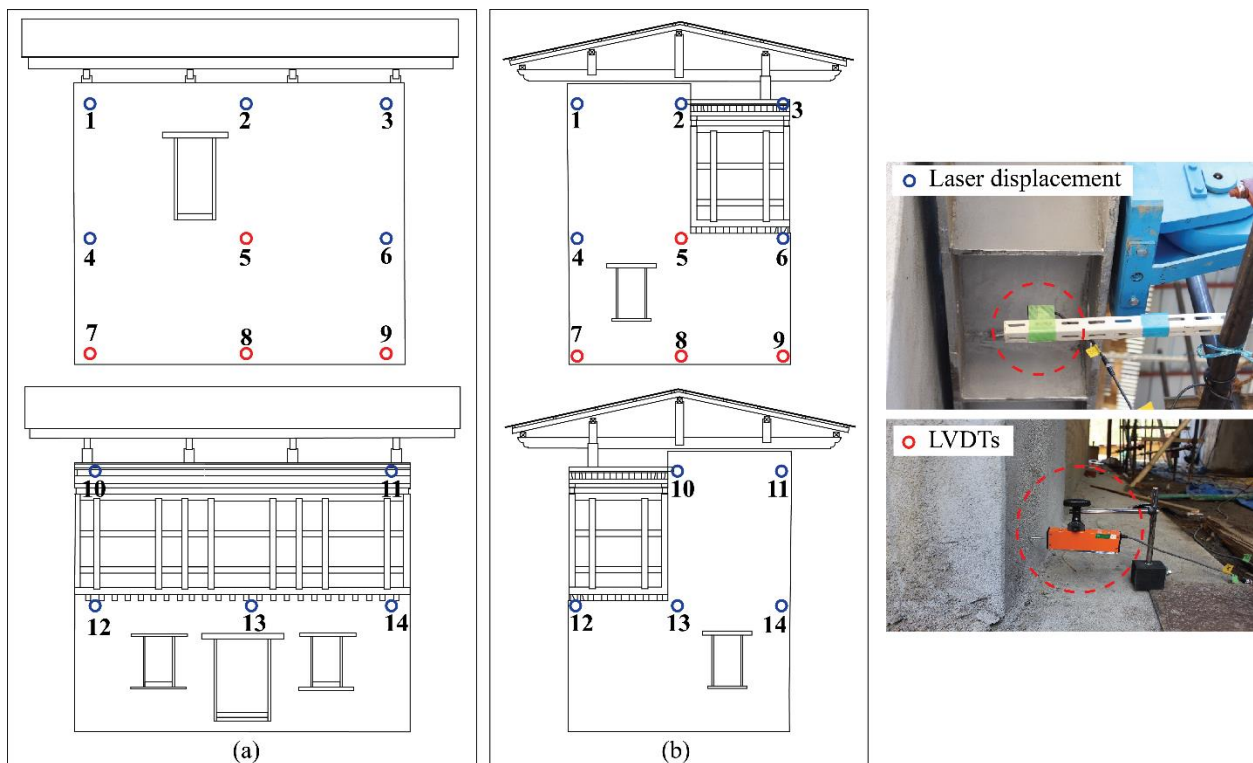


Figure 5.35 Sensor locations: (a) Loaded in short-span; (b) Loaded in long-span.

LVDTs (TML SDP-100C, SDP-50C) at three different levels (first floor, 2FL, RFL) of the test specimen placed both at the loading and the free side. A multi-channel dynamic strainmeter DS-50A is used for data logging with LAN interface setting (Figure 5.34).

## 5.6 Results and Discussion

### 5.6.1 Unreinforced RE Loaded in Short Span (U-RE-SHORT)

#### Capacity curve

Figure 5.36 (a) shows the plot between load and the storey drift in 2FL and RFL of U-RE-SHORT. It is observed that the roof floor having a large opening in almost half-length of the east and west wall has recorded less load than the 2FL which had almost the solid walls. The maximum load recorded in RFL was 80.75 kN, and in 2FL, the maximum horizontal load recorded was 239 kN. Figure 5.36(b) shows the capacity curve. The strength of the rammed earth building is represented in base shear, and the deformation is represented in terms of roof displacement and the top storey-drift. The base shear is taken as the summation of horizontal loads at RFL and 2FL. Further, an equivalent base shear coefficient is also presented, given by the ratio of the cumulative base shear of the building ( $V_b$ ) to the total seismic weight of the building ( $W_t = 1301$  kN). The ultimate strength for U-RE-SHORT was observed 294 kN with corresponding roof displacement of 8.99 mm. The displacement values at RFL was taken as the mean value of three sensors placed at RFL.

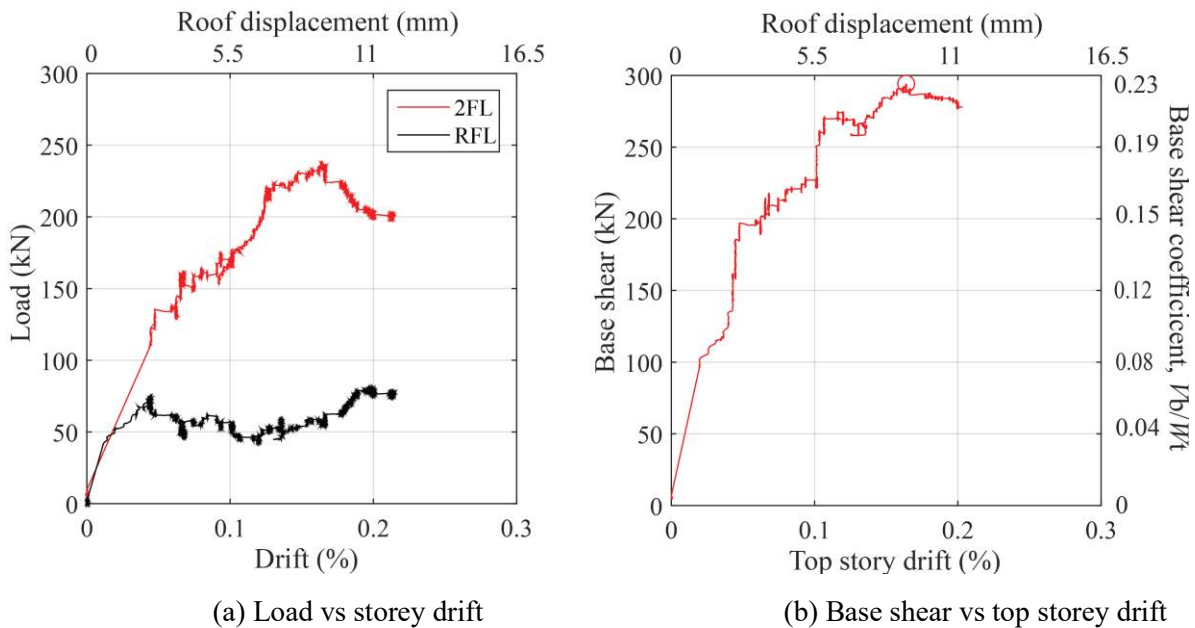


Figure 5.36 Capacity curve of U-RE-SHORT.

### ***Damages observed***

The damages for the specimens were monitored and documented at the predefined target storey-drift through visual observations and video recordings. Figure 5.37 presents damage observed at three-storey drifts, 1/1000, 1/750 and 1/500. The damages for only in-plane walls are presented since there were no significant damages observed in out-of-plane walls. In the initial phase within storey drift of 1/2000, no cracks were visible. The first few hair-line cracks originated near openings, window sill, loading point in 2FL and at top rammed earth block in east elevation, when storey drift was 1/1000. Within the same storey drift, small cracks were observed near lintel and *jugshing* holes in west elevation. At storey drift of 1/750, the crack propagated below the door sill and loading point in 2FL of the east elevation. There was also the appearance of new cracks. In the west elevation, there were numerous small cracks within the rammed earth blocks. In the final storey drift of 1/500, the existing cracks in east elevation widened. The crack below loading point in 2FL extended diagonally. New cracks appeared near the window opening and within rammed earth block in 1FL. A significant amount of inclined cracks appeared with the rammed earth block of 1FL. All cracks were seen originating from the *jugshing* holes. A vertical corner crack evolved

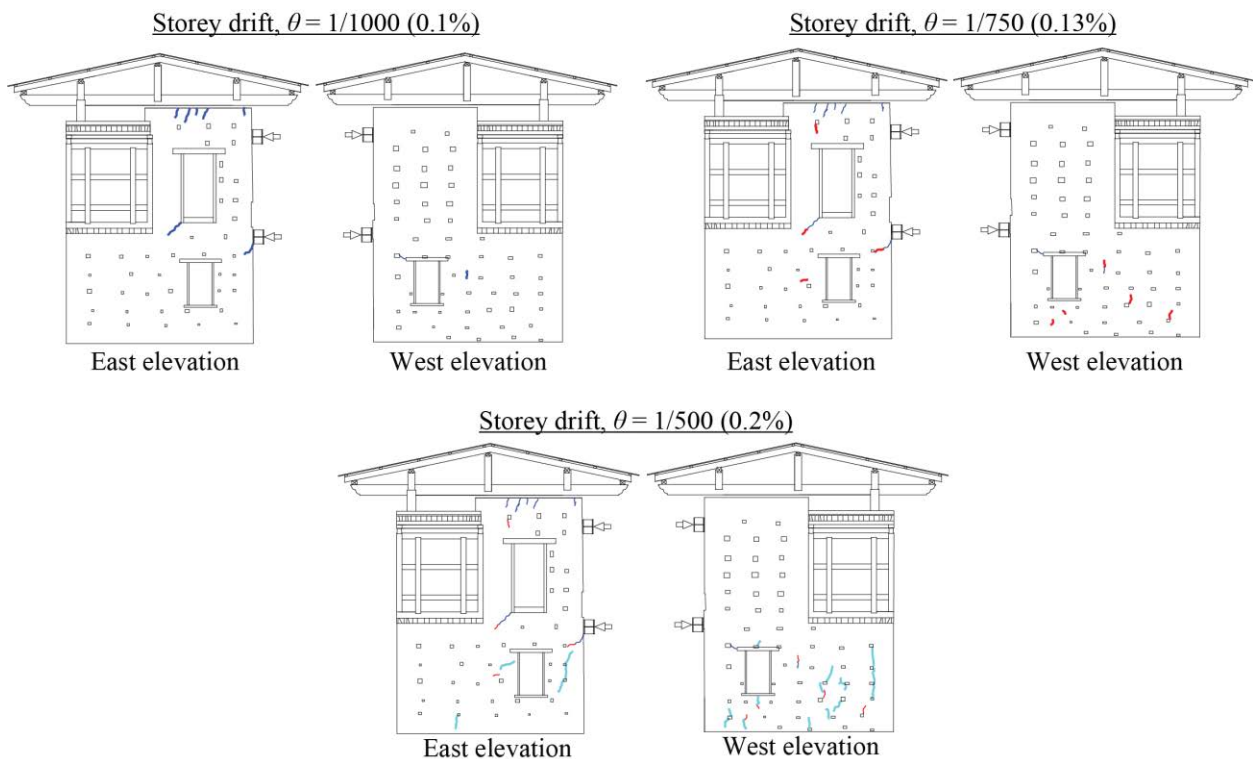


Figure 5.37 Failure mode of U-RE-SHORT.

600 mm away from the corner in 1FL. The test was stopped at this point to retrofit later and retest the same building.

### ***Ductility index and energy absorption***

It is essential to assess the ductility of the unreinforced specimen to later compare with the ductility of the strengthened specimens to understand their strengthening effect. The ductility is the characteristic of a material representing its capacity to undergo considerable deformation while resisting loads. There are different ways in which ductility can be measured, and the most common methods are in the following:

- i. The absolute deformation ( $\Delta_y$ ) or inelastic deformation ( $\Delta_{\max} - \Delta_y$ )
- ii. The ductility index ( $\mu$ ) =  $\Delta_{\max} / \Delta_y$
- iii. Energy absorbed by the structure ( $\Psi$ ) represented by the area under the force-deformation diagram.

In the current case, the second and third method described above is used to assess the ductility of the rammed earth wall. The ductility index ( $\mu$ ) and energy absorption ( $\Psi$ ) for each test specimen. The ductility here is defined as the ratio of the corresponding roof displacement at maximum base shear ( $\Delta_{\max}$ ) to the displacement at yielding point ( $\Delta_y$ ). The yielding point here is considered to a point from the non-linear region right after the almost linear region of the capacity curve, where base shear imposed caused the appearance of the first crack in the building. The  $\Delta_{\max}$  from the capacity curve is observed at 8.99 mm, and  $\Delta_y$  is observed at 2.59 mm, which gives a ductility value of 3.47. The energy absorption for U-RE-SHORT is calculated as 1813.6 kN-mm.

### **5.6.2 Unreinforced RE Loaded in Long Span (U-RE-LONG)**

#### ***Capacity curve***

Figure 5.38(a) shows the plot between the horizontal load and the storey drift in 2FL and RFL of U-RE-LONG. As in the case of U-RE-SHORT, the load required to push the same amount of displacement in 2FL is greater than the force required to push the RFL. The maximum load recorded in RFL was 164.25 kN, and in 2FL, the maximum load recorded was 239 kN. Figure 5.37(b) shows the capacity curve with plot between base shear and the top storey drift. The roof displacement and base shear coefficient are also presented. The ultimate strength for U-RE-LONG was observed 309.25 kN with a corresponding roof displacement of 12.16 mm. The displacement

values at RFL was taken as the mean value of three sensors placed at RFL.

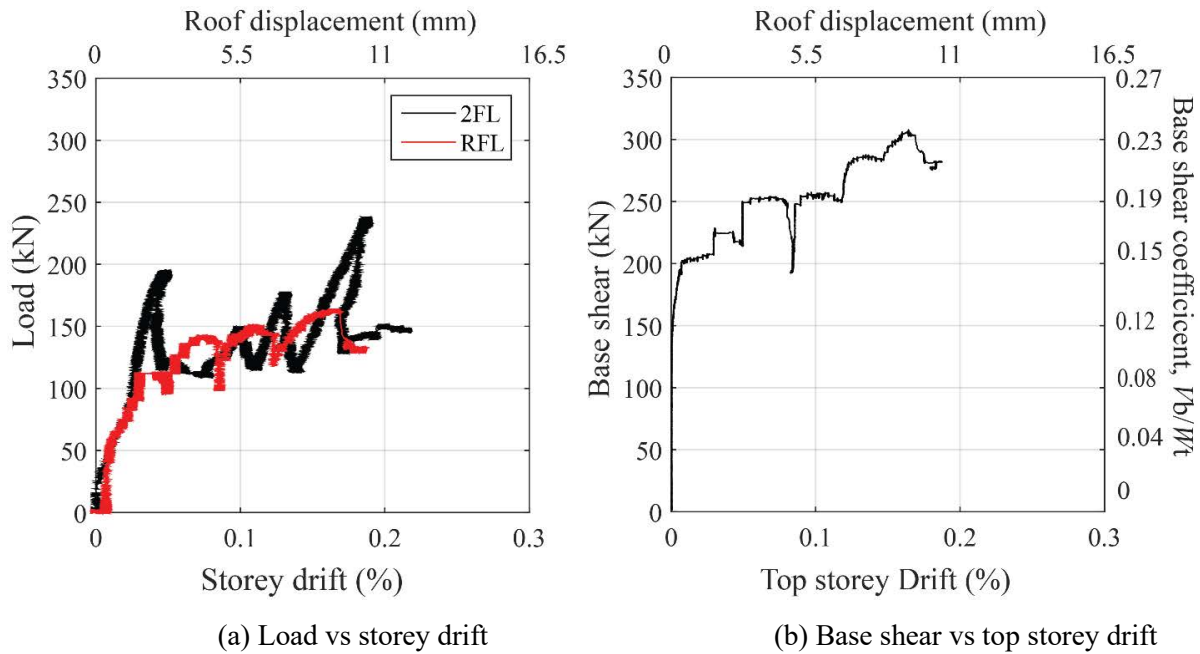


Figure 5.38 Capacity curve of U-RE-LONG.

### ***Damages observed***

The appearance of cracks was primarily affected by the building orientation towards the loading. U-RE-SHORT was symmetrical in plan with respect to the loading direction. The in-plane walls (east and west walls) had almost the same mass distribution, and the cracks were distributed uniformly along the elevations. However, U-RE-LONG was asymmetrical with respect to the loading direction. The mass distribution between two in-plane walls varied, where the north wall had solid walls and the south walls had large openings in 2FL. Subsequently, the damages in two walls varied. The north wall suffered a larger amount of damages than the south wall. The sequence of damages observed for U-RE-LONG at four-storey drifts, 1/2000, 1/1000, 1/750 and 1/500 are presented in Figure 5.39. Even here, the damages for only in-plane walls are presented, i.e. walls at south and north elevations. At first loading up to storey drift of 1/2000, few hair-line shear cracks were observed near the lintel and within the rammed earth blocks of the south wall. The cracks were mainly originating near *jugshing* holes. A horizontal crack was also observed below the loading point in 2FL. In the north wall, small cracks were found below the door sill originating from the *jugshing* hole. When the storey drift was up to 1/1000, the horizontal crack below the loading point of 2FL propagated towards the window lintel in the south wall. Few minor cracks



also appeared above the window in the south wall. In the north wall, the existing long vertical crack (formed during the drying period) widened which could have been induced by an inside transverse wall perpendicular to this crack during the loading. In the next loading up to storey drift of 1/750, the existing cracks in the south wall extended. Furthermore, new cracks were also observed within the rammed earth blocks for both south and north walls. The damage observed within this storey drift was moderate. The next loading was applied up to the storey drift of 1/500. Within this storey drift, numerous shear cracks initiated in the north wall. In the south wall, a minor shear crack appeared above the door lintel. The test was stopped here to carry the retrofitting work and test again later.

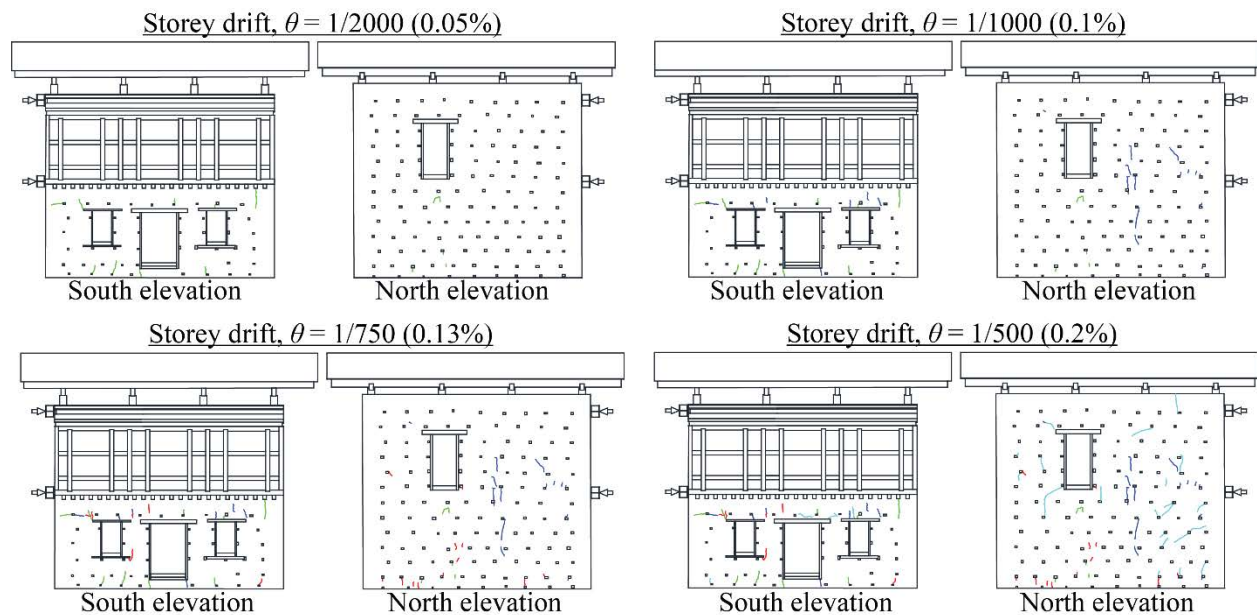


Figure 5.39 Failure mode of U-RE-LONG.

### ***Ductility index and Energy absorption***

The ductility and energy absorption for U-RE-LONG was 4.90 and 2852.5 kN-mm, respectively. These values are found higher than the values observed for U-RE-SHORT.

### **5.6.3 Retrofitted RE Loaded in Short Span (R-RE-SHORT)**

#### ***Capacity curve***

The capacity curve for R-RE-SHORT is presented in Figure 5.40. Figure 5.40(a) shows the plot between the horizontal load and the storey drift in 2FL and RFL of R-RE-SHORT. As reported in the previous specimens, the load required in 2FL is higher than the RFL to maintain the same

storey drift in 2FL and RFL, respectively. The maximum load recorded in RFL and 2FL was 227 kN and 580.5 kN, respectively. Figure 5.40(b) presents the plot between base shear and the top storey drift along with the roof displacement, and the base shear coefficient is also presented. The ultimate strength for R-RE-SHORT was observed 714 kN with corresponding roof displacement of 38.48 mm. The use of mesh-wrap retrofitting technique not only regain its original strength but its capacity has improved by 2.43 times. Further, the roof displacement of R-RE-SHORT was observed 4.2 times the U-RE-SHORT.

The cumulative base shears are also compared with the design base shear value computed with Eq. (5.9) and Eq. (5.10). It gives the design base shear value of 390.33 kN for the unreinforced building specimen, and it is represented in Figure 5.40(b) with a red dashed line. It is observed that R-RE-SHORT exceeded the design base shear value by 1.83 times of U-RE-SHORT.

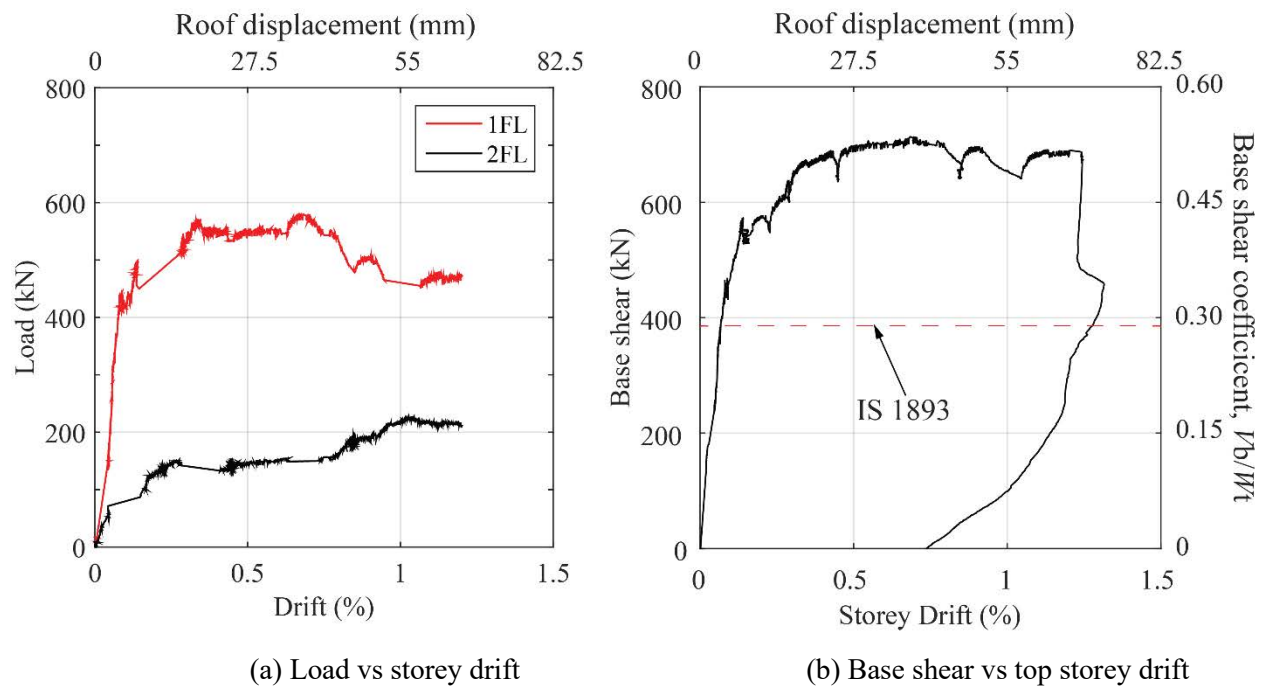


Figure 5.40 Capacity curve of R-RE-SHORT.

**Damages observed**

The cracks observed for R-RE-SHORT is illustrated in Figure 5.41 for six different storey drift levels: 1/750, 1/500, 1/250, 1/150, 1/100 and 1/75. No cracks detected during the first and second phase of loading, i.e. at storey drift of 1/2000 and 1/1000. However, at storey drifts of 1/750, minor cracks started to appear near the lintels of openings at both floors of the east wall. In the west wall,

hairline cracks developed near lintels and below the *rabsey* openings. When the load was applied up to storey drift of 1/500, there was a vertical crack appeared along with the lapping in the corner in the east wall. A shear cracks were also observed originating below the sills of door and window of the east wall. Within the same drift, the previous crack near the lintel extended in the west wall, and horizontal cracks along the lapping were also observed. Until this drift, only hairline cracks were observed, and the damages were minor. It should be noted that all the cracks were hairline cracks up to this load level. When the storey-drift was within 0.4%, a horizontal crack evolved near the window of east elevation and corner crack in the topmost rammed earth block. There was also crack due to toe crushing near the base of the east wall. In west elevation, a long vertical crack appeared along the lapping region. At storey drift of 1/150, there was significant cracks and slight spalling of plaster, with apparent long horizontal cracks along with the sill level, possibly the lapping region of the mesh. The previous cracks kept extending for storey drift of 1/100, followed by extensive spalling of plaster above the door opening (2FL) and also near the window opening (1FL). There was also plaster crushing at the toe near the base of the east wall (Limit state: LS4 Extensive damage). The rocking at the base was observed with the appearance of the long horizontal crack in the north wall. At storey drift of 1/75, the previous cracks propagated both in size and length, extending over the whole length of the wall. The spalling of plaster continued, and clear rocking of the whole building was visible. A crackling sound due to dislocation of timber components was heard on further application of load, and the test had to be stopped for safety reasons. Furthermore, the building also showed clear residual drift post the release of load. Based on the observation, it should be noted that there was no delamination or separation of the mesh from the specimen throughout the whole test, showing the effectiveness of the anchor rods in keeping the mesh intact even at such adverse damage levels.

### ***Ductility index and energy absorption***

R-RE-SHORT showed significantly higher ductility and energy absorption than U-RE-SHORT. It is evident from the capacity curve in Figure 5.40(b) that R-RE-SHORT has undergone substantial deformation without significant loss in the strength compared to the U-RE-SHORT. The ductility of R-RE-SHORT was 7.71, which is 2.22 times the U-RE-SHORT. The mesh-wrap retrofitting technique also enhanced energy absorption significantly. R-RE-SHORT could dissipate enormous

input energy compared to the U-RE-SHORT. The energy absorption for R-RE-SHORT was 22679 kN-mm, which is 12.5 times the U-RE-SHORT.

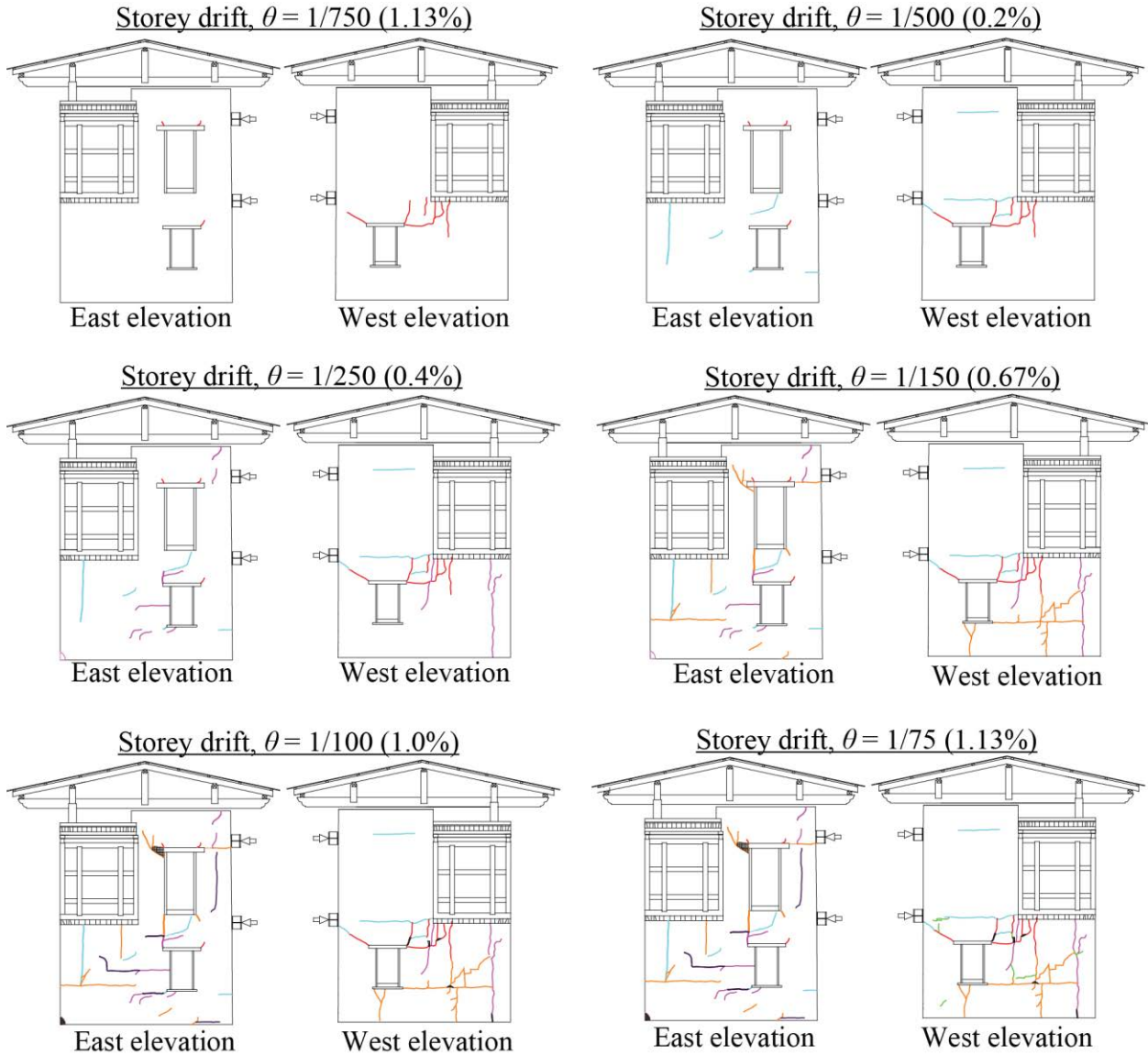


Figure 5.41 Failure mode of R-RE-SHORT.

### 5.6.3 Retrofitted RE Loaded in Long Span (R-RE-LONG)

#### *Capacity curve*

The capacity curve for R-RE-LONG is presented in Figure 5.42. Figure 5.42(a) shows the plot between the horizontal load and the storey drift in 2FL and RFL of R-RE-LONG. It is clear from the figure that the horizontal recorded for 2FL is higher than the RFL. It means that the load

required in 2FL is greater than the load required in RFL to displace the floor to have the same storey drift. The maximum load recorded in RFL and 2FL was 339.35 kN and 876.2 kN, respectively. Figure 5.42(b) presents the plot between base shear and the top storey drift along with the roof displacement and base shear coefficient. The ultimate strength for R-RE-LONG was observed in 1004 kN with a corresponding roof displacement of 27.33 mm. Even here, the use of mesh-wrap retrofitting technique not only regain its original strength, but its capacity was improved by 3.25 times. Further, the roof displacement of R-RE-LONG was observed 2.25 times the U-RE-LONG.

The cumulative base shear of R-RE-LONG is also compared with the design base shear value. The Eq. (5.9) and Eq. (5.10) gives the design base shear value of 399.91 kN for the unreinforced building specimen, and it is represented in Figure 5.42(b) with a red dashed line. It is observed that R-RE-LONG exceeded the design base shear value by 2.51 times of U-RE-LONG.

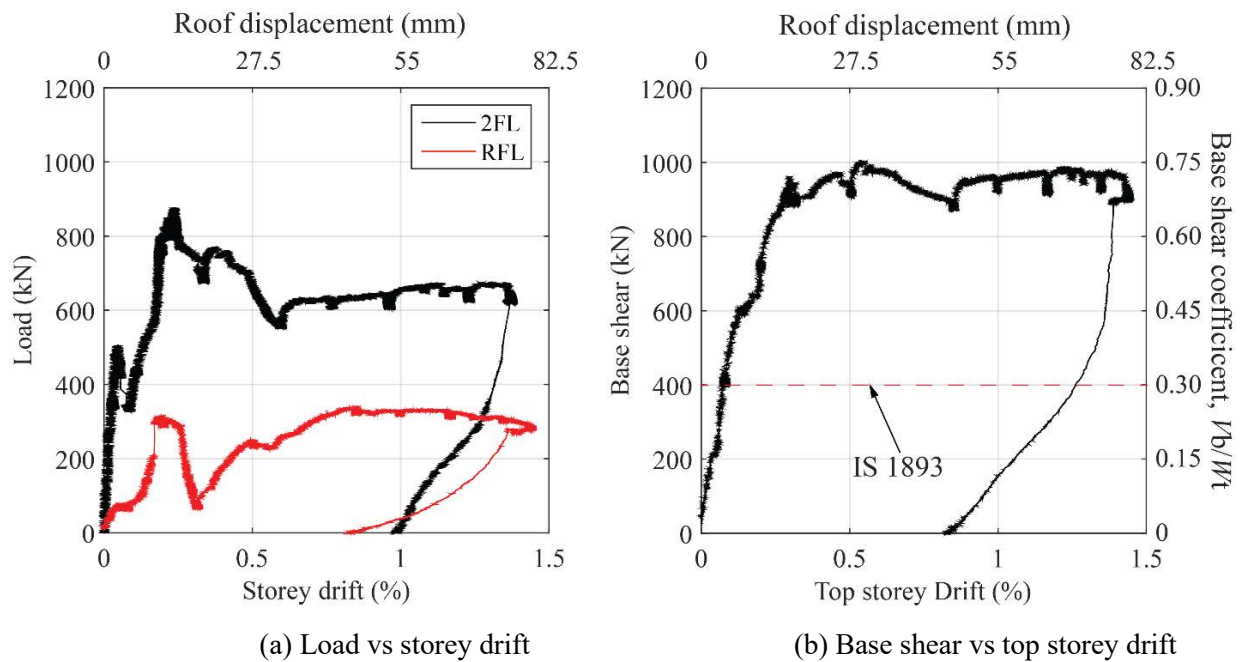


Figure 5.42 Capacity curve of R-RE-LONG.

### Damages

The cracks observed for R-RE-LONG is illustrated in Figure 5.43 for seven different storey drift levels: 1/1000, 1/750, 1/500, 1/250, 1/150, 1/100 and 1/75. For specimen R-RE-SHORT, there was no sign of cracks during the first of loading, i.e. at storey drift of 1/2000. In the next loading up to

storey drift 1/1000, a minor crack evolved near the sill level of the door in the south wall. Few new minor cracks were visible near lintels and sills of both in-plane walls within the storey-drift of 1/750. At storey drift of 1/500, a notable large horizontal crack appeared along the lapping region of the south wall followed by spalling of plaster. A vertical crack also appeared at the same position of existing shrinkage crack. Only minor cracks were seen in the north wall. In the next stage of loading within the storey-drift of 1/250, the horizontal crack near the loading point initiated in both in-plane walls. The horizontal crack elongated, followed by the appearance of a new vertical crack below the door of south elevation when storey-drift was up to 1/150. Within this drift, delamination of mesh was also observed at an elevation where the load was applied. At the next stage of loading up to storey drift of 1/100, there was an extension of the previous crack with propagation in crack width. Some plaster fell off at the top part of the south wall. At the final stage, the loading was applied until the storey-drift was 1/75. In this stage, numerous shear cracks were visible in the north wall, and in the south wall, there was spalling of plaster exposing the mesh inside.

### ***Ductility index and energy absorption***

As in the case of R-RE-SHORT, the specimen R-RE-LONG also showed significantly higher ductility and energy absorption than U-RE-LONG. The capacity curve in Figure 5.42(b) shows that R-RE-LONG has undergone substantial deformation without significant loss in the strength compared to the U-RE-LONG. The ductility of RE-R-LONG was obtained 6.76, which is 1.38 times the U-RE-LONG. A significant improvement in energy absorption was observed with the use of the mesh-wrap retrofitting technique. R-RE-LONG dissipated larger input energy as evident from the crack appearance before the collapse. The energy absorption for R-RE-LONG was 21339 kN-mm, which is 7.48 times the U-RE-LONG.

It is observed that the improvement in ductility and energy absorption of R-RE-LONG is lower than the R-RE-SHORT with their unreinforced counterpart U-RE-LONG and U-RE-SHORT, respectively. The efficacy of mesh-wrap retrofitting technique was influenced by the orientation of the building towards the loading. The building when loaded in short-span (R-RE-SHORT) was symmetrical in plan with respect to the loading, and therefore, it was able to undergo larger deformation before it reached its maximum capacity.

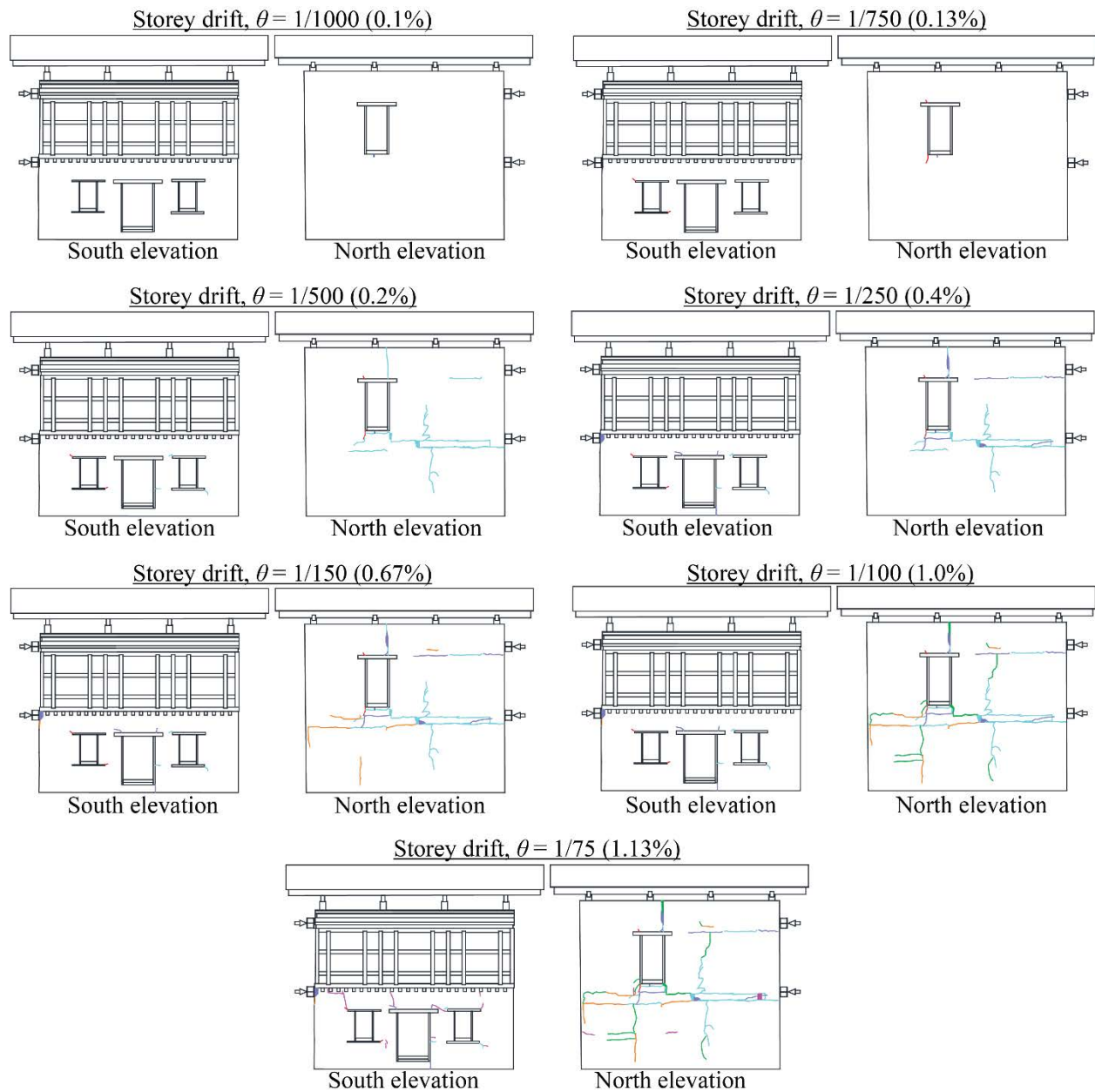


Figure 5.43 Failure modes of R-RE-LONG.

#### 5.6.4 Reinforced RE Loaded in Short Span (New-RE-SHORT)

##### *Capacity curve*

The capacity curve for New-RE-SHORT is presented in Figure 5.44. Figure 5.44(a) shows the plot between the horizontal load and the storey drift in 2FL and RFL of New-RE-SHORT. The maximum load recorded in RFL and 2FL was 179.1 kN and 606.4 kN, respectively. Figure 5.44(b) presents the plot between base shear and the top storey drift along with the roof displacement and base shear coefficient. The ultimate strength for New-RE-SHORT was observed 747.55 kN with

a corresponding roof displacement of 167.22 mm. The presence of the RC post and RC bands have improved the carrying capacity by 2.54 times. Further, the roof displacement of New-RE-SHORT was observed 18.6 times the U-RE-SHORT. The cumulative base shear of New-RE-SHORT is also compared with the design base shear value computed with Eq. (5.9) and Eq. (5.10), and it is represented in Figure 5.44(b) with a red dashed line. It is observed that New-RE-SHORT exceeded the design base shear value by 1.87 times of U-RE-SHORT.

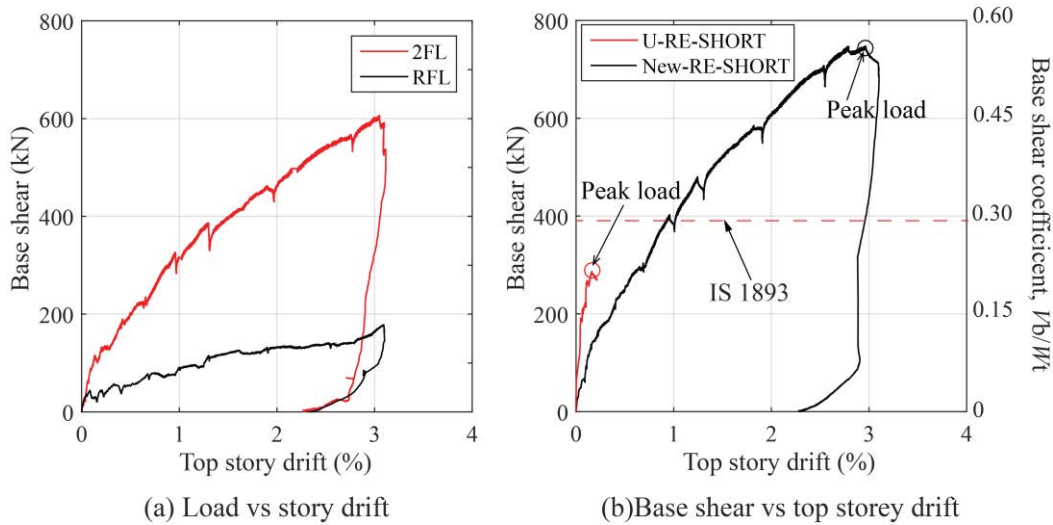


Figure 5.44 Capacity curve of New-RE-SHORT.

On contrary, the presence of the RC posts affected the ramming process. The poor compaction near RC posts resulted in undesirable cracks, as shown in Figure 5.45. This is the reason for having lower stiffness in New-RE-SHORT comparing to its unreinforced counterpart, as shown in Figure 5.44(b) despite having a higher capacity. Therefore, the construction process has to be strictly monitored to avoid such problems.



Figure 5.45 Cracks near RC posts of New-RE-SHORT.



### ***Damages***

Figure 5.45 presents the cracks documented for New-RE-SHORT for seven different storey drift levels: 1/500, 1/250, 1/150, 1/100, 1/75, 1/50 and 1/30. For specimen New-RE-SHORT, cracks did not appear up to storey drift of 1/750. The cracks appeared when the loading was up to storey drift 1/500. A minor crack evolved below the resting point of *gha* that supports *dingri* in the east wall. Cracks were also observed above lintel band of 2FL originating from *jugshing* hole in the same wall. Further, a vertical crack was observed below sill level of 1FL. There was no sign of cracks in the west wall. In next loading up to storey drift of 1/250, new minor cracks were visible in both in-plane walls. In the east wall, the crack appeared in between lintel and sill band, and below sill band of 2FL. The cracks also evolved below floor band and sill band of 1FL. In the west wall, a minor inclined crack was visible within the rammed earth block of 1FL. In the next loading up to storey drift of 1/150, the crack width of existing cracks widen. Also, few new cracks were developed in the east wall near the *rabsey* opening and above floor band of 2FL. The crack also evolved within the rammed earth block of 1FL. In the west wall, long inclined crack emerged below the sill band and extended towards *rabsey* opening of 2FL. At storey drift of 1/100, the existing crack propagated in both the in-plane walls. Numerous shear cracks were developed. In next phase of loading up to storey drift of 1/75, the shear cracks in west wall extended and few cracks also originated above lintel band of 2FL. In the east wall, new shear cracks developed originating from holes and a bed joint crack was also observed in 1FL. At storey drift of 1/50, the building suffered significant damages, characterised by the appearance of larger cracks. The existing cracks in both in-plane walls are seen propagating in width and length. The sill band of 1FL in east wall cracked. In the west wall, new inclined cracks emerged in both floor levels. The horizontal load was further applied up to storey drift of 1/30. At this stage, the building underwent significant damages without collapsing. The cracks widened, and numerous shear cracks were evolved. The test was stopped here for safety reasons.

### ***Ductility index and energy absorption***

The specimen New-RE-SHORT also showed significantly higher ductility and energy absorption than U-RE-SHORT. The capacity curve in Figure 5.44(b) shows that New-RE-SHORT has undergone substantial deformation without significant loss in the strength compared to the U-RE-LONG. The ductility of New-RE-SHORT was obtained 14.82, which is 4.27 times the U-RE-

SHORT. A significant improvement in energy absorption was observed in presence of RC posts and bands. The energy absorption for NEW-RE-SHORT was 80043 kN-mm, which is 44 times the U-RE-SHORT.

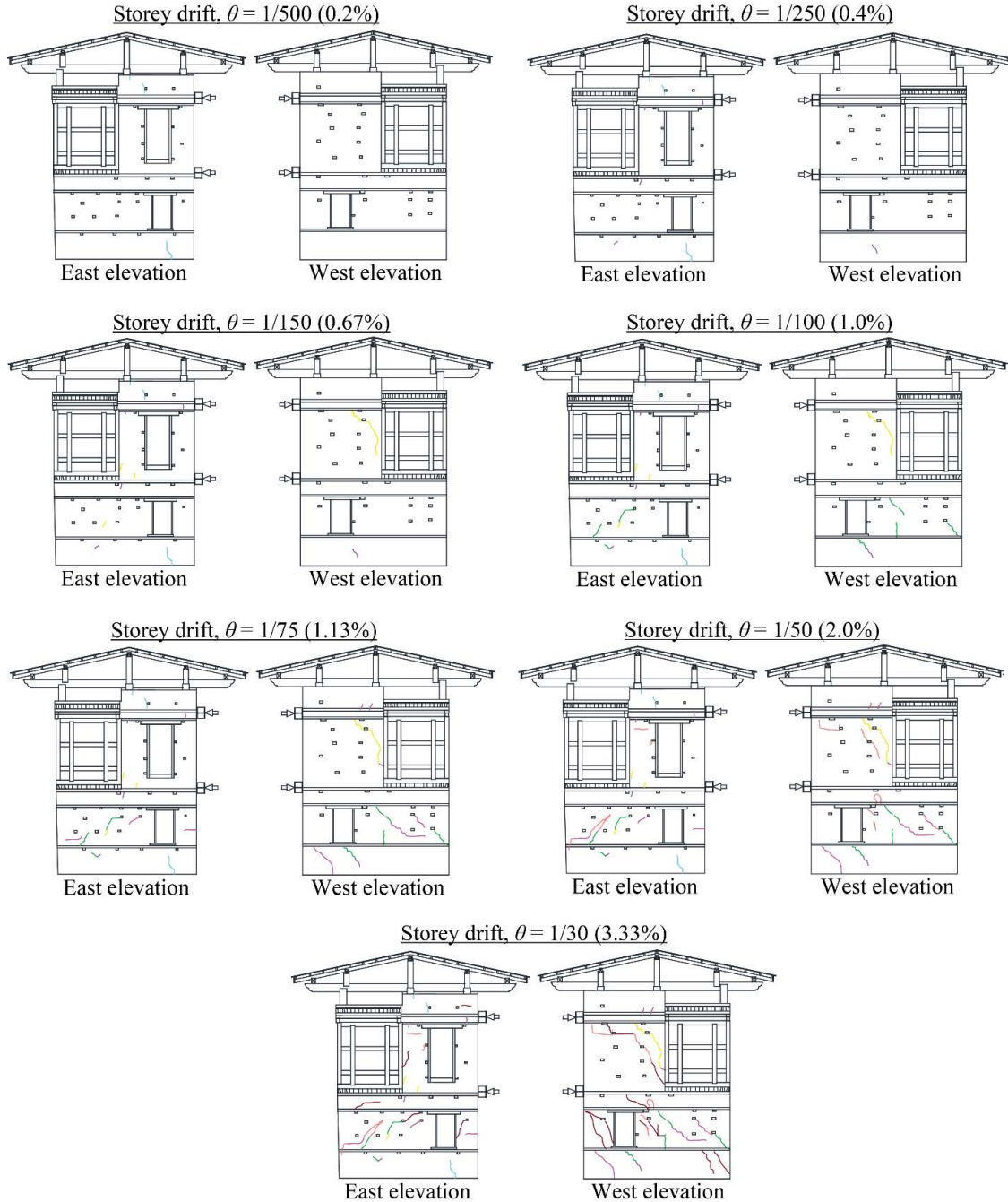


Figure 5.46 Failure modes of New-RE-SHORT.

### 5.6.5 Defining Limit States for Rammed Earth Buildings

The limit states (LS) for each building specimen are defined based on the damage observed during the tests for each predefined storey drifts and is presented in Table 5.24. The proposed LS are modified form of Nabouch et al. [22] for rammed earth walls based on in-plane shear tests on individual RE walls. However, since the present LS are proposed from full-scale structure, the proposed LS are more practical and representative of the actual real scale building. Figure 5.46 presents the LS for all buildings loaded in short-span.

Table 5.24 Limit states for rammed earth building.

Limit states	Damage	Observations
LS1	No damage	No cracks observed.
LS2	Slight damage	First appearance of cracks. Hairline cracks near the openings.
LS3	Moderate damage	Diagonal cracks. Wider cracks near the opening. Initiation of toe crushing.
LS4	Extensive damage	Extension of diagonal cracks. Extensive toe crushing. Initiation of spalling of plaster/ stones.
LS5	Total Collapse	Excessive spalling and damage not economically repairable. Visual residual drift.

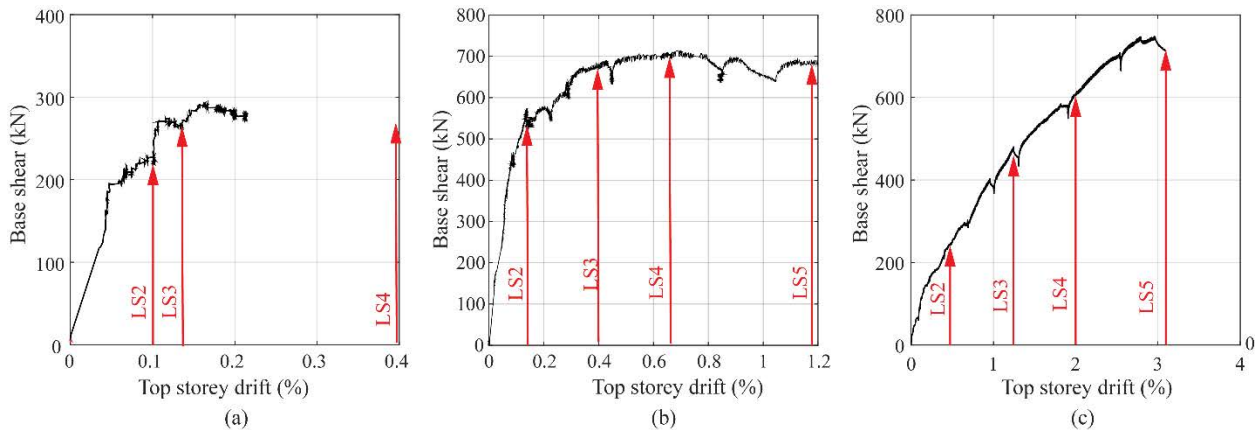


Figure 5.47 Limit states for: (a) U-RE-SHORT; (b) R-RE-SHORT; and (c) New-RE-SHORT.

## 5.7 Nonlinear Pushover Analysis in Seismic Evaluation

### 5.7.1 Introduction

The nonlinear static analysis gives a better understanding and more accurate seismic evaluation of buildings as the progression of damage is traced. Simplified approaches for the seismic evaluation

of structures, which account for inelastic behaviour, generally use the results of static collapse analysis to define the global performance of the structure. Non-linear pushover analysis is a powerful tool for evaluating the inelastic seismic behaviour of structures. There are several simplified non-linear methods as following:

- i) The capacity spectrum method (CSM)
- ii) The displacement coefficient method (DCM)
- iii) Modal Pushover Analysis (MPA)

In this thesis, the CSM procedure is used because of its simplicity and satisfactory performance, and the method is described in detail in the next section.

### 5.7.2 The Capacity Spectrum Method (CSM)

CSM is a method to evaluate the maximum earthquake response of a building using demand spectrum and the capacity spectrum ( $S_a$ - $S_d$ ) on the assumption that the multi-storey building can be reduced to an equivalent single degree of freedom (ESDOF) system corresponding to the first mode of vibration. There are different methodologies available for CSM method; however, in this study follows the procedures proposed by Building Standard Law of Japan [23].

#### *Capacity curve*

The first step in CSM method requires conversion of the capacity curve of a building into Acceleration Displacement Response Spectrum (ADRS) format, i.e. Spectral acceleration  $S_a$  versus Spectral Displacement  $S_d$  after Mahaney et al. [24]. Here, the capacity curves presented in the previous section in terms of base shear versus roof displacement is converted point-by-point into Spectral acceleration  $S_a$  versus Spectral Displacement  $S_d$ . For example, if for a base shear  $V_i$ ,  $\Delta_{roof}$  is the roof displacement then this point on the capacity curve is converted into the corresponding point  $S_{ai}$ ,  $S_{di}$  on the capacity spectrum using the following expressions:

$$S_{ai} = \frac{V_i/W}{\alpha_1} \quad 5.22$$

$$S_{di} = \frac{\Delta_{roof}}{(PF_1\phi_{1,roof})} \quad 5.23$$

where,

$$\alpha_1 = \frac{(\sum_{i=1}^N (m_i \phi_{1i}))^2}{\{\sum_{i=1}^N m_i\} \{\sum_{i=1}^N (m_i \phi_{1i}^2)\}} \quad 5.24$$

and

$$PF_1 = \frac{\sum_{i=1}^N (m_i \phi_{1i})}{\sum_{i=1}^N (m_i \phi_{1i}^2)} \quad 5.25$$

Where,

$W$  = seismic weight;

$\phi_{1i}$  = amplitude of mode 1 at level  $i$  (here, taken as roof displacement);

$m_i$  = mass assigned to level  $i$ ;

$n$  = number of level;

$PF_1$  = modal participation factor for the first natural mode;

$\alpha_1$  = modal mass coefficient for the first natural mode.

The capacity curves of all specimens are presented in Figure 5.47 in  $S_a$ - $S_d$  format based on the Eq. (5.21) to Eq. (5.24).

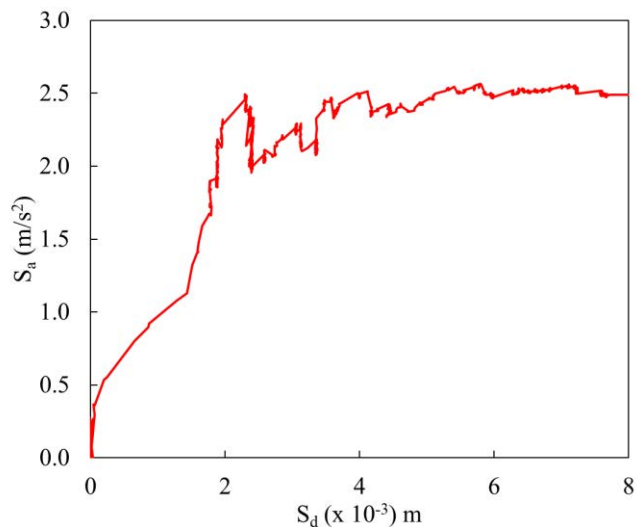


Figure 5.48 Capacity curve of U-RE-SHORT in ADRS.

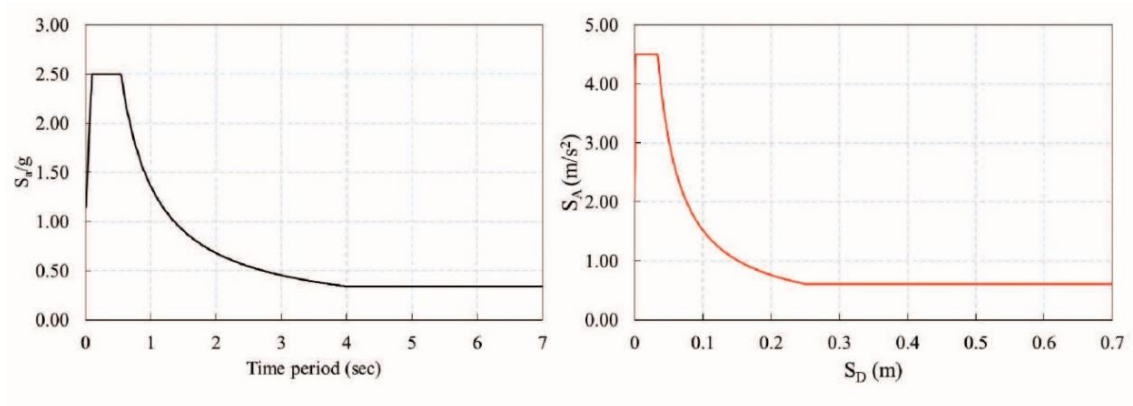
### ***Demand curve***

There are no codal provisions in Bhutan, and standard widely practised in the region is the Indian Standard codes. Therefore, this study uses the standard elastic response spectrum from IS 1893

(Part 1): 2002 [12], shown in Figure 5.49(a). Figure 5.49(b) presents the response spectrum being converted into ADRS format. The elastic response spectrum, which is in terms of time period ( $T$  in second) in x-axis and  $S_a/g$  in y-axis, also need to be converted into ADRS format with the equation:

$$S_{di} = \frac{T^2}{4\pi^2} S_{ai}g \quad 5.26$$

$$T = 2\pi \sqrt{\frac{S_d}{S_a}} \quad 5.27$$



(a)

(b)

Figure 5.49 (a) Response spectrum for medium soil; (b) Demand spectrum for Design Level earthquake [12].

### 5.7.3 Performance Point

Both the capacity curve and demand curve are plotted together, and their intersection point is the performance point of the building for one Peak Ground Acceleration (PGA) level of the particular EQ spectrum. The details procedure is explained below:

1. Decide the first yield point of the structure under consideration. In this study, the yield point corresponds to the spectral displacement ( $D_y$ ) when the storey drift ratio reaches 0.1% for U-RE-SHORT.
2. Assume the ductility,  $\mu = 1$ , and locate a point ( $\bullet$ ) tangential to the spectral displacement axis on the capacity spectrum for the decided first yield point.

3. Draw the line of equivalent stiffness, passing through the origin and the point ( • ).
4. Find the performance point ( ◦ ), which is the point of intersection of the demand spectrum and the line of equivalent stiffness,  $\mu = 1$ .
5. Now, change the ductility factor,  $\mu = 2$ , and locate the second point ( • ) on the capacity curve, equivalent to multiplying factor times (n) to the first yield displacement ( $D_y$ ). The multiplying factor corresponds to the ductility factor, which describes the limit states of the structure.
6. Draw the second line of equivalent stiffness, passing through the origin to the second point ( • ).
7. Calculate the equivalent damping ratio,  $h_e$ , from the following empirical formula:

$$h_e = 0.25 \left( 1 - \frac{1}{\sqrt{\mu}} \right) + 0.05 \quad (5.28)$$

The equivalent damping ratio ( $h_e$ ), for the first mode, is assumed as 0.05 for the damage-initiation limit state because structure behavior remains elastic at this stage.

8. The demand spectra are prepared for a damping ratio of 5% up to the damage initiation limit state and for an equivalent damping ratio at life safety limit state. The response reduction factor of the demand spectrum,  $F_h$ , is derived from the following formula:

$$F_h = \frac{1.5}{1+10h_e} \quad (5.29)$$

9. Reduce the demand spectrum by multiplying both parameters  $S_A$  and  $S_D$  by  $F_h$  and draw the demand spectrum.
10. Find the second performance point ( ◦ ), which is the point of intersection of the demand spectrum and the line of equivalent stiffness,  $\mu = 2$ .
11. Repeat the steps 5 to 10.
12. Now, connect all the performance points with different ductility factors that give the demand curve.
13. The intersection of the obtained demand curve and the capacity curves provides the final performance points.

Figure 5.50 illustrates the performance point of U-RE-SHORT at various PGA of 0.1G, 0.15G, 0.2G, 0.25G, 0.3G and 0.36G for medium soil classification. Similarly, Figure 5.51 and Figure 5.52 presents the performance points for R-RE-SHORT and New-RE-SHORT at various PGA level, respectively. This result is later used in developing the conventional fragility curves.

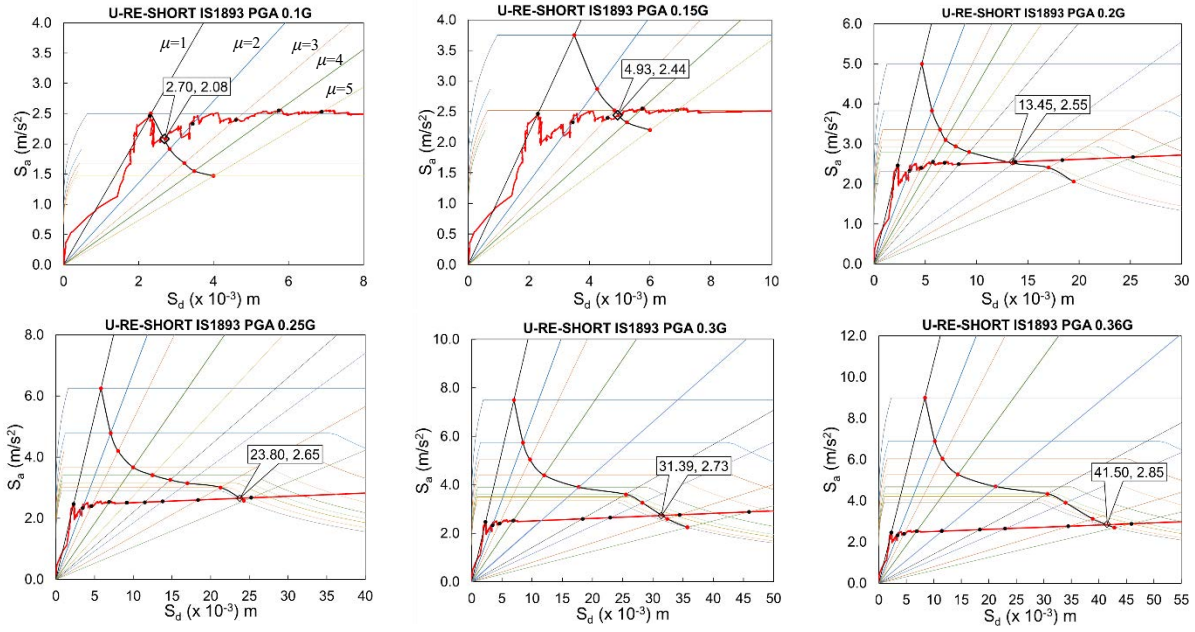


Figure 5.50 Performance point of U-RE-SHORT at various PGA level for medium soil.

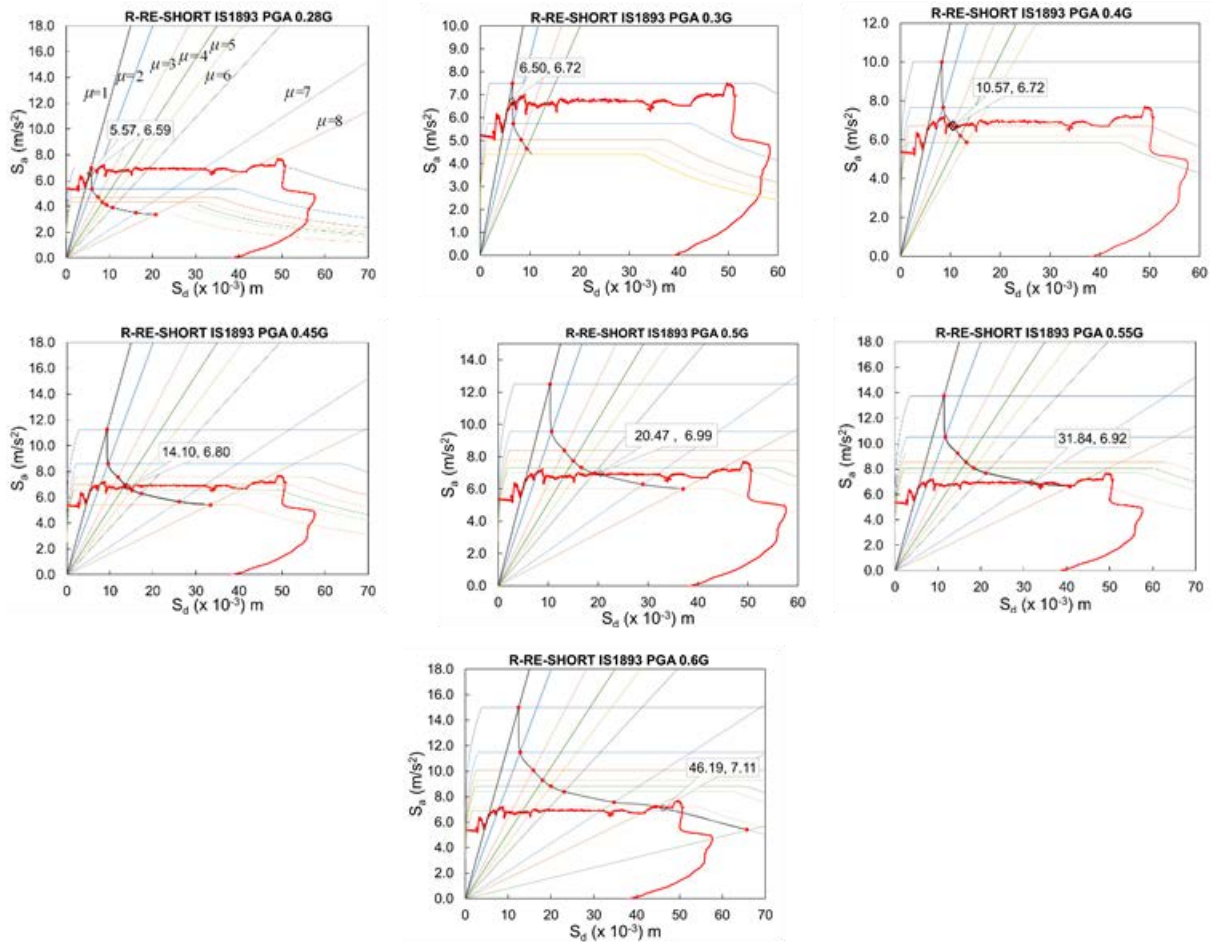


Figure 5.51 Performance point of R-RE-SHORT at various PGA level for medium soil.



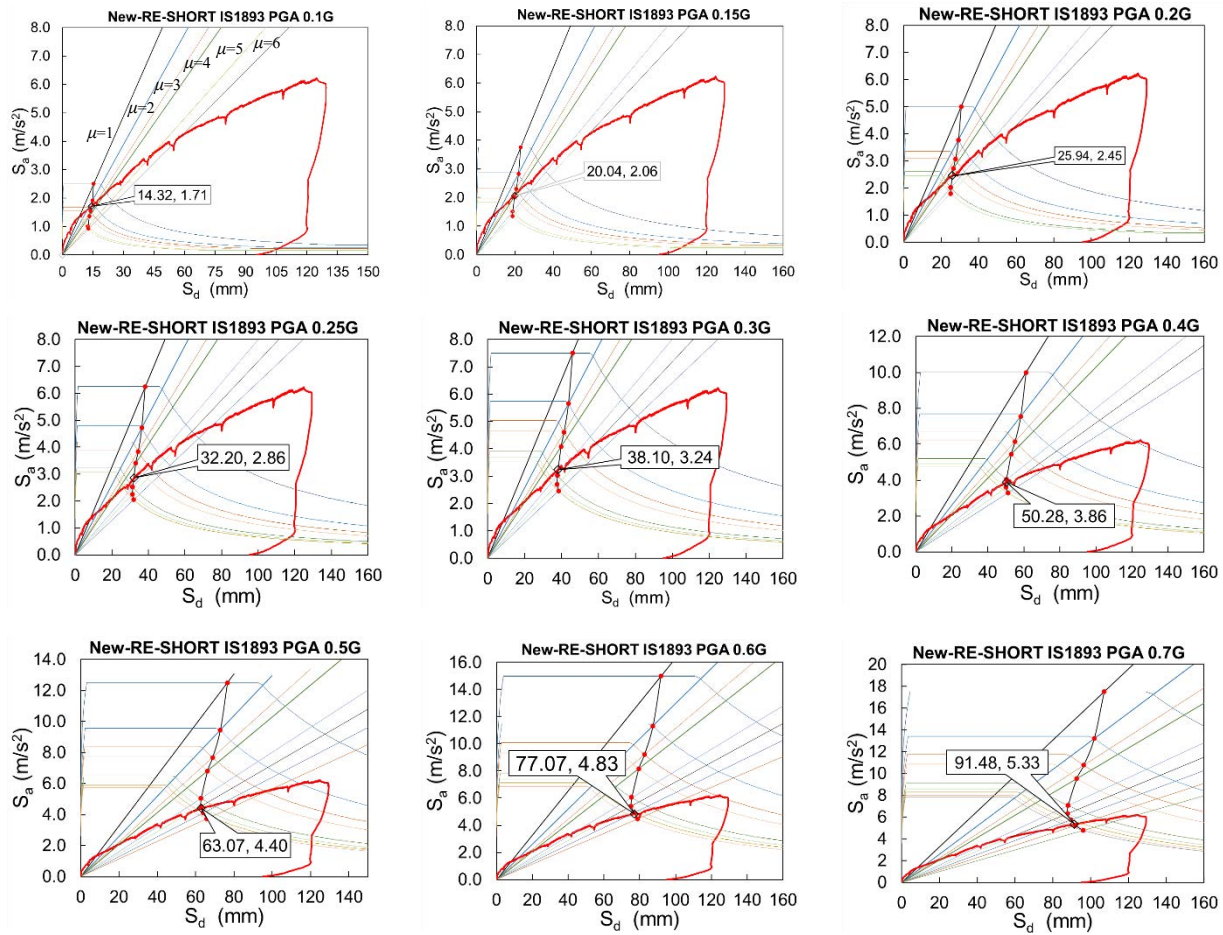


Figure 5.52 Performance point of New-RE-SHORT at various PGA level for medium soil.

### 5.7.4 Fragility Curves

The fragility curve expresses the probability that a building may reach or exceed a set of damage states, for a given earthquake intensity parameters (such as PGA, Peak Ground Velocity (PGV), Spectral Acceleration (SA), etc.). In this study, the author uses the methodology proposed by Wen et al. [25] for the generation of fragility curves. The probability that the given structure exceeds the limit-damage state for given ground motion intensity is given by Eq. (5.30).

$$(LS_i/GMI) = 1 - \phi \left( \frac{\lambda_{CL}^i - \lambda_{D/GMI}}{\beta_{D/GMI}} \right) \quad (5.30)$$

Where

$P(LS_i/GMI)$  is the probability of exceeding a particular limit state given ground motion intensity;

(GMI),  $\phi(\bullet)$  is the standard normal cumulative distribution function;

$\lambda_{CL}^i$  is  $\ln$  (median storey drift for a particular limit state,  $i$ );

$\lambda_{D/GMI}$  is  $\ln$  (calculated median demand storey drift given the GMI from the best fit power-law line) and;

$\beta_{D/GMI}$  is the demand uncertainty.

The parameters  $\lambda_{D/GMI}$  and  $\beta_{D/GMI}$  are given by Eq. (5.31) and Eq. (5.32):

$$\lambda_{D/GMI} = \ln a_1 + a_2 \ln(GMI) \quad (5.31)$$

$$\beta_{D/GMI} = \sqrt{\frac{\sum_{k=1}^n [LN(GMI_k) - \lambda_{D/GMI}(GMI_k)]^2}{n-2}} \quad (5.32)$$

The constants  $a_1$  and  $a_2$  are obtained through linear regression analysis, by plotting natural logarithmic values corresponding to storey drift and PGA (which is the GMI).

The storey drift corresponding to spectral displacement at the performance point of each PGA level are obtained. All these data were plotted against PGA in natural log forms, as in Figure 5.50 to derive the constants  $a_1$  and  $a_2$ . Here, from the Figure 5.53(a),  $\ln a_1$  is -0.2646 and  $a_2$  is 0.9819 for U-RE-SHORT.

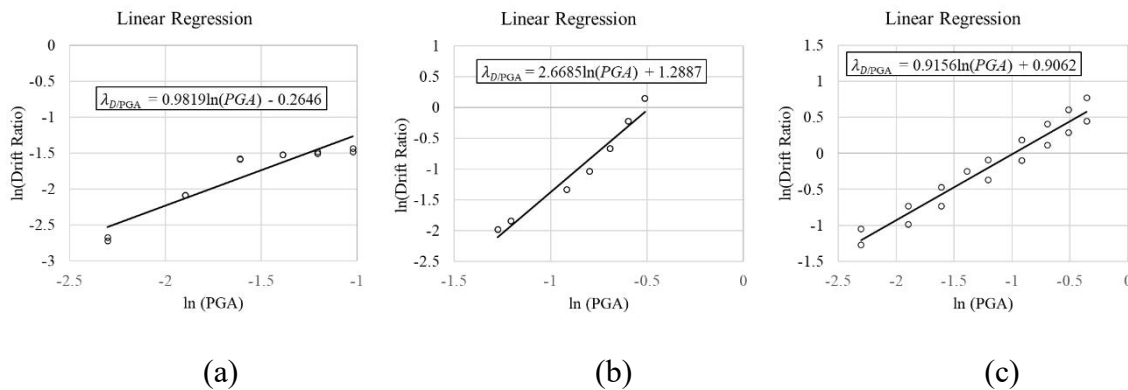


Figure 5.53 Linear regression analysis for: (a) U-RE-SHORT; (b) R-RE-SHORT; (c) New-RE-SHORT.

Following the statistical analysis, fragility curves are generated for all building specimens, a plot showing the probability of exceeding the damage limit-state threshold values as a function of ground motion intensity (PGA). Figure 5.54 presents the fragility curve generated for U-RE-SHORT, R-RE-SHORT and New-RE-SHORT. The black, green, and red curves represent Immediate Occupancy (IO), Life Safety (LS), and Collapse Prevention (CP), respectively. They were defined based on the observation of the full-scale quasi-static test. The black dashed line

represents PGA of 0.36g, which corresponds to the Maximum Considered Earthquake (MCE) as per IS 1893. Under this level of PGA, the U-RE-SHORT building has a 100% probability of exceeding the IO, and 92% probability of exceeding LS and 10% probability of exceeding CP limit state. In the case of R-RE-SHORT, the probability of exceeding IO and LS are 87% and 15%, respectively while the probability of exceeding CP is almost negligible. Clearly, R-RE-SHORT has better seismic capacity than the U-RE-SHORT. On the other hand, for New-RE-SHORT, the probability of exceeding IO, LS and CP are 80%, 38% and 25%, respectively, which is higher comparing to U-RE-SHORT. For easier understanding, a comparison between the buildings is illustrated in Figure 5.55 at different limit states. Clearly, a greater probability of exceedance is observed at lower PGA for all limit states in case of New-RE-SHORT. As already mentioned, the compaction near RC posts are compromised, and it has resulted in appearance of larger cracks during the drying period. Thus the probability of exceedance of any limit states is observed higher at the lower PGA level. Nevertheless, the probability of exceedance is minimal at higher PGA compared to the other two buildings.

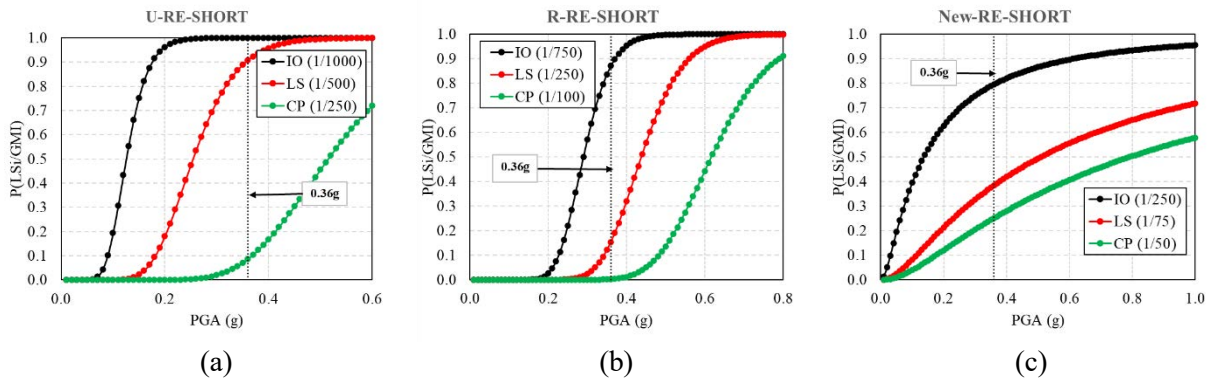


Figure 5.54 Fragility curve for (a) U-RE-SHORT; (b) R-RE-SHORT; (c) New-RE-SHORT.

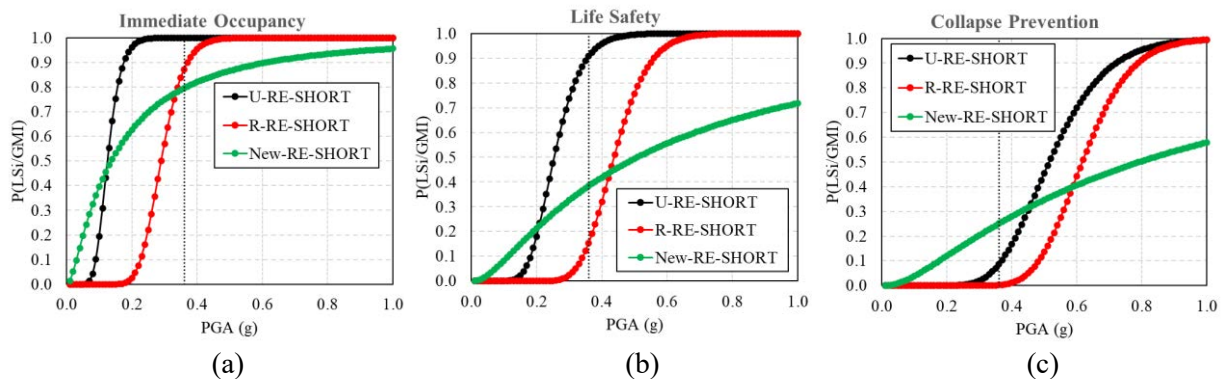


Figure 5.55 Comparisons of fragility curves at: (a) IO; (b) LS; (c) CP.

## 5.8 Conclusions

The chapter first presented the detailed seismic evaluation for traditional Rammed earth building with a typical plan with three distinctive parts: (a) Specification code, (b) Allowable stress calculation, and (c) Horizontal load-carrying capacity. From the specification code, it was clear that some of the geometrical configurations were not within the regulations prescribed. The analysis under allowable stress calculation showed that the RE building fails to satisfy allowable stress for both medium and severe level earthquakes. In the third level of analysis, the horizontal carrying capacity of RE building was found lower than the required value.

The strengthening technique (both for new construction and existing buildings) applied to the U-shaped wall, reported in Chapter 4, was further adopted into the full-scale building, and their efficacy is evaluated by the full-scale static test. Five full-scale rammed earth buildings having the same geometry and architectural plan are considered for the test: i) Unreinforced RE loaded in short span (U-RE-SHORT), ii) Unreinforced RE loaded in long span (U-RE-LONG), iii) Retrofitted RE loaded in short span (R-RE-SHORT), iv) Retrofitted loaded in long span (R-RE-LONG) and v) Reinforced RE loaded in short span (New-RE-SHORT). The use of mesh-wrap retrofitting technique not only regained its original strength but its capacity was improved by 2.43 and 3.25 times, respectively for R-RE-SHORT and R-RE-LONG. With the use of RC post and RC bands, the capacity of the building (New-RE-SHORT) was found to be 2.54 times its unreinforced counterpart U-RE-SHORT. There was also a significant improvement in the energy absorption and ductility using mesh-wrapped retrofitting technique and the use of RC posts and bands. The energy absorption increment of R-RE-SHORT, R-RE-LONG and New-RE-SHORT was 12.5, 7.48 and 44 times their counterparts, respectively. And the increment in ductility for R-RE-SHORT, R-RE-LONG and New-RE-SHORT was 2.22, 1.38 and 4.27 times their counterparts, respectively. The proposed strengthening techniques also controlled the failure mechanism. The limit state of RE houses was derived based on the degree of damage observed during the experimentation.

The last section of the chapter presents the non-linear pushover analysis for seismic evaluation of rammed earth buildings. The non-linear pushover analysis is a powerful tool for evaluating the inelastic seismic behaviour of structures. Among several simplified methods, the Capacity Spectrum Method (CSM) procedure specified by Japan's Building Standard Law is used. The performance point of a particular PGA level was acquired for each building specimens, which

forms the basis for the generation of fragility curves. The first fragility curves are generated for traditional Bhutanese houses. It can be used to assess the seismic vulnerability or predict the potential damage during an earthquake. It was observed that the poor compaction near RC posts led to the appearance of shrinkage cracks near it, which affected the overall performance of the building. Therefore, it is essential to monitor during the construction process to avoid poor compaction strictly.

## References

- [1] P. Roberto, F. De Filippi, M. Bosetti, T. Aoki, and P. Wangmo, “Influence of Traditional Building Practices in Seismic Vulnerability of Bhutanese Vernacular Rammed Earth Architecture,” *Int. J. Archit. Herit.*, pp. 1–20, 2020, doi: 10.1080/15583058.2020.1785044.
- [2] NRICPT and Department of Culture Ministry of Home and Cultural Affairs, “Study on the Conservation of Rammed Earth Buildings in the Kingdom of Bhutan,” 2015. [Online]. Available: <http://www.tobunken.go.jp>.
- [3] DCHS, *Typology study on Bhutanese rammed earth buildings*. Thimphu: Division for Conservation of Heritage Sites, Department of Culture, Ministry of Home and Cultural Affairs, Royal government of Bhutan, 2017.
- [4] DCHS, *General Guideline for improved seismic resilient construction techniques for rammed earth structures in Bhutan*. Division for Conservation of Heritage Sites, Department of Culture, Ministry of Home and Cultural Affairs, Royal government of Bhutan, 2017.
- [5] K. C. Shrestha *et al.*, “Full–Scale Pull–Down Tests on a Two–Storied Rammed Earth Building with Possible Strengthening Interventions,” in *Structural Analysis of Historical Constructions, RILEM Bookseries*, 2019, pp. 1557–1565, doi: 10.1007/978-3-319-99441-3\_167.
- [6] P. Wangmo, K. C. Shrestha, M. Miyamoto, and T. Aoki, “Assessment of out-of-plane behavior of rammed earth walls by pull-down tests,” *Int. J. Archit. Herit.*, vol. 13, no. 2, pp. 273–287, 2019, doi: 10.1080/15583058.2018.1433903.
- [7] M. Miyamoto, Pema, T. Aoki, and Y. Tominaga, “Pull-down test of the rammed earth walls

- at Paga Lhakhang in the Kingdom of Bhutan,” *Int. J. Sustain. Constr.*, vol. 2, no. 1, pp. 51–59, 2014, doi: 10.14575/gl/rehab2014/033.
- [8] K. C. Shrestha, T. Aoki, M. Miyamoto, P. Wangmo, and Pema, “In-plane shear resistance between the rammed earth blocks with simple interventions: Experimentation and finite element study,” *Buildings*, vol. 10, no. 3, pp. 1–13, 2020, doi: 10.3390/buildings10030057.
- [9] K. C. Shrestha *et al.*, “Strengthening of rammed earth structures with simple interventions,” *J. Build. Eng.*, vol. 29, p. 101179, 2020, doi: 10.1016/j.jobbe.2020.101179.
- [10] I. : 875 (Part 2)- 1987, “IS : 875 (Part 2) - 1987 (Reaffirmed) Code of Practice for Design Loads ( Other Than Earthquake ) for Buildings and Structures,” *Struct. Saf.*, vol. 875, no. March 1989, 2003.
- [11] IS:1893:2002, “Criteria for Earthquake Resistant Design of Structures - General Provisions and Buildings Part-1,” *Bur. Indian Stand. New Delhi*, vol. 1893 Part, 2002.
- [12] IS 456:2000, “Indian Standard 456:2000, Plain and Reinforced Concrete - Code of Practice,” *Bur. Indian Stand. Dehli*, pp. 1–114, 2000.
- [13] P. Wangmo, K. C. Shrestha, M. Miyamoto, and T. Aoki, “Assessment of out-of-plane behavior of rammed earth walls by pull-down tests,” *Int. J. Archit. Herit.*, vol. 13, no. 2, pp. 273–287, 2019, doi: 10.1080/15583058.2018.1433903.
- [14] ASTM Standard E8/E8M, “Tension Testing of Metallic Materials,” *ASTM International*. 2016, doi: 10.1520/E0008\_E0008M-16A.
- [15] J. S. J. Cheah, P. Walker, A. Heath, and T. K. K. B. Morgan, “Evaluating shear test methods for stabilised rammed earth,” *Proc. Inst. Civ. Eng. Constr. Mater.*, vol. 165, no. 6, pp. 325–334, 2012, doi: 10.1680/coma.10.00061.
- [16] K. Liu, M. Wang, and Y. Wang, “Seismic retrofitting of rural rammed earth buildings using externally bonded fibers,” *Constr. Build. Mater.*, vol. 100, pp. 91–101, 2015, doi: 10.1016/j.conbuildmat.2015.09.048.
- [17] Y. Wang, M. Wang, K. Liu, W. Pan, and X. Yang, “Shaking table tests on seismic

- retrofitting of rammed-earth structures,” *Bull. Earthq. Eng.*, vol. 15, no. 3, pp. 1037–1055, 2017, doi: 10.1007/s10518-016-9996-2.
- [18] ASTM C496, “Standard Test Method for Splitting Tensile Strength of Cylindrical Concrete Specimens,” *ASTM Int.*, 2011, doi: 10.1520/C0496.
- [19] ASTM C39, “Standard Test Method for Compressive Strength of Cylindrical Concrete Specimens: C39/C39M-18,” *American Society for Testing and Materials*. 2018.
- [20] M. Ekenel, F. De Caso, and A. N. Basalo, “Acceptance criteria for concrete and masonry strengthening using fabric-reinforced cementitious matrix (FRCM) and steel reinforced grout (SRG) composites,” 2018.
- [21] ATC 40, “Seismic evaluation and retrofit of concrete buildings,” *Appl. Technol. Council.*, 1996, doi: 10.1193/1.1586093.
- [22] R. El-Nabouch, Q. B. Bui, O. Plé, and P. Perrotin, “Assessing the in-plane seismic performance of rammed earth walls by using horizontal loading tests,” *Eng. Struct.*, 2017, doi: 10.1016/j.engstruct.2017.05.027.
- [23] Otani, S., Hiraishi, H., Midorikawa, M., and Tashigawara, M., 2000, New Seismic Design Provisions in Japan. *ACI Special Publication*, 197, 87–104.
- [24] J. A. Mahaney, T. F. Paret, B. E. Kehoe, and S. A. Freeman, “The capacity spectrum method for evaluating structural response during the Loma Prieta earthquake,” 1993.
- [25] Y. K. Wen, B. R. Ellingwood, and J. Bracci, “Vulnerability function framework for consequence-based engineering,” *Mid-America Earthq. Cent. Proj.*, pp. 1–101, 2004.

## SUMMARY AND FUTURE SCOPE

### 6.1 Summary

This thesis aims to evaluate and improve the seismic performance of the traditional Bhutanese rammed earth buildings, for both new construction and existing structures. This required the understanding of rammed earth from the mechanical and structural point of view. Further, it required to verify the appropriateness and effectiveness of proposed strengthening interventions.

In general, rammed earth is vulnerable to earthquakes due to its low tensile strength and heavyweight [1-3]. In addition to that, the traditional Bhutanese rammed earth buildings are irregular and lack an adequate connection between wall to wall, and wall to floor, which is undesirable under seismic actions. A thorough review has been made to understand the failure mechanism observed under earthquakes and the types of failure mechanism with their possible causes are highlighted in Chapter 2. Its vulnerability is further confirmed through the detailed structural analysis carried out with the available guideline on RE [4].

An experimental study on static element test was performed under compression and shear loading, and it is reported in Chapter 3. Here, the effect of thickness of the layer (50 mm and 100 mm) and the drying period (3 months and 12 months) was studied. The test results have shown that the compressive strength increases with the increase in drying period while its effect on shear strength was marginal. The thinner layer achieved better compaction than the thicker layer wallette and consequently improved the compressive strength and shear strength of the rammed earth wallette. Therefore, it is recommended to have a thinner layer in the wall block. The study also observed that mechanical strength improved as the vertical stress increased. A Mohr-Coulomb failure envelope is derived through a linear fit for shear strength values at various vertical stresses. From these, the critical parameters like cohesion and friction angle in shear strength of rammed earth are obtained.

The mesh-wrap strengthening technique was thoughtfully selected based on the material availability in the local market and its simplicity of the application. This technique involved the



use of mesh wrapped to the specimen wall surface on both faces anchored with screws and then plastered with cement mortar. The proposed mesh-wrap strengthening method is found to be effective in strengthening the RE walls under compression and shear loading. However, the mesh participation in increasing the strength was not as expected. Therefore, it is recommended to connect the mesh together, which not only enhance the strength but also avoid the mechanical incompatibility between the rammed earth wall and mesh composite. The non-linear behaviour of rammed earth was modelled with a two-dimensional finite element (FE) following both macro and micro-modelling approach based on the total strain rotating crack model. Both models were able to simulate the shear behaviour; however, only micro-model was able to reproduce the shear sliding. The modelling strategy used here can be referred to in the future analysis of whole rammed earth building.

The damage assessment report [5] showed that significant numbers of the rammed earth building failed in out-of-plane. In chapter four, four possible strengthening measures were presented for both new construction and existing buildings to improve their out-of-plane behaviour. For new construction, the strengthening measure included the use of only RC dowels and wedges as one method and the use of RC posts, wedges and bands as another method. In the first method, RC wedges and RC dowels were introduced between the RE blocks horizontally and vertically, respectively, to improve the wall's integrity. Both RC dowels and RC wedges were precasted. In the second method, RC dowels were replaced by RC posts, and they were casted on-site during the wall construction. Unlike RC dowels, RC posts were provided from the foundation base to the wall's top. The second method also involved the use of RC wedges embedded within the RE blocks in horizontal. Additionally, RC band was provided at the top of the wall, which not only integrated two side walls with the front wall but also connected all RC posts together to achieve box action. The test results have shown the RC dowels and wedges alone does not improve the overall integrity of the wall. Therefore, it is recommended to provide RC posts starting from the foundation to the wall top and also RC band to connect the whole wall. The use of the second reinforcing method increased the wall's strength by 3.19 times the unreinforced counterpart. For the existing buildings, the mesh-wrapped and timber-framed technique were evaluated as possible strengthening measures. The mesh-wrapped retrofitting technique involved the use of mild steel mesh wrapped around the wall in both faces with stabilized earth-based plaster finishing. A timber-framed retrofitting technique involved the placement of timber member on both faces of the wall,

configured in a grid system. Among the two techniques considered, timber framing was found clearly disrupting the visual aspects of the wall's facade and further, it needed special considerations for anchoring the vertical posts to the foundation. On the other hand, the mesh-wrapped strengthening technique is found a comparatively more straightforward and practical approach for retrofitting the existing RE wall. The use of mesh-wrapped retrofitting technique improved the wall's strength by 1.72 times the unreinforced wall. The experimental results for unreinforced wall are further reinforced and supported by the three-dimensional finite element modelling based on the total strain rotating crack model. The FE results satisfactorily reproduced the experimental results. The finite element tool developed here serve as an essential tool for verification as well as check for design specifications for rammed earth walls, whose experimental works cost a substantial amount of money and time.

RC posts with RC bands and mesh-wrapped strengthening technique with cement plaster finishing were selected as appropriate and feasible strengthening measures for new construction and existing structures, respectively, based on the element test and pull-down test observations. Although the mesh-wrapped retrofitting technique is applicable for the new construction as well, RC bands and RC posts are chosen since their contribution to strength increment was observed significantly higher, as detailed in Chapter 4. Their effectiveness and feasibility were further reinforced through conducting a full-scale test on five prototypes traditional RE buildings loaded in short span and long span. Both the techniques were found too have effective in improving the base shear capacity and energy absorption, and further delayed the damages on the structures. The use of mesh-wrapped retrofitting technique has improved the capacity of the building by 2.43 and 3.25 times for the building loaded in short span and long span, respectively. The use of RC bands and RC posts have improved the capacity of the building by 2.55 times the unreinforced building. Based on the experimental results, the following strengthening measures are proposed: appropriate and straightforward for Bhutanese RE buildings. They have the potential to be adopted in the neighbouring countries:

- i. Mesh-wrapped retrofitting technique with cement plaster is recommended for strengthening the existing buildings. To avoid the material incompatibility, anchor rods are necessary to connect the mesh at both faces of the wall, and therefore it is highly recommended. As for the aesthetic view, many rammed earth houses in Bhutan are

whitewashed with quicklime; therefore, a building owner can opt for whitewashing after the cement plaster. The other option is to use stabilized earth-based plaster, as reported for retrofitting a U-shaped wall with mesh under Chapter 4. The adopted earth-based plaster is aesthetically compatible with the actual rammed earth finishing; however, the strength increment was recorded 1.75 times its unreinforced counterpart, which is lower compared to the strength enhancement achieved with use of cement plaster finishing. Although the mesh-wrapped retrofitting technique is found to have improved the behaviour of rammed earth walls, their durability is questionable. Therefore, future research should address the durability of the proposed retrofitting technique.

- ii. RC posts and RC bands are recommended for the new rammed earth construction. The use of RC post will improve the building's tensile strength, while the use of RC bands will achieve integral box action in the building. RC band at all floor, lintel and sill levels are recommended. It should be noted that when RC posts are embedded with the wall, it is likely to result in poor compaction near the RC post areas. Ramming carefully with extra effort and attention near those areas can avoid such poor compaction. Another way of avoiding compromised compaction near RC post can be achieved by using a rammer with a different shape at the base that can ease the compaction in a circular motion. A compaction steel plate with holes can also be used, as illustrated in Figure 6.1. A similar compaction technique was used in the previous study [6].

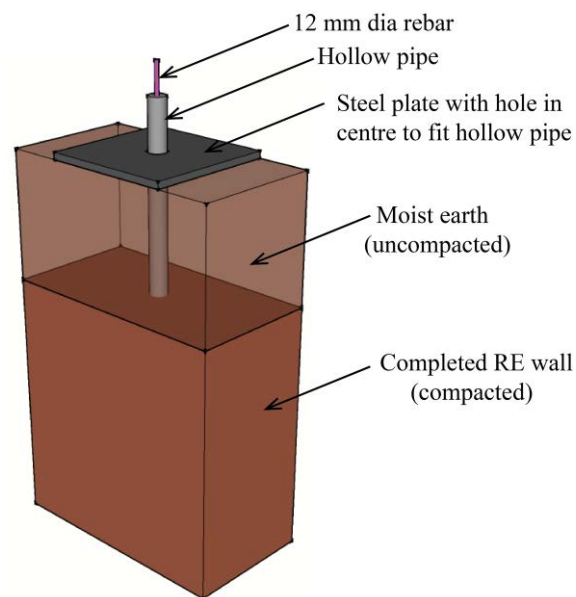


Figure 6.1 Schematic illustration of compaction technique with steel plate.

Limit states for unreinforced, reinforced and retrofitted rammed earth buildings are proposed based on the damages observed. Furthermore, the first conventional fragility curves for traditional Bhutanese rammed earth residential houses are presented, generated based on the Capacity Spectrum Method. Bhutan currently does not have seismic risk maps. Therefore, the fragility curves developed in this study can be referred in future to prepare the seismic risk maps.

## 6.2 Future Work

Some potential developments in the present work are summarised as follows:

- Although the proposed strengthening measures are found practical and feasible, their durability can be questionable. Therefore, we will adopt proposed strengthening measures on traditional RE houses, in particular the mesh-wrapped retrofitting technique. The durability will be monitored on long term basis.
- The current work presents only the static behaviour of traditional RE buildings, and their dynamic behaviour is not studied. We will perform dynamic shaking table test on 1/3<sup>rd</sup> scale of building specimen presented in Chapter 5. The experiment will be conducted using real-time earthquake data. The torsional effect and efficacy of strengthening measures will be assessed while studying the dynamic behaviour.
- Detailed finite element modelling on the full-scale RE building would be an interesting subject in itself. Future work will include 3D modelling using experimental data. The influence of physical characteristics of the wall (such as length, height and thickness) and mechanical characteristics (such as compressive strength, tensile strength and Young's Modulus) will be assessed through sensitivity analysis.
- Bhutan does not have proper seismic hazard map, and the one available is rudimentary. The concerned agency, Department of Geology and Mines, are making a constant effort to have one for the country. Seismic risk maps will be prepared for the two pilot sites (Eusana, Paro for Rammed earth and Ura, Bumthang for stone masonry) integrating the fragility curves and seismic hazard map.
- There is no proper guidelines and buildings standards for Bhutan. The outcome of the thesis will be used in the development of the guidelines and finally into a building standard.

- A series of capacity building programs will be developed inclusive of both hands-on training and seminars and disaster risk reduction education, targeting at technical personnel, local artisans, and the general public on how to build seismic resilient homes.

## References

- [1] J. S. J. Cheah, P. Walker, A. Heath, and T. K. K. B. Morgan, “Evaluating shear test methods for stabilised rammed earth,” *Proc. Inst. Civ. Eng. Constr. Mater.*, vol. 165, no. 6, pp. 325–334, 2012, doi: 10.1680/coma.10.00061.
- [2] K. Liu, M. Wang, and Y. Wang, “Seismic retrofitting of rural rammed earth buildings using externally bonded fibers,” *Constr. Build. Mater.*, vol. 100, pp. 91–101, 2015, doi: 10.1016/j.conbuildmat.2015.09.048.
- [3] Y. Wang, M. Wang, K. Liu, W. Pan, and X. Yang, “Shaking table tests on seismic retrofitting of rammed-earth structures,” *Bull. Earthq. Eng.*, vol. 15, no. 3, pp. 1037–1055, 2017, doi: 10.1007/s10518-016-9996-2.
- [4] DCHS, *General Guideline for improved seismic resilient construction techniques for rammed earth structures in Bhutan*. Division for Conservation of Heritage Sites, Department of Culture, Ministry of Home and Cultural Affairs, Royal government of Bhutan, 2017.
- [5] DCHS, *Damage Assessment of Rammed Earth Buildings-After the September 18, 2011 Earthquake*. Division for Conservation of Heritage Sites, Department of Culture, Ministry of Home and Cultural Affairs, Royal Government of Bhutan, 2011.
- [6] D. D. Tripura and K. D. Singh, “Mechanical behaviour of rammed earth column: A comparison between unreinforced , steel and bamboo reinforced columns,” *Mater. Construction*, vol. 68, no. 332, pp. 1–11, 2018, doi: <https://doi.org/10.3989/mc.2018.11517>

## List of Publications

### Refereed Journal Papers (Full paper reviewed)

- [1] P. Wangmo, K. C. Shrestha, M. Miyamoto, and T. Aoki, “Assessment of out-of-plane behavior of rammed earth walls by pull-down tests,” *International Journal of Architectural Heritage*, vol. 13, no. 2, pp. 273–287, 2019, doi: 10.1080/15583058.2018.1433903. {in Chapter 4}
- [2] K. C. Shrestha, T. Aoki, M. Miyamoto, P. Wangmo, Pema, J. Zhang, and N. Takahashi, “Strengthening of rammed earth structures with simple interventions,” *Journal of Building Engineering*, vol. 29, p. 101179, 2020, doi: 10.1016/j.job.2020.101179. {in Chapter 4}
- [3] K. C. Shrestha, T. Aoki, M. Miyamoto, P. Wangmo, and Pema, “In-plane shear resistance between the rammed earth blocks with simple interventions: Experimentation and finite element study,” *Buildings*, vol. 10, no. 3, 2020, doi: 10.3390/buildings10030057. {in Chapter 4}
- [4] P. Roberto, F. De Filippi, M. Bosetti, T. Aoki, and P. Wangmo, “Influence of traditional building practices in seismic vulnerability of Bhutanese vernacular rammed earth architecture,” *International Journal of Architectural Heritage*, pp. 1–20, 2020, doi: 10.1080/15583058.2020.1785044. {in Chapter 5}
- [5] P. Wangmo, K. C. Shrestha, and T. Aoki, “Exploratory study of rammed earth walls under static element test,” *Construction and Building Materials*, 2020, doi: 10.1016/j.conbuildmat.2020.121035. {in Chapter 3}
- [6] P. Wangmo, K.C. Shrestha, T. Aoki, M. Miyamoto, and Pema. “Strengthening Strategies for Existing Rammed Earth Walls Subjected to Out-of-Plane Loading”. *CivilEng*, 1(3), 229–242, 2020, doi:<https://doi.org/10.3390/civileng1030014>. {in Chapter 4}

### International conference proceedings (Abstract reviewed)

- [1] K. C. Shrestha, T. Aoki, T. Konishi, M. Miyamoto, J. Zhang, N. Takahashi, P. Wangmo, T. Aramaki, and N. Yuasa, “Full-scale pull-down tests on a two-storied rammed earth building with possible strengthening interventions,” in *Structural Analysis of Historical Constructions*, RILEM Bookseries, 2019, pp. 1557–1565, 2019, doi: 10.1007/978-3-319-99441-3\_167. {in Chapter 4}
- [2] K. C. Shrestha, T. Aoki, T. Konishi, M. Miyamoto, N. Takahashi, J. Zhang, P. Wangmo, N. Yuasa, S. Shin, Pema, K. Tenzin, “Static test on full scale rammed earth building with mesh-wrap retrofitting strategy,” in *12th International Conference on Structural Analysis of*

Historical Constructions, RILEM Bookseries, 2020. (Submitted for publication) {in Chapter 5}

- [3] P. Wangmo, K. C. Shrestha, T. Aoki, M. Miyamoto, N. Takahashi, J. Zhang, N. Yuasa, S. Shin, Pema, F.D. Filippi, R. Pennacchio, Mesh –wrap retrofitting for rammed earth buildings- Test results of full-scale static tests,” in 17th World Conference on Earthquake Engineering, Bosai/Disaster Management Expo, 2020. {in Chapter 5}

### **Domestic Conference Proceedings**

- [1] P. Wangmo, T. Aoki, K.C. Shrestha, M. Miyamoto, T. Konishi, T. Aramaki, J. Zhang, N. Takahashi, N. Yuasa, and H. Aoki, “Study on earthquake resistance technology of composite masonry buildings in Bhutan, Part 3: Element tests on reduce-scaled rammed earth walls,” in Summaries of technical papers of Annual Meeting, Architectural Institute of Japan, Structures-IV, pp. 907–908, 2018. {in Chapter 4}
- [2] N. Yuasa, T. Aoki, T. Aramaki, M. Miyamoto, K.C. Shrestha, N. Takahashi, J. Zhang, and P. Wangmo, “Study on earthquake resistance technology of composite masonry buildings in Bhutan, Part 2: Material strength of rammed earth.,” in Summaries of technical papers of Annual Meeting, Architectural Institute of Japan, Structures-IV, pp. 905–906, 2018. {in Chapter 3}
- [3] T. Konishi, T. Aoki, M. Miyamoto, K.C. Shrestha, N. Yuasa, N. Takahashi, J. Zhang, P. Wangmo, and T. Aramaki, “Study on earthquake resistance technology of composite masonry buildings in Bhutan, Part 4: Pull-down tests on real-scale rammed earth house: Test set-up and details,” in Summaries of technical papers of Annual Meeting, Architectural Institute of Japan, Structures-IV, pp. 909–910, 2018. {in Chapter 4}
- [4] K.C. Shrestha, T. Aoki, M. Miyamoto, J. Zhang, T. Aramaki, P. Wangmo, T. Konishi, N. Takahashi, N. Yuasa, and H. Aoki, “Study on earthquake resistance technology of composite masonry buildings in Bhutan, Part 5: Pull-down tests on real-scale rammed earth house: Test results and discussions,” in Summaries of technical papers of Annual Meeting, Architectural Institute of Japan, Structures-IV, pp. 911–912, 2018. {in Chapter 4}
- [5] S. Shin, N. Yuasa, T. Aoki, P. Wangmo, K.C. Shrestha, M. Miyamoto, N. Takahashi, and J. Zhang, “Study on earthquake resistance technology of composite masonry buildings in Bhutan, Part 7: Effect of water content at mixing and drying moisture content in specimen on

- the strength of rammed earth,” in Summaries of technical papers of Annual Meeting, Architectural Institute of Japan, Structures-IV, pp. 849-850, 2019. {in Chapter 3}
- [6] N. Yuasa, S. Shin, T. Aoki, K.C. Shrestha, P. Wangmo, M. Miyamoto, N. Takahashi, and J. Zhang, “Study on earthquake resistance technology of composite masonry buildings in Bhutan, Part 8: Quality control of cement mortar for stone masonry,” in Summaries of technical papers of Annual Meeting, Architectural Institute of Japan, Structures-IV, pp. 851-852, 2019.
- [7] S. Kanai, T. Aoki, K.C. Shrestha, M. Miyamoto, P. Wangmo, H. Aoki and S. Murai, “Study on earthquake resistance technology of composite masonry buildings in Bhutan, Part 9: Verification of seismic reinforcement for existing and new construction of rammed earth walls by pull-down tests,” in Summaries of technical papers of Annual Meeting, Architectural Institute of Japan, Structures-IV, pp. 853-854, 2019. {in Chapter 4}
- [8] S. Murai, M. Miyamoto, T. Aoki, K.C. Shrestha, P. Wangmo, H. Aoki and K. Shin, “Study on earthquake resistance technology of composite masonry buildings in Bhutan, Part 10: Verification of reinforcement effect for existing stone masonry wall by element tests and pull-down tests,” in Summaries of technical papers of Annual Meeting, Architectural Institute of Japan, Structures-IV, pp. 855-856, 2019.
- [9] H. Aoki, T. Aoki, K.C. Shrestha, M. Miyamoto, P. Wangmo, S. Murai and S. Kanai, “Study on earthquake resistance technology of composite masonry buildings in Bhutan, Part 11: Verification of reinforcement effect of new stone masonry by pull-down test,” in Summaries of technical papers of Annual Meeting, Architectural Institute of Japan, Structures-IV, pp. 857-858, 2019.
- [10] T. Aoki, K.C. Shrestha, M. Miyamoto, P. Wangmo, H. Aoki, S. Kanai, J. Zhang, N. Takahashi, N. Yuasa, and S. Murai, “Study on earthquake resistance technology of composite masonry buildings in Bhutan, Part 12: Full scale tests on composite masonry buildings: Test set-up, Instrumentation, Specimen details,” in Summaries of technical papers of Annual Meeting, Architectural Institute of Japan, Structures-IV, pp. 859-860, 2019.
- [11] P. Wangmo, T. Aoki, K.C. Shrestha, M. Miyamoto, H. Aoki, S. Kanai, J. Zhang, N. Takahashi, N. Yuasa, S. Murai, and S. Shin, “Study on earthquake resistance technology of composite masonry buildings in Bhutan, Part 13: Full scale tests on composite masonry buildings: Unreinforced and mesh-wrapped rammed earth construction,” in Summaries of



- technical papers of Annual Meeting, Architectural Institute of Japan, Structures-IV, pp. 861-862, 2019. {in Chapter 5}
- [12] K.C. Shrestha, T. Aoki, M. Miyamoto, P. Wangmo, H. Aoki, S. Kanai, J. Zhang, N. Takahashi, N. Yuasa, S. Murai, and S. Shin, “Study on earthquake resistance technology of composite masonry buildings in Bhutan, Part 14: Full scale tests on composite masonry buildings: Meshwrapped stone masonry with mud mortar,” in Summaries of technical papers of Annual Meeting, Architectural Institute of Japan, Structures-IV, pp. 863-864, 2019.
- [13] P. Wangmo, T. Aoki, K.C. Shrestha, M. Miyamoto, H. Aoki, S. Kanai, J. Zhang, N. Takahashi, N. Yuasa, S. Murai, and S. Shin, “Study on earthquake resistance technology of composite masonry buildings in Bhutan, Part 16: Full scale tests on composite masonry buildings: Strengthening techniques on rammed earth building,” in Summaries of technical papers of Annual Meeting, Architectural Institute of Japan, Structures-IV, pp. 819-820, 2020. {in Chapter 5}
- [14] K.C. Shrestha, T. Aoki, M. Miyamoto, P. Wangmo, S. Kanai, H. Aoki, S. Murai, J. Zhang, N. Takahashi, N. Yuasa, and S. Shin, “Study on earthquake resistance technology of composite masonry buildings in Bhutan, Part 17: Full scale tests on composite masonry buildings: Mesh-wrapped stone masonry with cement mortar construction,” in Summaries of technical papers of Annual Meeting, Architectural Institute of Japan, Structures-IV, pp. 821-822, 2020.
- [15] S. Kanai, T. Aoki, K.C. Shrestha, M. Miyamoto, N. Takahashi, J. Zhang, P. Wangmo, and S. Murai, “Study on earthquake resistance technology of composite masonry buildings in Bhutan, Part 20: Exhaustive survey of traditional architectural settlements in Western Bhutan,” in Summaries of technical papers of Annual Meeting, Architectural Institute of Japan, Structures-IV, pp. 827-828, 2020. {in Chapter 1}